CURRENT ADVANCES IN SOFT ROBOTICS: BEST PAPERS FROM ROBOSOFT 2018

EDITED BY: Helmut Hauser, Thrishantha Nanayakkara, S. M. Hadi Sadati, Fumiya Iida and Perla Maiolino

PUBLISHED IN: Frontiers in Robotics and AI

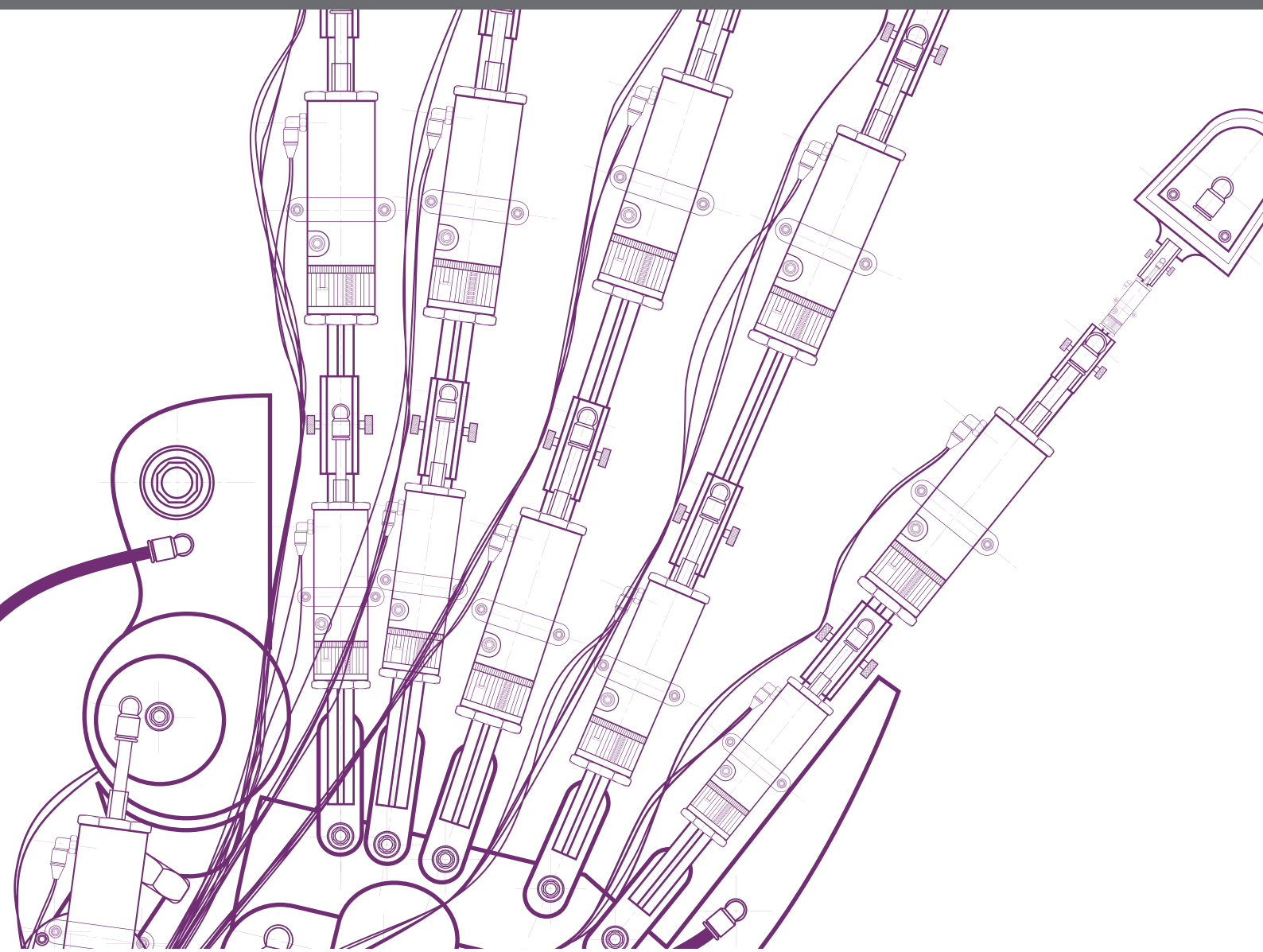

frontiers Research Topics

frontiers

ISSN 1664-8714
ISBN 978-2-88963-780-5
DOI 10.3389/978-2-88963-780-5

About Frontiers

Frontiers is more than just an open-access publisher of scholarly articles: it is a pioneering approach to the world of academia, radically improving the way scholarly research is managed. The grand vision of Frontiers is a world where all people have an equal opportunity to seek, share and generate knowledge. Frontiers provides immediate and permanent online open access to all its publications, but this alone is not enough to realize our grand goals.

Frontiers Journal Series

The Frontiers Journal Series is a multi-tier and interdisciplinary set of open-access, online journals, promising a paradigm shift from the current review, selection and dissemination processes in academic publishing. All Frontiers journals are driven by researchers for researchers; therefore, they constitute a service to the scholarly community. At the same time, the Frontiers Journal Series operates on a revolutionary invention, the tiered publishing system, initially addressing specific communities of scholars, and gradually climbing up to broader public understanding, thus serving the interests of the lay society, too.

Dedication to Quality

Each Frontiers article is a landmark of the highest quality, thanks to genuinely collaborative interactions between authors and review editors, who include some of the world's best academicians. Research must be certified by peers before entering a stream of knowledge that may eventually reach the public - and shape society; therefore, Frontiers only applies the most rigorous and unbiased reviews.
Frontiers revolutionizes research publishing by freely delivering the most outstanding research, evaluated with no bias from both the academic and social point of view. By applying the most advanced information technologies, Frontiers is catapulting scholarly publishing into a new generation.

What are Frontiers Research Topics?

Frontiers Research Topics are very popular trademarks of the Frontiers Journals Series: they are collections of at least ten articles, all centered on a particular subject. With their unique mix of varied contributions from Original Research to Review Articles, Frontiers Research Topics unify the most influential researchers, the latest key findings and historical advances in a hot research area! Find out more on how to host your own Frontiers Research Topic or contribute to one as an author by contacting the Frontiers Editorial Office: researchtopics@frontiersin.org

CURRENT ADVANCES IN SOFT ROBOTICS: BEST PAPERS FROM ROBOSOFT 2018

Topic Editors:
Helmut Hauser, University of Bristol, United Kingdom
Thrishantha Nanayakkara, Imperial College London, United Kingdom
S. M. Hadi Sadati, University of Bristol, United Kingdom
Fumiya Iida, University of Cambridge, United Kingdom
Perla Maiolino, University of Oxford, United Kingdom

Citation: Hauser, H., Nanayakkara, T., Sadati, S. M. H., Iida, F., Maiolino, P., eds. (2020). Current Advances in Soft Robotics: Best Papers From RoboSoft 2018. Lausanne: Frontiers Media SA. doi: 10.3389/978-2-88963-780-5

Table of Contents

frontiers in Robotics and AI

EDITORIAL
published: 21 April 2020
doi: 10.3389/frobt.2020.00056

Editorial: Current Advances in Soft Robotics: Best Papers From RoboSoft 2018

S. M. Hadi Sadati[1]*, *Perla Maiolino*[2], *Fumiya Iida*[3], *Thrishantha Nanayakkara*[4] and *Helmut Hauser*[5]

[1] Department of Surgical and Interventional Engineering, King's College London, London, United Kingdom, [2] Department of Engineering Science, Oxford Robotics Institute, University of Oxford, Oxford, United Kingdom, [3] Department of Engineering, University of Cambridge, Cambridge, United Kingdom, [4] Dyson School of Design Engineering, Imperial College London, London, United Kingdom, [5] Department of Engineering Mathematics, University of Bristol, Bristol, United Kingdom

Keywords: soft robot, soft actuator, soft sensor, continuum manipulator, fiber jamming, growing, 3D printing, learning-based modeling

Editorial on the Research Topic

Current Advances in Soft Robotics: Best Papers from RoboSoft 2018

The field of Soft Robotics extends the notion of conventional robotics by using material and actuation systems that go beyond rigid body parts and electric motors. Often, soft robots are inspired by soft and compliant structures in biological creatures. The result is a new, remarkable set of systems and solutions with high dexterity, reconfigurability, multi-functionality, and robustness. Furthermore, the Soft Robotics approach enables us to build mechanisms for growing and healing. Soft Robotics opens a new design space by developing and using novel materials and manufacturing approaches. The Soft Robotics community takes inspiration from nature and employs a highly multi-disciplinary approach involving several disciplines such as Material Science, Chemistry, Applied Mathematics, Physics, Biology, Control Theory, and Computer Science, etc. As a results, Soft Robotics can provide novel solutions for challenges that weren't possible or hard to overcome with conventional, rigid approaches. However, using soft technologies also poses new challenges, especially, related to sensing and actuation, modeling and control, and manufacturing and durability. Soft Robotics is a research field still in its infancy, but it has remarkable potential. Nevertheless, it still has to overcome a number of challenges before it can deliver off-the-shelf solutions. To address these challenges and form a community, the first IEEE international conference of Soft Robotics (RoboSoft 2018) was organized in Livorno (Italy) on 24-28 April 2018. This special issue includes 10 articles from this conference which have been picked by a committee. These papers highlight some of the challenges and new trends of the field.

For example, Soft Robotics is at the frontier of bio-inspiration. It uses solutions found by natural evolution as a source of inspiration. Along this lines, Del Dottore et al. proposed a kinematic model for the tip motion of growing robots to navigate 3D environments while negotiating confined spaces and large cavities by adapting their body. However, bio-inspiration can go even beyond simply copying biological systems. Chen et al. introduced RUBIC (the Rolling, Untethered, Ballooning, Intelligent Cube) uses controlled inflation to roll from one face of the cube to another, in any one of four planar directions. The result is a safe and predictable locomotion in complex environments. Another challenge is to design soft sensors and actuators. They must be flexible themselves. Furthermore, an integrated manufacturing approach is required to guarantee higher durability and repeatability of the system. Yirmibeşoğlu et al. showed

Edited and reviewed by:
Matteo Cianchetti, Sant'Anna School of Advanced Studies, Italy

***Correspondence:**
S. M. Hadi Sadati
smh_sadati@kcl.ac.uk

Specialty section:
This article was submitted to Soft Robotics, a section of the journal Frontiers in Robotics and AI

Received: *25 March 2020*
Accepted: *30 March 2020*
Published: *21 April 2020*

Citation:
Sadati SMH, Maiolino P, Iida F, Nanayakkara T and Hauser H (2020) Editorial: Current Advances in Soft Robotics: Best Papers From RoboSoft 2018. Front. Robot. AI 7:56. doi: 10.3389/frobt.2020.00056

the superior reliability of 3D printed pneumatic actuators with their molded counterpart made of polydimethylsiloxane (PDMS) when exposed to high radiation. For soft sensing, especially proprioceptive sensing capabilities are needed for precise motion and deformation control. The paper by Shih et al. presents a method which exploits 3D printing technology and commercial available 3D printing material to integrate resistive sensors in soft actuators. This provides a fully integrated system with proprioceptive capability and high repeatability. Soft actuation is another challenges. The field offers a wide range of possible approaches, like Dielectric Elastomer Actuators (DEA), Shape Memory alloy (SMA), and many other. For example, Minaminosono et al. use DEA to design a soft rotational motor that continues to function even under deformation. Cao et al. use DEAs to build a Micro Air Vehicle. It takes inspiration from insects that use their elastic thorax and muscle system as a damped oscillator to flap their wings at resonant frequency. The paper successfully demonstrated the use of DEA technology to implement such a design. While softness provides new capabilities, it also inherently carries new limitations. For example, compliant materials are often lacking durability, which is a key requirement for industrial systems. Dåmmer et al. proposed a Finite Element Approach framework for the optimized design of polyJet-printed bellows actuators and showed that a design made of Agilus30^{TM}soft material could withstand more load cycles, but suffer from material characteristic time dependency compared to one with TangoBlackPlus^{TM}material. Application-specific designs are another direct pathway for soft robots into real-world applications. Gong et al. presented an underwater robot equipped with a pneumatic manipulator benefiting from an opposite-bending-and-extension mechanism for delicate manipulation of irregularly shaped seafood animals of different sizes and stiffness at the bottom of the natural oceanic environment. Precision, often required in real-world scenarios such as surgical interventions, asks for high-stiffness modes in soft robot. Brancadoro et al. investigated fiber jamming transition as an effective technological approach for obtaining variable stiffness in slender soft structures. Finally, control challenges posed by soft robot composed of irregular shapes, and complex deformations are also one of the bottlenecks for industrial deployment. Learning-based control methods can offer flexibility and precision without a detailed theoretical model of the robot. Hyatt et al., for example, investigated model-based control of a pneumatic actuator using learned nonlinear discrete-time models and showing the potential of combining empirical modeling approaches with model-based control.

This special issue is a snapshot of current challenges in Soft Robotics. It highlights the great potential of the field, but also shows the number of exciting research questions it can offer. This includes the use of bio-inspiration, the development of novel soft actuation, sensing and computation capabilities, the integration of various materials with the help of novel manufacturing approaches, and the search for improved model and optimization frameworks, and many others. Using a highly interdisciplinary approach Soft Robotics has significantly extended the tool box for robot design and, therefore, enabled solutions to previously unsolved problems. We have now potential solutions at our fingertips for safe human-robot interaction, non-invasive surgery, robust autonomous locomotion, soft grippers for agricultural application, safe rehabilitation systems, haptic interfaces, and many others. The field is growing fast and soon Soft Robotics will be an integral part of a the common robotics approach.

AUTHOR CONTRIBUTIONS

All authors listed have made a substantial, direct and intellectual contribution to the work, and approved it for publication.

FUNDING

This work was partly funded by the Physical Sciences Research Council (EPSRC) MOTION grant [EP/N03211X/2]; and the Leverhulme Trust Morphological Computation with Spiders' Web Research Project [RPG-2016-345].

ACKNOWLEDGMENTS

We appreciate the work of the editorial and production staff of Frontiers in Robotics and AI and the members of the Research Topics team who encouraged us to undertake this project and helped with its implementation. We also acknowledge the work of the authors, editors, and reviewers who made this project possible.

Conflict of Interest: The authors declare that the research was conducted in the absence of any commercial or financial relationships that could be construed as a potential conflict of interest.

frontiers in Robotics and AI

ORIGINAL RESEARCH
published: 23 January 2019
doi: 10.3389/frobt.2018.00137

Toward a Dielectric Elastomer Resonator Driven Flapping Wing Micro Air Vehicle

*Chongjing Cao [1,2], Stuart Burgess [1,3] and Andrew T. Conn [1,3]**

[1] Bristol Robotics Laboratory, Bristol, United Kingdom, [2] Department of Aerospace Engineering, University of Bristol, Bristol, United Kingdom, [3] Department of Mechanical Engineering, University of Bristol, Bristol, United Kingdom

In the last two decades, insect-inspired flapping wing micro air vehicles (MAVs) have attracted great attention for their potential for highly agile flight. Insects flap their wings at the resonant frequencies of their flapping mechanisms. Resonant actuation is highly advantageous as it amplifies the flapping amplitude and reduces the inertial power demand. Emerging soft actuators, such as dielectric elastomer actuators (DEAs) have large actuation strains and thanks to their inherent elasticity, DEAs have been shown a promising candidate for resonant actuation. In this work a double cone DEA configuration is presented, a mathematic model is developed to characterize its quasi-static and dynamic performance. We compare the high frequency performance of two most common dielectric elastomers: silicone elastomer and polyacrylate tape VHB. The mechanical power output of the DEA is experimentally analyzed as a DEA-mass oscillator. Then a flapping wing mechanism actuated by this elastic actuator is demonstrated, this design is able to provide a peak flapping amplitude of 63° at the frequency of 18 Hz.

Keywords: flying robots, bio-inspired robotics, insect flight, electro-active polymer, dielectric elastomer actuator, resonance

OPEN ACCESS

Edited by:
Perla Maiolino, University of Cambridge, United Kingdom

Reviewed by:
Claudio Rossi, Polytechnic University of Madrid, Spain
Massimiliano Gei, Cardiff University, United Kingdom

***Correspondence:**
Andrew T. Conn
a.conn@bristol.ac.uk

Specialty section:
This article was submitted to Soft Robotics, a section of the journal Frontiers in Robotics and AI

Received: *21 September 2018*
Accepted: *17 December 2018*
Published: *23 January 2019*

Citation:
Cao C, Burgess S and Conn AT (2019) Toward a Dielectric Elastomer Resonator Driven Flapping Wing Micro Air Vehicle. Front. Robot. AI 5:137. doi: 10.3389/frobt.2018.00137

INTRODUCTION

In the last two decades, insect-inspired flapping wing micro air vehicles (MAVs) have attracted significant research interest for their potential for highly agile flight. Many MAV designs have been developed, such as Microrobotic Fly , DelFly (De Croon et al., 2009) and Robotic hummingbird (Keennon et al., 2012). One challenge all flapping wing MAV researchers have been facing is the extremely high power demands required for autonomous flight at micro scales. In nature, insects solve this problem by taking advantage of their elastic thorax and muscle system as a damped oscillator and flap their wings at its resonant frequency . Most species of flying insects utilize indirect flight muscles called dorsoventral (dvm) and dorsolateral (dlm) muscles to elevate and depress their wings, respectively, as illustrated in **Figures 1A,B**. The muscles are described as indirect as instead of directly driving the wings, they deform the highly elastic notum, the top plate of the thorax, which then drives the wings through the pleural wing process. Insects naturally excite this natural oscillator at its resonant frequency which amplifies the flapping stroke and greatly reduces inertial power demands . In conventional robotic technologies, actuators and power transmission mechanisms are all rigid, in order to incorporate elasticity into the MAV designs, additional elastic elements have to be added, which increase the weight and complexity of the system. To date, only few studies have utilized resonant excitation in flapping wing MAV designs [see e.g., (Baek et al., 2009; Bolsman et al., 2009; Zhang and Deng, 2017)]. By adding a spring to a motor driven flapping wing MAV, Baek et al. (2009) showed a 30% average power reduction by

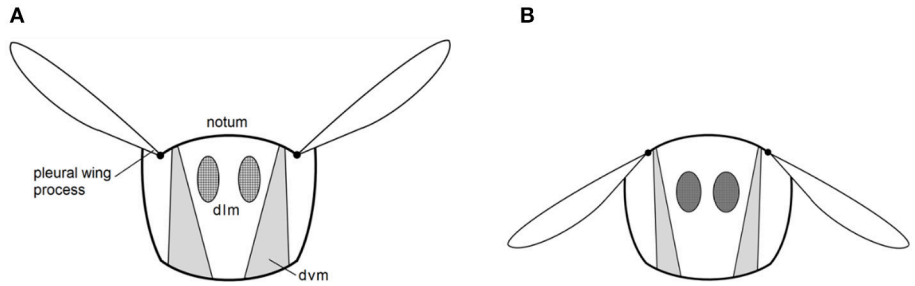

FIGURE 1 | Transverse view of the thorax of a typical indirect flight insect. The dorsoventral (dvm) and dorsolateral (dlm) muscles elevating **(A)** and depressing **(B)** the wings indirectly via the notum and pleural wing process (redrawn from Pringle, 1957).

driving the MAV at its resonance. Microrobotic Fly utilized the inherent elasticity of piezoelectric actuator and achieved a tethered flight at the resonant frequency of this system of 110 Hz. A comprehensive review on flapping wing MAV designs with integrated elastic elements can be found in Zhang and Rossi (2017).

Emerging soft actuators, such as dielectric elastomer actuators (DEAs) offer an alternative paradigm for designing flapping wing MAVs. Firstly, as an actuator, a DEA can generate large linear actuation strains that are comparable and even greater than muscles. Secondly, as an elastomer, the inherent elasticity of this material makes it capable of storing and releasing elastic energy, which is like the highly efficient elastomeric protein (resilin) found in the thorax of insects (Dudley, 2002). The large linear stroke and the inherent elasticity make DEA ideal for a novel flapping wing MAV design that mimics the resonant actuation found in insects without the complex transmission mechanisms and any additional elastic elements found in conventional flapping wing MAV designs. Another advantage of DEAs for MAV applications is the good scaling capability. Miniaturizing DEAs can be fairly easy, DEA membranes with the thickness of hundreds of nanometers have been reported (Töpper et al., 2015; Weiss et al., 2016), and multiple layers of DEA membranes can be stacked to generate a lager force and power output (Carpi et al., 2007; Kovacs et al., 2009). To date, only few DEA actuated flapping wing MAVs have been developed [see e.g., (Burgess et al., 2009; Henke et al., 2017; Lau et al., 2017)]. Lau and his co-workers (Lau et al., 2014, 2017) have developed rolled and stacked DEAs to flap the wings and these two designs demonstrated a flapping stroke of 10 and 2°, respectively at 1 Hz. Henke et al. (2017) have demonstrated a dragonfly-like flapping robot using a minimum energy structure mechanism and the flapping stroke is estimated to be about 15° at a few hertz. It should be noted that no aforementioned DEA-driven flapping mechanisms has utilized resonant actuation and the generated stroke and frequency are far from being high enough to enable flight. In contrast, insects have a typical flapping stroke of 120° and frequencies of 20 to over 200 Hz depending on the size of the species (Brodsky, 1994). In this work, we present a DEA-driven flapping wing MAV design which seeks to achieve a larger stroke amplitude and wingbeat frequency by utilizing the resonance actuation of DEAs. The concept of this design is illustrated in **Figures 2A,B** which is clearly inspired by the insect elastic thorax.

This paper is organized as follows. In section Double Cone Linear DEA Design, the design of the double cone linear actuator is introduced. The performance of two types of elastomers for DEAs in high frequency domain at which insect inspired MAV operate is compared. Analytical model is developed to predict the quasi-static performance of the double cone DEA and a spring-mass model is used to characterize its natural frequency. In section Power Output of the Double Cone DEA, we investigate the mechanical power output of the DEA as a function of actuation frequency. Then in section Flapping Wing MAV Design the resonant actuation of the DEA on a flapping mechanism is investigated. Finally, conclusions and future work are discussed.

DOUBLE CONE LINEAR DEA DESIGN

Design Overview

In this work, a double cone DEA configuration is employed as was developed in Choi et al. (2003) and Conn and Rossiter (2012). The general concept involves two dielectric elastomer membranes being separately bonded to two circular frames with a protrusion from a strut deforms the center of the membranes out-of-plane to form a double cone shape, as shown in **Figure 2**. The two membranes can be actuated separately to achieve bidirectional actuation. Apart from the advantage of natural agonist-antagonist configuration, the double cone DEA design also has a good compactness, high mass-specific energy density and can be fabricated consistently. The actuation principle of a double cone DEA is explained as follows. Due to the similar geometry and stretch ratio, top and bottom membranes exert an equal reaction force on the strut, which makes the strut balance in the middle (assuming the weight of the strut is negligible). However, when an electric field is applied on one membrane, the generated Maxwell stress reduces the force exerted by this membrane, the imbalance in forces drives the strut toward the actuated membrane side until another force equilibrium is achieved. As the Maxwell stress is directly related to the electric field applied to the DEA, electric fields in the range of 50–100 V/μm are usually used.

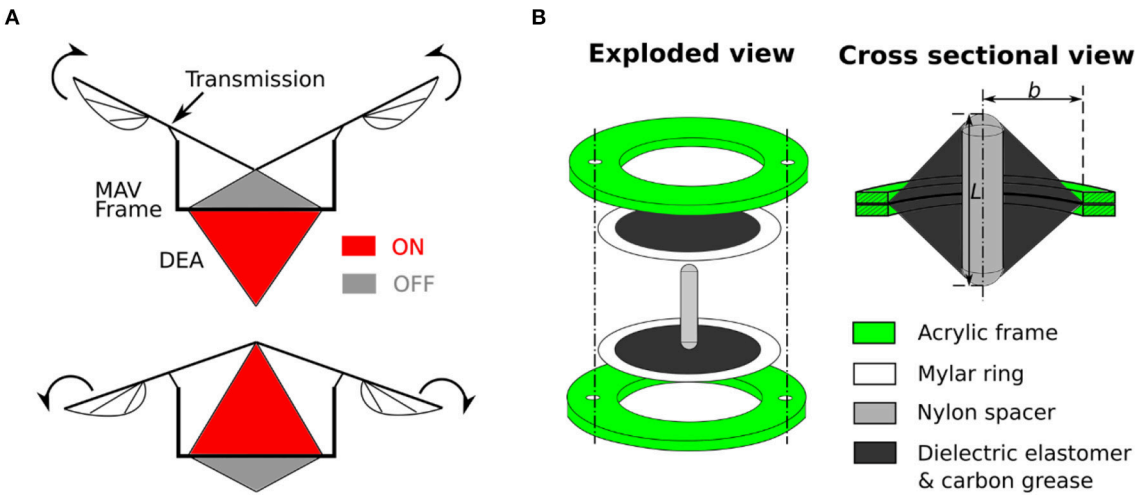

FIGURE 2 | (A) Proposed flapping mechanism where the antagonistic linear double cone DEA is attached to the frame and drives the wings via a transmission mechanism. **(B)** Schematic design of a double cone actuator with the inner frame radius, *b*, and spacer height, *L*, labeled.

Actuator Material Characterization

Polyacrylate tape VHB (3M) and silicone elastomers are the two predominant DEA materials. VHB has the advantages of large energy density and actuation strain (Carpi et al., 2011), its inherent adhesiveness and wide commercial availability also make it ideal for DEA prototyping. A potential drawback of VHB elastomer is its high viscoelasticity which limits the actuation bandwidth. On the other hand, silicone elastomers typically have a lower viscoelasticity, which makes them potentially more suitable for high frequency applications, such as MAVs where the frequency is usually over 10 Hz. The low viscoelasticity of silicone elastomers also makes them more likely to achieve resonance than VHB. To determine which material is more suitable for MAV applications, in this work, we compare the performance of VHB 4905 against an off-the-shelf silicone membrane (PARKER EAP 40 μm).

The fabrication process of the double cone DEA is described as follows. For VHB based DEA, a 0.5 mm thick VHB 4905 membrane was stretched biaxially by 4 × 4 and then bonded to a rigid acrylic frame with an inner radius *b*. For the silicone DEA, the elastomer membrane has an initial thickness of 40 μm, it was bonded to a 0.1 mm thickness Mylar ring using silicone adhesive (Smooth-On Sil-Poxy) without any pre-stretch and then attached to the acrylic frame. No pre-stretch was introduced to the Parker silicone elastomer as the out-of-plane deformation can introduce significant stretch on the membrane. In our previous study, the Parker silicone double cone DEAs with no pre-stretch showed the highest stroke and work output (Cao and Conn, 2018). Second, carbon conductive grease (M.G. Chemicals Ltd) was used as the compliant electrodes and was applied using a fine brush. Copper tape was used to connect the compliant electrodes and high voltage cables. Finally, the two circular frames were connected together using nylon fasteners. One nylon spacer with a height *L* was used as the support strut to deform the DEA membranes. The DEA components are shown in **Figure 2**.

In this work, the dynamic performance of the double cone DEAs is characterized by the free stroke as a function of the excitation frequency. The experiment followed the protocol suggested in Carpi et al. (2015) and is described as follows. Two double cone DEA specimens were fabricated, one using Parker silicone elastomer and the other one using VHB 4905. The geometries of the two specimens are identical, where the radius of the actuator membrane $b = 20$ mm and the strut height $L = 30$ mm. The frames of the actuator were fixed to the testing rig, while leaving the nylon spacer free to move. For each DEA, the two membranes were driven by two 180° out-of-phase sinusoidal voltage actuation waves with the amplitude of 1,920 V for Parker silicone membranes and 2,500 V for VHB (which equates to a nominal electric field of 60 and 100 V/μm, respectively). A frequency sweep from 1 to 100 Hz with a step of 5 Hz (step was reduced to 2 Hz near resonance) were conducted and at each frequency, 50 cycles were repeated to allow the actuator to reach a steady state. The actuation signals were generated using MATLAB (MathWorks) and sent to a high voltage amplifier (Ultravolt 5HVA23-BP1) via a DAQ (National Instruments BNC-2111). A laser displacement sensor (LK-G152 and LKGD500, Keyence) was used to measure the displacement of the DEA.

The displacement amplitudes of the DEAs and the phase differences between the input (actuation voltage) and output (displacement) signals against excitation frequency are shown in **Figures 3A,B**. As can be seen in **Figure 3A**, at low frequencies, both silicone and VHB specimens have a stroke close to 2 mm. Two peaks can be observed for silicone DEA specimen at 20 and 52 Hz, respectively. The first peak has a lower amplitude of 3 mm while the second peak has the amplitude of 7.1 mm, and is the mechanical resonant frequency of this specimen. The two amplitude peaks for silicone cone DEAs also have been demonstrated by Rizzello et al. (2015a,b) and is believed to due to the non-linearity of the Maxwell pressure (Maxwell pressure is proportional to the square of the actuation voltage)

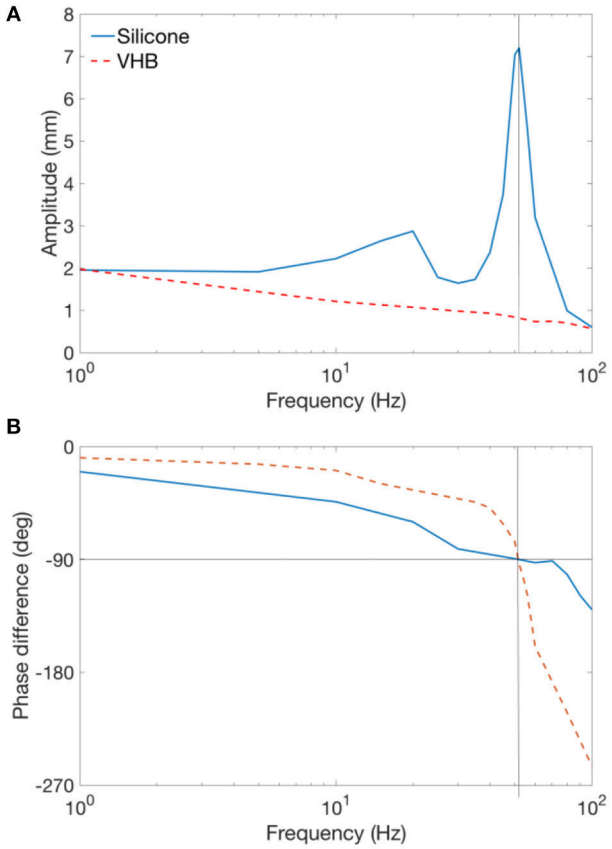

FIGURE 3 | Frequency sweep experiment for Parker silicone and VHB double cone DEA. **(A)** Amplitudes of the silicone and VHB specimen against actuation frequency. **(B)** Phase difference of the input and output signals of the silicone and VHB specimen against actuation frequency.

and this complex electro-mechanical dynamic phenomenon will be investigated further in the future. The amplitude at the resonance of this silicone DEA is over 355% than that at low frequencies (<10 Hz). The amplitude of the VHB specimen reduces continuously with the increasing actuation frequency and no peak was observed, this is due to the significant viscoelasticity of the material. As pointed out by Carpi et al. (2015) that, for high viscous damping materials which have no amplitude peak, the resonant frequency can be determined by the value that causes a phase shift of 90°. From **Figure 3B**, a 90° phase shift is found at 52 Hz for both silicone and VHB specimens. Which indicates that 52 Hz is the mechanical resonant frequency for both Parker silicone and VHB samples. This experiment clearly shows that silicone elastomer is superior to VHB for this double cone DEA configuration at in terms of bandwidth and resonant actuation thanks to its low viscous damping. In later sections, Parker silicone elastomer will be adopted for double cone DEA design.

Double Cone DEA Model

In this section we present a double cone DEA mathematic model. Hodgins et al. (2014) and Rizzello et al. (2015a,b) have developed approximated mathematical models to characterize the performance of conical DEAs with biasing springs and biasing mass. In their simulations, two important simplification assumptions were made, the first being a truncated cone shape approximation and the second involves homogeneous stress distribution on the membrane. However, as have been shown by an analytical model developed by He et al. (2010), Wang et al. (2016), and Wang (2018), the membrane deformation is in fact non-truncated and the stress distribution on the membrane is inhomogeneous. By utilizing this analytical approach, Bortot and Gei (2015) attempted to maximum the harvested energy of a cone DE generator by tuning the pre-stretch, geometrical ratio and intensity of maximum external load. Here we adopt this approach which is able to characterize the complex deformation and stress distribution on a conical DEA. We extend this to characterize double cone DEAs quasi-statically, and the simulation is then verified against experiments. Due to the extremely high computational cost to use this approach in a dynamic manner, we then use a simplified mass-spring oscillator model to predict the dynamic performance of this actuator.

Quasi-Static Model

As can be seen from **Figure 2**, the double cone configuration is in fact two pre-deformed single cones with an inertial load (Nylon spacer in this case). Due to the symmetry of the top and bottom cones, we will analyse a single cone first. A piece of elastomer membrane with an initial thickness T is first pre-stretched biaxially by a stretch ratio of λ_p. Then this pre-stretched membrane is bounded to a rigid ring with the radius b and an inner disk of radius a, as shown in **Figure 4A**. Compliant electrodes are coated on both sides of the membrane. A force F moves the inner disk out-of-plane relative to the outer ring by a distance h with an actuation voltage V applied across the electrodes. The membrane is deformed into a conical shape, as illustrated in **Figure 4B**. Due to this out-of-plane deformation, a particle on the membrane at position R (as marked red **Figure 4A**) now moves to the position of $[r(R), z(R)]$ in **Figure 4B**, where r is the current radius and z is the distance to the undeformed plane. The coordinates of (r, z) for $R = [a, b]$ describe the geometry of the conical DEA, and a summarize of this model is presented as follows [after (He et al., 2010) and adopted from Cao and Conn (2018)].

The state of the point R (r, z, θ) can be expressed as

$$\frac{dr}{dR} = \lambda_1' \cos\theta, \tag{1}$$

$$\frac{dz}{dR} = -\lambda_1' \sin\theta, \tag{2}$$

$$\frac{d\theta}{dR} = -\frac{s_2}{Rs_1} \sin\theta, \tag{3}$$

where s_1 and s_2 are the nominal longitudinal and radial stress, respectively and λ_1' is the radial stretch due to the out-of-plane deformation.

In quasi-static state, the external force F and the reaction force exerted by the deformed membrane are balanced, and this

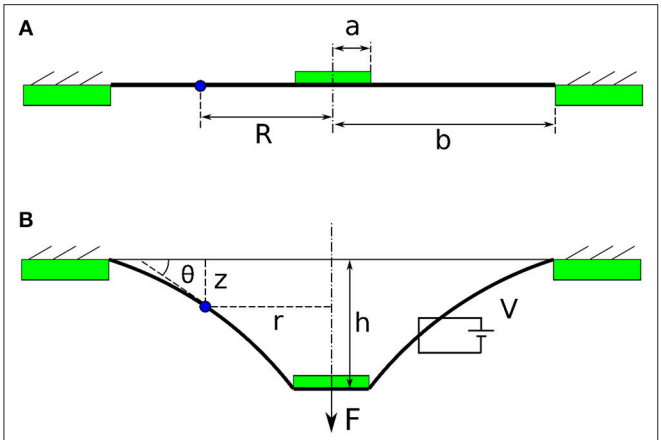

FIGURE 4 | The conceptual illustrations of a single cone DEA. **(A)** Pre-stretched membrane is bonded to a rigid ring and a central disk. **(B)** DEA membrane deforms out-of-plane with the existence of a force *F* and a voltage *V*.

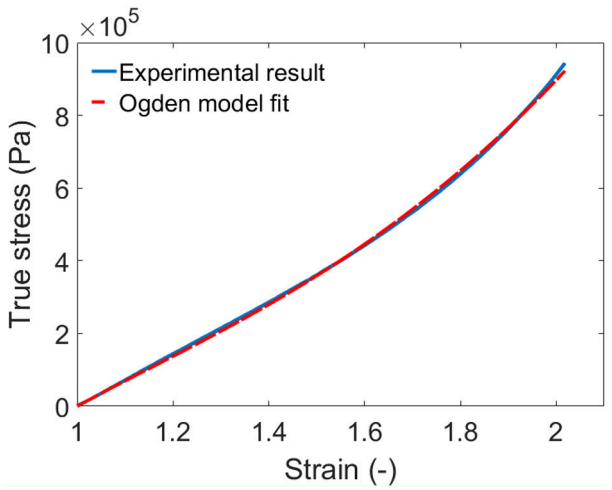

FIGURE 5 | Pure shear test of the silicone elastomer and the Ogden model fit.

relationship gives

$$2\pi \frac{T}{\lambda_1 \lambda_2} R\sigma_1 \sin\theta = F, \tag{4}$$

where $\sigma_1 = \lambda_1 s_1$.

The three differential equations (1–3) and an algebraic equation (4) govern the state of the DEA and are numerically solved in MATLAB using shooting method and "*ode15*" function.

This model can be used in two ways such that if the force F and voltage V are given, this model can predict the out-of-plane deformation h of the single cone DEA, or if the out-of-plane deformation h and the voltage V are known, this model can predict the force F. This model can be extended to a double cone DEA by the constrain: the sum of the out-of-plane deformation of the two membranes h_1 and h_2 is a constant value L. The physical meaning of this constrain is that as the out-of-plane deformation for a double cone DEA is caused by the spacer (as shown in **Figure 2**), the total deformation of the two membranes should always be the length of the spacer L. For a given deformation of the double cone DEA, the force exerted by the DEA can be solved using this model as $-F_1+F_2$ where F_1 and F_2 the forces exerted by top and bottom membranes, respectively.

Quasi-Static Model Validation

The stress–strain relationship of the silicone elastomer is described using the Ogden hyperelastic model (Ogden, 1972) in this work, as written in equation (5). In order to obtain the parameters in the Ogden model, a pure-shear pull test was conducted on a sample of the elastomer. **Figure 5** shows the experimental result and the fitted Ogden model. The model agrees very well with the measured data with the parameters of $\mu_1 = 1.287 \times 10^5\ Pa$, $\mu_2 = 2.6 \times 10^4\ Pa$, $\alpha_1 = 2$ and $\alpha_2 = 4$.

$$\sigma_1 = \mu_1 \left((\lambda_1)^{\alpha 1} - \frac{1}{(\lambda_1)^{\alpha 1} (\lambda_2)^{\alpha 1}} \right) + \mu_2 \left((\lambda_1)^{\alpha 2} - \frac{1}{(\lambda_1)^{\alpha 2} (\lambda_2)^{\alpha 2}} \right) \tag{5}$$

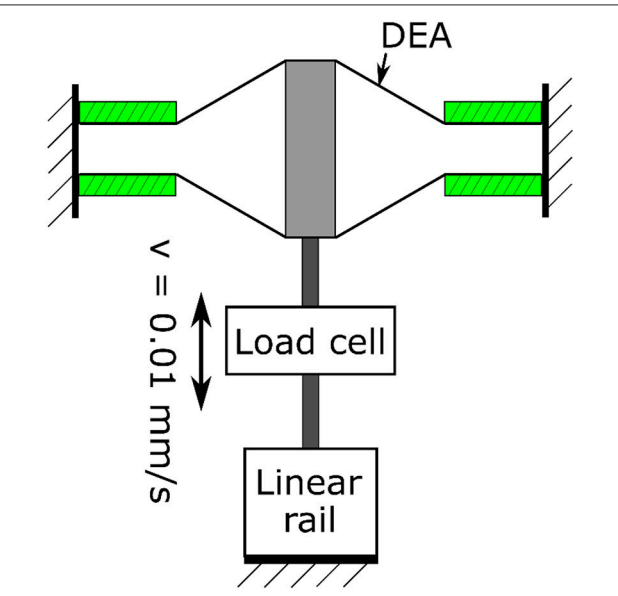

FIGURE 6 | Double cone DEA passive quasi-static test setup.

To verify the quasi-static model developed, three double cone DEAs with the spacer heights $L = 20$, 25 and 30 mm were used. The pre-stretch ratio is 1.0×1.0, $a = 4$ mm and $b = 20$ mm. The DEA was fixed to the testing rig and was deformed from its equilibrium position by a linear rail at a speed of 0.01 mm/s to eliminate the effect of viscosity. The experimental setup is illustrated in **Figure 6** and the experimental results are shown in **Figure 7**. The model agrees very well with the experimental results. Despite the non-linearity of the elastomer, the double cone DEA demonstrates an approximated linear passive force-displacement relationship, which means the stiffness of the actuator is approximately constant.

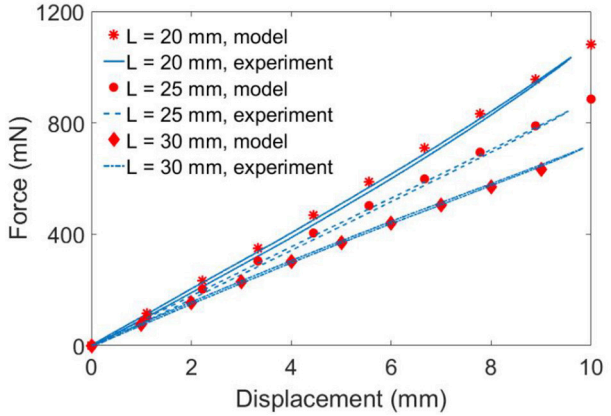

FIGURE 7 | Passive quasi-static experimental results and model predictions. $L = 20, 25, 30$ mm.

Double Cone DEA Resonance Characterization

In the last section, we have shown that a double cone DEA has an approximated linear force-displacement relationship, and can be treated as a linear spring. In dynamic actuation, this DEA can be simplified as a linear spring with an inertial load (mass of the spacer and any additional inertial load connected to the spacer). This configuration is very similar to that of a mechanical undamped oscillator, hence for dynamic characterization, in this work we simplify the DEA-mass oscillator as a linear undamped oscillator. As a result, the natural frequency f_0 of the DEA-mass oscillator can be expressed as $f_0 = \frac{\sqrt{\frac{K}{M}}}{2\pi}$, where K (N/m) is the approximated stiffness of the DEA and M (kg) is the mass of the spacer and any payload in the undamped oscillator (assuming the mass of the DEA membranes is negligible). The damping ratio of the DEA is neglected in the natural frequency characterization as the Parker silicone elastomer shows very low viscoelasticity thus we assume effect of damping from the elastomer can be negligible and the good agreement between the model prediction and experimental results suggests that this assumption holds.

To verify the simplified dynamic model, five DEA-mass oscillator specimens were fabricated with different stiffness and mass values. To adjust the stiffness K of these specimens, different spacer length L were used, as the spacer becomes longer, the two DEA membranes deform out-of-plane further and causing an increase in the stiffness K. The stiffness was also adjusted by adding a second layer of elastomer on the DEA. By adding an additional layer of membrane with the same pre-stretch to both top and bottom cones, the stiffness is doubled. The payload was adjusted by adding nuts to the spacer. **Table 1** lists the detailed values of the stiffness and mass of the five specimens, as well as their model predicted and measured resonant frequencies. The predicted resonant frequencies show a very good agreement with the experimental results with an average relative error of 1.98%. The promising results confirm that the linear spring simplification and the negligible damping ratio assumption hold. By comparing the five specimens, it can be noticed that the DEAs with heavier payload and lower stiffness have larger amplitudes at their resonance.

TABLE 1 | Comparison of the measured and model predicted resonant frequencies for the five DEA-mass oscillators.

	DEA 1	DEA 2	DEA 3	DEA 4	DEA 5
K (N/m)	63.5	63.5	63.5	41.4	127
M (g)	0.603	1.26	2.538	1.26	1.26
d (mm)	7.2	8.8	9.35	10.85	8.12
f_0 predicted (Hz)	51.8	35.7	25.2	28.8	50.5
f_0 measured (Hz)	52	37	26	28	51
Relative error of f_0	0.39%	3.64%	1.98%	2.9%	0.98%

POWER OUTPUT OF THE DOUBLE CONE DEA

Mechanical Power Output Against Excitation Frequency

High power output from the actuator is crucial for flapping wing MAV designs. The large amplitude of the silicone double cone DEA at its resonance could lead to a high power output. In this section, we investigate the mechanical power output of the silicone double cone DEA against its excitation frequency. Stacking multiple layers of DEA membranes have been shown to be able to amplify the force output of a DEA (Carpi et al., 2007; Kovacs et al., 2009). So in addition to exploiting resonance, increasing the number of layers of the DEA membrane may also increase the power output of the DEA. In this section, we also analyze the effect of layer numbers to the power output of the actuator. As increasing the number of layers will also increase the stiffness and the resonant frequency, in order to the keep the resonant frequency constant and ensures a consistent comparison, the payload also increases together with the layer number (recall that $f_0 = \frac{\sqrt{\frac{K}{M}}}{2\pi}$, as K increases, the mass M should increase with the same ratio to ensure a constant f_0). As the DEA-mass system oscillates, the instant mechanical power output is written as $P_{mech} = M\frac{d^2x}{dt^2}\frac{dx}{dt}$, where x is the displacement of the payload and t is time. The average mechanical power output is simply $P_{mech\_avg} = \frac{1}{T}\int_0^T P_{mech}dt$, where T is the period of one actuation cycle.

Experiment and Results

Four silicone double cone DEA specimens with different numbers of layers of membranes were fabricated, each specimen has the same frame radius b of 13 mm and the spacer height L of 13 mm. As discussed in previous section, to keep the resonant frequency constant, the payload has to increase with the layer numbers. Hence for the four specimens with 2, 4, 6 and 8 layers of silicone membranes, the payload for each specimen is 1, 2, 3 and 4 grams, respectively, which results in a constant resonant frequency of 45.8 Hz predicted by the dynamic model. Each layer includes Parker silicone elastomer, Mylar ring frame, carbon grease electrode and copper tape connection, the total mass is

0.12 g. Same frequency sweep from 1 to 100 Hz as described in Section Double Cone Linear DEA Design was conducted, and the experimental data was analyzed in MATLAB.

Figure 8 shows the measured average mechanical power output of each specimen against the excitation frequency. It can be noticed that at low frequencies (<35 Hz), the DEA outputs very low mechanical power. Then the average mechanical power output increases rapidly as the excitation frequency increases and peaks at the resonant frequency. The power output then drops when the excitation frequency is greater than the resonant frequency. **Figure 9** shows the time series of the displacement of the payload, the kinetic energy of the payload and the elastic energy stored in the elastomer at the resonance of the 2 layers DEA specimen. It is clear that at resonance, a close to 90° phase shift can be observed between the elastic energy stored in elastomer and the kinetic energy of the payload, which means that when each half stroke starts, the elastic energy of the elastomer is converted into the kinetic energy of the payload, this gives the mass a higher acceleration and faster velocity, hence a larger mechanical power output. When the mass approaches the end of a half stroke, its kinetic energy is converted into the elastic potential energy in the membranes, which is then released in the next half cycle. Apart from increasing the mechanical power output of the DEA, elastic energy recovery can also increase the efficiency, a detailed elastic energy recovery study on double cone DEAs can be found in Cao and Conn (2017).

From **Figure 8**, by comparing the mechanical power output of the four specimens, increasing the number of layers can increase the mechanical power output of a DEA. It should be noted that increasing the layer numbers also increases the capacitance of the DEA which increases the payload on the high voltage amplifier hence the maximum number of layers can be added is restricted by the high voltage amplifier (current amplifier has a maximum power output of 1 W). **Table 2** compares the average mechanical power output of the DEAs of 2, 4, 6, and 8 layers of membranes and the mass-specific powers at their resonant frequency, the mechanical power scaled up with the layer number as expected. However, maybe due to the increase in capacitance and the connection issue between DEA electrodes and high voltage channels, n layer specimens ($n > 2$) did not generate as much mechanical powers as $n/(n = 2)$ times than the 2-layer one. The mass-specific power, which is the mechanical power output divided by the total mass of the actuator, is about 100 mW/g at resonance. By comparison, the mass-specific power of insect flight muscle is estimated to be between 80 to 83 mW/g (Lehmann and Dickinson, 1997; Tu and Daniel, 2004). Piezoelectric actuators can have a mass-specific power as high as 400 mW/g (Steltz and Fearing, 2007), however, the actuation strokes is very low (<1%) and only this high mass-specific power is only achieved at high frequencies (say > 100 Hz) (Huber et al., 1997). On the contrary, the double cone DEA presented in this work has a very large stroke at its resonance (e.g., 99% stroke relative to the height of the DEA in **Figure 9**), it also has a mass-specific power close to insect flight muscle and an actuation bandwidth close to medium to large insect species, which makes it ideal for insect-inspired flapping wing MAV applications.

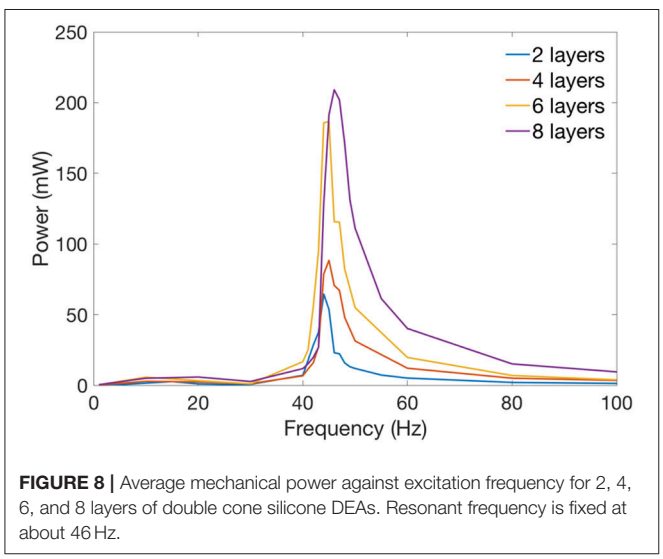

FIGURE 8 | Average mechanical power against excitation frequency for 2, 4, 6, and 8 layers of double cone silicone DEAs. Resonant frequency is fixed at about 46 Hz.

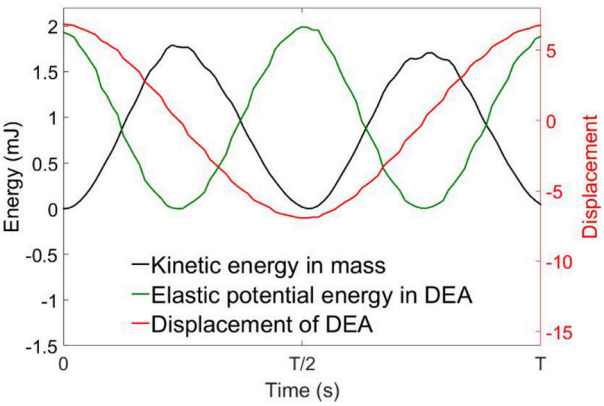

FIGURE 9 | Time series of the displacement, kinetic energy of the mass and elastic potential energy in the DEA membrane at its resonance. Kinetic energy and elastic energy are 90° out-of-phase.

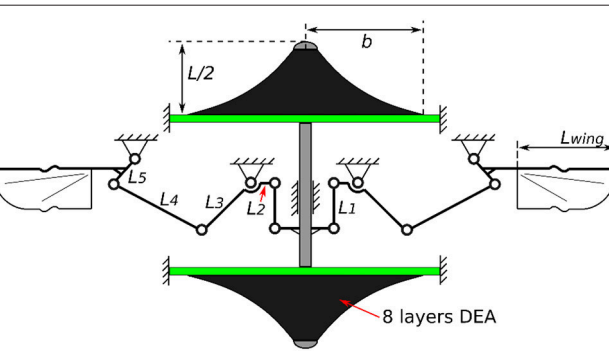

FIGURE 10 | Schematic diagram of the DE resonator driven flapping wing MAV design (not to scale).

FLAPPING WING MAV DESIGN

Design Overview

In this section we present a double cone DEA driven flapping wing MAV design with no additional elastic element added since the elasticity is embedded in the actuator itself. A schematic illustration of this design is shown in **Figure 10** with all the parameters listed in **Table 3**. In the last section we have shown that increasing the number of layers of DEA membranes can increase its mechanical power output, as a result, in this MAV design, eight layers of silicone elastomer were used to ensure a good power output from the actuator. The flapping mechanism includes a slider crank mechanism which converts the linear motion of the DEA into a reciprocal flapping motion and a double rocker mechanism to amplify the flapping stroke. Singularities are avoided by including two mechanical stops the slider. It should be pointed out that since the aim of this design is to demonstrate the concept of a DE resonator driven flapping wing MAV in benchtop tests and hence no optimization has been done to the size and weight of this mechanism to achieve free flight.

Flapping Tests and Results

The experimental setup is similar to that of the DEA-mass dynamic test. The flapping wing MAV was fixed to the testing rig and two square waves with an amplitude of 1,920 V and 180° phase shift were used to drive the antagonistic DEA membranes. An actuation frequency from 1 to 50 Hz with the steps of 5 Hz (step was reduced to 2 Hz near amplitude peak) was tested. The experiments were recorded by a camera (GoPro Session 5) at 100 frames-per-second. The stroke of the DEA was measured by the laser displacement sensor and the flapping stroke was estimated based on the DEA stroke and the DEA to flapping transmission ratio of this mechanism and verified against video footage (example video in **Supplementary Materials**).

In the first test, wings were not included to the mechanism, hence the DEA actuated the mechanism only. As is shown as the blue curve in **Figure 11**, the rotational stroke of this mechanism increases with the increasing actuation frequency first and peaks at a frequency of 34 Hz. The stroke then begins to reduce as the frequency increases further above 34 Hz, this is due to the inertia of the linkages and frictional loss.

In the second test, only the wing frames were connected to the flapping mechanism, which introduced the inertia of the wings to this system. No aerodynamic force was included in this set of experiment. As is shown in red dash curve in **Figure 11**, the inertia of the wings lowers the resonant frequency from 34 to 22 Hz, the flapping stroke is also reduced from 96 to 83°. Above the resonant frequency, the flapping stroke drops sharply as the frequency increases.

In the last test, wing membranes were included, which introduces aerodynamic drag to the system. The aerodynamic force reduces the peak flapping stroke to 63° at 18 Hz. **Figure 12** shows the flapping wing MAV with full wings attached at its top and bottom stop at 18 Hz. The measured displacement of the DEA and the estimated flapping angle of the mechanism at 18 Hz are shown in **Figure 13A**, as can be seen, despite that a square wave was applied to the DEA, the displacement is approximately sinusoidal.

An empirical equation that describes the mass that can be supported during hovering is given by Ellington (1999) in Equation 6, based on this equation, the current prototype can generate a lift of about 133 mg.

$$m = 0.387\frac{\varnothing^2 n^2 R^4 C_L}{AR}, \tag{6}$$

where m is mass (kg), $\varnothing$ is flapping stroke (rad), n is frequency (Hz), R is the wing length (m), C_L is the lift coefficient ($C_L = 2$ to 3 for insect hovering) and AR is the aspect ratio of the wing.

TABLE 2 | Average mechanical power at resonance and the corresponding mass-specific power of 2, 4, 6, and 8 layers of double cone silicone DEA.

Number of layers n	**2**	**4**	**6**	**8**
P_{max} (mW)	64.49	88.38	186.6	209.1
$P_{max}/P_{max}(n=2)$	100%	137%	289%	324%
Mass-specific power (mW/g)	134.35	92.06	129.58	108.91

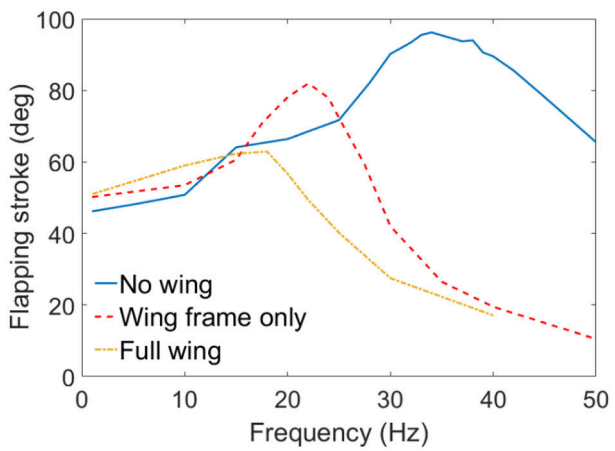

FIGURE 11 | Flapping strokes of the MAV against excitation frequency with no wing connected, wing frames only and full wings attached.

TABLE 3 | Design parameters and values for the flapping wing MAV design.

Parameter	L	b	L_1	L_2	L_3	L_4	L_5	L_{wing}	m_{wing}	AR
Value	13 mm	13 mm	8 mm	4 mm	8.5 mm	18 mm	5 mm	40 mm	0.14 g	6

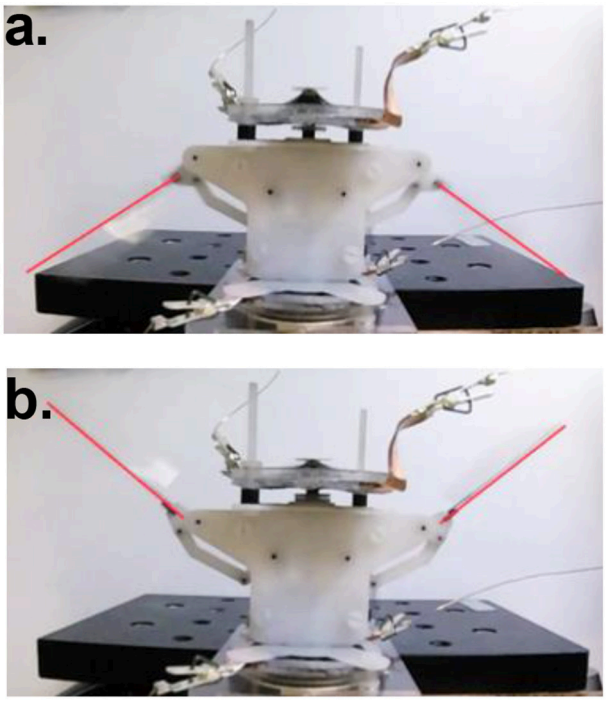

FIGURE 12 | DEA driven flapping wing MAV with full wings attached at 18 Hz, showing upper **(a)** and lower **(b)** stroke reversal.

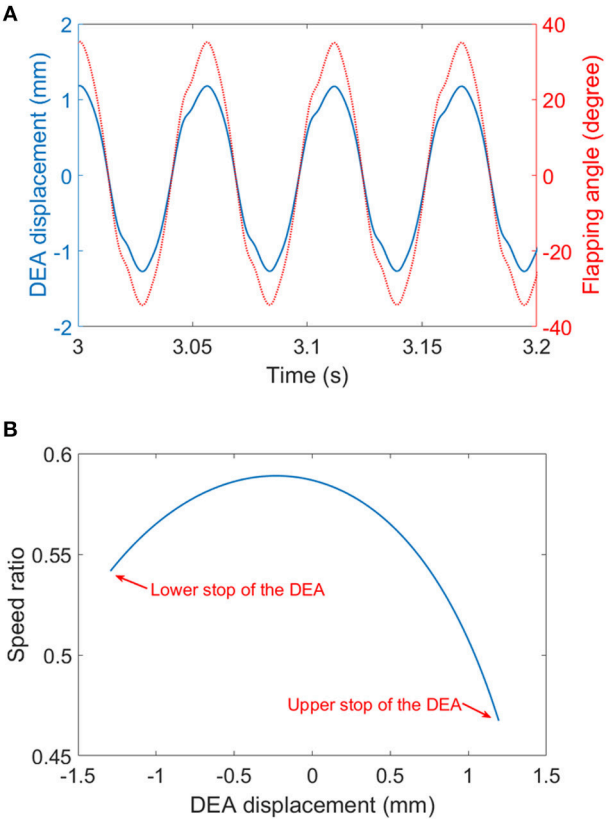

FIGURE 13 | (A) The displacement of the DEA (measured) and the flapping angle (estimated) at 18 Hz. **(B)** the speed ratio of the four-bar mechanism.

Discussion

The MAV test shows promising initial results for DEA driven flapping wing MAVs, however, it also suggests that to achieve hovering, significant improvements have to be made in both DEA designs and flapping mechanism optimizations. As the empirical aerodynamic equation (equation 6) suggests, to generate sufficient lift for a 10 g flapping wing MAV to achieve hovering flight, and by assuming the stroke amplitude $\varphi = 120°$ and $AR = 7$ [commonly seen in flying insects], the MAV has to flap its wings at 100 Hz for a wing length of 40 mm or at 20 Hz for a wing length of 80 mm. For DEAs with multiple layers stacked together, due to its large RC time constant ($\tau = RC$, where R is the resistance and C is the capacitance), it is favorable to actuate the DEAs at relatively low frequencies which will allow sufficient charging and discharging periods. As a result, a DEA actuated MAV with a pair long wings and a low resonant frequency possibly are preferred. Based on this discussion, further development can be made several key areas. First is to improve the electrode conductivity using alternative materials, such as carbon nanotubes [such as in Yuan et al. (2008)]. The reduction in the surface resistant of the DEA will improve its RC time constant, which means the actuator can respond faster to the input signal thus increasing the mechanical power output. Second is to optimize the coupling between the DEA and flapping mechanism so that long wings are used, and the resonance frequency is tuned at a relatively low value (say 15–25 Hz). Last but not least, the flapping mechanism can be optimized in terms of speed ratios by adjusting the link ratios.

In **Figure 13B,** the speed ratio of the flapping wing mechanism against the displacement of the DEA is plotted. It can be noted that the two reversals (i.e., upper and lower end stops) the speed ratios are the lowest, which suggest that when the DEA is trying the accelerate the wings, it has the poorest mechanical advantage. The low speed ratios at two reversals can be a significant limitation of this mechanism design. In the future work, the mechanism design should ensure that the speed ratios at the two reversals are the highest in one complete cycle. Compliant transmission mechanisms, such as active hinges as adopted in Wood (2008) can be used in the future mechanism designs to eliminate the effect of frictions and the elastic energy stored in the hinges can help accelerate the wings in the beginning of each stroke.

CONCLUSION

In this work, a double cone DEA driven flapping wing MAV was presented. First, two predominant dielectric elastomer materials polyacrylate tape VHB (3M) and silicone elastomers were compared. Frequency sweep test showed that the DEA made with silicone elastomer demonstrates a high peak in amplitude at its resonance while the DEA made with VHB has no peak at resonance due to its high viscoelasticity. This

result suggested that the low viscoelasticity of silicone elastomers makes them a better candidate for flapping wing MAV actuations. An analytical model and a simplified mass-spring model were used to characterize the quasi-static and dynamic performance of the silicone double cone DEA, respectively. The analytical model adopted in this work was able to predict the quasi-static performance of the actuator accurately and both the model and experimental results showed that double cone DEA has an approximated linear force-displacement relationship, which suggested that the DEA can be simplified as a linear spring. This finding then allowed us to use a classic spring-mass oscillator model to estimate the natural frequency of the DEA-mass oscillator in an extremely simple way yet high accuracy. The mechanical power output of the DEA was analyzed against the excitation frequency and the number of layers of membranes stacked to the DEA. The mechanical power output was shown to have a peak at the predicted resonant frequency of the DEA-mass system and the power scaled up with the number of layers of DEA membranes added to the DEA. A 209.1 mW average mechanical power output and an equivalent of 108.9 W/kg mass-specific mechanical power density from an 8-layer DEA was demonstrated. Subsequently, by using the same 8-layer DEA to drive the proposed insect-inspired flapping wing MAV, a peak flapping stroke of 63° at 18 Hz was demonstrated. While this flapping performance requires further optimization toward a hovering flight, this prototype far outperforms previous DEA-based flapping mechanisms without exploiting resonant actuations [e.g., a flapping amplitude of 15° in Henke et al. (2017) and 10° at a frequency of 5 Hz in Lau et al. (2014)]. For future work, we will continue working on optimizing the actuator and maximizing its mass-specific power, also, new flapping mechanism designs and fabrication techniques will be attempted to optimize the power transmission and efficiency.

DATA AVAILABILITY STATEMENT

Data are available at the University of Bristol data repository, data.bris, at https://doi.org/10.5523/bris.1pcnxotj9hpfr2wnjnhf1x5xst.

AUTHOR CONTRIBUTIONS

CC: data curation. CC, SB, and AC: formal analysis. CC, SB, and AC: investigation. CC, SB, and AC: methodology. SB and AC: supervision. CC: writing–original draft. AC: writing–review and editing.

ACKNOWLEDGMENTS

This work was supported by the EPSRC Centre for doctoral training in Future Autonomous and Robotic Systems (FARSCOPE) at the Bristol Robotics Laboratory where CC is a PhD student. AC was supported by EPSRC grant EP/P025846/1.

SUPPLEMENTARY MATERIAL

The Supplementary Material for this article can be found online at: https://www.frontiersin.org/articles/10.3389/frobt.2018.00137/full#supplementary-material

REFERENCES

Baek, S. S., Ma, K. Y., and Fearing, R. S. (2009). "Efficient resonant drive of flapping-wing robots," in *Intelligent Robots and Systems, IROS 2009. IEEE/RSJ International Conference* (St. Louis, MO).

Bolsman, C., Goosen, J., and Van Keulen, F. (2009). Design overview of a resonant wing actuation mechanism for application in flapping wing MAVs. *Int. J. Micro. Air Vehicles* 1, 263–272. doi: 10.1260/175682909790291500

Bortot, E., and Gei, M. (2015). Harvesting energy with load-driven dielectric elastomer annular membranes deforming out-of-plane. *Extreme Mech. Lett.* 5, 62–73. doi: 10.1016/j.eml.2015.09.009

Brodsky, A. K. (1994). *The Evolution of Insect Flight.* Oxford: Oxford University Press.

Burgess, S., Ling, C., Conn, A., Araromi, S., Wang, J., and Vaidyanathan, R. (2009). "Development of a novel Electro Active Polymer (EAP) actuator for driving the wings of flapping micro air vehicle," in *Computer Aided Optimum Design in Engineering*, eds S. Hernández and C. A. Brebbia (Southampton, UK: WIT Press), 207–217.

Cao, C., and Conn, A. (2018). Performance optimization of a conical dielectric elastomer actuator. *Actuators* 7:32. doi: 10.3390/act7020032

Cao, C., and Conn, A. T. (2017). "Elastic actuation for legged locomotion," in *Electroactive Polymer Actuators and Devices (EAPAD) 2017* (Portland).

Carpi, F., Anderson, I., Bauer, S., Frediani, G., Gallone, G., Gei, M., et al. (2015). Standards for dielectric elastomer transducers. *Smart Materials Struct.* 24:105025. doi: 10.1088/0964-1726/24/10/105025

Carpi, F., Kornbluh, R., Sommer-Larsen, P., and Alici, G. (2011). Electroactive polymer actuators as artificial muscles: are they ready for bioinspired applications? *Bioinspir. Biomim.* 4:045006. doi: 10.1088/1748-3182/6/4/045006

Carpi, F., Salaris, C., and De Rossi, D. (2007). Folded dielectric elastomer actuators. *Smart Materials Struct.* 16:S300. doi: 10.1088/0964-1726/16/2/S15

Choi, H. R., Jung, K. M., Kwak, J. W., Lee, S. W., Kim, H. M., Jeon, J. W., et al. (2003). "Digital polymer motor for robotic applications," in *Robotics and Automation, 2003. 2003 IEEE International Conference on Robotics and Automation (ICRA'03)* (Taipei).

Conn, A. T., and Rossiter, J. (2012). Towards holonomic electro-elastomer actuators with six degrees of freedom. *Smart Mater. Struct.* 3:035012. doi: 10.1088/0964-1726/21/3/035012

De Croon, G., De Clercq, K., Ruijsink, R., Remes, B., and de Wagter, C. (2009). Design, aerodynamics, and vision-based control of the DelFly. *Int. J. Micro Air Vehicles* 1, 71–97. doi: 10.1260/1756829097894 98288

Dudley, R. (2002). *The Biomechanics of Insect Flight: Form, Function, Evolution.* Princeton, NJ: Princeton University Press.

Ellington, C. P. (1999). The novel aerodynamics of insect flight: applications to micro-air vehicles. *J. Exp. Biol.* 23, 3439–3448.

He, T., Cui, L., Chen, C., and Suo, Z. (2010). Nonlinear deformation analysis of a dielectric elastomer membrane–spring system. *Smart Mater. Struct.* 8:085017. doi: 10.1088/0964-1726/19/8/085017

Henke, E., Wilson, K., and Anderson, I. (2017). "Entirely soft dielectric elastomer robots," in *Electroactive Polymer Actuators and Devices (EAPAD) 2017*, (Portland).

Hodgins, M., Rizzello, G., Naso, D., York, A., and Seelecke, S. (2014). An electro-mechanically coupled model for the dynamic behavior of a dielectric electro-active polymer actuator. *Smart Mater. Struct.* 10:104006. doi: 10.1088/0964-1726/23/10/104006

Huber, J., Fleck, N., and Ashby, M. (1997). The selection of mechanical actuators based on performance indices. *Royal Soc.* 453, 2185–2205. doi: 10.1098/rspa.1997.0117

Keennon, M., Klingebiel, K., Won, H., and Andriukov, A. (2012). "Development of the nano hummingbird: a tailless flapping wing micro air vehicle," in *AIAA Aerospace Sciences Meeting* (Reston, VA).

Kovacs, G., Düring, L., Michel, S., and Terrasi, G. (2009). Stacked dielectric elastomer actuator for tensile force transmission. *Sensors Actuators A Phys.* 2, 299–307. doi: 10.1016/j.sna.2009.08.027

Lau, G. K., Chin, Y. W., and La, T. G. (2017). "Development of elastomeric flight muscles for flapping wing micro air vehicles," in *Electroactive Polymer Actuators and Devices (EAPAD) 2017* (Portland, OR).

Lau, G. K., Lim, H. T., Teo, J. Y., and Chin, Y. W. (2014). Lightweight mechanical amplifiers for rolled dielectric elastomer actuators and their integration with bio-inspired wing flappers. *Smart Mater. Struct.* 2:025021. doi: 10.1039/9781782625209

Lehmann, F., and Dickinson, M. (1997). The changes in power requirements and muscle efficiency during elevated force production in the fruit fly Drosophila Melanogaster. *J. Exp. Biol.* 7, 1133–1143.

Ogden, W. (1972). Large deformation isotropic elasticity-on the correlation of theory and experiment for incompressible rubberlike solids. *Proc. R. Soc. A* 326, 565–584. doi: 10.1098/rspa.1972.0026

Pringle, J. (1957). *Insect Flight.* Cambridge: Cambridge University Press.

Rizzello, G., Hodgins, M., Naso, D., York, A., and Seelecke, S. (2015a). Modeling of the effects of the electrical dynamics on the electromechanical response of a DEAP circular actuator with a mass–spring load. *Smart Materials Struct.* 9:094003. doi: 10.1088/0964-1726/24/9/094003

Rizzello, G., Hodgins, M., Naso, D., York, A., and Seelecke, S. (2015b). Dynamic modeling and experimental validation of an annular dielectric elastomer actuator with a biasing mass. *J. Vibration Acoustics* 1:011005. doi: 10.1115/1.4028456

Steltz, E., and Fearing, R. (2007). "Dynamometer power output measurements of piezoelectric actuators," in *2007 IEEE/RSJ International Conference on Intelligent Robots and Systems (IROS)* (Rome).

Töpper, T., Weiss, F., Osmani, B., Bippes, C., Leung, V., and Müller, B. (2015). Siloxane-based thin films for biomimetic low-voltage dielectric actuators. *Sensors Actuators A Phys.* 233, 32–41. doi: 10.1016/j.sna.2015.06.014

Tu, M., and Daniel, T. (2004). Submaximal power output from the dorsolongitudinal flight muscles of the hawkmoth Manduca sexta. *J. Exp. Biol.* 26, 4651–4662. doi: 10.1242/jeb.01321

Wang, B., Wang, Z., and He, T. (2016). Investigation on the viscoelastic behaviors of a circular dielectric elastomer membrane undergoing large deformation. *AIP Adv.* 12:125127. doi: 10.1063/1.4973639

Wang, H. (2018). Viscoelastic analysis of a spring-connected dielectric elastomer actuator undergoing large inhomogeneous deformation. *Int. J. Mech. Sci.* 17–23. doi: 10.1016/j.ijmecsci.2017.12.004

Weiss, F., Töpper, T., Osmani, B., Peters, S., Kovacs, G., and Müller, B. (2016). Electrospraying nanometer-thin elastomer films for low-voltage dielectric actuators. *Adv Electron. Mater.* 2:1500476. doi: 10.1002/aelm.201500476

Wood, R. J. (2008). "The first take off of a biologically inspired at-scale robotic insect," in *IEEE Transcations on Robotics* 24, 341–347. doi: 10.1109/TRO.2008.916997

Yuan, W., H. L., Yu, Z. B., Lam, T., Biggs, J., Ha, S. M., et al. (2008). Fault-tolerant dielectric elastomer actuators using single-walled carbon nanotube electrodes. *Adv. Materials* 3, 612–625. doi: 10.1002/adma.200701018

Zhang, C., and Rossi, C. (2017). A review of compliant transmission mechanisms for bio-inspired flapping-wing micro air vehicles. *Bioinspir. Biomim.* 12:p025005. doi: 10.1088/1748-3190/aa58d3

Zhang, J., and Deng, X. (2017). Resonance principle for the design of flapping wing micro air vehicles. *IEEE Trans. Robot.* 33, 183–197. doi: 10.1109/TRO.2016.2626457

Conflict of Interest Statement: The authors declare that the research was conducted in the absence of any commercial or financial relationships that could be construed as a potential conflict of interest.

frontiers in Robotics and AI

ORIGINAL RESEARCH
published: 08 February 2019
doi: 10.3389/frobt.2019.00001

A Deformable Motor Driven by Dielectric Elastomer Actuators and Flexible Mechanisms

*Ayato Minaminosono[1], Hiroki Shigemune[1,2], Yuto Okuno[1], Tsubasa Katsumata[1], Naoki Hosoya[1] and Shingo Maeda[1]**

[1] Department of Mechanical Engineering, Shibaura Institute of Technology, Tokyo, Japan, [2] Department of Applied Physics, Waseda University, Tokyo, Japan

Soft robots with dynamic motion could be used in a variety of applications involving the handling of fragile materials. Rotational motors are often used as actuators to provide functions for robots (e.g., vibration, locomotion, and suction). To broaden the applications of soft robots, it will be necessary to develop a rotational motor that does not prevent robots from undergoing deformation. In this study, we developed a deformable motor based on dielectric elastomer actuators (DEAs) that is lightweight, consumes little energy, and does not generate a magnetic field. We tested the new motor in two experiments. First, we showed that internal stress changes in the DEAs were transmitted to the mechanism that rotates the motor. Second, we demonstrated that the deformable motor rotated even when it was deformed by an external force. In particular, the rotational performance did not decrease when an external force was applied to deform the motor into an elliptical shape. Our motor opens the door to applications of rotational motion to soft robots.

Keywords: dielectric elastomer actuator, internal stress, rotational performance, symmetry, strain, deformable

OPEN ACCESS

Edited by:
Thrishantha Nanayakkara, Imperial College London, United Kingdom

Reviewed by:
Priyanshu Agarwal, University of Texas at Austin, United States
Virgilio Mattoli, Fondazione Istituto Italiano di Technologia, Italy

***Correspondence:**
Shingo Maeda
maeshin@shibaura-it.ac.jp

Specialty section:
This article was submitted to Soft Robotics, a section of the journal Frontiers in Robotics and AI

Received: *30 June 2018*
Accepted: *11 January 2019*
Published: *08 February 2019*

Citation:
Minaminosono A, Shigemune H, Okuno Y, Katsumata T, Hosoya N and Maeda S (2019) A Deformable Motor Driven by Dielectric Elastomer Actuators and Flexible Mechanisms. Front. Robot. AI 6:1. doi: 10.3389/frobt.2019.00001

INTRODUCTION

Traditional robots are generally made of hard materials, but soft robots, which are made of rubber, gels, or paper, can provide dynamic motion, and innate safety based on the properties of their constituent materials (Maeda et al., 2015, 2016; Hosoya et al., 2016a; Shigemune et al., 2016, 2017). The advantages of soft robots will promote the development of human–robot coexistence. For example, in contrast to hard robots, soft robots can handle many kinds of materials: hard or soft, fragile or robust, and thick or thin (Suzumori et al., 1992; Shintake et al., 2015b; Galloway et al., 2016; Okuno et al., 2018), which is difficult for hard robots.

Rotational motion has been applied in robotics (Anderson et al., 2010). In traditional robots, magnetic motors are normally used to produce rotational motion. In previous works, researchers have developed motors driven by soft actuators (Kornbluh et al., 1998; Anderson et al., 2010, 2011; O'Brien et al., 2010; Hwang and Higuchi, 2014; Ainla et al., 2017). Ainla et al. developed a motor based on a pneumatic actuator that functions by feeding air into a flexible structure (Diesel and Brock, 2013; Cacucciolo et al., 2016). Although the pneumatic actuator has the potential to produce a large force, an additional pump is needed to feed the air, causing the whole system required to drive the motor via the pneumatic actuator to be large and heavy. In other studies, Hwang et al. developed a rotational motor based on shape memory alloys (SMAs). SMAs can recover their shape by increasing their temperature (Minetaa et al., 2002). SMAs are capable of generating large strokes

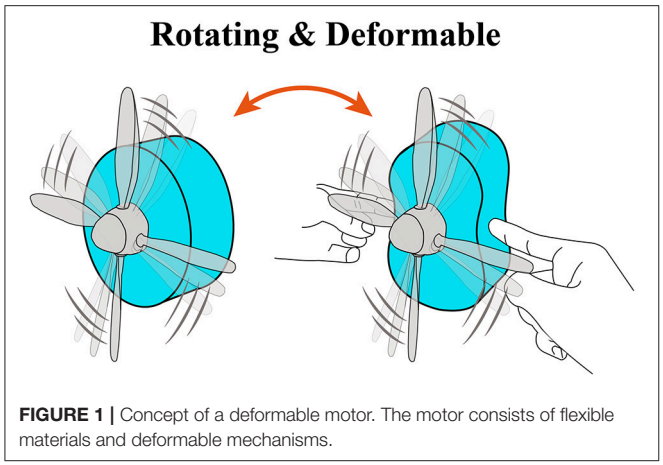

FIGURE 1 | Concept of a deformable motor. The motor consists of flexible materials and deformable mechanisms.

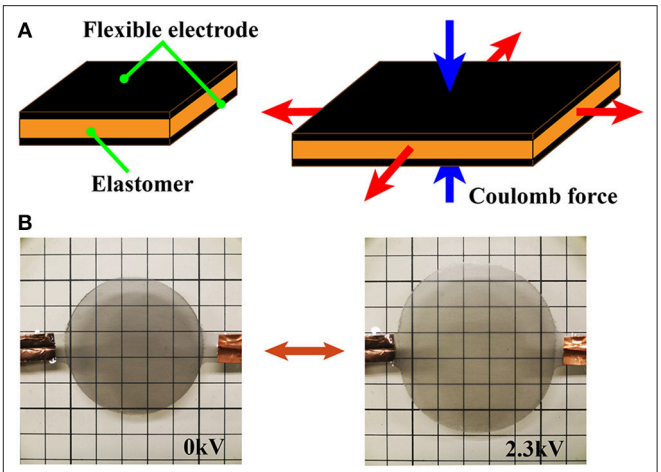

FIGURE 2 | Three-dimensional models and images of the mechanisms in the deformable motor. **(A)** Pressure determined by Equation (1). **(B)** Activation of a DEA when a voltage is applied.

and forces. However, SMAs consume a lot of energy and have slow response times. Anderson et al. developed a rotational motor based on dielectric elastomer actuators (DEAs) (Anderson et al., 2010). DEAs consist of elastomers sandwiched between compliant electrodes. Applying a voltage to the electrodes generates electrostatic forces, which produces a large displacement (Pelrine et al., 2000; Madden et al., 2004; Hosoya et al., 2015). The advantages of DEAs include: (1) simple and lightweight structures, (2) compatibility with low energy consumption, (3) generation of large actuation strokes, and (4) fast response time (Plante and Dubowsky, 2007). In addition, DEAs can be driven under deformation. Anderson et al. proposed a mechanism for converting the expansion of DEA into rotational motion by building a crank mechanism. They showed that the performance (torque per weight) in a motor based on DEAs was higher than that of the traditional magnetic motors. Although the idea of DEA motors is unique, their motion and behavior are same as those of solid motors. Motors that can deform and operate in a deformed state of them would enable the development of novel soft machines that could function in a wide range of environments.

Herein, we propose a deformable motor based on DEAs. Due to the flexibility of the frame and DEA, our deformable motor could rotate even when it was deformed by external force (**Figure 1**, **Video S1**). To create the new motor, we employed the mechanism proposed by Anderson et al. together with a flexible frame (Kofod et al., 2006; Shintake et al., 2015b). Furthermore, we succeeded in visualizing the dynamic stress changes of the deformable motor, and then used a high-speed polarization-imaging camera to obtain proof that the stress changes of the DEA led to rotational motion. Moreover, we revealed the relationship between rotational performance and the strain of the deformable motor.

MECHANISM

DEA Activation

Figure 2A shows the structure of the DEA, which consists of flexible electrodes that sandwich a dielectric elastomer. The flexible electrodes are composed of conductive materials such as carbon powder, carbon grease, rubber, or hydrogels. Upon application of a voltage, electric charges accumulate on the stretchable electrodes and generate a Coulomb force between them. The Coulomb force compresses the dielectric elastomer, and the elastomer stretches in a perpendicular direction due to the incompressibility of the elastomer. Due to its elasticity, the elastomer returns to its original shape when the electric charges are removed from the electrodes. Equation 1 describes equivalent electrostatic Maxwell stress P (N/m^2) induced by the compression force (Wissler and Mazza, 2007):

$$P = \varepsilon_r \varepsilon_0 E^2 = \varepsilon_r \varepsilon_0 \left(\frac{V}{z}\right)^2, \quad (1)$$

where ε_r is the relative dielectric constant of the elastomer, ε_0 is the permittivity of free space ($\varepsilon_0 = 8.854 \times 10^{-12}$ F/m), E is the electric field (V/m), V is applied voltage (V), and z is the thickness of the elastomer (m). **Figure 2B** and **Video S3** illustrates the operation of a DEA.

Rotation and Deformation of the Motor

Figure 3A depicts the design for the deformable motor, which is composed of the thin frame, central parts, a crank mechanism, and four DEAs. We employed a thin frame to achieve deformation by application of an external force. The central parts have four joints and are connected to the four fulcrums of the frame in such a manner that the shaft is positioned at the center of the motor.

We classified previous motors for use with soft materials into two classes, based on the type of activation in the shaft: those in which the shaft of the motor moves around in a circle (O'Brien et al., 2010; Anderson et al., 2011), and those in which the shaft spins in the upright state (Kornbluh et al., 1998; Anderson et al., 2010). We employed the latter type of actuation; the shaft of

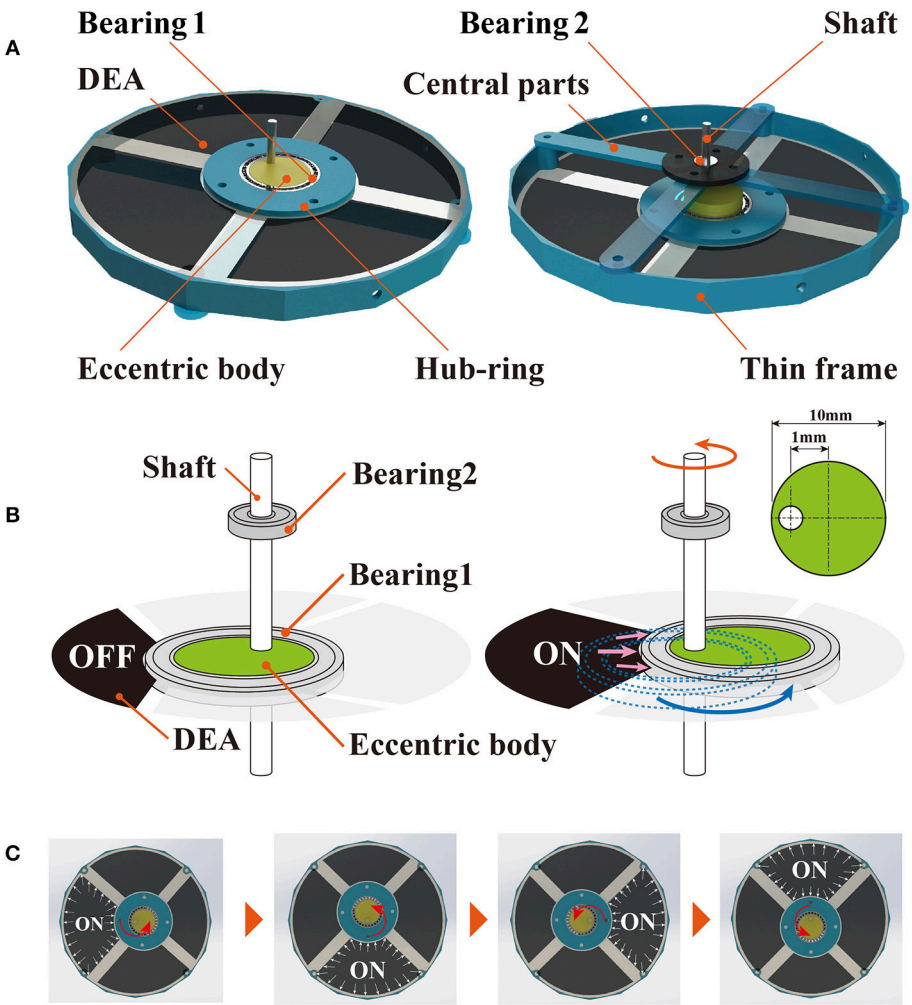

FIGURE 3 | Mechanisms of the deformable motor. **(A)** Crank mechanism consists of bearing 1, bearing 2, eccentric body, and shaft. DEAs are fixed by a thin frame and hub-ring. **(B)** Rotational mechanism of the deformable motor. The crank moves under the force generated by the DEA. **(C)** The crank mechanism is activated when the four DEAs are stretched in order.

our deformable motor spins in the upright state. Anderson et al. described a method for rotating the shaft by combining the crank mechanism with a DEA (Anderson et al., 2010). We used their proposed mechanism to convert the expansion of the DEA into rotational motion.

Here, we explain the mechanism underlying rotation of the deformable motor. The crank mechanism is composed of bearing 1, bearing 2, the eccentric body, and the shaft. When one of the four DEAs is expanded, the eccentric body moves around the shaft as shown in **Figure 3B**. Because the eccentric body and the shaft are integrated, the movement of the eccentric body rotates the shaft. We can then generate rotational motion by activating the four DEAs in order (**Figure 3C**, **Video S6**). Bearing 1 keeps the shaft at the center of the motor by connecting with the thin frame through the central parts shown in **Figure 3A**. By changing the eccentricity of the eccentric body, we can adjust the maximum torque and rotational speed of the motor.

Figure 4 shows the activation of the deformable motor. When the frame deforms as shown in **Figure 4A**, eight joints work to arrange the shaft at the center of the motor. **Figure 4B** shows the rotational motion without the external force (Original state). **Figure 4C** shows the rotational motion of the motor when an external force is applied from the top and bottom sides (Deformed state). In the figure, an arrow has been placed at the center of the motor to clarify the direction of rotation. Notably, the motor works while under deformation.

FABRICATION

Deformable Motor

To prepare DEAs, we used VHB Y-4905J (VHB Y-4905J; 3M, Maplewood, MN, USA) as the elastomer and multi-walled carbon nanotubes (MWNTs) (multi-walled carbon nanotube 724769; Sigma-Aldrich, Saint Louis, MO, USA) as the electrode. According to Equation 1, the relative dielectric constant of

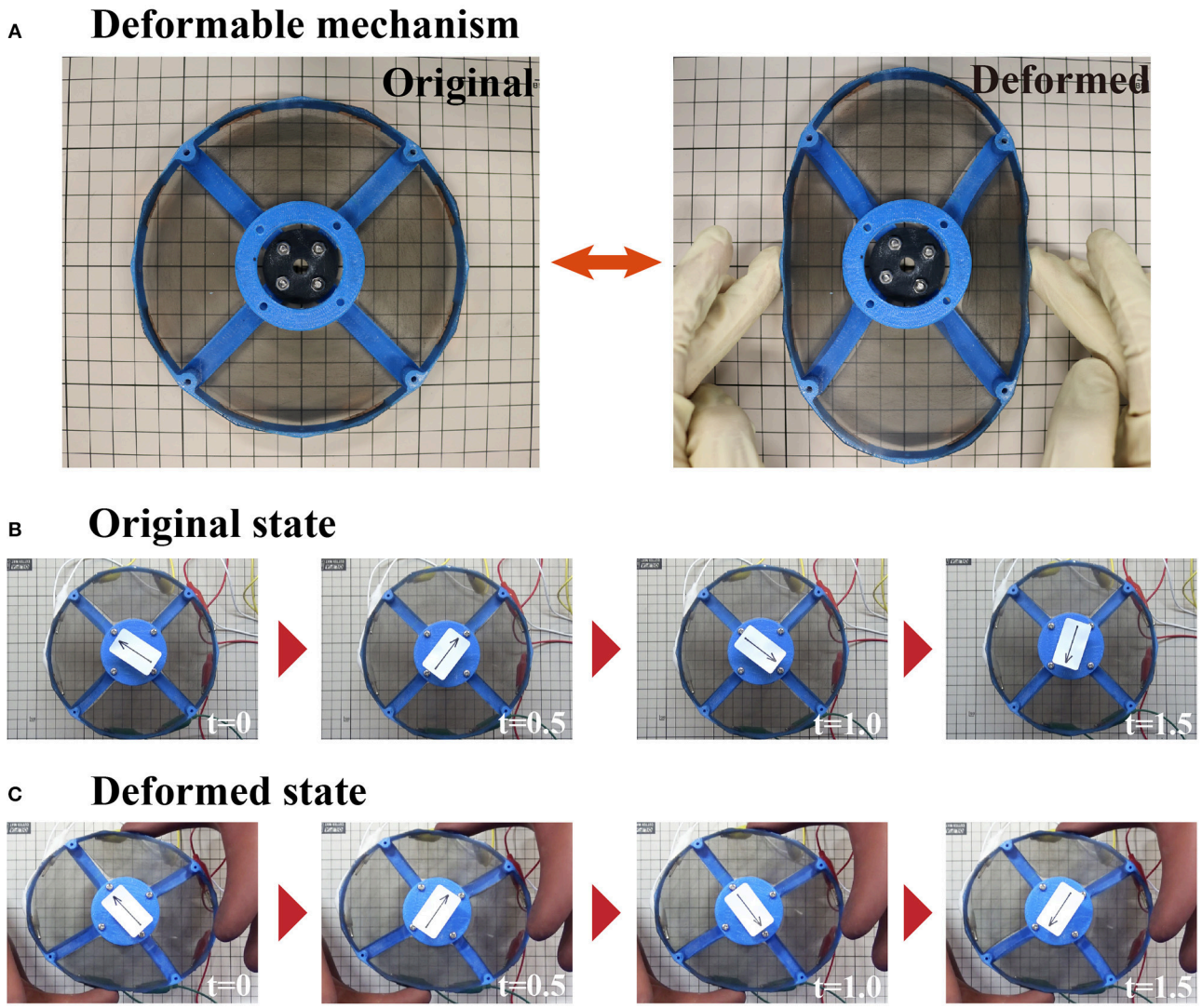

FIGURE 4 | The deformable mechanism and images of the motor under deformation. **(A)** The deformable mechanism consists of the thin frame and central parts. **(B)** Time-series imagines of a rotating deformable motor. The motor rotates without deforming the frame. **(C)** Motor rotating within a deformed frame.

the elastomer affects the extension of the DEA. The dielectric constant of VHB Y-4905J is 4.8, and the strain of a DEA made with VHB Y-4905J is >300% (Anderson et al., 2010). In addition, the extension of a DEA made with 300% pre-strained VHB is larger than that of a silicon DEA (Pelrine et al., 2000). We applied 300% pre-strain to the elastomer because pre-straining makes the elastomer softer (Pelrine et al., 2000), and employed MWNTs as electrodes because DEAs made with MWNTs have high work density (Hughes and Spinks, 2005). The MWNTs were applied to the elastomer by brushing (Shigemune et al., 2018). To reduce friction and weight, for the crank mechanism we selected an eccentric body, bearings, and a rotating shaft that were of small scale. We employed an eccentric body with a diameter of 10 mm and a 1-mm gap from center of the circle, as shown in **Figure 3B**. The diameters of the rotating shaft and the inner diameter of the Bearing 2 were both 3 mm. We used a three-dimensional printer (Dreamer; Flashforge, Jinhua, China) and an ABS resin (ABS 600 g; FlashForge) to fabricate the frame of the motor and the parts for placement of the rotational shaft at the center. Because ABS resin is ductile, the frame is not likely to be broken by deformation (Perez et al., 2014).

Controller

To drive the deformable motor, we developed a circuit to control the four DEAs. DEAs have the advantage of high energy efficiency per unit weight. When the circuit that controls the DEAs becomes large, the system loses this efficiency. Hence, we developed a compact control circuit to maintain the energy efficiency advantage. We designed a controller that drove the four DEAs with one DC/DC converter. **Figure 5** shows the system of the controller and how the controller is connected to the deformable motor. The controller consists of a microcomputer

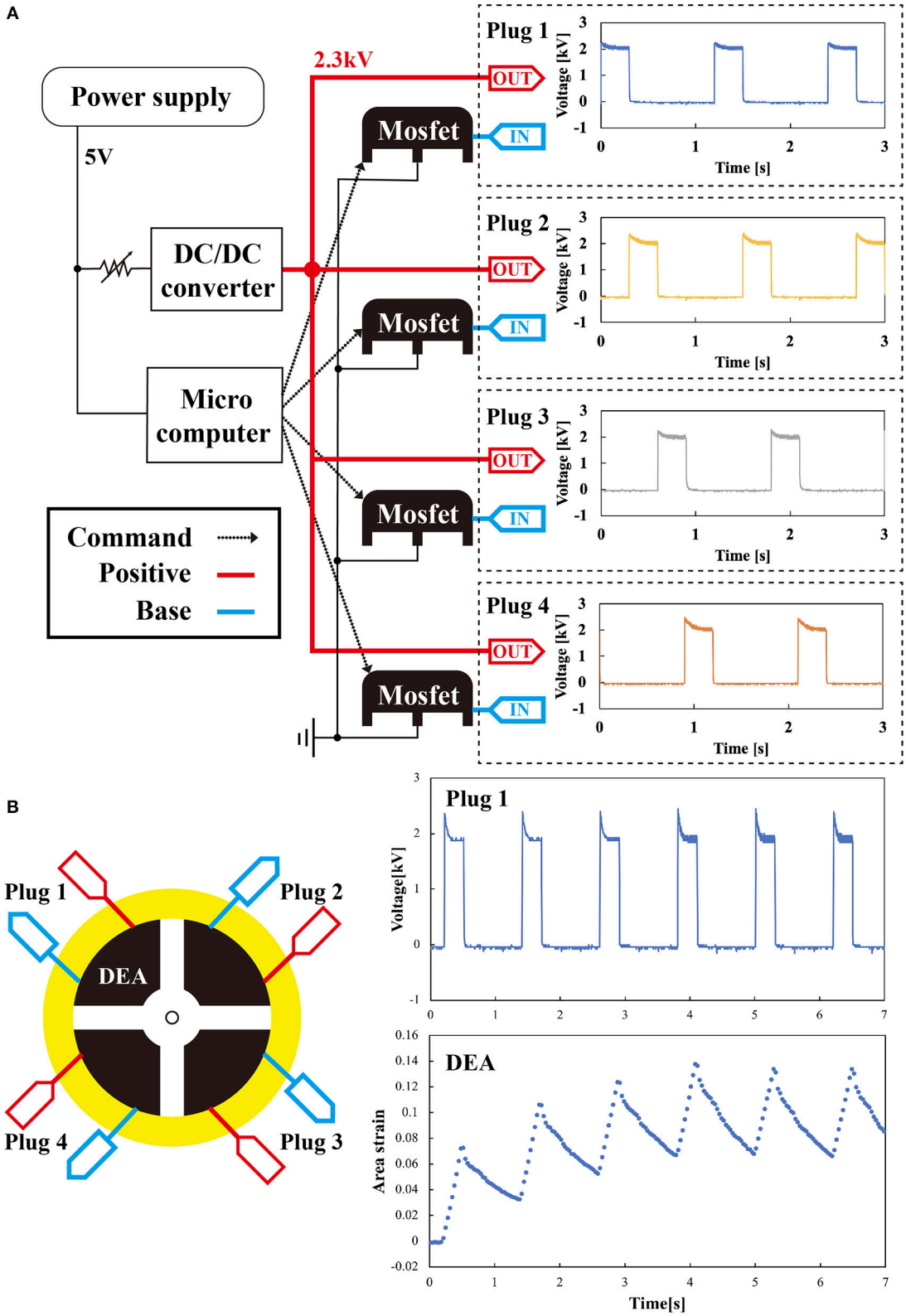

FIGURE 5 | System for connecting the controller to the deformable motor **(A)** system diagram of the controller and the waveform of the voltage outputted from the Plugs 1–4. **(B)** Signal of the controller and the response of the DEA to the signal. As time passes, the area strain in one cycle gradually stabilizes.

(Nucleo-f 401 re), a DC/DC converter (EMCO Q 101-5), and power MOSFETs (IXTH 02 N 450 HV). The microcomputer outputs signals to each DEA (plugs 1–4). The DC/DC converter is required to generate the high voltage that drives the DEA. Previous studies demonstrated that EMCO Q 101-5 works acceptably on robots made with DEAs (Wingert et al., 2006; Ahmadi et al., 2012; Shintake et al., 2015a). We set the maximum output to 3 kV because electrical breakdown within the DEAs occurred above this voltage. The power MOSFETs can switch the voltage up to 4.5 kV. We used the same power supply to provide energy to both the microcomputer and the DC/DC converter.

We measured the output voltage produced from the controller. IN and OUT of the controller in **Figure 5A** were connected to each DEA in the motor shown in **Figure 5B**. Physically, the controller and the DEAs were connected by a copper tape. To provide high voltage, we clamped the copper tape with clips from the controller. The right of **Figure 5A** shows waveforms of the voltage outputted from the four plugs (Plugs 1–4). To measure the voltage, we directly connected plugs of the controller to an oscilloscope. We used the following conditions: output voltage of 2 kV, frequency of 0.833 Hz, and a duty ratio with a rectangular pulse wave of 25%. The waveforms showed transient characteristics, which are attributed to the thermal resistance of the power MOSFET. Each of the four outputs converged to 2 kV, and we confirmed that the controller could output and control the voltage to drive the DEA. The right panel of **Figure 5B** shows that the behavior of the DEA reached a steady state after 4 s. The maximum area strains of the DEAs controlled by the system were ∼114%.

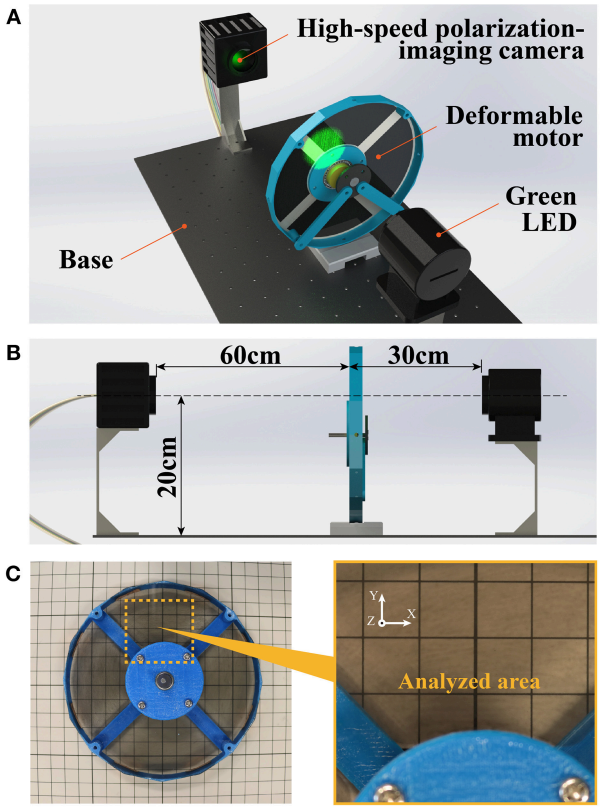

FIGURE 6 | Experimental setup for measurement of internal stress. **(A)** Green light penetrates the deformable motor, and birefringence information is transmitted to the camera. **(B)** Placement of the experimental instrument. The light and lens of the camera are in a straight line. **(C)** Analysis area is 40 × 40 mm.

EXPERIMENTS

Visualization of the Internal Stress Distribution

To determine whether the deformable motor could be driven by the DEAs, we visualized the spatio-temporal changes of stress distribution inside the DEA while driving the deformable motor. Previous studies showed that the motors rotate under force from the DEAs, and proved that the mechanism works in a simulated environment. However, those reports never confirmed the application of the force to the motor in an actual environment. **Figure 6** shows the experimental setup used to visualize the internal stress distribution in the DEA. For this experiment, we used a high-speed polarization-imaging camera and an LED light (**Figure 6A**). This camera is capable of measuring the birefringence phase difference (birefringence) of transparent materials (Hosoya et al., 2016b,c, 2017a,b).

We used the birefringence of DEA as a parameter to indicate the condition of a material's stress and structure. During measurement of a thin film with a uniform thickness, the material's birefringence changes due to internal stress, such as the pre-strain and coulomb force of the DEA. Therefore, birefringence is correlated with relative stress. For example, phase difference is large in areas with large stress.

The experimental setup was as follows: three camera and motor were 60 cm apart, whereas the motor and the light were 30 cm apart (**Figure 6B**). The center of the measurement area was 20 cm above the fixed base. The high-speed polarization-imaging camera had a speed of 125 fps, an exposure time of 5 s, and a visualization area of 40 × 40 mm. **Figure 6C** shows the visualization area. The light source was a green LED (operating wavelength: 480–540 nm; bandwidth of band-pass filter: 520 ± 10 nm; power of incident light: 2.5 W/m^2). The driving voltage of the DEA was 2.3 kV, the driving frequency was 15 Hz with a rectangular wave, and the duty ratio was 25%. The phase difference of the driving frequency among the four DEAs was $\pi/2$, and the four DEAs functioned in order.

Figure 7 visualizes the spatio-temporal change of the stress inside the DEA via the high-speed polarization-imaging camera. The stress inside the DEA increased with the driving voltage. In addition, high stress occurred at the center part and the boundary between the DEA and the hub-ring. The stress at the center was a compressive stress in the vertical direction of the DEA (z-axis direction in **Figure 7**). We assume that this stress affects the rotational motion of the deformable motor. On the other hand, we presume that the stress at the boundary between the DEA and

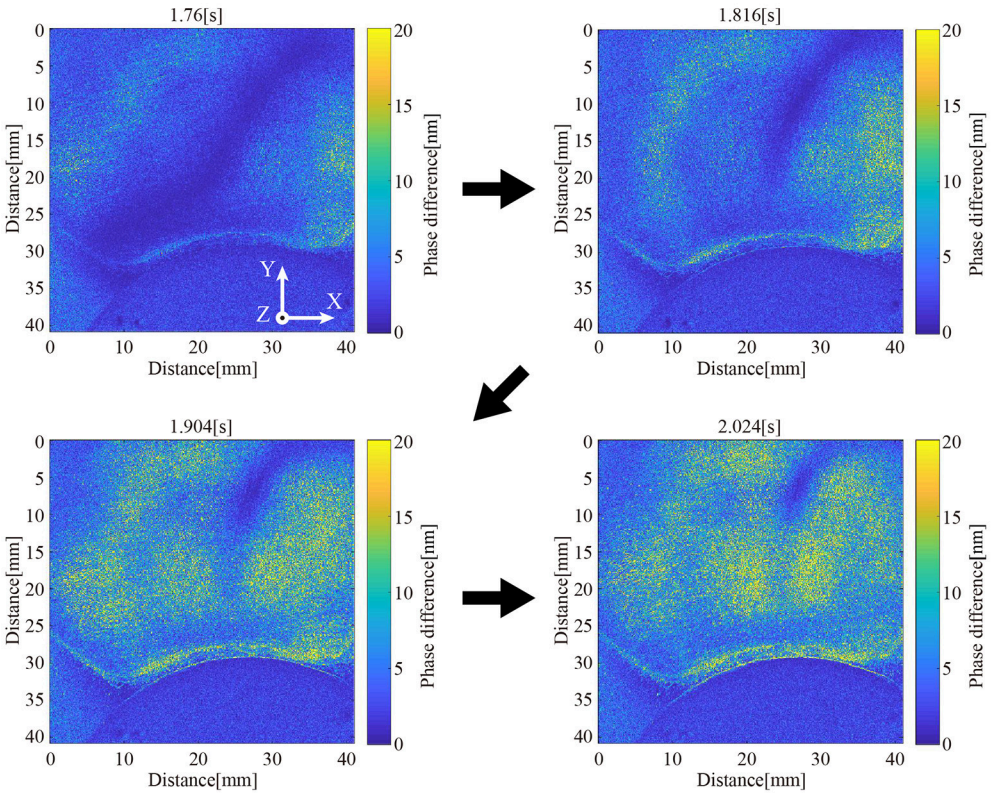

FIGURE 7 | Visualization of internal stress distribution. The internal stress distribution changes upon application of a voltage to the DEA.

hub-ring compressed in the negative direction of the Y axis, as shown in the visualized phase of 2.024 s (**Figure 7**).

Furthermore, we could determine the rotational performance of the deformable motor from this experiment. We confirmed high internal stress in almost all of the area after ∼0.25 s from activation of the DEA. In other words, the motor required a minimum of 0.25 s to move the crank by the DEA when 2.3 kV was applied. It takes 1 s to rotate the motor with the four DEAs. We then presumed that the deformable motor rotates at 60 rpm under the fastest condition. Eventually, we designed a control program for the deformable motor with a maximum speed of 60 rpm.

Mechanical Characteristics of the Deformable Motor

Setup

To elucidate the performance of the deformable motor, we measured its mechanical characteristics. We designed the motor to be capable of deformation into various shapes. Here, we defined three deformed states to compare the mechanical characteristics of each state. To quantify the deformation, we added four sets of long screws, vertical spacers, and parts with two joints. **Figure 8** shows each state deformed by the additional parts. Turning a screw clockwise places pressure on one point of the frame, and the radius r [mm] from the shaft changes as shown in **Figure 8A**. The pitch of the screw was 0.5 mm. Thus, one turn of the screw decreased the radius by 0.5 mm. **Figure 8A** and **Video S4** illustrate the original state. **Figure 8B** and **Video S5** show a one-directional state. **Figures 8C** and **D** show a vertical-directional state, and a horizontal-directional state respectively. Equation (2) derives the radial strain δ of the frame:

$$\delta = \frac{\Delta r}{r} = \frac{0.5}{r}\left(n + \frac{\theta}{360}\right), \tag{2}$$

where r[mm] is the radial displacement, n is the number of screw rotations, and θ [°] is the rotation angle, which is added to the rotational times.

We investigated the relationship between the radial strain and the maximum torque. Additionally, we examined the radial strain and the maximum rotational speed when the motor was deformed. We set the two radial strains of the horizontal-directional and vertical-directional states to the same value in order to define the type of the deformed states.

Figure 9 illustrates an experimental setup used to measure the torque of the deformable motors. The motor shaft was placed in the vertical orientation relative to the ground, and the wire was placed parallel to the ground. We suspended a weight from the tip of the wire to apply torque on the shaft. The length L [cm] of the wire from the pulley to the mass was 30 cm. The weight of the mass included the weight of the wire.

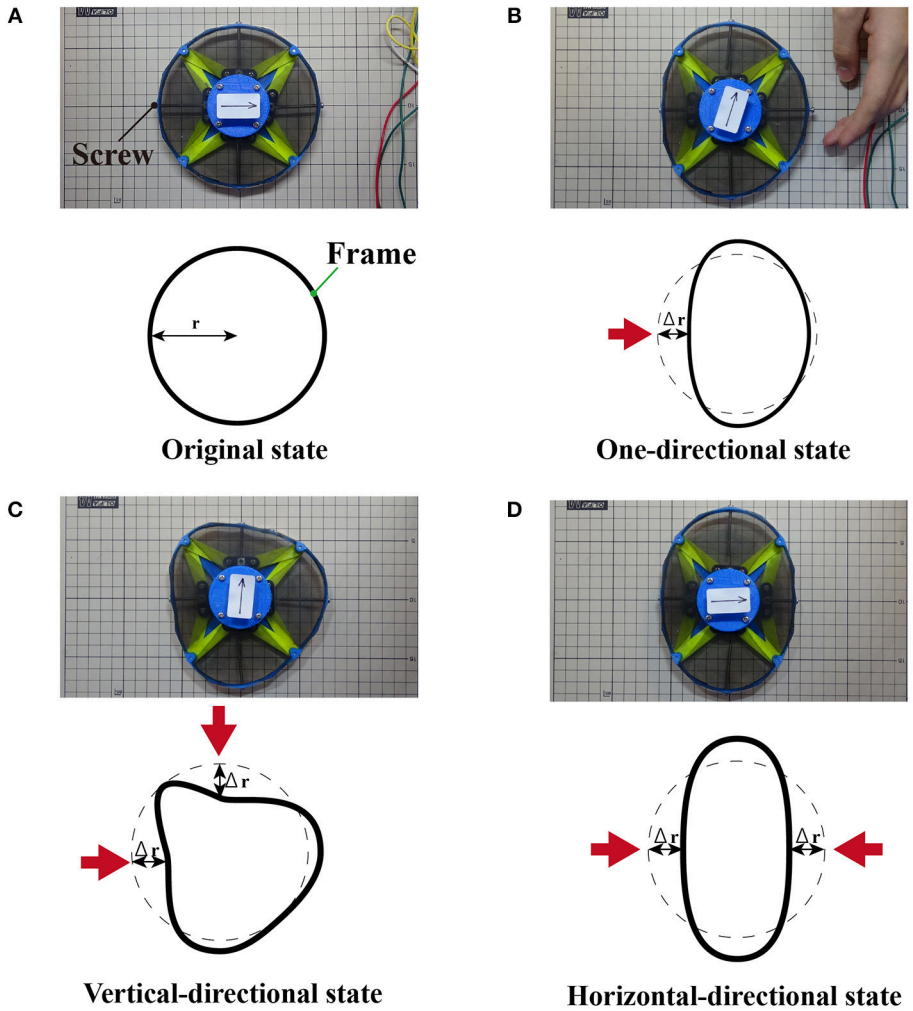

FIGURE 8 | Experimental setup. **(A)** Original state without deformation. **(B)** The one-directional state deforms the motor from one direction. **(C)** The vertical-directional state deforms the motor from one horizontal and one vertical direction. **(D)** The horizontal-directional state deforms the motor from two horizontal directions.

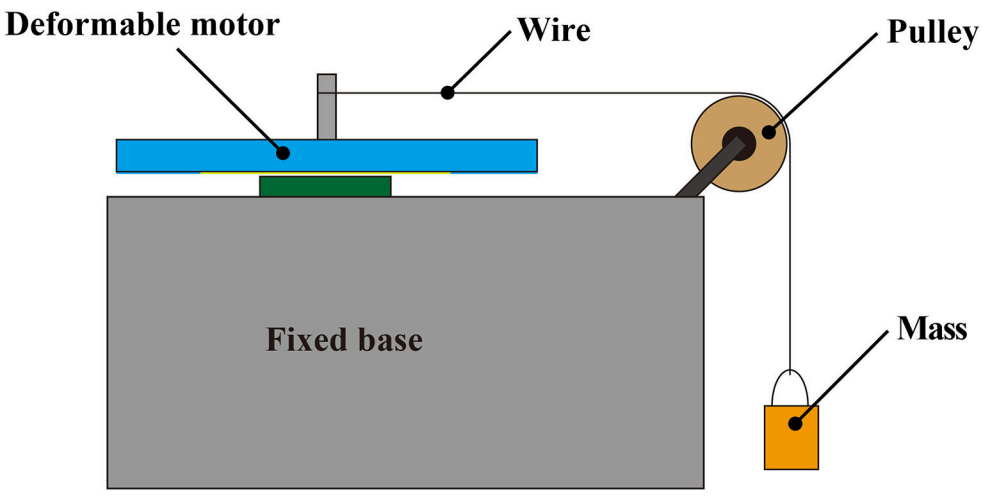

FIGURE 9 | Experimental device for measuring torque. To reduce interference from gravity, the shaft of the motor is placed in a vertical orientation relative to the ground.

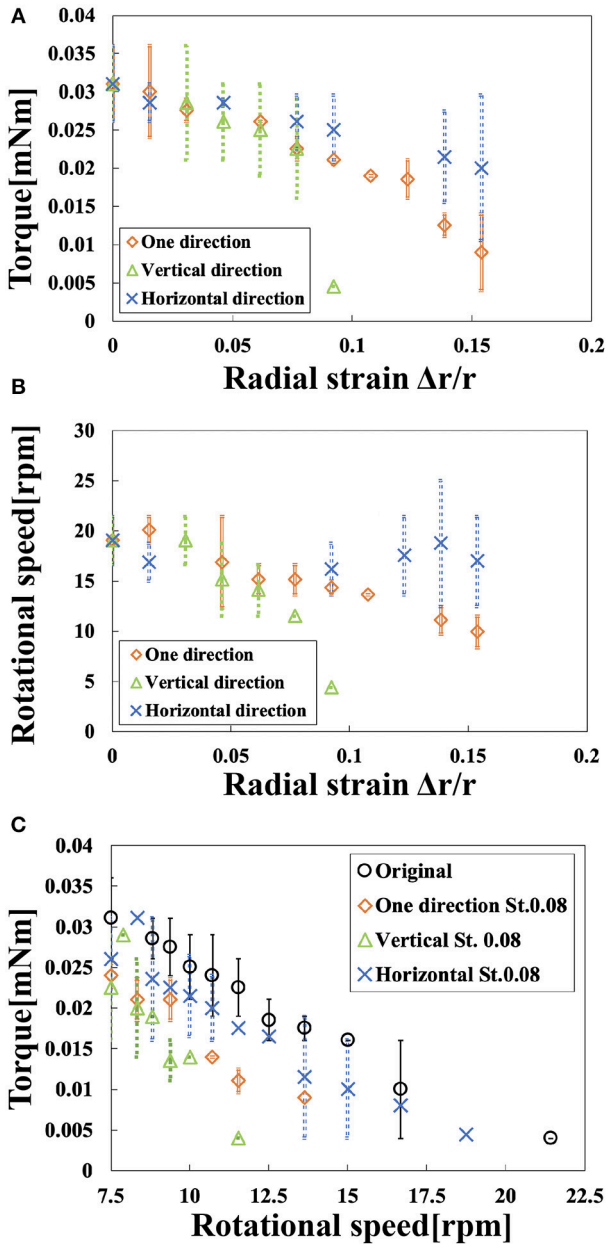

FIGURE 10 | Rotational performance. **(A)** Torque vs. radial strain in the three deformed states. **(B)** Rotational speed vs. radial strain in the three deformed states. **(C)** Motor torque vs. rotational speed.

Equation (3) derives the torque T [mN·m] of the deformable motor:

$$T = rF = r\,(w_i + w_o)\,g; \qquad xw_i = kL, \tag{3}$$

where r [m] is the radius of the shaft, F [mN] is the external force, w_i $[g]$ is the weight of the wire, w_o $[g]$ is the weight of the mass, g is the gravitational acceleration ($g = 9.81$ m/s^2), and k is the weight per wire length ($k = 0.0024$ g/cm). We neglected the friction of the pulley.

Results and Discussion

Figure 10A shows the relationship between the radial strain and the torque in the three deformed states. **Table 1** shows the torque generated by the motor at each deformed state when the radial strain was 0, 0.09, and 0.15. We conducted the experiment twice; **Table 1** shows the average, maximum, and the minimum values of the torque in the two replicates. The torque of the original state was 0.031 mN m. The one-directional state had a torque of 0.009 mN m when the radial strain was 0.15. The vertical-directional state had a torque of 0.004 mN m when the radial strain was 0.09. When the radial strain was over 0.1 in the vertical-directional state, the motor could not rotate. The torque of the horizontal-directional state was 0.021 mN m when the radial strain was 0.15. As shown in **Figure 10A**, the torque of the horizontal-directional state did not change significantly when a large strain was applied. We observed a significant decrease in the torque in the vertical-directional state. Thus, the nature of the deformed state affects the torque of the motor.

Figure 10B shows the relationship between radial strain and the rotational speed in the three deformed states. **Table 2** shows the rotational speed generated by the motor in each deformed state when the radial strain was 0, 0.09, and 0.15. We also conducted this experiment twice; **Table 2** includes the average, maximum, and minimum values of the rotational speed in the two attempts. The rotational speed of the original state was 19 rpm. When the radial strain was 0.15, the one-directional state had the rotational speed of 9.93 rpm, half the speed of the original state. The vertical-directional state had a torque of 4.4 rpm when the radial strain was 0.09. The rotational speed of the horizontal-directional state was 16.2 rpm when the radial strain was 0.15. As shown in **Figure 10B**, the rotational speed did not change significantly when a large strain was applied in the horizontal-directional state. In the three deformed states with a strain of 0.09, the vertical-directional state exhibited the worst performance, as in the torque experiment. Thus, rotational speed behaved similarly to torque.

Figure 10C shows the relationship between rotational speed and torque. At a strain of 0.08 rotational performance decreased in the following order: original, horizontal-directional, one-directional, and vertical-directional. In other words, we revealed that the elliptical shape of the motor prevented its rotational performance from dramatically decreasing in the three deformed states. This property, i.e., that torque decreased as rotational speed increased, matched the features of the magnetic motor.

The performance of the deformable motor was strongly affected by the friction on the bearing in the crank mechanism. When the force acts on the crank, the rotational performance of the motor decreases because the friction on the bearing increases. The direction of the force applied to the crank represents the summation of the external force vectors. In the vertical-directional state, a large force acts on the crank in the lower right direction, as shown in **Figure 11B**. The force is smaller in the one-directional state than in the vertical-directional state, as shown in **Figure 11A**. On the other hand, the force does not act on the horizontal-directional state because the force vectors applied to the frame cancel, as shown in **Figure 11C**. Eventually, the friction of the bearing becomes the smallest in the

TABLE 1 | Torque experiment.

	Strain 0 [mN m] (Original state)			Strain 0.09 [mN m]			Strain 0.15 [mN m]		
	AVE	MAX	MIN	AVE	MAX	MIN	AVE	MAX	MIN
One-directional	0.031	0.036	0.026	0.021	0.021	0.021	0.009	0.014	0.004
Vertical				0.004	0.009	0.000	–	–	–
Horizontal				0.026	0.029	0.021	0.021	0.026	0.014

TABLE 2 | Rotational speed experiment.

	Strain 0 [rpm] (Original state)			Strain 0.09 [rpm]			Strain 0.15 [rpm]		
	AVE	MAX	MIN	AVE	MAX	MIN	AVE	MAX	MIN
One-directional	19.0	21.4	16.7	14.3	15.0	13.6	9.9	11.5	8.3
Vertical				4.4	8.8	0.0	–	–	–
Horizontal				16.2	18.8	13.6	17.0	21.4	12.5

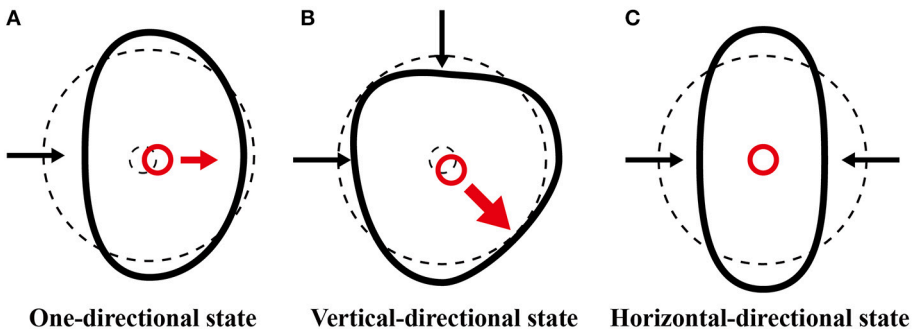

FIGURE 11 | Diagram showing the force applied to the crank. **(A)** In the original state, the force applied to the crank is small. **(B)** In the vertical-directional state, the force applied to the crank is large. **(C)** In the horizontal-directional state, the forces applied to the crank cancel.

horizontal-directional state. Hence, the horizontal-directional state demonstrates the best performance in the three deformed states. These results demonstrate that the symmetricity of the frame affects the rotational performance of the deformable motor.

Although the motor in the horizontal-directional state maintains the symmetricity, the rotational performance is lower than that of the original state. We conjectured that a decrement in the displacement of the DEAs degraded the performance of the motor. In the area of the frame that deforms toward the center of the motor, the pre-strain of the DEA close to the area becomes small. As the pre-strain of the DEA decreases, the elastic modulus of the DEA elastomer increases (Pelrine et al., 2000), and the displacement of the DEA decreases. This decrement in the displacement caused the performance of the motor to be lower in the horizontal-directional state than in the original state.

Eventually, because the effects of the friction of the crank or the displacement of the DEAs were small, the motor rotated in the all deformed states when the radial strain was <0.07. The motor worked acceptably in the horizontal-directional state because of the symmetrical deformation.

CONCLUSION

We developed a deformable motor that can rotate its shaft under deformation due to the flexibility of its frame and DEAs. By visualizing the internal stress distribution, we observed the force generated by the DEA. The results revealed that the DEAs in the motor drove the crank mechanism to rotate the deformable motor. We also conducted an experiment to clarify the relationship between the rotational performance and deformations of the motor. When the deformation of the motor was small, the rotational speed and torque were almost same as those of the undeformed motor (strain, 0.07). Moreover, in the horizontal-directional state, a large deformation (strain 0.15) did not cause a significant decline in rotational speed or torque. A deformable motor with one layer of DEA yielded 2% of the torque of a traditional electromagnetic motor (RE-280RA; Mabuchi

Motor, Chiba, Japan; deformable motor: 0.03 mN m; traditional electromagnetic motor: 1.47 mN m). We deduced that the performance of the deformable motor could be improved by stacking the DEAs. Theoretically, a motor using 48 layers of DEAs (thickness: 1.5 mm) would generate 48 times as much torque. We believe that stacking DEA layers has the potential to increase torque without making the motor enormous. In regard to energy efficiency per weight, our deformable motor generated 0.30 mN m/W g, whereas the traditional electromagnetic motor and one with DEAs (Anderson et al., 2010) generated 0.023 and 2.91 mN m/W g, respectively. The basic performances of the deformable motor can be improved by optimizing the design and materials (**Video S2**). In future studies, we hope to improve the performance of the deformable motor. Development of a deformable motor opens the possibility of applying rotational motion to soft robots.

AUTHOR CONTRIBUTIONS

All authors made intellectual contributions to this paper and approve of its publication. In particular, AM conducted the device design, experimental setup, data analysis, and participated in writing the manuscript. TK and NH designed the experimental setup and participated in writing the manuscript. HS and SM provided advice about the fundamentals of this research and participated in writing the manuscript.

FUNDING

We thank the Japan Society for the Promotion of Science for their support under Grants-in-Aid for Scientific Research programs [Grants-in-Aid for Scientific Research (B), Project No. JP16H04306, and No. JP16H04291, Grants-in-Aid for Challenging Exploratory Research, Project No. JP16K14201, and No. JP17K18858, and Grants-in-Aid for Research Activity start-up JP18H05895].

ACKNOWLEDGMENTS

The authors are grateful to Mizuki Komiyama for advice about DEA circuits. We thank the members of the Smart Materials Lab.

SUPPLEMENTARY MATERIAL

The Supplementary Material for this article can be found online at: https://www.frontiersin.org/articles/10.3389/frobt.2019.00001/full#supplementary-material

Video S1 | A deformable motor rotating with deformed state.

Video S2 | A deformable motor rotating with centrifugal force.

Video S3 | Activation of a dielectric elastomer actuator.

Video S4 | Rotation of a deformable motor in an original state.

Video S5 | Rotation of a deformable motor in an one-directional state.

Video S6 | Rotational mechanism of a deformable motor.

REFERENCES

Ahmadi, S., Mattos, A. C., Barbazza, A., Soleimani, M., Boscariol, P., and Menon, C. (2012).Fabrication and performance analysis of a DEA cuff designed for dry-suit applications. *Smart Mater. Struct*. 22:035002. doi: 10.1088/0964-1726/22/3/035002

Ainla, A., Verma, M. S., Yang, D., and Whitesides, G. M. (2017). Soft, rotating pneumatic actuator. *Soft Robot*. 4, 297–304. doi: 10.1089/soro.2017.0017

Anderson, I. A., Hale, T., Gisby, T., Inamura, T., McKay, T., O'Brien, B., et al. (2010). A thin membrane artificial muscle rotary motor. *Appl. Phys. A Mater. Sci. Process*. 98, 75–83. doi: 10.1007/s00339-009-5434-5

Anderson, I. A., Tse, T. C. H., Inamura, T., O'Brien, B. M., McKay, T., and Gisby, T. (2011). A soft and dexterous motor. *Appl. Phys. Lett*. 98:123704. doi: 10.1063/1.3565195

Cacucciolo, V., Renda, F., Poccia, E., Laschi, C., and Cianchetti, M. (2016). Modelling the nonlinear response of fibre-reinforced bending fluidic actuators. *Smart Mater. Struct*. 25:105020. doi: 10.1088/0964-1726/25/10/105020

Diesel, R., and Brock, O. (2013). "A compliant hand based on a novel pneumatic actuator. robotics and automation (ICRA)," in *2013 IEEE International Conference on Robotics and Automation* (Karlsruhe), 2047–2053.

Galloway, K. C., Becker, K. P., Phillips, B., Kirby, J., Licht, S., Tchernov, D., et al. (2016). Soft robotic grippers for biological sampling on deep reefs. *Soft Robot*. 3, 23–33. doi: 10.1089/soro.2015.0019

Hosoya, N., Baba, S., and Maeda, S. (2015). Hemispherical breathing mode speaker using a dielectric elastomer actuator. *J. Acoust. Soc. Am*. 138, EL424–EL428. doi: 10.1121/1.4934550

Hosoya, N., Kajiwara, I., and Umenai, K. (2016a). Dynamic characterizations of underwater structures using non-contact vibration test based on nanosecond laser ablation in water: investigation of cavitation bubbles by visualizing shockwaves using the Schlieren method. *J. Vibrat. Control* 22, 3649–3658. doi: 10.1177/1077546314564693

Hosoya, N., Kajiwara, I., Umenai, K., and Maeda, S. (2017b). Dynamic characterizations of underwater structures using noncontact vibration tests based on nanosecond laser ablation in water: evaluation of passive vibration suppression with damping materials. *J. Vib. Control*. 140, 486–492. doi: 10.1177/1077546317710158

Hosoya, N., Mishima, M., Kajiwara, I., and Maeda, S. (2017a). Non-destructive firmness assessment of apples using a non-contact laser excitation system based on a laser-induced plasma shock wave. *Postharvest Biol. Technol*. 128, 11–17. doi: 10.1016/j.postharvbio.2017.01.014

Hosoya, N., Terashima, Y., Umenai, K., and Maeda, S. (2016b). High spatial and temporal resolution measurement of mechanical properties in hydrogels by non-contact laser excitation. *AIP Adv*. 6:095223. doi: 10.1063/1.4964305

Hosoya, N., Umino, R., Kajiwara, I., Maeda, S., Onuma, T., and Mihara, A. (2016c). Damage detection in transparent materials using non-contact laser excitation by nano-second laser ablation and high-speed polarization-imaging camera. *Exp. Mech*. 56, 339–343. doi: 10.1007/s11340-015-0089-y

Hughes, M., and Spinks, G. M. (2005). Multiwalled carbon-nanotube actuators. *Adv. Mater*. 17, 443–446. doi: 10.1002/adma.200401076

Hwang, D., and Higuchi, T. (2014). A rotary actuator using shape memory alloy (SAM) wires. *IEEE/ASME Trans. Mech*. 19, 1625–1635. doi: 10.1109/TMECH.2013.2290545

Kofod, G., Paajanen, M., and Bauer, S. (2006). Self-organized minimum-energy structures for dielectric elastomer actuators. *Appl. Phys. A* 85, 141–143. doi: 10.1007/s00339-006-3680-3

Kornbluh, R., Pelrine, R., Eckerle, J., and Joseph, J. (1998). "Electrostrictive polymer artificial muscle actuators," in *IEEE International Conference on Robotics & Automation* (Leuven), 2147–2154.

Madden, J. D. W., Vandesteeg, N. A., Anquetil, P. A., Madden, P. G. A., Takshi, A., Pytel, R. Z., et al. (2004). Artificial muscle technology: physical principles and naval prospects. *IEEE J. Ocean. Eng*. 29, 706–728. doi: 10.1109/JOE.2004.833135

Maeda, S., Kato, T., Kogure, H., and Hosoya, N. (2015). Rapid response of thermo-sensitive hydrogels with porous structures. *Appl. Phys. Lett*. 106:171909. doi: 10.1063/1.4919585

Maeda, S., Kato, T., Otsuka, Y., Hosoya, N., Cianchetti, M., and Laschi, C. (2016). Large deformation of self-oscillating polymer gel. *Phys. Rev. E* 93:010501. doi: 10.1103/PhysRevE.93.010501

Minetaa,T., Mitsuia, T., Watanabea, Y., Kobayashia, S., and Hagab, Y., Esashib, M. (2002). An active guide wire with shape memory alloy bending actuator fabricated by room temperature process. *Sens. Actuat. A* 97–98, 632–637. doi: 10.1016/S0924-4247(02)00021-3

O'Brien, B. M., Calius, E. P., Inamura, T., Xie, S. Q., and Anderson, I. A. (2010). Dielectric elastomer switches for smart artificial muscles. *Appl. Phys. A. Mater. Sci. Process*. 100, 385–389. doi: 10.1007/s00339-010-5857-z

Okuno, Y., Shigemune, H., Kuwajima, Y., and Maeda, S. (2018). Stretchable suction cup with electro adhesion. *Adv. Mater. Technol.* 4:1800304. doi: 10.1002/admt.201800304

Pelrine, R., Kornbluh, R., Pei, Q., and Joseph, J. (2000). High-speed electrically actuated elastomers with strain greater than 100%. *Science* 287, 836–839. doi: 10.1126/science.287.5454.836

Perez, A. R. T., Roberson, D. A., and Wicker, R. B. (2014). Fracture surface analysis of 3D-printed tensile specimens of novel ABS-based materials. *J. Fail. Anal. Prevent*. 14, 343–353. doi: 10.1007/s11668-014-9803-9

Plante, J. S., and Dubowsky, S. (2007). On the performance mechanisms of dielectric elastomer actuators. *Sen. Actuat. A* 137, 96–109. doi: 10.1016/j.sna.2007.01.017

Shigemune, H., Maeda, S., Cacucciolo, V., Iwata, Y., Iwase, E., Hashimoto, S., et al. (2017). Printed paer robot driven by electrostatic actuator. *IEEE Robot. Autom. Lett*. 2,1001–1007. doi: 10.1109/LRA.2017.2658942

Shigemune, H., Maeda, S., Hara,Y., Hosoya, N., and Hashimoto, S. (2016). Origami robot: a self-folding paper robot with an electrothermal actuator created by printing. *IEEE/ASME Trans. Mech*. 21, 2746–2754. doi: 10.1109/TMECH.2016.2593912

Shigemune, H., Sugano, S., Nishitani, J., Yamaguchi, M., Hosoya, N., Hashimoto, S., et al. (2018). Dielectric elastomer actuator with carbon nanotube electrodes painted with a soft brush. *Actuators* 7:51. doi: 10.3390/act7030051

Shintake, J., Rosset, S., Schubert, B., Floreano, D., and Shea, H. (2015b). Versatile soft grippers with intrinsic electroadhesion based on multifunctional polymer actuators. *Adv. Mater*. 28, 231–238. doi: 10.1002/adma.201504264

Shintake, J., Rosset, S., Schubert, B. E., Floreano, D., and Shea, R. (2015a). A foldable antagonistic actuator. *IEEE/ASME Trans. Mech*. 20, 1997–2008. doi: 10.1109/TMECH.2014.2359337

Suzumori, K., Eikura, S., and Tanaka, H. (1992). Applying a flexible microactuator to robotic mechanisms. *IEEE Control Syst*. 12, 21–27.

Wingert, A., Lichter, M. D., and Dubowsky, S. (2006). On the design of large degree-of-freedom digital mechatronic devices based on bistable dielectric elastomer actuators. *IEEE/ASME Trans. Mech*. 11, 448–456. doi: 10.1109/TMECH.2006.878542

Wissler, M., and Mazza, E. (2007). Electromechanical coupling in dielectric elastomer actuators. *Sens. Actuat. A*. 138, 384–393. doi: 10.1016/j.sna.2007.05.029

Conflict of Interest Statement: The authors declare that the research was conducted in the absence of any commercial or financial relationships that could be construed as a potential conflict of interest.

frontiers in Robotics and AI

ORIGINAL RESEARCH
published: 19 March 2019
doi: 10.3389/frobt.2019.00012

Toward a Variable Stiffness Surgical Manipulator Based on Fiber Jamming Transition

Margherita Brancadoro†, Mariangela Manti†, Fabrizio Grani, Selene Tognarelli, Arianna Menciassi and Matteo Cianchetti*

The BioRobotics Institute, Scuola Superiore Sant'Anna, Pisa, Italy

Soft robots have proved to represent a new frontier for the development of intelligent machines able to show new capabilities that can complement those currently performed by robots based on rigid materials. One of the main application areas where this shift is promising an impact is minimally invasive surgery. In previous works, the STFF-FLOP soft manipulator has been introduced as a new concept of using soft materials to develop endoscopic tools. In this paper, we present a novel kind of stiffening system based on fiber jamming transition that can be embedded in the manipulator to widen its applicability by increasing its stability and with the possibility to produce and transmit higher forces. The STIFF-FLOP original module has been re-designed in two new versions to incorporate the variable stiffness mechanism. The two designs have been evaluated in terms of dexterity and variable stiffness capability and, despite a general optimization rule did not clearly emerge, the study confirmed that fiber jamming transition can be considered an effective technological approach for obtaining variable stiffness in slender soft structures.

Keywords: soft robotics, surgical manipulator, variable stiffness system, jamming transition, minimally invasive surgery

OPEN ACCESS

Edited by:
Helmut Hauser,
University of Bristol, United Kingdom

Reviewed by:
Dongming Gan,
Khalifa University,
United Arab Emirates
Sanja Dogramadzi,
University of the West of England,
United Kingdom

***Correspondence:**
Mariangela Manti
mariangela.manti@santannapisa.it

†These authors have contributed equally to this work

Specialty section:
This article was submitted to Soft Robotics, a section of the journal Frontiers in Robotics and AI

Received: *22 October 2018*
Accepted: *18 February 2019*
Published: *19 March 2019*

Citation:
Brancadoro M, Manti M, Grani F, Tognarelli S, Menciassi A and Cianchetti M (2019) Toward a Variable Stiffness Surgical Manipulator Based on Fiber Jamming Transition. Front. Robot. AI 6:12. doi: 10.3389/frobt.2019.00012

INTRODUCTION

Robots today rely on a long tradition in the use of rigid materials for the most of their body. The use of rigid materials implies the possibility to use some basic simplifications, assumptions, and conventions that can support their design. This framework can lead to very advanced and complex machines, but most of the times the effectiveness of the robot is still heavily relying on the control performance. This traditional approach for making intelligent machines has been questioned when roboticists started to look at natural agents (e.g., humans, animals, and even plants) and their interaction with the environment (Laschi and Mazzolai, 2016). Observing the key role played by soft and flexible structures within the body to cope with the unstructured and unpredictable environments in everyday tasks, roboticists started to re-think the basic principle for designing, manufacturing and controlling robots. This paradigmatic revolution is now known as soft robotics (Rus and Tolley, 2015). In this new paradigm, softness, and flexibility have acquired a strategic role for developing versatile, dexterous, and intrinsically safe systems (Shen, 2016), but the real game changer that makes soft robotics effective is the variable stiffness capability. This ability allows for soft robots to maintain their own structural strength without losing the capability of reversibly transit between a stiff state and a compliant one for a better adaptation of the shape to unstructured environments.

The attention of researchers approaching the design and manufacturing of a soft robot is firstly devoted to the definition of a body that counts on three main characteristics: shape, arrangement, and material properties of the constituting elements that serve, wherever it is possible, both as passive (structural) and active elements (Zambrano et al., 2014). This vision implies a significant increase in bodyware complexity, but also a simplification on control algorithms: a rich behavior does not necessarily come from a complex control, but may be the result of the interaction between body, control and environment (Pfeifer and Bongard, 2006).

In this framework, the innovative actuation technologies, investigated and developed by soft roboticists, represent the ground for a new generation of soft robots with advanced abilities, such as elongation, squeezing, growing, self-healing, and variable stiffness (Laschi et al., 2016). The topic is still an open issue. Literature reports some reviews and tentative approaches to identify, design and combine soft robotics technologies for stiffness tuning (Manti et al., 2016; Sun et al., 2017; Wang et al., 2018).

Among the most corroborated semi-active technologies for stiffness tuning (Manti et al., 2016), the material jamming transition has been largely investigated because of its simplicity, versatility, reversibility and possibility to customize the system according to the target application. The integration of a jamming mechanism into a device involves the presence of an external soft, elastic membrane filled with solid discrete material. At atmospheric pressure, the system presents high softness and compliance given by the fact that filler can easily and freely move inside the soft membrane; upon the application of vacuum, the membrane collapses on the filler material, thus freezing the dynamics of the overall system. Consequently, the material is densely packed and the friction prevents every kind of relative displacement. As a result, the entire structure behaves like a rigid material (Liu and Nagel, 1998).

The working principle that stands behind the phenomenon is today reproduced and frequently exploited in soft robotic systems at the macroscale; on the other hand, the physical principle that occurs at the microscale is still under investigation (Behringer and Chakraborty, 2018). Despite the fact that the technology is very easy to use and the advantages are undeniable, there is a lack of information on the underlying physical principle involved in the jamming transition and, as a consequence, there are no suitable models and tools able to guide the design choice, thus preventing its exploitation at market level (Amend et al., 2016).

Jamming transition has been investigated, for the first time, with grains encapsulated in an elastic membrane that, upon the application of vacuum, transit from a compliant state to a rigid one. This semi-active technology is commonly used in combination with other active actuation technologies to allow selective stiffening or shape locking of bending states in anthropomorphic grippers (Wall et al., 2015) or in highly articulated manipulators (Follmer et al., 2012). They can be also exploited as a mean to introduce selective anisotropies in the material behavior thus enabling locomotion patterns, such as rolling (Steltz et al., 2009), or vibration (Kaufhold et al., 2012). A widespread use of the technology is confirmed by its application as haptic or tactile interfaces (Follmer et al., 2012; Stanley et al., 2013; Li et al., 2014). The phenomenon has been then extended to the use of laminar material inside an elastic membrane in order to obtain layer jamming (Kim et al., 2013; Ou et al., 2014; Narang et al., 2018).

Literature analysis demonstrates that research prototypes are only based on granular and layer jamming, while the possibility of exploiting jamming transition using fibers as filler material is completely neglected. A preliminary study of this configuration has been investigated, for the first time, by Brancadoro et al. (2018): here, a comparative approach has been proposed to experimentally assess the performances of the jamming transition induced on fibers. In the same work, a first discussion on the main parameters affecting the system behavior has been introduced: fiber material, dimension, cross section and shape. The present paper builds upon the main results achieved in that previous work and focuses on the integration of a variable stiffness system based on fiber jamming transition in the STIFF-FLOP soft manipulator developed by the same research group (Abidi et al., 2018), hereafter called "original" to avoid confusion. This manipulator is based on three-flexible fluidic chambers that can be inflated to obtain omnidirectional bending and elongation. The STIFF-FLOP manipulator has already proved to introduce significant advantages into minimally invasive surgical procedures and specifically it has been successfully used as an endoscope in a total mesorectal excision procedure that was performed in two human cadaver models (Arezzo et al., 2017). Nevertheless, the manipulator has limited applications as surgical tool because of its poor capability of force application. This is the reason why, in its current configuration, it is best suited for endoscopic tasks, where safe interaction with organs and delicate tissues and dexterity are the main important features (Abidi et al., 2018). An endoscopic tool is devoted to inspection within the human body, thus it mainly requires dexterity and intrinsic safety (softness) in case of interaction with soft tissues. On the other hand, a surgical tool requires the ability of an effective interaction with human organs/tissues (e.g., for cutting, moving, pushing) thus it needs to be sufficiently rigid or (as in our case) the ability of tuning its stiffness. It implies that, in the two-module STIFF-FLOP surgical manipulator, the activation of the stiffening system of the proximal module is used to provide stabilization to the distal module while this latter is interacting with the tissues.

Earlier versions of the manipulator could count on a variable stiffness system based on granular jamming transition (Ranzani et al., 2015). It was effective and suitable for the surgical environment in terms of safety, but the miniaturization process revealed that this technology becomes very ineffective when used in almost 2D or 1D structures. Grains better act with 3D volumes, layers work well in planar structures while the mono-dimensionality of fibers is appropriate for long, slender systems. Thus, jamming transition based on fibers presents the right features for introducing a remarkable variable stiffness capability in the original STIFF-FLOP manipulator. Moreover, the manipulator is already driven by fluidic actuation

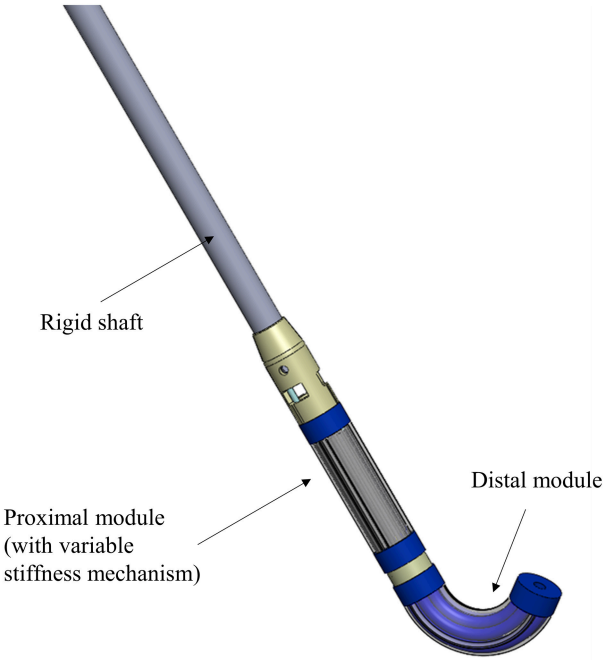

FIGURE 1 | Representation of the two-module STIFF-FLOP manipulator attached to a rigid shaft used as support. The proximal module has been redesigned to lodge a variable stiffness system that can become rigid on demand and provide stability to the distal module (unvaried with respect to the original version).

technologies, thus the additional components needed to drive jamming transitions are limited.

With this in mind, the main driver of this study is the integration of a variable stiffness system in the STIFF-FLOP soft manipulator. This system already has the flexibility and dexterity needed for a safe tool for medical application. Moreover, the system is able to reach remote areas from different points of view using the same access port. The integration of the semi-active technology extends the already available functionalities of the system making possible also surgical actions.

In this framework, the new concept tested in the present work investigates the possibility to re-design the proximal module of the original STIFF-FLOP manipulator to integrate a variable stiffness system without affecting the original dimensions in terms of diameter and length. This will enable stiffness variation that provides support and acts as a stabilizer for the distal module, which in turn exploits its flexibility and dexterity to interact with organs or human tissues. The complete surgical manipulator proposed in **Figure 1** will be composed of a proximal module (to be chosen between the two designs proposed in the present work) where the fiber jamming technology is integrated and a distal module that is the original one, as proposed in Abidi et al. (2018). The whole system could be then attached to a rigid shaft, which can be positioned and maneuvered at the insertion point by a surgeon or by a robot (Diodato et al., 2018) for performing minimally invasive surgery (MIS) procedures.

MATERIALS AND METHODS

Before presenting in detail the new design and the manufacturing procedure of the tested modules, it is worth briefly recapping the main characteristics the original STIFF-FLOP soft manipulator relies on. It includes three pairs of inflatable chambers, radially arranged around a central axis, and entirely made of silicone. These chambers are lined with a thin inextensible thread in a tight helical winding. The minimization of the helical pitch brings two advantages: it prevents a radial expansion and maximizes the longitudinal elongation when the chamber is under pressure (Fraś et al., 2015). This combination enables the possibility to obtain omnidirectional bending and longitudinal elongation depending on the pressure applied to each chamber. The chamber can be considered as an actuator that generates one motion primitive (MP). For continuum soft manipulators, the traditional degrees of freedom (DoFs) are replaced by MPs which result more appropriate for a soft robot that theoretically has infinite positions (Abidi et al., 2018). Considering this convention, the soft manipulator has three MPs for bending motion due to the inflation of each pair of chambers at different pressure values and one MP that describes the elongation due a simultaneous inflation of all the chambers at the same pressure value.

For this work, the original STIFF-FLOP module has been modified and declined into two different versions according to the following specifications:

- the dimensions of the module itself, in terms of external diameter and total length, remain constant in order both to pass through the trocar used in MIS and have comparable results with respect to the workspace covered by the original STIFF-FLOP module;
- the module should have at least one motion primitive to guarantee a minimum level of dexterity and flexibility;
- the module should have a free lumen.

The first one, referred as Module A in the next section, is based on the original design but hosts the fiber jamming system in the central channel (free lumen), not fulfilling the third requirement. The second one, referred as Module B, counts on a substantial revision of the actuation system: two pairs of fluidic actuators are substituted by two sites for fiber jamming, thus affecting the second requirement. While the omni directionality can be compensated externally (i.e., using the roll DoF of the rigid shaft reported in **Figure 1**), the free lumen is something that improves the system functionalities and surgeon's abilities.

Moreover, the integration of the variable stiffness system does not imply any modifications in terms of modularity of the overall final systems as described in **Figure 1** or dimensions of the module itself. For this reason, the two designs here proposed as an alternative to the original proximal STIFF-FLOP module, are still compliant with the miniaturization constraints and, moreover, the covered workspace is comparable with the previous results.

The design and the functionalities of each module are described in the next two subsections while the manufacturing

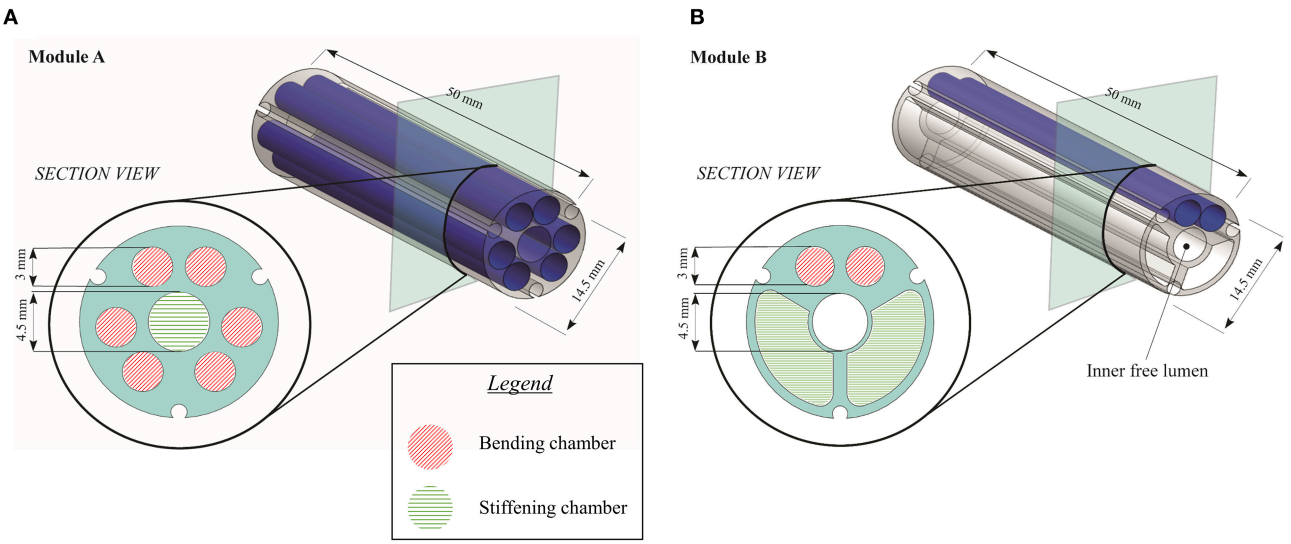

FIGURE 2 | Design and section view of **(A)** Module A and **(B)** Module B.

procedure, being mostly the same for both, is presented in a single subsequent section.

Re-design of the Module

Module A. The single module is 50 mm in length and 14.5 mm in external diameter thus resulting suitable for standard MIS applications (i.e., it is able to pass through a standard 15 mm trocar). **Figure 2A** shows the section view of the module containing three pairs of chambers, each measuring 3 mm in diameter and able to elongate only. With respect to the original version of the STIFF-FLOP module where the lumen (4.5 mm in diameter) was properly designed to allow the insertion of thin surgical equipment up to the tip, in the current version of the module the central channel hosts the fibers to produce the jamming transition (called "stiffening chamber"). With this design, the module is characterized by the variable stiffness functionality and by four MPs that supply the omnidirectional bending and the elongation.

Module B. The single module is again 50 mm in length and 14.5 mm in external diameter. With respect to Module A, this version has only one MP, supplied by a pair of chambers, while the remaining space is equally split into two chambers (each one with 27.41 mm^2 in area) that host fibers for varying the module stiffness, as depicted in the section view reported in **Figure 2B**. This design implies that the module has one single bending plane and variable stiffness functionality, while the inner free lumen (4.5 mm in diameter) is preserved for inserting suitable surgical tools (e.g., graspers, mini ultrasound probes and radio-frequency tools), for housing electric wires (e.g., for a laparoscopic micro camera) or for routing pressure lines (in case of a multi-modules architecture).

Fiber Selection

The choice of the fibers to be used in the jamming-based system has been driven by the main achievements that authors have reported in the previous work (Brancadoro et al., 2018). In this earlier paper, a series of cylindrical samples made of a latex membrane filled with different fibrous materials has been tested and compared to identify the material that present the highest stiffness variation. In particular, PTFE, PVC, Nylon, Silicone, Waxed cotton, and Leather have been investigated and tested in two different configurations: bundle-type (BT) and comb-type (CT). The first one (i.e., BT) counts on fibers that are longitudinally arranged in a bundle fixed on one side only and without a specific organization (**Figure 3A**), while the CT configuration presents fibers organized as two tooth-interlocking combs (**Figure 3B**).

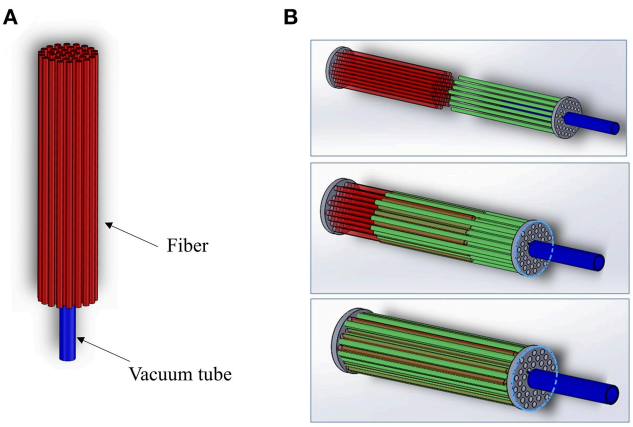

FIGURE 3 | CAD model for the **(A)** BT and **(B)** CT joint.

It is worth mentioning that, since the jamming transition is affected by friction effects among the filling fibers and between the fibers and the external membrane, the preliminary study proposed in Brancadoro et al. (2018) took this feature into

TABLE 1 | Summary of the results from Brancadoro et al. (2018).

Fiber material	Surface finishing	Design approach	Pressure (bar)	Force max. (N)	Stiffness variation ($F_{max\ jammed}/F_{max\ unjammed}$) (%)
PTFE	Very smooth	BT	1.01325	5.33 ± 0.16	+93 ± 13
			0.1	10.26 ± 0.39	
		CT	1.01325	5.89 ± 0.7	+108 ± 27
			0.1	12.06 ± 0.12	
PVC	Smooth	BT	1.01325	2.75 ± 0.07	+180.5 ± 10.5
			0.1	7.70 ± 0.09	
		CT	1.01325	2.92 ± 0.08	+216.5 ± 14.5
			0.1	9.24 ± 0.17	
Nylon	Very smooth	BT	1.01325	8.01 ± 0.15	+135 ± 12
			0.1	18.79 ± 0.61	
		CT	1.01325	19.07 ± 1.59	+43 ± 19
			0.1	26.96 ± 1.32	
Silicone	Rough	BT	1.01325	4.25 ± 0.11	+89 ± 8
			0.1	8.01 ± 0.13	
		CT	1.01325	2.55 ± 0.35	+205 ± 44
			0.1	7.63 ± 0.05	
Waxed cotton	Very rough	BT	1.01325	2.65 ± 0.11	+254 ± 20
			0.1	9.36 ± 0.13	
		CT	1.01325	2.56 ± 0.02	+377.5 ± 7.5
			0.1	12.23 ± 0.10	
Leather	Very rough	BT	1.01325	3.54 ± 0.13	+79.5 ± 14.5
			0.1	6.35 ± 0.28	
		CT	1.01325	3.86 ± 0.07	+291.5 ± 26.5
			0.1	15.09 ± 0.76	

The fiber type and the design approach selected for the present study is highlighted in the table (BT – Bundle Type; CT – Comb Type).

account investigating the surface finishing of the selected fibers and its correlation with the jamming transition for the two configurations. In particular, despite a numerical analysis is still missing, in that paper all the materials selected for the preliminary assessment have been compared also from this point of view in order to relate the stiffness variation of the joint configuration (Bundle type BT or comb type CT) to the material type. In particular, authors noticed that the fiber roughness order has a role in the effectiveness of the jamming effect, being directly correlated with the sliding capability of the fibers. In the present study, authors decided to adopt the combination of joint configuration and fiber type that has demonstrated the best performances in terms of stiffness variation. Although other materials and configurations are possible, currently there is no specific study or general model, thus the choice can be only guided by a comparative experimental analysis. According to those results (summarized in **Table 1**), the waxed cotton in the CT configuration has demonstrated the most promising stiffening features (increase of 377.5%) and have been incorporated in the modules.

Fibers have been confined in the dedicated sites by using the same guidelines defined in the previous work in terms of packing factor (i.e., the volume of the fibers divided by the volume of the section). In particular, keeping the same packing factor, 8 fibers have been used for Module A while 14 fibers have been inserted into each chamber of Module B, since each fiber has a diameter of 0.9 mm.

Manufacturing

The manufacturing of the two kinds of module consists of several steps based on silicone molding procedure. All the components for the module fabrication are realized using a 3D printer (ProJet MJP 3600, 3D Systems, South Carolina, US). For a better representation of the manufacturing procedure, the main phases are listed below and summarized in **Figure 4**:

a. Firstly, the mold for the chambers is prepared by winding an inextensible polyester thread around a 3D printed cylinder. This cylinder is composed of three assembled parts, an inner core and two side parts (**Figure 4a**). Six chamber molds and two chamber molds are prepared for Module A and Module B, respectively.
b. The fabrication of Module A starts positioning six chamber molds into a cylindrical-shaped mold composed of three identical parts and a central cylinder for the realization of the inner free lumen. To guarantee a precise mold alignment, that is essential for avoiding any asymmetries in the module, a thin Plexiglas plate is located on the top of the module for lodging all molds and for keeping them in place. The Plexiglas component is cut with a laser

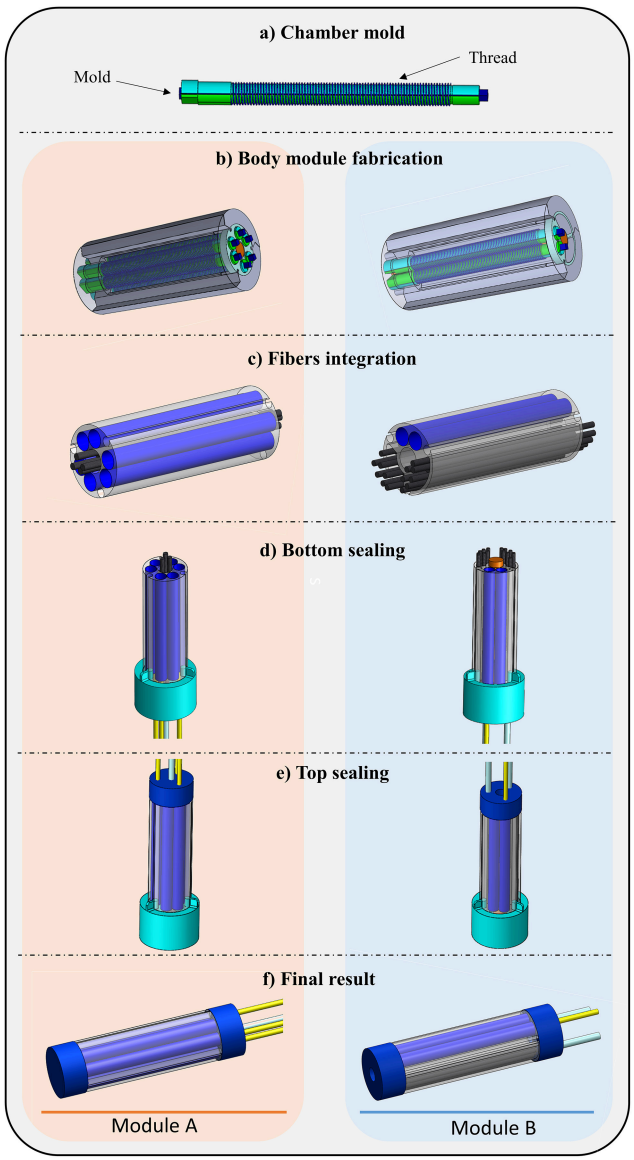

FIGURE 4 | (a–f) Modules manufacturing steps.

cutting machine (Universal Laser XLS10MWH, Universal Laser System Inc., US). The fabrication of Module B starts from the realization of the mold. It is composed of two chamber molds, two molds for the stiffening chambers, an inner cylinder and the upper Plexiglas plate for the alignment. **Figure 4b** shows the two assembly molds. Then, uncured silicone (Ecoflex 0050, Smooth On Inc., Macungie, PA) is poured into the molds and left to cure at room temperature. After the silicone has completely cured, all molds are removed.

c. Once this step is completed, a total of 36 fibers (i.e., 8 fibers for Module A and 28 fibers for Module B) are inserted with a CT configuration in the lumen and in the two lateral chambers of the Module A and Module B, respectively (**Figure 4c**). For creating the CT configuration, in each module, half of fibers exceed of 3 mm from the bottom face of the module and the residual fibers exceed of the same length from the other side. In this way, it is possible to encapsulate the fibers into the silicone base, thus guaranteeing that the fibers are arranged as two tooth-interlocking combs.

d. After fibers integration, the modules are sealed on bottom side using a dedicated cup mold filled with harder silicone (Smooth Sil 950, Smooth On Inc., Macungie, PA) (**Figure 4d**). At this stage, the pipes for the fluidic actuation (i.e., three for Module A and only one for Module B) and for the vacuum (i.e., one for Module A and two for Module B) are incorporated into the soft structure.

e. The last step concerns the sealing of the top side of the modules and it follows the same procedure described above (**Figure 4e**). The fluidic chambers are connected in pairs through a small silicone pipe located internally as a bridge between chambers. **Figure 4f** shows the final result.

The weight of each module is 9.2 g and 7.6 g for the Module A and B, respectively.

Experimental Set-Up and Protocol

In order to investigate the performances of the two different modules, several tests were carried out by using an *ad hoc* experimental set-up. Four different characteristics have been experimentally evaluated and compared with the performances achieved by the original STIFF-FLOP module: (i) variable stiffness at rest position; (ii) variable stiffness in bent configuration; (iii) workspace; (iv) shape locking capability.

The experimental set-up counts on parts that are used to drive the modules in all the tests (i.e., vacuum pump and air compressor) while specific equipment is introduced to perform the single tests (e.g., load cell, magnetic tracking system).

For driving the modules, a simple On/Off vacuum control was selected and implemented by using a vacuum pump (Oil Lubricated Rotary Vane Pumps MM56p2, D.V.P Vacuum Technology s.r.l., Carpanelli S.p.A.). The vacuum working state, measured by an absolute pressure sensor (SWCN-V01-P3-2, Camozzi Group), corresponds to 0.1 bar pressure level whereas the ambient pressure state is set to the atmospheric pressure (1.01325 bar). Regarding the fluidic actuation, the pressure inside each pair of chambers is controlled by a proportional pressure regulator directly connected to an air compressor (S.A. 30/6 type, Werther International Inc., Houston, USA). The specific tests are detailed in the subsections reported below.

Variable Stiffness at Rest Position

This test needed an *ad-hoc* metallic housing to host the base of the two modules (i.e., Module A and Module B). The module tip was deflected horizontally (along the x-axis referring to the reference Cartesian coordinate system of **Figure 5**) by an anthropomorphic robotic arm with six DoFs (RV-6SL; Mitsubishi Electric) for a distance of 15 mm at a speed of 5 mm/s, as shown in **Figure 5**. An ATI-mini 45 Force/Torque sensor (ATI Industrial

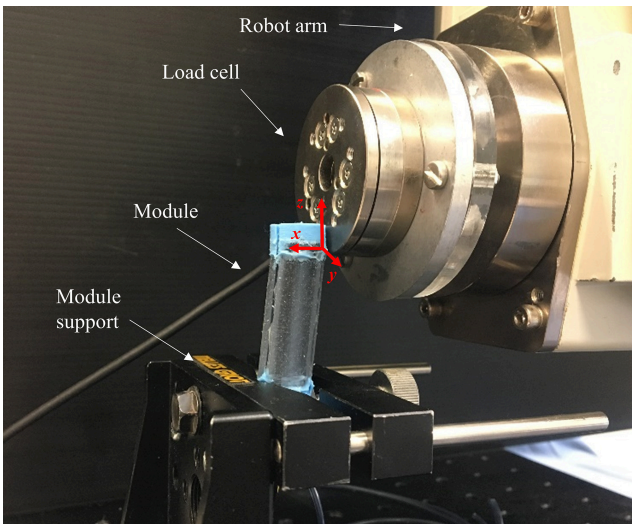

FIGURE 5 | Setup for testing variable stiffness at rest position (Module A is reported as example).

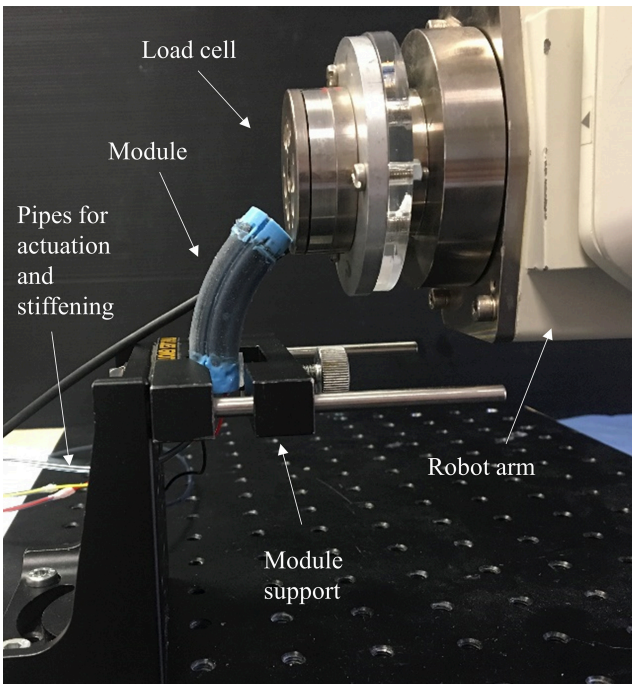

FIGURE 6 | Setup for testing variable stiffness in bent configuration (Module A is reported as example).

Automation, USA), mounted on the end-effector of the robotic arm, measured the resistive force developed by each module. The interaction surface between the module tip and the force sensor is properly defined for each test such that the application point of the force by the load cell to the module is kept as the origin of the reference Cartesian coordinate system, guaranteeing the same working conditions for all the experimental sessions. This point was conventionally defined as the lowest edge of the ATI-mini 45 sensor in contact with the most rigid silicone part of the module (the blue one). This point represents the origin of the reference Cartesian coordinate system and it is horizontally centered and vertically positioned 5 mm below the module tip. In order to guarantee the same setup for all the bending tests, the application point is manually reached before each test session. This experimental setup was controlled with a LabVIEW GUI (LabVIEW System Design Software—National Instrument), also used for data recording (sample rate of 10 kHz). Ten experimental trials were performed for each module: five tests keeping the stiffening chamber at atmospheric pressure (i.e., 1.01325 bar) and five under vacuum conditions (i.e., 0.1 bar). These tests are carried out for quantifying the contribution of the fiber jamming transition to the overall stiffness of the modules when at rest position.

Variable Stiffness in Bent Configuration

The same setup has been used to quantify variable stiffness in bent configuration (**Figure 6**), but a different protocol has been followed. Before applying the lateral load, one MP of each module is activated using 1 bar pressure. The robot arm, equipped with the load cell, pushes the module for 10 mm at 5 mm/s velocity. Five trials have been carried out with the jamming system at atmospheric pressure, and five with the application of vacuum conditions. The application point is the same of the test mentioned above.

Maximum force for all tests are recorded and compared; the stiffness variation is also related to the previously tested configuration in order to evaluate if the deformed state of the module affects the stiffening capability of the fiber jamming system.

Module's Workspace

To evaluate the module's workspace, the bending angle has been measured in relation with the applied pressure. The input air pressure ranges from 0 to 1.2 bar with an increment of 0.2 bar and inflates a pair of chambers for each module. The workspace is evaluated as the capability of each chamber to bend the module on a single plane. An electro-magnetic system (NDI Medical Aurora Northern Digital Inc., Waterloo, Canada), with 0.48 mm as maximum accuracy, was used as a ground truth pose measuring device. In particular, one Aurora Mini 6 DOF Sensor (1.8×9 mm) was fixed on the tip of the module while an Aurora 6 DOF Reference probe (25 mm Disc) is located on the module support, close to the module base (**Figure 7A**). The two probes are used to monitor the position and orientation of the module tip with respect to the base. By using the ground truth system, the bending angle (α) is derived as the angle between the vectors normal to the module base and tip surfaces on the bending plane (**Figure 7B**).

A total of five trials were conducted for each module activating only a pair of chambers. This test aims at evaluating how much the presence of the fibers affects the dexterity of the manipulator.

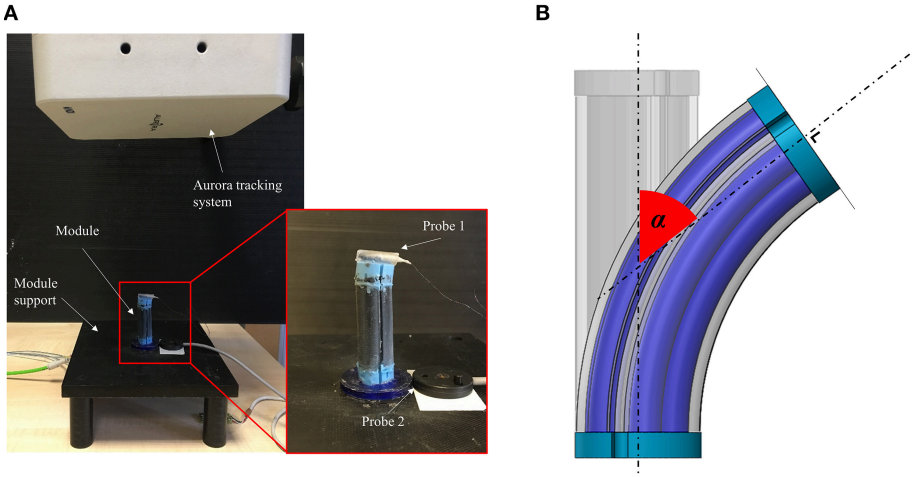

FIGURE 7 | (A) Test setup used for workspace and shape locking evaluation (Module A is reported as an example) and **(B)** bending angle (α) evaluation method.

Shape Locking

The same setup described for the workspace evaluation has been used for the shape locking tests following a multiphase procedure:

a. The module is bent supplying a 1.2 bar pressure to a pair of chambers
b. The angle α_1 is recorded
c. The vacuum is applied to the stiffening chamber for 30 s
d. The pressure is removed from the fluidic chambers
e. The angle α_2 is recorded.

Five tests for Modules A and B have been carried out.

RESULTS AND DISCUSSION

In this section, the results obtained for each experimental test are reported and discussed. The analysis is based on the comparison between the performances of the two proposed designs with respect to the original STIFF-FLOP module.

Variable Stiffness at Rest Position

Table 2 summarizes the results concerning the maximum stiffness variation that can be achieved for each configuration. For a comprehensive comparative analysis of the system performances, the maximum force developed by the original STIFF-FLOP module is reported as reference.

A first observation concerns the maximum force generated by each single module when the vacuum is not applied. It is reasonable that the original STIFF-FLOP module presents a lower maximum force with respect to Module A, because of the introduction of fibers in the inner free lumen. This change in the design can introduce an additional resistance to the bending motion that explains a value of 0.47 N for Module A with respect to 0.36 N of the original STIFF-FLOP module. Furthermore, the maximum force of the Module B is less than the maximum force of the other two configurations because the Module B has only one MP (i.e., two actuation chambers) instead of three (i.e., six actuation chambers) and two actuation chambers are more rigid than a chamber filled with fibers. This may seem counterintuitive, but, referring to **Figure 2**, it is easy to see that the cross section of Module A relies on a larger part of silicone that opposes to tensile forces developed during bending. In Module B, the most of the silicone is substituted by flexible fibers that can easily slide and bend when free to move.

TABLE 2 | Results of the bending tests carried out at rest configuration to evaluate the maximum stiffness variation for the three designs [i.e., original STIFF-FLOP module (Abidi et al., 2018), Module A and Module B].

Configuration	Maximum force (Vacuum off) [N]	Maximum force (Vacuum on) [N]	Stiffness variation
STIFF-FLOP module	0.36 ± 0.03	-	-
Module A	0.47 ± 0.02	0.57 ± 0.04	22 ± 15%
Module B	0.33 ± 0.02	0.85 ± 0.03	160 ± 28%

The last column of the **Table 2** reports the ratio between the maximum force measured in the jammed and the unjammed condition. This is the most appropriate parameter to assess the module performances and to provide a direct comparison of stiffening capability. The stiffening performance has a trend that is coherent with the design of the modules, namely the stiffness variation increases with the volume of the stiffening chamber and the number of fibers. Module A contains 8 fibers and presents a very limited stiffness variation with respect to Module B, which contains 14 fibers for each stiffening chamber (28 in total). Moreover, the location of the fibers plays a significant role. The bending moment of inertia of the module increases much more if the fibers are placed in the outer part of the cross section rather than in the central part.

In addition to these quantitative data, it is worth reporting that during these tests, once the imposed displacement is completely removed and no vacuum is applied, the modules equipped with fibers completely recover their initial position without showing

any permanent deformations. This means that fibers remain free to move also when the module is deformed if there is no fluidic input.

Variable Stiffness in Bent Configuration

The dominant role played by the fiber jamming is also confirmed in the stiffening test in bent configuration. Module B shows a remarkable stiffness variation, while Module A seems to be barely affected by the activation of the fiber jamming system, as reported in **Table 3**. The presence of two stiffening chambers enhances the module ability to keep its shape against external disturbances.

These data, together with those reported in section Variable stiffness at rest position, support the overall concept of using such kind of modules to provide stability to the distal segment of a two-module soft manipulator. The substantial stiffness variation of the proximal module demonstrates the ability to compensate external disturbances providing stability to the distal module that instead remains more dexterous and flexible.

Workspace

The results related to the workspace are limited to the evaluation of the module performances on a single bending plane. In particular, **Figure 8** shows the angles achieved by the module tip at increasing pressure. For a given pressure, the bending angle reached by Module B is considerably lower with respect to the Module A. This different response might be due to the structural role played by the fibers in the module. In both the cases the fiber jamming system is not active, but the fibers experience a sliding motion that is subject to friction. However, Module B includes many more fibers and they are arranged in a way that the area moment of inertia is much higher, thus causing a stiffer structure.

Observing the performances in terms of workspace for both modules and comparing the results with the STIFF-FLOP module (i.e., the bending angle is 132.2° at 1.2 bar Abidi et al., 2018), the integration of the fibers considerably decreases the module workspace. This effect was predictable and is supported by the data about stiffness variation, but this is an acceptable limitation for the intended application. In this work, the main aim is to improve the effectiveness of the two-module surgical manipulator by increasing its stability and this can be done by using a proximal module equipped with the stiffening systems (sacrificing part of the workspace) and a distal one with high dexterity and no stiffening capabilities.

TABLE 3 | Stiffness variation obtained in bent configuration for the two modules.

Configuration	Maximum force (Vacuum off) [N]	Maximum force (Vacuum on) [N]	Stiffness variation
Module A	0.28 ± 0.03	0.29 ± 0.02	Statistically irrelevant
Module B	0.36 ± 0.04	0.70 ± 0.03	99 ± 29%

Shape Locking Capability

The shape locking capability has been evaluated as the residual bending angle the module is able to maintain once the vacuum in the stiffness chambers is activated and the pressure in the fluidic chambers is removed. This effect is strictly related to the amount of fibers that are involved in the jamming transition phenomenon.

As expected, Module B presents a higher residual bending angle (**Table 4**). This module relies on a higher number of fibers and, looking at its overall design, its body has less silicone parts that in general give a large contribution in the elastic return of the module (i.e., recovery of its initial configuration once the deformation has been removed).

Overall Comparison

The results of the comparative analysis are summarized in **Figure 9**. Considering the STIFF-FLOP module as a reference

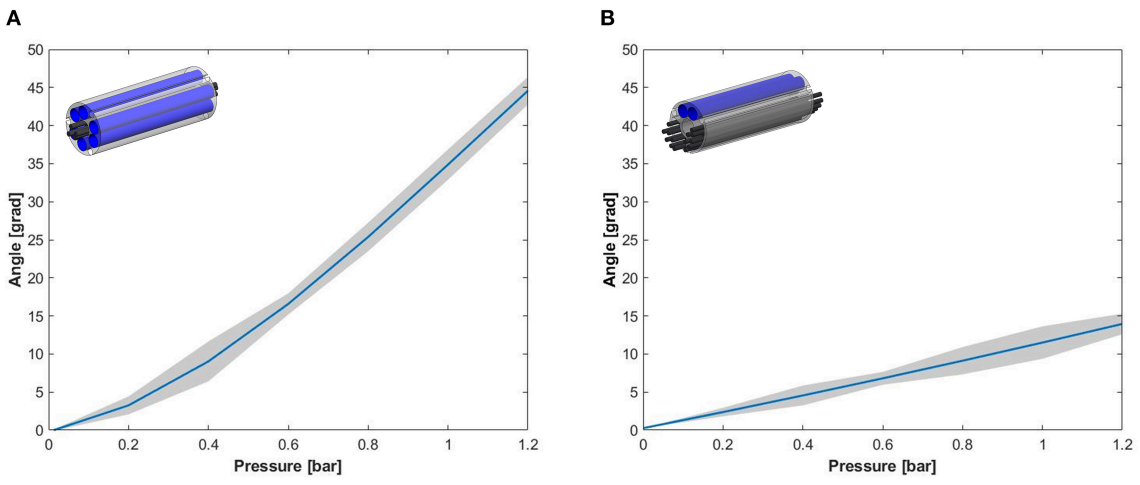

FIGURE 8 | Experimental results for the angular workspace obtained through the activation of a single pair of chambers of **(A)** Module A and **(B)** Module B.

starting point, both modules represent an improvement as they both demonstrated stiffening capability. However, this came with a significant reduction on flexibility and dexterity. This affected Module B more than Module A, mainly because of the higher number of fibers that have been integrated. It implies that the stiffening/stability is better for Module B (being directly proportional to the number of fibers), but to the detriment of dexterity. The only exception is represented by the passive tests (reported in **Table 2**) where the presence of the fibers seems to have a negative effect more on Module A than B. This suggests that: the presence of the fiber jamming system tends to make the module more flexible, but if a fluidic input is applied (whether it be vacuum to the jamming-based system or inflation of the fluidic chambers), a stiffness variation is induced and this variation is directly proportional to the volume of the fiber jamming chamber. This means that the fiber jamming system influences the behavior of the module both through direct or indirect activation.

Having a look at the system in terms of MPs and operational functionalities that a surgical manipulator should have in order to augment surgeon's abilities, Module A does not alter the motion capabilities of the STIFF-FLOP module, the central free lumen can no more be used for instrument insertion. Module B keeps the internal free lumen, but can only bend in one direction, meaning that the rotation of the supporting rod (the roll degree of freedom) must be enabled to restore omnidirectional bending (with severe implications on maneuverability).

The results highlight that, so far, there is no optimal solution that satisfies all the desired requirements in terms of miniaturized dimensions, free lumen for passing tools up to the tip, stiffness variation, flexibility and dexterity. The approach used in this work revealed an inverse relation between stiffness variation and motion performances, thus an optimal balance should be identified on the base of the target application. In particular, stiffness, and motion capabilities can be tuned in order to guarantee dexterity and flexibility for a soft and delicate navigation within the human body until the target district for the surgical task (e.g., retraction, suturing, and dissection) is reached, where on contrary stiffening is required for an effective force transmission.

TABLE 4 | The table summarizes the residual angles measured for the two modules.

Configuration	α_1 Angle @ 1.2 bar & Vacuum off	α_2 Angle @ 0 bar & Vacuum on	Residual angle $\frac{\alpha 2}{\alpha 1} \times 100$
Module A	46.66 ± 1.21°	9.31 ± 0.74°	20 ± 2.1%
Module B	14.80 ± 1.06°	10.32 ± 0.80°	70.18 ± 10.7%

CONCLUSION AND FUTURE WORK

Starting from the preliminary results obtained by Brancadoro et al. (2018), here we presented a possible exploitation of the fiber jamming transition technology as a variable stiffness mechanism integrated in the STIFF-FLOP soft manipulator. The STIFF-FLOP original module has been re-designed following two different approaches. The two new modules have been evaluated in terms of dexterity and variable stiffness capability. A comparative analysis has been carried out to study to what extent these two characteristics influence each other and to identify suitable compromises.

	WEIGHT	WORKING CHANNEL	MP	VARIABLE STIFFNESS	STIFFENING/ STABILITY	FLEXIBILITY AND DEXTERITY
STIFF-FLOP	8.5 g	YES	4 (3 bending + 1 elongation)	NO	0	+++
Module A	9.2 g	NO	4 (3 bending + 1 elongation)	YES	+	++
Module B	7.6 g	YES	1 (bending)	YES	++	+

FIGURE 9 | Module features: for each module architecture, weight, the presence of the inner free lumen (i.e., working channel), the number of MPs, the integration of a variable stiffness mechanism and the performance in terms of stability and flexibility are reported.

Results allowed defining the layout that presents the better trade-off between technical requirements and stiffness variation. A further outcome of the present study regards the awareness that the technology still needs further studies to be mastered, to define protocols and to standardize the manufacturing procedure, which so far is carried out through multiple manual steps as summarized in **Figure 4**.

In this view, the fiber jamming technology demonstrated to have suitable features for enabling a stiffness variation in soft bodied devices and in our specific case it is facilitating the shift from an endoscopic tool (mainly devoted to inspection and whose main requirements are dexterity, maneuverability and safe interaction), to a surgical tool (that should be able to transfer effective forces to the tissues and stabilization).

While the performances of the original STIFF-FLOP soft manipulator used as an endoscopic tool have been already proved in cadaver tests, the new capabilities enabled by the introduction of the fiber jamming technology still need to be tested in a real environment. Future activities will be focused on the assessment of the effectiveness and the advantages of such an approach in real surgical procedures (such as organ retraction, suturing, or dissection). On the other side, further studies on the physical principle at the base of fiber jamming transition itself could elucidate the main parameters affecting its performances and help defining design guidelines for the use of this technology.

AUTHOR CONTRIBUTIONS

MB, MM, and FG designed and fabricated the modules. All authors designed the experiments. MB and FG implemented the scenario and carried out the tests and the data analysis is made by MB, FG, and ST. MB, MM, and MC wrote the manuscript. ST, AM, and MC supervised the study.

REFERENCES

Abidi, H., Gerboni, G., Brancadoro, M., Fras, J., Diodato, A., Cianchetti, M., et al. (2018). Highly dexterous 2-module soft robot for intra-organ navigation in minimally invasive surgery. *Int. J. Med. Robot. Comput. Assist. Surg.* 14:e1875. doi: 10.1002/rcs.1875

Amend, J., Cheng, N., Fakhouri, S., and Culley, B. (2016). Soft robotics commercialization: jamming grippers from research to product. *Soft. Robot.* 3, 213–222. doi: 10.1089/soro.2016.0021

Arezzo, A., Mintz, Y., Allaix, M. E., Arolfo, S., Bonino, M., Gerboni, G., et al. (2017). Total mesorectal excision using a soft and flexible robotic arm: a feasibility study in cadaver models. *Surg. Endosc.* 31, 264–273. doi: 10.1007/s00464-016-4967-x

Behringer, R. P., and Chakraborty, B. (2018). *The Physics of Jamming for Granular Materials: A Review*. Reports on Progress in Physics.

Brancadoro, M., Manti, M., Tognarelli, S., and Cianchetti, M. (2018). "Preliminary experimental study on variable stiffness structures based on fiber jamming for soft robots," in *2018 IEEE International Conference on Soft Robotics (RoboSoft)* (Livorno: IEEE).

Diodato, A., Brancadoro, M., De Rossi, G., Abidi, H., Dall'Alba, D., Muradore, R., et al. (2018). Soft robotic manipulator for improving dexterity in minimally invasive surgery. *Surg. Innov.* 25, 69–76. doi: 10.1177/1553350617745953

Follmer, S., Leithinger, D., Olwal, A., Cheng, N., and Ishii, H. (2012). "Jamming user interfaces: programmable particle stiffness and sensing for malleable and shape-changing devices," in *Proceedings of the 25th Annual ACM Symposium on User Interface Software and Technology* (Massachusetts, MA: ACM).

Fraś, J., Czarnowski, J., Maciaś, M., Główka, J., Cianchetti, M., and Menciassi, A. (2015). "New STIFF-FLOP module construction idea for improved actuation and sensing," in *2015 IEEE International Conference on Robotics and Automation (ICRA)* (Seattle, WA:IEEE), 2901–2906. doi: 10.1109/ICRA.2015.7139595

Kaufhold, T., Böhm, V., and Zimmermann, K. (2012). "Design of a miniaturized locomotion system with variable mechanical compliance based on amoeboid movement," in *2012 4th IEEE RAS and EMBS International Conference on Biomedical Robotics and Biomechatronics (BioRob)* (Roma: IEEE), 1060–1065. doi: 10.1109/BioRob.2012.6290779

Kim, Y.-J., Cheng, S., Kim, S., and Iagnemma, K. (2013). A novel layer jamming mechanism with tunable stiffness capability for minimally invasive surgery. *IEEE Trans. Robot.* 29, 1031–1042. doi: 10.1109/TRO.2013.2256313

Laschi, C., and Mazzolai, B. (2016). Lessons from animals and plants: the symbiosis of morphological computation and soft robotics. *IEEE Robot. Autom. Mag.* 23, 107–114. doi: 10.1109/MRA.2016.2582726

Laschi, C., Mazzolai, B., and Cianchetti, M. (2016). Soft robotics: technologies and systems pushing the boundaries of robot abilities. *Sci. Robot.* 1:eaah3690. doi: 10.1126/scirobotics.aah3690

Li, M., Ranzani, T., Sareh, S., Seneviratne, L. D., Dasgupta, P., Wurdemann, H. A., et al. (2014). Multi-fingered haptic palpation utilizing granular jamming stiffness feedback actuators. *Smart Mater. Struct.* 23:095007. doi: 10.1088/0964-1726/23/9/095007

Liu, A. J., and Nagel, S. R. (1998). Nonlinear dynamics: jamming is not just cool any more. *Nature* 396:21. doi: 10.1038/23819

Manti, M., Cacucciolo, V., and Cianchetti, M. (2016). Stiffening in soft robotics: a review of the state of the art. *IEEE Robot. Autom. Mag.* 23, 93–106. doi: 10.1109/MRA.2016.2582718

Narang, Y. S., Vlassak, J. J., and Howe, R. D. (2018). Mechanically versatile soft machines through laminar jamming. *Adv. Funct. Mater.* 28:1707136. doi: 10.1002/adfm.201707136

Ou, J., Yao, L., Tauber, D., Steimle, J., Niiyama, R., and Ishii, H. (2014). "JamSheets: thin interfaces with tunable stiffness enabled by layer jamming," in *Proceedings of the 8th International Conference on Tangible, Embedded and Embodied Interaction* (Munich: ACM), 65–72.

Pfeifer, R., and Bongard, J. (2006). *How the Body Shapes the Way We Think: A New View of Intelligence*. Kadaikala: MIT Press.

Ranzani, T., Gerboni, G., Cianchetti, M., and Menciassi, A. (2015). A bioinspired soft manipulator for minimally invasive surgery. *Bioinspir. Biomimetics* 10:035008. doi: 10.1088/1748-3190/10/3/035008

Rus, D., and Tolley, M. T. (2015). Design, fabrication and control of soft robots. *Nature* 521:467. doi: 10.1038/nature14543

Shen, H. (2016). Meet the soft, cuddly robots of the future. *Nature* 530:24. doi: 10.1038/530024a

Stanley, A. A., Gwilliam, J. C., and Okamura, A. M. (2013). "Haptic jamming: a deformable geometry, variable stiffness tactile display using pneumatics and particle jamming," in *2013 World Haptics Conference (WHC)* (Daejeon: IEEE), 25–30. doi: 10.1109/WHC.2013.6548379

Steltz, E., Mozeika, A., Rodenberg, N., Brown, E., and Jaeger, H. M. (2009). "Jsel: Jamming skin enabled locomotion," in *IEEE/RSJ International Conference on Intelligent Robots and Systems, 2009. IROS 2009* (St. Louis, MO: IEEE), 5672–5677. doi: 10.1109/IROS.2009.5354790

Sun, Y., Yap, H. K., Liang, X., Guo, J., Qi, P., Ang M. H. Jr., et al. (2017). Stiffness customization and patterning for property modulation of silicone-based soft pneumatic actuators. *Soft Robot.* 4, 251–260. doi: 10.1089/soro.2016.0047

Wall, V., Deimel, R., and Brock, O. (2015). "Selective stiffening of soft actuators based on jamming," in *2015 IEEE International Conference on Robotics and Automation (ICRA)* (Seattle, WA: IEEE), 252–257. doi: 10.1109/ICRA.2015.7139008

Wang, L., Yang, Y., Chen, Y., Majidi, C., Iida, F., Askounis, E., et al. (2018). Controllable and reversible tuning of material rigidity for robot applications. *Materials Today* 21, 563–576. doi: 10.1016/j.mattod.2017.10.010

Zambrano, D., Cianchetti, M., Laschi, C., Hauser, H., Füchslin, R., and Pfeifer, R. (2014). The morphological computation principles as a new paradigm for robotic design. *Opin. Outlooks Morphol. Comput.* 214–225. doi: 10.13140/2.1.1059.4242

Conflict of Interest Statement: The authors declare that the research was conducted in the absence of any commercial or financial relationships that could be construed as a potential conflict of interest.

frontiers in Robotics and AI

ORIGINAL RESEARCH
published: 09 April 2019
doi: 10.3389/frobt.2019.00022

Model-Based Control of Soft Actuators Using Learned Non-linear Discrete-Time Models

Phillip Hyatt[1], *David Wingate*[2] *and Marc D. Killpack*[1]*

[1] Robotics and Dynamics Lab, Department of Mechanical Engineering, Brigham Young University, Provo, UT, United States,
[2] Perception, Control, Cognition Lab, Department of Computer Science, Brigham Young University, Provo, UT, United States

Soft robots have the potential to significantly change the way that robots interact with the environment and with humans. However, accurately modeling soft robot and soft actuator dynamics in order to perform model-based control can be extremely difficult. Deep neural networks are a powerful tool for modeling systems with complex dynamics such as the pneumatic, continuum joint, six degree-of-freedom robot shown in this paper. Unfortunately it is also difficult to apply standard model-based control techniques using a neural net. In this work, we show that the gradients used within a neural net to relate system states and inputs to outputs can be used to formulate a linearized discrete state space representation of the system. Using the state space representation, model predictive control (MPC) was developed with a six degree of freedom pneumatic robot with compliant plastic joints and rigid links. Using this neural net model, we were able to achieve an average steady state error across all joints of approximately 1 and 2° with and without integral control respectively. We also implemented a first-principles based model for MPC and the learned model performed better in terms of steady state error, rise time, and overshoot. Overall, our results show the potential of combining empirical modeling approaches with model-based control for soft robots and soft actuators.

Keywords: soft robot control, soft robot actuation, model predictive control, DNN, machine learning

OPEN ACCESS

Edited by:
S. M. Hadi Sadati,
University of Bristol, United Kingdom

Reviewed by:
Sunan Huang,
National University of Singapore, Singapore
Mohsen Khadem,
University of Edinburgh, United Kingdom

***Correspondence:**
Marc D. Killpack
marc_killpack@byu.edu

Specialty section:
This article was submitted to Soft Robotics, a section of the journal Frontiers in Robotics and AI

Received: *05 December 2018*
Accepted: *12 March 2019*
Published: *09 April 2019*

Citation:
Hyatt P, Wingate D and Killpack MD (2019) Model-Based Control of Soft Actuators Using Learned Non-linear Discrete-Time Models. Front. Robot. AI 6:22. doi: 10.3389/frobt.2019.00022

1. INTRODUCTION

Although model-based control can generally result in control that is superior to methods that do not rely on models, it is often difficult to justify the effort required to perform system identification or model development for complex systems. A common result is that we identify models that describe the system dynamics poorly and result in control that is barely (if at all) on par with basic feedback control methods such as PID control. As an example, soft robots are especially hard to model accurately for model-based control. The specific platform shown in **Figure 1** has three joints that are made of antagonistic blow-molded plastic pneumatic chambers, where each joint has two degrees of freedom. In past work, Gillespie et al. (2018), we have shown that for a single degree of freedom soft robot, we could learn a model that performed on par with a linear model that we derived from first principles and traditional system identification techniques. However, in the case of the platform in **Figure 1**, we have all of the same problems that exist with the previous one degree of freedom platform (e.g., non-linear gas dynamics, hysteresis in joint behavior, state dependent stiffness and torque output, etc.), in addition to having to deal with linearizing and discretizing a 24 dimensional non-linear set of ordinary differential equations to describe the rigid body dynamics of a 3-link, 6-DoF pneumatic robot.

FIGURE 1 | Series of joint configurations showing how this six degree of freedom pneumatic continuum robot can move.

As a first step toward learning models for soft robot control with a large number of degrees of freedom, we show that we can learn a discretized, non-linear model of the full robot from a non-linear simulation which allows us to achieve better control performance than the linearized model that is based on first principles. Although we are not advocating ignoring all physical intuition, we propose in this paper that it is possible to use recent advances in machine learning to rapidly develop an empirical model that can handle some of the non-linearities and complexities listed above for this system, and that can be used for control.

To model the unknown dynamics of our soft robot, we turn to the tools of deep learning. Deep learning is one of the most compelling advances in machine learning in recent memory. It has swept over both industry and academia, crushing benchmarks and generating impressive progress across fields as diverse as speech recognition (Dahl et al., 2012; Hinton et al., 2012; Deng et al., 2013; Abdel-Hamid et al., 2014), parsing of natural scenes (Lee et al., 2009; Socher et al., 2011), machine translation (Cho et al., 2014; Sutskever et al., 2014; Zhang and Zong, 2015), robotics (Eitel et al., 2015; Wulfmeier et al., 2015; Zhang et al., 2015; Levine et al., 2016), machine vision (Krizhevsky et al., 2012; Schmidhuber, 2012; Szegedy et al., 2015; Zeng et al., 2015), and even the game of Go (Silver et al., 2016).

A system like the robot described in this work, with severe hysteresis and unknown state interactions, is difficult to model even with explicit non-linear dynamics. These difficult-to-model dynamics are a perfect candidate for universal function approximation with deep neural networks, or DNNs. The only requirements for the approach proposed in this paper are that we must define the state variables and inputs based on our physical intuition about the problem. Additionally, we must be able to record data at each time step for our current states and randomized control inputs. Then we can train a deep neural net to approximate the non-linear, discretized dynamics and then linearize that model at each time step for control.

Our specific contributions include the following:

- Development of a non-linear neural network (NN) architecture for dynamic modeling of a 6 DoF pneumatic robot with soft actuators based on data from a full non-linear model.
- Development of a model predictive controller that can use the partial derivatives of the NN at every time step in order to remain tractable for low-level, high-bandwidth control while modeling joint configurations, joint velocities, and joint pressures.
- Development of a first-principles-based model and a model predictive controller for a 6 DoF continuum pneumatic robot with soft actuators.
- Identification of specific open questions relative to learning more accurate dynamic models for future model-based soft robot control.
- Validation and benchmarking of the non-linear NN model for model-based control against the first principles model for a large number of degrees of freedom.

The last contribution is especially interesting as we expect this approach to generalize to other difficult-to-model actuators or robot systems where model-based control would be expected to improve low-level control performance but system identification or even model development is particularly difficult.

The rest of this paper is organized as follows, we first describe related work in section 2.1. In section 2.2, we describe our robot platform. Section 2.3 describes the modeling and control of the robot. Our results are presented in section 3 and we discuss the results in section 4.

2. MATERIALS AND METHODS

2.1. Related Work

Past research that is related to the work we present in this paper can be divided into two main areas. The first is using neural networks either as a model for model-based control or as a controller itself. The second area is other parametric models that are used to produce optimal control policies. After discussing these areas, we also briefly address related work on controlling soft robots. More background on research using model predictive control in robotics can be found in Jain (2013) and Best et al. (2016). However, it is important to note that model predictive control solves a finite horizon optimal control problem at each time step subject to the model dynamics as an equality constraint along with any other defined constraints on the states and inputs.

2.1.1. Other Learned Models for Model-Based Control

Although traditional robotics modeling has focused on system identification of traditional physics-based models (see Swevers et al., 1997; Park et al., 2011), the last 20 years has seen a significant increase in the number of empirical models and methods that have been developed (see Nguyen-Tuong and Peters, 2011). One common approach is to use Gaussian Processes (GP) to model the dynamic system and this seems to have first been done in the chemical processing industry (see

Kocijan et al., 2004 for example). Currently in robotics, GP has been used to develop a policy search algorithm for a robot arm with imprecise actuators and cheap sensors (Deisenroth et al., 2011), or for more general purpose control policy development (Deisenroth et al., 2015). Other researchers have used Gaussian Mixture Models such as in Calinon et al. (2007). We make no direct comparison to these other modeling methods in this paper, but expect that this would be a worthwhile comparison in future work.

Although there exists a large number of other learning methods that we could have used or compared against (e.g., Gaussian Processes, or support vector machines), we have chosen DNNs for their unique properties that make them an ideal choice for this application. Specifically, both GPs and SVMs require fixed-size data sets, but our vision is to extend this work to on-line scenarios where system identification happens concurrently with control. In addition, an important aspect of using DNNs is differentiability. Part of the appeal of using DNNs is the fact that many off-the-shelf frameworks for deep learning (Tensorflow, MXNet, pytorch) all support automatic differentiation. This makes it easy to compute the gradients of dynamics with respect to control inputs, which is needed for MPC. In contrast, we are not aware of any existing GP/SVM packages that have similar capabilities.

2.1.2. Neural Nets

The approach of using neural networks (similarly to model predictive control), appears to have come from the chemical processing industry and work that is most relevant to our approach for robotics was found in Psichogios and Ungar (1991), Piche et al. (1999), and Draeger et al. (1995) and is still an active area of research (Patan, 2015).

Early work using neural networks for modeling robots was done in Kiguchi et al. (1999), but it was not used for control. In Tan et al. (2007) they use neural networks to learn disturbance models online while controlling, while in Huang et al. (2000) and Huang et al. (2002) radial basis functions are used to learn friction effects modeled in an adaptive control scheme. These adaptive control ideas could be particularly applicable to our platform in future work as the air bladders in our soft robot tend to wear or shift over time, which then changes the dynamic model. In Yan and Wang (2011) Yan and Wang use a recursive neural net to represent the higher order error terms that result from a Taylor series linearization. While in Yan and Wang (2014) they use a minimax optimization and learn a neural net model for part of their unknown dynamics. In both cases, the only results shown are in simulation.

More recent work has focused on learning controllers or models for high-level tasks. In Lenz et al. (2015) for example, they use a recurrent neural net to learn features of specific classes of fruits and other foods in order to more efficiently slice the food. The formulation is application specific but uses the neural network gradients similarly to our approach. For the work in Zhang et al. (2016), they used a DNN to learn a MPC control policy for UAVs. Levine and Abbeel do policy search using locally linear dynamics models to learn neural network controllers for different robot tasks (e.g., swimming, insertion) in Levine and Abbeel (2014). Finally, Fu et al. (2015) use neural networks to generate and adapt models online that can be used for model-based reinforcement learning to learn a control policy that makes use of iterative LQR. Although the output is a low-level torque for each joint, this approach does not generalize to more basic capabilities such as force or position control. Low-level control is our current interest given the inherent non-linearity and complexity of our platform even without interacting with complicated environments.

In general, using neural nets for system identification is a well-known method (Narendra and Parthasarathy, 1990), but the novelty of our paper is that we apply the method to control soft robot platforms by combining neural nets with MPC for low-level control. There is an inherent trade-off for controllers when using these types of black box modeling. The trade-off is that we can either develop controllers that can be used for multiple tasks when the tasks can be decomposed into specific and explicit force or position requirements or we can develop controllers for tasks where even the desired force and position profiles are uncertain with respect to the robot hardware. In the second case, learning the task rather than (or in addition to) the robot dynamics is necessary but is a next step to the work we present here for low-level control of soft robots.

2.1.3. Soft Robot Control

A significant portion of soft robot research described in the survey (Rus and Tolley, 2015) was focused on design methodologies instead of closed-loop control performance and so most robots were controlled with open-loop strategies such as in Shepherd et al. (2011) and Tolley et al. (2014). Research that is most related to ours in terms of trying to control a robot to a specific configuration includes the use of inflatable links with cable tendons (Sanan et al., 2009, 2011), fluid drive elastomer (Marchese et al., 2014a,b; Marchese and Rus, 2015), or rotary elastic chamber actuators such as in Ivlev (2009) and Gaiser et al. (2014). However, in addition to other differences with past soft robot control work that we outline more specifically in Best et al. (2016), as far as we know they have not developed control for these robots based on learned empirical models like those that we present in this paper. This is true except for work in Thuruthel et al. (2017) where they learn dynamic models similar to what we present. However, they use those models in an open-loop control scheme which may be problematic in the case of model error, change over time, or any kind of disturbance. A recent survey that explains the state of the field for soft and continuum robot control can be found in George Thuruthel et al. (2018).

2.2. Robot Platform Description

The platform used for this research was a compliant, continuum robot with six actuated degrees of freedom (see **Figure 1**). Each joint consists of four pneumatic chambers made of blow-molded plastic. The top and bottom sections of the actuator are connected with a cable putting the bellow actuators in compression to some degree. By filling or venting each chamber, we can get motion about two different axes of rotation as shown in **Figure 2**. The platform was developed and built by Pneubotics, an affiliate of Otherlab. In our previous work, we applied the methods

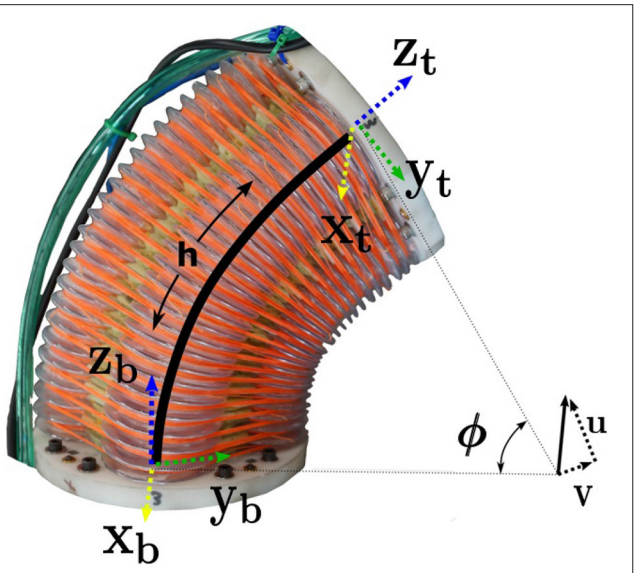

FIGURE 2 | Kinematic frames and model used for blow-molded continuum joint.

presented in this paper on a one degree of freedom, fabric-based, soft robot joint. In this paper, the platform we use still has soft joints and is pneumatic. However, rigid components are used to connect the soft joints. The motivation for using learning is however unchanged since the joints exhibit very non-linear behavior including the gas dynamics, hysteresis, non-linear stiffness, and other non-linearities.

Because each joint is a continuum with two degrees of freedom, it is necessary to describe its configuration with two joint variables. We represent rotation at the joint using a vector constrained to be in the plane of the base of the joint as seen in **Figure 2**. Because it is constrained to a plane, the vector only has two components which we name u and v. These are our joint configuration variables. The magnitude of this vector (ϕ) is the rotation angle about a single axis, while the vector describes that rotation axis. Joint configuration estimation is accomplished in real-time using software supplied by the manufacturer. This software uses data from IMUs mounted on the rigid links to estimate u, v, $\dot{u}$, and $\dot{v}$.

Joints are actuated by controlling pressure separately in each of the 4 chambers in each joint (12 pressures total for the arm). While the bottom joint has 8 chambers, these are controlled in pairs of two, so it is effectively a larger version of the 4 chamber joints. For this work, supply pressure was maintained at 70 PSI while pressures in the chambers were limited between 18 and 55 PSI by the controller. These pressure limits were enforced to ensure the robot did not damage itself.

We use the Robot Operation System (ROS) to access state estimates as well as to send pressure commands. Our MPC controller code is operating in non-realtime on an Ubuntu workstation, while the state estimation and low level pressure control is being executed at 1,000 Hz on a PC with a real-time linux kernel.

2.3. Development of Dynamic Models

2.3.1. First Principles Dynamics Model

A model of the evolution of system states was derived from first principles based on material properties, lengths, and masses provided by the manufacturer of the robot. Because commanded pressures were not achieved instantaneously, it was deemed necessary to model the dynamics of pressures and the high rate pressure controller. The entire state of our system is therefore $\mathbf{x} = [p, \dot{q}, q]^T$ where p is the vector of the pressures in the 12 chambers (4 per joint), $\dot{q}$ is the vector of 6 joint velocities ($[\dot{u}_1, \dot{v}_1, \dot{u}_2, \dot{v}_2, \dot{u}_3, \dot{v}_3]$), and q is the vector of 6 joint positions ($[u_1, v_1, u_2, v_2, u_3, v_3]$). The inputs to our system are $\mathbf{u} = [p_{ref}]$ where p_{ref} is a column vector of commanded pressures sent to the high rate PID pressure controller.

The pressure dynamics were modeled as first order according to the differential equation

$$\dot{p} = \alpha(p_{ref} - p) \tag{1}$$

where α is a diagonal matrix of constant coefficients which represent the speed of filling or venting a chamber.

The dynamics of the links were modeled using the equation

$$M(q)\ddot{q} + C(\dot{q}, q)\dot{q} = K_d\dot{q} + K_{spring}q + \tau_{grav} + K_{prs}p \tag{2}$$

where $M(q)$ is the joint space inertia matrix, $C(\dot{q}, q)$ is the joint space Coriolis matrix, K_{spring} and K_d are spring and viscous damping terms which are significant in our elastic continuum joints, τ_{grav} is a vector of the torques caused by gravity, K_{prs} is a matrix which maps the pressures in the chambers to torques at the joints. While this model could benefit greatly from further system identification, we report results using this model and leave model improvement for future work.

Placing all of the state variables and derivatives into state space form we can write

$$\dot{\mathbf{x}} = \mathbf{A}\mathbf{x} + \mathbf{B}\mathbf{u} + \mathbf{w} \tag{3}$$

where

$$\mathbf{A} = \begin{bmatrix} -\alpha & 0 & 0 \\ M^{-1}K_{prs} & M^{-1}(K_d - C) & M^{-1}K_{spring} \\ 0 & 1 & 0 \end{bmatrix} \tag{4}$$

$$\mathbf{B} = \begin{bmatrix} \alpha \\ 0 \\ 0 \end{bmatrix} \tag{5}$$

$$\mathbf{w} = \begin{bmatrix} 0 \\ \tau_{grav} \\ 0 \end{bmatrix} \tag{6}$$

By writing the model in this way, we are assuming that the state dependent matrices in A change slowly over the time horizon in our controller [similar to our models in past work Killpack et al. (2016) for rigid robots with compliance at the joints]. The discretization of the continuous time state space matrices is done using the matrix exponential, which gives

$$\mathbf{x_{k+1}} = \mathbf{A}_d\mathbf{x}_k + \mathbf{B}_d\mathbf{u} + \mathbf{w}_d. \tag{7}$$

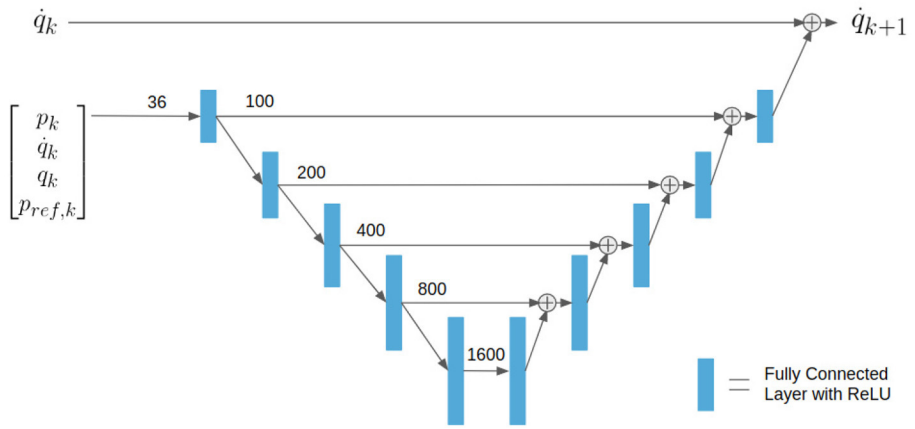

FIGURE 3 | DNN architecture implemented to predict future velocities.

where

$$\mathbf{A}_d = e^{\mathbf{A}\Delta t} \tag{8}$$

$$\mathbf{B}_d = \mathbf{A}^{-1}(\mathbf{A}_d - \mathbf{I})\mathbf{B} \tag{9}$$

$$\mathbf{w}_d = \mathbf{w}\Delta t \tag{10}$$

2.3.2. Deep Neural Net Architecture and Model

A Deep Neural Net (DNN) of the form shown in **Figure 3** was trained as a discrete-time dynamic model for the velocity states of our system. Because we have fairly accurate and simple representations for pressure and position, we represent those using first principles methods. The entire model consisted of about 3.4 million nodes in an architecture similar to the Unet architecture used for image processing (Ronneberger et al., 2015), except our architecture uses fully connected layers with ReLU activations instead of convolutions. The model used for this work was trained for less than 1 h on a NVIDIA Titan X GPU. The DNN can be described as finding the change in velocity between time steps k and $k+1$ taking as inputs the entire state and inputs at time k. Assuming our system is a first order Markov system, this approach should be very reasonable. The DNN can be represented as a function of the form

$$\dot{q}_{k+1} = f(\mathbf{x}_k, \mathbf{u}_k). \tag{11}$$

As a method of collecting a large amount of data very quickly and without wear or danger to the actual robot, we used the non-linear first principles model outlined above (before discretization and linearization) to train the DNN. Non-linear simulation was accomplished by integrating the state space equations at a discretization of 0.001 s. In order to train the DNN to predict $\dot{q}_{k+1}$ at a discretization of 0.05 s, the non-linear simulation was carried out for 50 integration steps. Because p_k, q_k, and p_{ref} all have definite bounds, these were sampled uniformly within their bounds. However, $\dot{q}_k$ is not bounded, so samples were drawn from a mean zero normal distribution. In an attempt to scale the input space equally, p and p_{ref} were scaled and offset to be mean zero values between –1 and 1. Using units of radians q was bounded by +- $\frac{2\pi}{3}$.

It should be noted that a method to learn new features while maintaining old ones could be used to improve this model (Rusu et al., 2016), however our control results demonstrated acceptable performance without this step. An example of open loop prediction of joint positions using the DNN compared to the first principles model and measured data can be seen in **Figure 4**. The error statistics for both position and velocity are reported in **Table 1**.

Using a non-linear optimization, this non-linear model could be used for MPC, however in order to ensure that we solve at fast enough rates for real-time control we choose to linearize this DNN model using the Taylor Series expansion. The Taylor expansion of our DNN model (Equation 11) linearized about $\mathbf{x}_0, \mathbf{u}_0$ is

$$\dot{q}_{k+1} = \left.\frac{\partial f}{\partial \mathbf{x_k}}\right|_{\mathbf{x}_0,\mathbf{u}_0} (\mathbf{x}_k - \mathbf{x}_0) + \left.\frac{\partial f}{\partial \mathbf{u_k}}\right|_{\mathbf{x}_0,\mathbf{u}_0} (\mathbf{u}_k - \mathbf{u}_0) + f(\mathbf{x}_0, \mathbf{u}_0) \tag{12}$$

where the partial derivatives are of the DNN's outputs with respect to its inputs. While these partial derivatives of the entire non-linear DNN may be too long and complex to write by hand, they are easily obtained using the automatic differentiation library already included as part of the DNN training library.

Because the DNN only predicts the velocities at the next time step ($\dot{q}_{k+1}$), we must supply a discrete model for pressures (p_{k+1}) and positions (q_{k+1}). For positions we use a simple numerical integration using the trapezoidal rule:

$$q_{k+1} = q_k + \frac{\Delta t}{2}(\dot{q}_k + \dot{q}_{k+1}) \tag{13}$$

while for pressures we use the simple discretization of Equation 1

$$p_{k+1} = \alpha\Delta t(p_{ref}) + (I - \alpha\Delta t)p_k \tag{14}$$

The discrete-time state space equation for this system is given by

$$\mathbf{x_{k+1}} = \mathbf{A}_d(\mathbf{x}_k - \mathbf{x}_k) + \mathbf{B}_d(\mathbf{u}_k - \mathbf{u}_k) + \mathbf{w}_d \tag{15}$$

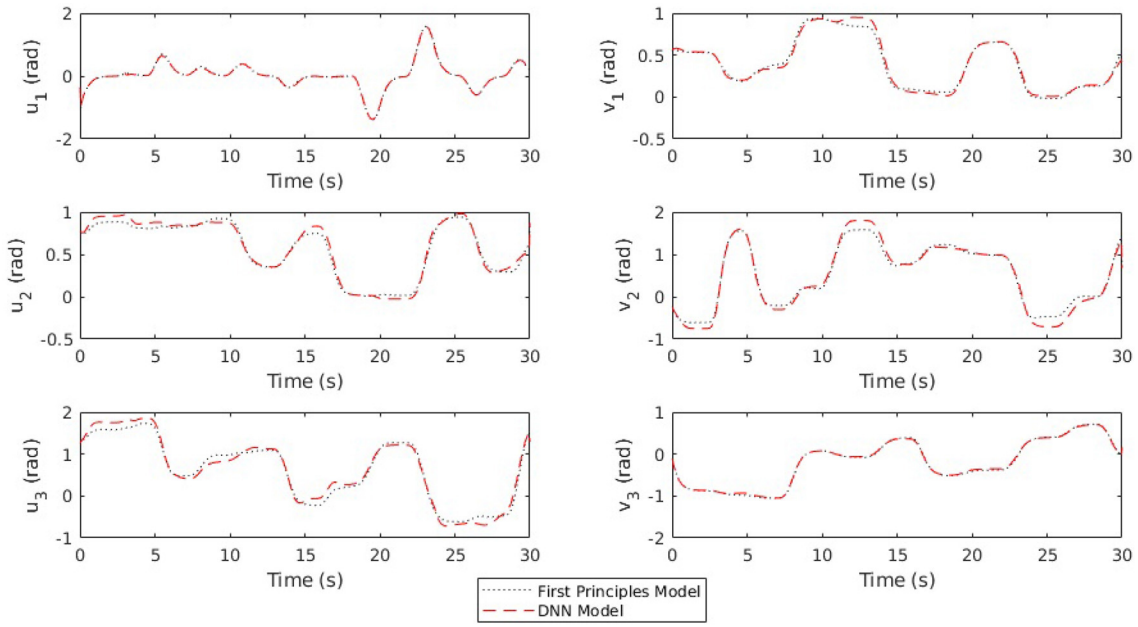

FIGURE 4 | Simulations using the same initial states and a 30 s input trajectory are rolled out using the DNN model and the first principles model. For most of the trajectory, these lines are indistinguishable.

TABLE 1 | Error statistics for a 30 s rollout of arm dynamics.

Non-linear DNN prediction error			
	Max	**Mean**	**Std. Dev.**
Velocity error (rad/s)	1.0721	−0.000003	0.0237
Position error (rad)	0.3736	−0.0012	0.0223

Error is reported as the difference between the non-linear DNN model prediction and the non-linear simulation used to train the arm.

where

$$\mathbf{A}_d = \begin{bmatrix} (I - \alpha\Delta t) & 0 & 0 \\ \frac{\partial f}{\partial p_k} & \frac{\partial f}{\partial \dot{q}_k} & \frac{\partial f}{\partial q_k} \\ \frac{\partial f}{\partial p_k}\frac{\Delta t}{2} & (\frac{\partial f}{\partial \dot{q}_k} + I)\frac{\Delta t}{2} & \frac{\partial f}{\partial q_k}\frac{\Delta t}{2} + I \end{bmatrix} \tag{16}$$

$$\mathbf{B}_d = \begin{bmatrix} \alpha\Delta t \\ \frac{\partial f}{\partial p_{ref,k}} \\ 0 \end{bmatrix} \tag{17}$$

$$\mathbf{w}_d = \begin{bmatrix} p_0 \\ f(\mathbf{x}_0, \mathbf{u}_0) \\ \frac{\Delta t}{2}\dot{q}_0 + q_0 \end{bmatrix} \tag{18}$$

2.4. Model Predictive Control Development

The linear discrete-time state space models (Equations 7, 15) are used as constraints in an MPC controller that is run at 20 Hz. A flow chart for the control process can be seen in **Figure 5**. The outputs from the model predictive controller are reference pressures that are sent to a low level PID pressure controller running at 1,000 Hz.

Feedback for the MPC controller is given by a state estimator supplied by the manufacturer. This state estimator uses IMUs and pressure sensors mounted on the arm to estimate p, $\dot{q}$, and q. This data is updated at a rate of 1,000 Hz.

The solver that we used for MPC was generated using CVXGEN (see Mattingley and Boyd, 2012 for more details about the optimization and constraint handling), a web-based tool for developing convex optimization solvers, with a horizon of 4 time steps. The cost function minimized across the horizon T is

$$minimize \sum_{k=1}^{T} \|q_{goal} - q_k\|_Q^2 + \|p_{ref,k} - p_{ref,k-1}\|_R^2 \tag{19}$$

subject to the system model as constraints, as defined in Equations (7, 15) (the first principles and DNN dynamic models respectively), as well as the following additional constraints:

$$q_{min} \leq q_k \leq q_{max} \quad \forall\ k \tag{20}$$

$$p_{min} \leq p_{ref,k} \leq p_{max} \quad \forall\ k \tag{21}$$

where Q and R are scalar weights manually tuned for performance, q_{min} and q_{max} are the joint limits, and p_{min} and p_{max} are minimum and maximum pressures. It is important to note that the weights in the cost function for MPC are what will determine the performance of the control to a large degree in terms of traditional metrics like rise time, steady state error, and overshoot. Also note that the weighting matrix R penalizes change in pressure from one step to another. This

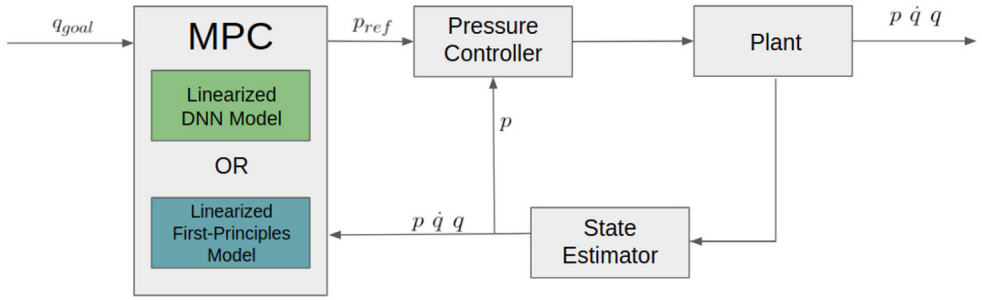

FIGURE 5 | Control loop diagram showing the MPC controller sending pressure commands (p_{ref}) to a low level PID pressure controller.

term discourages very fast motions and eliminates the need for velocity constraints.

We used the exact same weights and constraints for all controller comparisons. We instead varied only the model (either based on first principles or the DNN learned model) and whether or not an integrator was used. When an integrator was used, the following equation was used to handle steady state error with integral action:

$$q_{goal,k+1} = q_{goal,k} + k_i(q_{goal,k} - q_k) \tag{22}$$

When the integrator was used, it was only ever active when the combined error in joint angles versus their commanded angles was less than 0.4 radians to help with overshoot. Although step inputs are notorious for exciting overshoot and oscillation in underdamped systems, as opposed to trajectories smoothed with sinusoids or polynomials, we wanted to test the performance of our models and controllers and therefore we sent direct step inputs to each joint. In the future, these same commands could be smoothed to likely achieve better performance. However, the same could be argued if our models continue to improve and our model predictive controllers are able to make use of methods to predict further into the future (see more discussion in section 4).

3. RESULTS

In each trial for our experiments, the same set of commanded joint angles (u and v for each joint) were sent to the controller with 20 s intervals between commands. The commanded angles are found in **Table 2** and were selected in order to force the arm to move through most of its workspace. Step commands are not traditionally used in robotics due to the fact that they can induce unwanted dynamics or oscillation, even in traditional rigid robots. However, in this case, we want to test our controller's ability to use the model to mitigate unwanted behavior, similar to some of our past work (see Rupert et al., 2015; Terry et al., 2017). The results for the same model predictive controller using the two different linearized models (first-principles and DNN), and with and without integral action, are found in **Figure 6**. A video showing the robot moving through the same joint configurations as those found in **Table 2** and shown in **Figure 1** can be seen at https://youtu.be/ddA0g0yKjOc. The controller used in the video is the DNN MPC controller with no integral action. The video also shows the compliance of the soft actuators when perturbed by an external disturbance.

TABLE 2 | This set of joint angle commands move the continuum robot arm throughout the workspace and are used to evaluate performance.

	Joint angle commands				
	Initial	*Step*1	*Step*2	*Step*3	*Final*
u_1	0.0	0.5	0.707	−0.354	0.0
v_1	0.0	0.25	0.707	0.354	0.0
u_2	−0.4	−0.707	0.707	0.0	−0.4
v_2	−0.4	0.2	−0.2	0.0	−0.4
u_3	0.0	0.707	−0.5	0.2	0.0
v_3	0.0	0.354	0.707	0.354	0.0

In addition, the median steady state error, rise time, and overshoot for each joint and each controller is included in **Table 3**. We also included an average across all the joints for each controller and the controller that performed the best is shown in bold. Where C1 refers to the first principles MPC without integral control, C2 refers to the first principles MPC with integral control, C3 refers to the DNN MPC without integral control, and C4 refers to DNN MPC with integral control. In all cases, the controller that performed the best was one of the neural network model predictive controllers (C3 and C4, without or with integral control).

Although it may be desirable to track sinusoids or other trajectories for different applications, step inputs are the most difficult input for underdamped systems. In this case, if the soft, underdamped robot gives good control performance without having to slew the control input, we have evidence that the learned model is effective.

4. DISCUSSION OF RESULTS, FUTURE WORK, AND CONCLUSIONS

One of the most interesting results is that the both models make full use of the multi-input system by driving pressures in opposing chambers in opposite directions in order to get a joint to move more quickly. This is something that we expect to see in

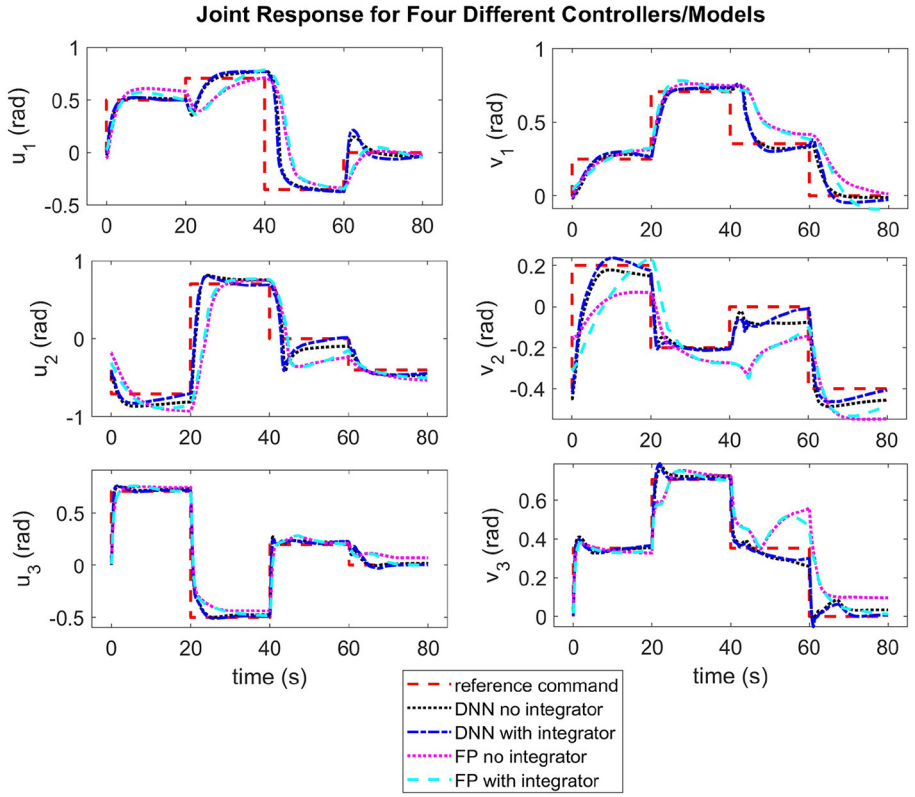

FIGURE 6 | Each plot shows a comparison of different time responses for a single joint in a single direction of actuation (where each joint has a degree of freedom in the *u* and *v* directions as shown in **Figure 2**). For each joint, the time response for four different conditions is shown–(1)MPC with a deep neural net (DNN) model, (2)MPC with a DNN model and an integrator, (3)MPC with a first principles (FP) model, (4)MPC with a first principles (FP) model and integrator.

TABLE 3 | The average steady state error, 90% rise time, and percent overshoot are all reported for each joint and controller.

	Steady state error (rad)				(10–90%) Rise time (s)				% Overshoot			
	C1	C2	C3	C4	C1	C2	C3	C4	C1	C2	C3	C4
u_1	0.029	0.032	0.030	0.030	5.04	4.38	2.38	2.19	5.50	6.29	4.48	4.91
v_1	0.046	0.046	0.020	0.020	10.2	7.22	3.60	3.41	36.4	35.8	32.1	34.9
u_2	0.157	0.112	0.079	0.019	3.77	3.83	2.21	2.11	17.5	14.7	13.9	11.5
v_2	0.124	0.074	0.047	0.012	11.5	9.94	7.00	5.68	18.7	22.8	6.11	10.4
u_3	0.048	0.006	0.024	0.010	6.61	4.19	1.77	1.82	12.1	12.8	11.2	8.22
v_3	0.086	0.033	0.038	0.019	7.61	4.84	0.71	0.55	29.8	28.1	33.0	31.3
Total Average	0.0816	0.051	0.040	**0.018**	7.46	5.74	2.94	**2.63**	20.0	20.1	**16.8**	16.9

In cases where 90% of steady state was not reached, a full 20 s was counted for that step. In cases where there was not overshoot, it was counted as 0% for that step.

the first principles when we explicitly model torque as a function of the two actuation pressures. However, in the DNN model, the behavior of the system was learned automatically by the DNN and exploited by the model predictive controller.

Both approaches have strengths and weaknesses with respect to ease of implementation. Given decent model parameters, a first principles model can be derived and verified with real data. This allows you to see the predictive power of your model and to reason about where errors are being introduced (e.g., underestimating mass causes velocities to be higher). While training a DNN model on data is theoretically much simpler and requires less system and theoretical knowledge, in practice it can be difficult to obtain large quantities of high quality data with which to train, especially on real robots. Moreover, if the DNN model does not predict well, it is difficult to discern if the problem is with the architecture, the training method, the data, or simply the quantity of the data.

Once both methods are implemented, it is again theoretically much simpler to update the DNN model given new data. This could be useful for slow system changes due to phenomenon

such as creep or possibly even for quick system changes such as when an object is grasped in a robotic end effector. The equivalent process with a first principles model is adaptive control, which is still an active area of research. Whether one of these is simpler in practice remains for exploration in future work.

As can be seen in **Figure 6** and **Table 3**, the DNN MPC was able to control to positions with lower rise time, overshoot, and steady state error, than the first principles MPC. This is interesting especially because the DNN was trained exclusively on data produced by the non-linear first principles model. We expect that this performance increase is in part due to how the DNN model is linearized (using the Taylor series expansion) as opposed to how the first principles model is linearized (maintaining **A** and **B** constant). This is supported in the findings of Terry et al. (2017). However, this ends up being one of the benefits of the learned model. It handles, the discretization *and* linearization in a more straight forward way than the when dealing with the non-linear first principles model, while still giving comparable or better performance.

It should be noted that in the DNN model, only velocities were predicted using the DNN, while pressures and positions were found using first principles models and discretization techniques. This was done because it proved to be much more difficult to train a DNN capable of predicting the entire state vector, as opposed to just velocities. While predicting the entire state was successfully accomplished in Gillespie et al. (2018), this was for a one degree of freedom system. We suspect that in order to extend this directly to many degrees of freedom, the DNN model would need to be much larger and be trained on much more data, or the DNN architecture would need to be changed to constrain the model to be more physically realistic. Since larger models require more data and would require more time to calculate gradients for control, smaller DNNs can be more useful in practice. We pose to the community as an open problem the correct architecture for discrete-time model prediction of dynamic states, since this will have a great impact on model and controller performance as well as training time and the amount of data required. Another open question is how to most safely and effectively collect data for learning the dynamics of a system such as a real robot, without damaging the robot.

Additionally, it is important to keep in mind that in this paper we are using a simple first-order Markov, feed-forward NN which cannot capture hysteresis. However, in future work, our same approach could be applied with more advanced DNN versions that can model hysteresis and other similar physical phenomenon. For example, it is possible to use k-th order Markov inputs, or train DNNs with state (e.g., LSTMs or GRUs) to remember inflection points.

We have shown that using a DNN with no initial knowledge about a complicated non-linear dynamical system except for assumed state variables and inputs, we can develop a high-performing model-based controller. Additionally, we have shown that our method which was first presented in Gillespie et al. (2018) is extensible to a more complex and large degree of freedom robot with soft actuators. In preliminary testing, the model predictive controller using a learned model performed better in terms of both overshoot and steady state error than a model predictive controller using a simplified linearized model based on first principles. Despite this success, we also note that it will be important in future work to extend our methods in two main ways. First we expect that constraining or parameterizing the model appropriately to cause a learned model to predict better after being trained on real data (as opposed to a non-linear simulation) will be essential to further improving performance. Additionally, in order to further improve dynamic response (such as rise time, overshoot, and settling time) we expect that using more tractable MPC methods with longer horizons and higher control rates (such as the method in Hyatt and Killpack, 2017 which make use of a GPU) will allow us to better control underdamped, difficult to model, soft robot actuators.

AUTHOR CONTRIBUTIONS

PH and MK contributed to the controller and first principles model development. PH and DW contributed to the design and training of the neural net. PH and MK tuned the MPC with all models and collected the data reported in the paper. All authors contributed to manuscript revision, read, and approved the submitted version.

ACKNOWLEDGMENTS

We gratefully acknowledge support from the NASA ECF grant NNX14A051G, which has made this research possible. A Utah NASA Space Grant Consortium fellowship also played an important role in supporting a student author. We also wish to acknowledge the hard work of the team at Pneubotics for collaboration in regards to our soft robot hardware platform. Finally, we wish to note that while all of our results presented in this paper are new, the problem formulation of using a DNN with MPC was first presented in our conference paper at the IEEE RoboSoft conference (see Gillespie et al., 2018).

REFERENCES

Abdel-Hamid, O., Mohamed, A.-R., Jiang, H., Deng, L., Penn, G., and Yu, D. (2014). Convolutional neural networks for speech recognition. *IEEE ACM Trans. Audio Speech Lang. Process.* 22, 1533–1545. doi: 10.1109/TASLP.2014.2339736

Best, C. M., Gillespie, M. T., Hyatt, P., Rupert, L., Sherrod, V., and Killpack, M. D. (2016). A new soft robot control method: using model predictive control for a pneumatically actuated humanoid. *IEEE Robot. Autom. Magaz.* 23, 75–84. doi: 10.1109/MRA.2016.2580591

Calinon, S., Guenter, F., and Billard, A. (2007). On learning, representing, and generalizing a task in a humanoid robot. *IEEE Trans. Syst. Man Cybern. B Cybern.* 37, 286–298. doi: 10.1109/TSMCB.2006.886952

Cho, K., Van Merriënboer, B., Gülçehre, Ç., Bahdanau, D., Bougares, F., Schwenk, H., et al. (2014). "Learning phrase representations using rnn encoder–decoder for statistical machine translation," in *Conference on Empirical Methods in Natural Language Processing (EMNLP)*. Doha, 1724–1734.

Dahl, G. E., Yu, D., Deng, L., and Acero, A. (2012). Context-dependent pre-trained deep neural networks for large-vocabulary speech recognition. *IEEE ACM Trans. Audio Speech Lang. Process.* 20, 30–42. doi: 10.1109/TASL.2011.2134090

Deisenroth, M., Rasmussen, C., and Fox, D. (2011). "Learning to control a low-cost manipulator using data-efficient reinforcement learning," in *Proceedings of Robotics: Science and Systems* (Los Angeles, CA). doi: 10.15607/RSS.2011.VII.008

Deisenroth, M. P., Fox, D., and Rasmussen, C. E. (2015). Gaussian processes for data-efficient learning in robotics and control. *IEEE Trans. Pattern Anal. Mach. Intell.* 37, 408–423. doi: 10.1109/TPAMI.2013.218

Deng, L., Hinton, G. E., and Kingsbury, B. (2013). "New types of deep neural network learning for speech recognition and related applications: an overview," in *Proceedings of International Conference on Acoustics, Speech, and Signal Processing (ICASSP)* (Vancouver, BC), 8599–8603.

Draeger, A., Engell, S., and Ranke, H. (1995). Model predictive control using neural networks. *IEEE Control Syst.* 15, 61–66.

Eitel, A., Springenberg, J. T., Spinello, L., Riedmiller, M., and Burgard, W. (2015). "Multimodal deep learning for robust RGB-D object recognition," in *IEEE/RSJ International Conference on Intelligent Robots and Systems (IROS)*. (Hamburg).

Fu, J., Levine, S., and Abbeel, P. (2015). One-shot learning of manipulation skills with online dynamics adaptation and neural network priors. *arXiv preprint* arXiv:1509.06841.

Gaiser, I., Wiegand, R., Ivlev, O., Andres, A., Breitwieser, H., Schulz, S., et al. (2014). Compliant robotics and automation with flexible fluidic actuators and inflatable structures. *Smart Actuation and Sensing Systems–Recent Advances and Future Challenges*. Hong Kong, 567–608.

George Thuruthel, T., Ansari, Y., Falotico, E., and Laschi, C. (2018). Control strategies for soft robotic manipulators: a survey. *Soft Robot.* 5, 149–163. doi: 10.1089/soro.2017.0007

Gillespie, M. T., Best, C. M., Townsend, E. C., Wingate, D., and Killpack, M. D. (2018). "Learning nonlinear dynamic models of soft robots for model predictive control with neural networks," in *2018 IEEE International Conference on Soft Robotics (RoboSoft)*(Livorno: IEEE), 39–45.

Hinton, G., Deng, L., Yu, D., Dahl, G., Rahman Mohamed, A., Jaitly, N., et al. (2012). Deep neural networks for acoustic modeling in speech recognition. *IEEE Signal Proces. Magaz.* 29, 82–97. doi: 10.1109/MSP.2012.2205597

Huang, S., Tan, K., and Lee, T. (2002). Adaptive motion control using neural network approximations. *Automatica* 38, 227–233. doi: 10.1016/S0005-1098(01)00192-3

Huang, S. N., Tan, K. K., and Lee, T. H. (2000). Adaptive friction compensation using neural network approximations. *IEEE Trans. Syst. Man Cybern. C Appl. Rev.* 30, 551–557. doi: 10.1109/5326.897081

Hyatt, P., and Killpack, M. D. (2017). "Real-time evolutionary model predictive control using a graphics processing unit," in *Humanoid Robotics (Humanoids), 2017 IEEE-RAS 17th International Conference on* (Birmingham, IEEE), 569–576.

Ivlev, O. (2009). "Soft fluidic actuators of rotary type for safe physical human-machine interaction," in *2009 IEEE International Conference on Rehabilitation Robotics, ICORR 2009*. Kyoto, 1–5.

Jain, A., Killpack, M. D., Edsinger, A., and Kemp, C. C. (2013). Reaching in clutter with whole-arm tactile sensing. *Int. J. Rob. Res.* 32, 458–482. doi: 10.1177/0278364912471865

Kiguchi, K., Jang, H.-H., and Fukuda, T. (1999). "Identification of robot manipulators using neural networks and genetic programming," in *Systems, Man, and Cybernetics, 1999. IEEE SMC'99 Conference Proceedings. 1999 IEEE International Conference on*, Vol. 4 (Tokyo: IEEE), 802–806.

Killpack, M. D., Kapusta, A., and Kemp, C. C. (2016). Model predictive control for fast reaching in clutter. *Auton. Robots* 40, 537–560. doi: 10.1007/s10514-015-9492-6

Kocijan, J., Murray-Smith, R., Rasmussen, C. E., and Girard, A. (2004). "Gaussian process model based predictive control. in *American Control Conference, 2004. Proceedings of the 2004*, Vol. 3 (Boston: IEEE), 2214–2219.

Krizhevsky, A., Sutskever, I., and Hinton, G. E. (2012). "Imagenet classification with deep convolutional neural networks," in *Advances in Neural Information Processing Systems (NIPS)* (Lake Tahoe), 1097–1105.

Lee, H., Grosse, R., Ranganath, R., and Ng, A. Y. (2009). "Convolutional deep belief networks for scalable unsupervised learning of hierarchical representations," in *International Conference on Machine Learning (ICML)* (Montreal, QC), 609–616.

Lenz, I., Knepper, R., and Saxena, A. (2015). "Deepmpc: learning deep latent features for model predictive control," in *Robotics Science and Systems (RSS)*. Rome.

Levine, S., and Abbeel, P. (2014). "Learning neural network policies with guided policy search under unknown dynamics," in *Advances in Neural Information Processing Systems*. Montreal, 1071–1079.

Levine, S., Finn, C., Darrell, T., and Abbeel, P. (2016). End-to-end training of deep visuomotor policies. *J. Mach. Learn. Res.* 17, 1–40.

Marchese, A. D., Katzschmann, R. K., and Rus, D. (2014a). "Whole arm planning for a soft and highly compliant 2d robotic manipulator," in *Intelligent Robots and Systems (IROS 2014), 2014 IEEE/RSJ International Conference on* (Chicago: IEEE), 554–560.

Marchese, A. D., Komorowski, K., Onal, C. D., and Rus, D. (2014b). "Design and control of a soft and continuously deformable 2d robotic manipulation system," in *Robotics and Automation (ICRA), 2014 IEEE International Conference on* (Hong Kong: IEEE), 2189–2196.

Marchese, A. D., and Rus, D. (2015). Design, kinematics, and control of a soft spatial fluidic elastomer manipulator. *Int. J. Robot. Res.* 35, 840–869. doi: 10.1177/0278364915587925 0278364915587925.

Mattingley, J., and Boyd, S. (2012). Cvxgen: a code generator for embedded convex optimization. *Optim. Eng.* 13, 1–27. doi: 10.1007/s11081-011-9176-9

Narendra, K. S., and Parthasarathy, K. (1990). Identification and control of dynamical systems using neural networks. *IEEE Trans. Neural Netw.* 1, 4–27. doi: 10.1109/72.80202

Nguyen-Tuong, D., and Peters, J. (2011). Model learning for robot control: a survey. *Cogn. Process.* 12, 319–340. doi: 10.1007/s10339-011-0404-1

Park, H.-W., Sreenath, K., Hurst, J. W., and Grizzle, J. W. (2011). Identification of a bipedal robot with a compliant drivetrain. *IEEE Control Syst. Magaz.* 31, 63–88. doi: 10.1109/MCS.2010.939963

Patan, K. (2015). Neural network-based model predictive control: fault tolerance and stability. *IEEE Trans. Control Syst. Technol.* 23, 1147–1155. doi: 10.1109/TCST.2014.2354981

Piche, S., Keeler, J. D., Martin, G., Boe, G., Johnson, D., and Gerules, M. (1999). "Neural network based model predictive control," in *NIPS*. Denver, 1029–1035.

Psichogios, D. C., and Ungar, L. H. (1991). Direct and indirect model based control using artificial neural networks. *Indus. Eng. Chem. Res.* 30, 2564–2573. doi: 10.1021/ie00060a009

Ronneberger, O., Fischer, P., and Brox, T. (2015). "U-net: Convolutional networks for biomedical image segmentation," in *Medical Image Computing and Computer-Assisted Intervention – MICCAI 2015* (Munich: Springer International Publishing), 234–241.

Rupert, L., Hyatt, P., and Killpack, M. D. (2015). "Comparing model predictive control and input shaping for improved response of low-impedance robots," in *Humanoid Robots (Humanoids), 2015 IEEE-RAS 15th International Conference on* (Seoul: IEEE), 256–263.

Rus, D., and Tolley, M. T. (2015). Design, fabrication and control of soft robots. *Nature* 521, 467–475. doi: 10.1038/nature14543

Rusu, A. A., Rabinowitz, N. C., Desjardins, G., Soyer, H., Kirkpatrick, J., Kavukcuoglu, K., et al. (2016). Progressive neural networks. *CoRR*, abs/1606.04671.

Sanan, S., Moidel, J., and Atkeson, C. (2009). "Robots with inflatable links," in *Intelligent Robots and Systems, 2009. IROS 2009. IEEE/RSJ International Conference on* (St. Louis, MI), 4331–4336.

Sanan, S., Ornstein, M. H., and Atkeson, C. G. (2011). "Physical human interaction for an inflatable manipulator," in *Engineering in Medicine and Biology Society, EMBC, 2011 Annual International Conference of the IEEE* (Boston: IEEE), 7401–7404.

Schmidhuber, J. (2012). "Multi-column deep neural networks for image classification," in *Conference on Computer Vision and Pattern Recognition (CVPR)* (Providence, RI), 3642–3649.

Shepherd, R. F., Ilievski, F., Choi, W., Morin, S. A., Stokes, A. A., Mazzeo, A. D., et al. (2011). Multigait soft robot. *Proc. Natl. Acad. Sci. U.S.A.* 108, 20400–20403. doi: 10.1073/pnas.1116564108

Silver, D., Huang, A., Maddison, C. J., Guez, A., Sifre, L., Driessche, G., et al. (2016). Mastering the game of Go with deep neural networks and tree search. *Nature* 529, 484–489. doi: 10.1038/nature16961

Socher, R., Lin, C., Ng, A. Y., and Manning, C. D. (2011). "Parsing natural scenes and natural language with recursive neural networks," in *International Conference on Machine Learning (ICML)* (Bellevue, WA).

Sutskever, I., Vinyals, O., and Le, Q. V. (2014). "Sequence to sequence learning with neural networks," in *Advances in Neural Information Processing Systems (NIPS)* (Montreal, QC), 3104–3112.

Swevers, J., Ganseman, C., Tukel, D. B., De Schutter, J., and Van Brussel, H. (1997). Optimal robot excitation and identification. *IEEE Trans. Robot. Autom.* 13, 730–740. doi: 10.1109/70.631234

Szegedy, C., Liu, W., Jia, Y., Sermanet, P., Reed, S. E., Anguelov, D., et al. (2015). "Going deeper with convolutions," *IEEE Conference on Computer Vision and Pattern Recognition (CVPR)* (Boston, MA).

Tan, K. K., Huang, S., Lee, T. H., and Tay, A. (2007). Disturbance compensation incorporated in predictive control system using a repetitive learning approach. *Syst. Control Lett.* 56, 75–82. doi: 10.1016/j.sysconle.2006.07.013

Terry, J. S., Rupert, L., and Killpack, M. D. (2017). "Comparison of linearized dynamic robot manipulator models for model predictive control," in *Humanoid Robotics (Humanoids), 2017 IEEE-RAS 17th International Conference on* (Birmingham: IEEE), 205–212.

Thuruthel, T. G., Falotico, E., Renda, F., and Laschi, C. (2017). Learning dynamic models for open loop predictive control of soft robotic manipulators. *Bioinspir. Biomimet.* 12:066003. doi: 10.1088/1748-3190/aa839f

Tolley, M. T., Shepherd, R. F., Mosadegh, B., Galloway, K. C., Wehner, M., Karpelson, M., et al. (2014). A resilient, untethered soft robot. *Soft Robot.* 1, 213–223. doi: 10.1089/soro.2014.0008

Wulfmeier, M., Ondruska, P., and Posner, I. (2015). Deep inverse reinforcement learning. *arXiv*, 1507.04888.

Yan, Z., and Wang, J. (2011). "A neural network approach to nonlinear model predictive control," in *IECON 2011-37th Annual Conference on IEEE Industrial Electronics Society* (Melbourne, VIC: IEEE), 2305–2310.

Yan, Z., and Wang, J. (2014). Robust model predictive control of nonlinear systems with unmodeled dynamics and bounded uncertainties based on neural networks. *IEEE Trans. Neural Netw. Learn. Syst.* 25, 457–469.

Zeng, T., Li, R., Mukkamala, R., Ye, J., and Ji, S. (2015). Deep convolutional neural networks for annotating gene expression patterns in the mouse brain. *BMC Bioinformatics* 16:147. doi: 10.1186/s12859-015-0553-9

Zhang, F., Leitner, J., Milford, M., Upcroft, B., and Corke, P. I. (2015). Towards vision-based deep reinforcement learning for robotic motion control. *arXiv*, 1511.03791.

Zhang, J., and Zong, C. (2015). Deep neural networks in machine translation: an overview. *IEEE Intell. Syst.* 30, 16–25. doi: 10.1109/MIS.2015.69

Zhang, T., Kahn, G., Levine, S., and Abbeel, P. (2016). "Learning deep control policies for autonomous aerial vehicles with mpc-guided policy search," in *2016 IEEE international conference on robotics and automation (ICRA)* (Stockholm: IEEE), 528–535.

Conflict of Interest Statement: The authors declare that the research was conducted in the absence of any commercial or financial relationships that could be construed as a potential conflict of interest.

frontiers in Robotics and AI

ORIGINAL RESEARCH
published: 24 April 2019
doi: 10.3389/frobt.2019.00026

An Opposite-Bending-and-Extension Soft Robotic Manipulator for Delicate Grasping in Shallow Water

*Zheyuan Gong[1], Bohan Chen[1], Jiaqi Liu[1], Xi Fang[1], Zemin Liu[1], Tianmiao Wang[1] and Li Wen[1,2]**

[1] School of Mechanical Engineering and Automation, Beihang University, Beijing, China, [2] Beijing Advanced Innovation Center for Biomedical Engineering, Beihang University, Beijing, China

Collecting seafood animals (such as sea cucumbers, sea echini, scallops, etc.) cultivated in shallow water (water depth: ∼30 m) is a profitable and an emerging field that requires robotics for replacing human divers. Soft robotics have several promising features (e.g., safe contact with the objects, lightweight, etc.) for performing such a task. In this paper, we implement a soft manipulator with an opposite-bending-and-extension structure. A simple and rapid inverse kinematics method is proposed to control the spatial location and trajectory of the underwater soft manipulator's end effector. We introduce the actuation hardware of the prototype, and then characterize the trajectory and workspace. We find that the prototype can well track fundamental trajectories such as a line and an arc. Finally, we construct a small underwater robot and demonstrate that the underwater soft manipulator successfully collects multiple irregular shaped seafood animals of different sizes and stiffness at the bottom of the natural oceanic environment (water depth: ∼10 m).

Keywords: inverse kinematics, soft robotics, underwater robot, soft manipulator, grasping

OPEN ACCESS

Edited by:
Helmut Hauser, University of Bristol, United Kingdom

Reviewed by:
Chaoyang Song, Southern University of Science and Technology, China
Zhigang Wu, Huazhong University of Science and Technology, China

***Correspondence:**
Li Wen
liwen@buaa.edu.cn

Specialty section:
This article was submitted to Soft Robotics, a section of the journal Frontiers in Robotics and AI

Received: *01 November 2018*
Accepted: *29 March 2019*
Published: *24 April 2019*

Citation:
Gong Z, Chen B, Liu J, Fang X, Liu Z, Wang T and Wen L (2019) An Opposite-Bending-and-Extension Soft Robotic Manipulator for Delicate Grasping in Shallow Water. Front. Robot. AI 6:26. doi: 10.3389/frobt.2019.00026

INTRODUCTION

Collecting seafood animals cultivated in the shallow water is a promising industry, which requires growing autonomic and robotic technologies. Traditionally, human divers are assigned to manually collect the seafood animals such as sea cucumbers, sea echini, scallops, etc. (**Figure 1a**). However, long-time working under the water depth of 10–30 m would cause the divers suffering from severe occupational disease including rheumatism, gout, osteonecrosis, etc. Collecting seafood animals in the harsh, shallow water environment requires small underwater robot and flexible manipulation system. Previously, the rigid robotic arms used for underwater manipulation have several challenging issues such as delicate grasping fragile and squishy seafood animals. Meanwhile, the traditional rigid hydraulic arms usually have large mass. The huge inertia caused by the rigid arm during locomotion would induce significant vibration for the small underwater vehicle (Fernandez et al., 2013).

Soft robots provide an alternative way to collect these fragile sea animals, due to the properties of compliance and safe interaction. Recently, increasing studies on soft robotics have focused on the underwater applications. For example, robotic octopus arms achieved underwater locomotion (Calisti et al., 2011; Cianchetti et al., 2015); soft gripper has been used for biological sampling the coral reefs (Galloway et al., 2016); the origami gripper was applied to collecting delicate midwater organisms (Teoh et al., 2018); the jamming gripping was exploited in handling in deep

sea (Licht et al., 2017); a soft glove was integrated to tele-operated control the soft wrist modules for biological underwater grasping (Kurumaya et al., 2018; Phillips et al., 2018).

Previously, the piecewise constant curvature (PCC) model has been developed (Webster Iii and Jones, 2010) and is used for modeling the flexible continuum robots (Webster et al., 2007) and soft elastomeric arms (Gong et al., 2017, 2018a,b), etc. The inverse kinematics modeling is another challenge issue. To address this challenge, previous studies have regarded the continuum joint as 3UPS-1PU-extensible structure for simplification and further developed the DH method for inverse kinematic modeling of flexible manipulator (Lakhal et al., 2014); Jacobian iteration was applied to determine the inverse kinematics for the underwater soft manipulator in the two-dimensional space (Marchese and Rus, 2016); machine learning algorithms were proposed to train a single soft actuator (Giorelli et al., 2015; Lee et al., 2017) and a two-dimensional soft manipulator (Jiang et al., 2017). Natural-CCD algorithm was proposed to generate simple, precise, and computationally efficient inverse kinematics (Martín et al., 2018). However, previous studies have not yet experimentally explored the spatial manipulation with inverse kinematics, particularly for the collecting tasks in natural underwater environment.

To complement a controllable underwater soft robotic manipulator for seafood grasping in shallow water, in this paper, we propose a novel inverse kinematic method. Based on an opposite-bending-and-extension structure of the robotic arm, our method enables point-point movements in three-dimensional space and trajectory planning. We mount the underwater soft manipulator on a small underwater vehicle and then demonstrate underwater picking and placing seafood animals. Our current study shows wide-open applications of soft robotic manipulator in the shallow water undersea environment.

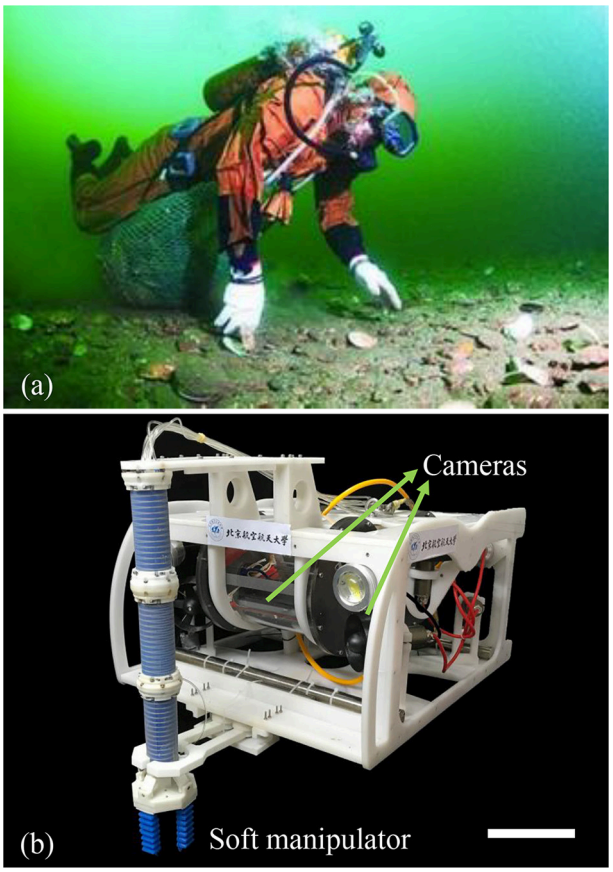

FIGURE 1 | (a) Seafood collection by a human diver. **(b)** The snapshot of the underwater robot with a soft manipulator for grasping fragile sea animals. Multiple cameras are applied to provide underwater vision. The length of scale bar is 100 mm.

MATERIALS AND METHODS

System Overview

Soft robots have intrinsic compliance, which have significant advantages for grasping these seafood animals (for instance, sea cucumber has a modules of $\sim 10^6$Pa). In order to implement the underwater grasping in shallow water, we construct a small underwater robot with a soft manipulator (modules around $\sim 10^5$Pa), as shown in **Figure 1b**. The underwater soft manipulator can achieve 3-DOF movement and grasping. A 4-DOF underwater remotely operated vehicle (ROV) is integrated with two cameras, one of which is for grasping from near top view, while another is for guiding movement from large side view. Through live cameras, both the underwater soft manipulator and ROV are remotely controlled by the human operator on a boat. The underwater soft manipulator is 360 mm in length (300 mm for only the soft arm) and 34 mm in diameter, with a total mass of 322 g. The robot measures 600 mm long, 500 mm width, and 300 mm tall, with a weight of 10 kg, and operated depth of 50 m.

The Underwater Soft Manipulator

We design and fabricate an entirely soft, underwater manipulator with soft gripper as the end effector (**Figure 2a**) (Martinez et al., 2013; Polygerinos et al., 2015; Hao et al., 2018). The underwater soft manipulator consists four sections: two bending segments, one elongation segment, and one soft gripper (**Figure 2b**). This bending segments and elongation segment are designed to have a circle shaped cross-section to decrease the hydrodynamic resistance in the water flow (Gong et al., 2018b). Each bending segment has three individual chambers. Meanwhile, it is covered with rubber tendons to reduce radial ballooning of the chambers when pressurizing (**Figure 2c**). We apply the fiber-reinforced actuator on the elongation segments to provide extension in the vertical direction while grasping underwater (**Figure 2e**).

Note that we actuate the underwater soft manipulator in a special manner to simplify the kinematic modeling (will introduce later): the two bending segments are actuated with the same bending curvature but opposite bending direction. We regard that the kinematics is established on this opposite-bending-extension actuation condition. We integrate two bending segments at an included angle of 180° (**Figure 2c**). When we actuate the opposite chambers of the two bending segments, the underwater soft manipulator always perform the opposite-bending-extension condition even in the spatial space. Besides, the air pressures in the opposing chambers have linear

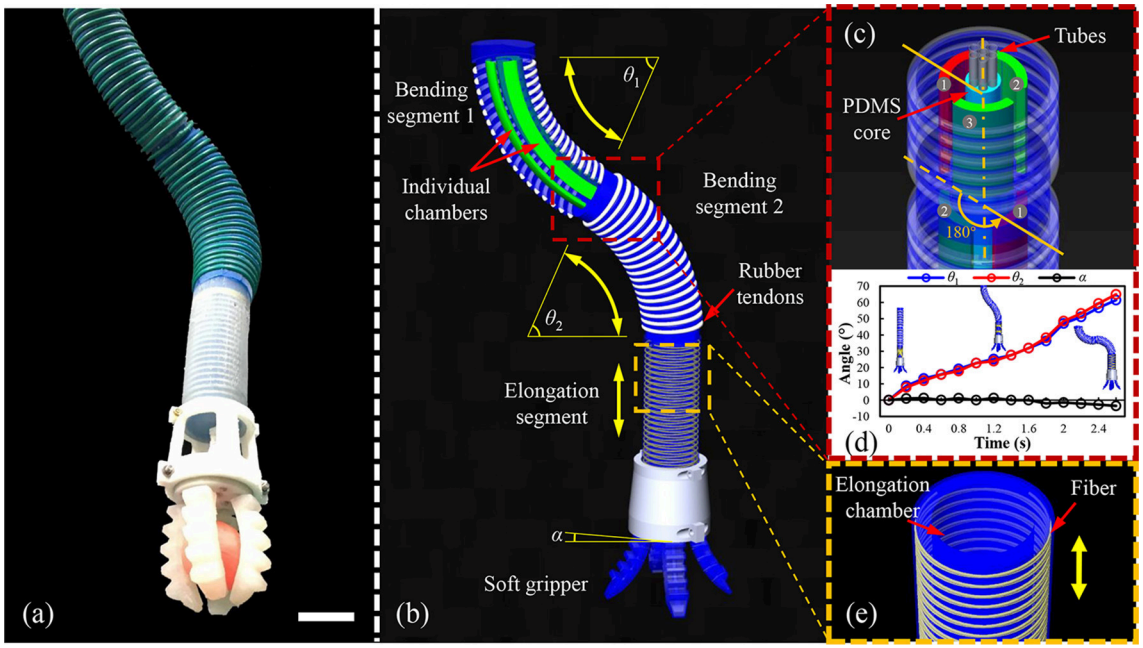

FIGURE 2 | The design and principle mechanics of the underwater soft manipulator. **(a)** An overall side image of the underwater soft manipulator (scale bar 50 mm). **(b)** The underwater soft manipulator is applied modularized design that consisted of two bending segments, an elongating segment, and a soft gripper. θ_1 and θ_2 represent the bending angles of the two bending segments, and α represents the horizontal angle of the manipulator tip. The manipulator is actuated with an opposing curvature where $\theta_1 = \theta_2$ and $\alpha = 0$. **(c)** The two bending segments had a joining angle of 180°. **(d)** θ_1, θ_2, and α are verified in one actuation with opposing curvature. The two bending angles (θ_1, θ_2) are almost equal, and the horizontal angle (α) is zero at each moment. **(e)** The fiber-reinforced elongating segment. The yellow arrow indicates the direction of elongation.

relationship, which means only one pressure is required for the kinematics model. Under this linear relationship, the curve angles of two bending segments (θ_1, θ_2) are almost the same and the intersection angle at the horizontal level of the underwater soft manipulator tip (α) is zero, which is the soft gripper is always facing vertically down to the ground. **Figure 2d** shows θ_1, θ_2, and α in one trial when actuating the underwater soft manipulator. We find that the values of θ_1, θ_2, and α confirm the design to realize opposing curvature.

Kinematics Modeling

Figure 3a demonstrates the kinematics of the underwater soft manipulator. With opposite-bending-extension condition, the two bending segments shared the degrees of freedom (DOF) only have 2 DOF (x-y plane), while one bending segment has the DOF of the rotation φ and bending θ_1 (or θ_2). Due to the elongation segment (z-axis), we can achieve three DOF movements and grasping.

Opposing curvature patterns offers plenty of advantages on kinematic modeling. First, the attitudes of two bending segments $\{\kappa_i, \varphi_i, \theta_i\}$ (κ_i refers to the bending curvature of the ith segment) have very straightforward relationships (Equations 4–6). And we only need to calculate the attitudes of one segments. Second, it reduces the number of inputs (seven independent chambers totally to four independent chambers). Thus, it reduces half of the computation contributed to the fast solution of kinematics.

The modeling procedure can be realized in two parts (**Figure 3b**): (1) the transformation between the coordinates of the end effector $\{x, y, z\}$ and chambers length $\{l_{i1}, l_{i2}, l_{i3}, l_e\}$ (l_{ij}, the indexes i and j mean segment i chamber j; l_e, the index e means the length of elongation segment; the same as below). The essential point of this part is how we can get an inverse solution from $\{x, y, z\}$ (three parameters) to $\{l_{i1}, l_{i2}, l_{i3}, l_e\}$ (four parameters) without other inputs. (2) The transformation between chambers length $\{l_{i1}, l_{i2}, l_{i3}, l_e\}$ and the pressure $\{p_{i1}, p_{i2}, p_{i3}, p_e\}$, the directly actuation parameter. By reason of the nonlinear response of soft material and complexity of structures, it is complicated to figure out (2) in a theoretical way, so we finish this work via experiments (**Figure 5**), and we fit formulas for the model-based control recording these results. In order to simplify the kinematics model, we make the following assumptions:

a) The bending section have the constant curvature rate, and the elongation section is straight. The curves are tangent at the intersection points.
b) The chambers in the same segment are parallel, and the cross sections are equal in the same section.

Forward Kinematics

Previous studies have already shown how to solve the forward transformation questions (Webster Iii and Jones, 2010; Gong et al., 2017). Combining these methods with the structures and sizes of our soft arm (shown in **Figure 3c**), we can obtain

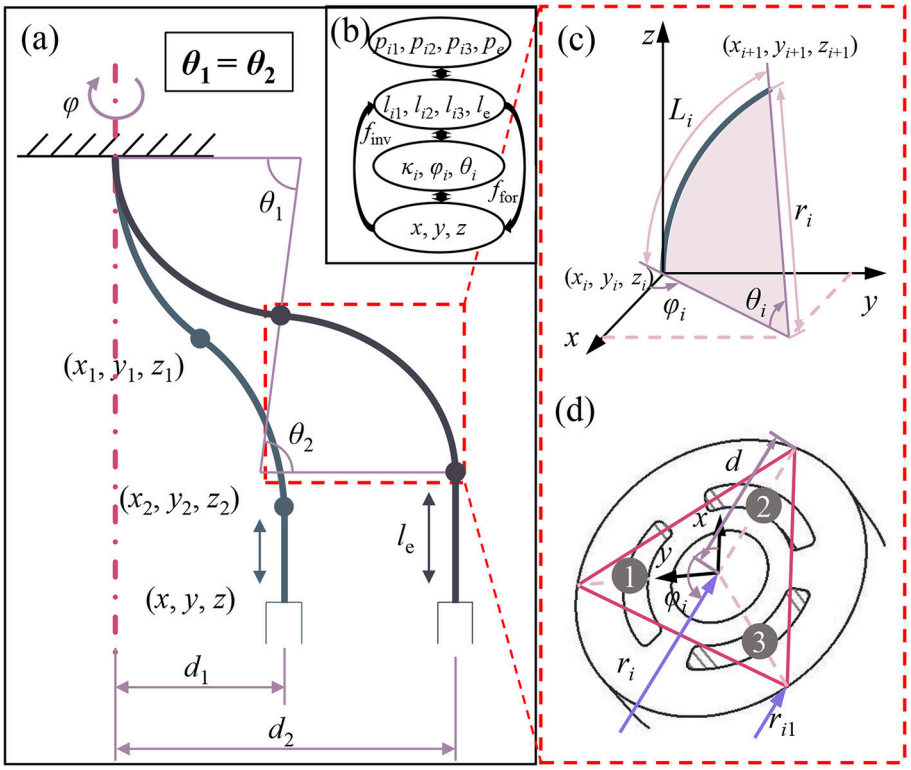

FIGURE 3 | Kinematics of the underwater soft manipulator. **(a)** The two bending segments of the underwater soft manipulator are always actuated with opposing curvatures. Thus, the bending angles are always equal ($\theta_1 = \theta_2$). **(b)** The kinematic transformation map. We focused on inverse kinematics (f_{inv}) from the position parameters (x_i, y_i, z_i) to chamber lengths (l_{i1}, l_{i2}, l_{i3}, l_e) via arc parameters (κ_i, φ_i, θ_i). **(c)** Geometric schematic in a bending segment, where φ_i represents the rotation angle around the z-axis; θ_i represents the bending angle around the y-axis; r_i represents the radii of the bending curve; and L_i represents the centerline length of the bending segment. **(d)** Geometric schematic of the cross-section, where h represents the distance between the arm surface and the center of the cross-section.

coordinates of the segments tip $\{x, y, z\}$ from the length of the chamber $\{l_{i1}, l_{i2}, l_{i3}, l_e\}$ with the help of attitudes $\{\kappa_i, \varphi_i, \theta_i\}$.

$$\kappa_1 = \frac{1}{r_1} = \frac{2\sqrt{l_{11}^2 + l_{12}^2 + l_{13}^2 - l_{11}l_{12} - l_{11}l_{13} - l_{12}l_{13}}}{(l_{11} + l_{12} + l_{13})\, d} \quad (1)$$

$$\varphi_1 = \tan^{-1}\left(\frac{l_{12} + l_{13} - 2l_{11}}{\sqrt{3}(l_{12} - l_{13})}\right) \quad (2)$$

$$\theta_1 = \frac{2\sqrt{l_{11}^2 + l_{12}^2 + l_{13}^2 - l_{11}l_{12} - l_{11}l_{13} - l_{12}l_{13}}}{3d} \quad (3)$$

In equations (1–3), d represents the radius of soft arm cross-section, and r_1 is the radius of the bending curve. Particularly, we use the surface length to represent the chamber length mainly considering it is more accessible for measurement. After we got the attitudes parameters from the bending segment 1, we can get attitudes of the bending segment 2:

$$\kappa_2 = \kappa_1 \quad (4)$$

$$\varphi_2 = \varphi_1 + \pi \quad (5)$$

$$\theta_2 = \theta_1 \quad (6)$$

Furthermore, we can also get the coordinate of soft arm tip $\{x, y, z\}$ from the attitudes $\{\kappa_i, \varphi_i, \theta_i\}$ we got previously. Mathematically, we consider the underwater soft manipulator simply consisted of constant curvature curves (bending segments) and lines (elongation segments) based on the assumptions. The coordinate transformation in both curves and lines can be described by homogeneous matrixes shown in equation (7), where R is the rotation matrix, and p is the translation vector.

$$\mathrm{T} = \begin{bmatrix} R & p \\ 0 & 1 \end{bmatrix}_{4\times4} \quad (7)$$

Figure 3c shows the modeling of a single segment. We define orientation angle φ_i represents the rotation angle around the z-axis, curvature angle θ_i represents the bending angle around the y-axis, where i indicates the ith segment. In the bending segments, we consider the bending procedure as: first the soft arm rotates around y-axis with angle θ_i; second, the soft arm rotates around z-axis with angle φ_i. Moreover, we need to post-multiply the homogeneous matrix with the rotation matrix $R(-\varphi_i)$ and zero translation. The transformation matrix for the bending segment is demonstrated in equation (8) In elongation segments,

we only need to consider the translation on z-axis with a length of l_e (Equation 9).

$$
{}^{i}_{i-1}T = \begin{bmatrix} R_z(\varphi_i) & 0 \\ 0 & 1 \end{bmatrix} \cdot \begin{bmatrix} R_y(\theta_i) & 0 \\ 0 & 1 \end{bmatrix} \cdot \begin{bmatrix} R_z(-\varphi_i) & 0 \\ 0 & 1 \end{bmatrix} = \begin{bmatrix} cos^2\varphi_i \cos\theta_i + sin^2\varphi_i & \cos\varphi_i \sin\varphi_i (\cos\theta_i - 1) & \cos\varphi_i \sin\theta_i & r\cos\varphi_i (1 - \cos\theta_i) \\ \cos\varphi_i \sin\varphi_i (\cos\theta_i - 1) & sin^2\varphi_i \cos\theta_i + cos^2\varphi_i & \sin\varphi_i \sin\theta_i & r\sin\varphi_i (1 - \cos\theta_i) \\ -\cos\varphi_i \sin\theta_i & -\sin\varphi_i \sin\theta_i & \cos\theta_i & r\sin\theta_i \\ 0 & 0 & 0 & 1 \end{bmatrix} \tag{8}
$$

$$
{}^{3}_{2}T = \begin{bmatrix} 1 & 0 & 0 & 0 \\ 0 & 1 & 0 & 0 \\ 0 & 0 & 1 & l_e \\ 0 & 0 & 0 & 1 \end{bmatrix} \tag{9}
$$

Thus, we can get the forward transformation of the whole soft manipulator (Equation 10).

$$
{}^{3}_{0}T = {}^{1}_{0}T \cdot {}^{2}_{1}T \cdot {}^{3}_{2}T \tag{10}
$$

Inverse Kinematics

With this inverse kinematics method, we can realize the coordinate based control and point to point movement of the underwater soft manipulator. That is the foundation of the picking and placing tasks, as well as the trajectory planning. Further, the quick solution of inverse kinematics also helps to improve the real-time control ability of soft manipulator. However, the inverse kinematics of soft robots (even continuum robots) is always a challenging problem (Webster Iii and Jones, 2010). The large group's nonlinear equations in the transformation matrix cause the huge complexity to the inverse solution.

We propose a rapid inverse solution on soft manipulators with the specific opposite-bending-extension condition. As we discuss above that the underwater soft manipulator has three DOF in coordinate space $\{x, y, z\}$. However, the underwater soft manipulator has four independent chambers $\{l_{i1}, l_{i2}, l_{i3}, l_e\}$. In order to get the chambers length $\{l_{i1}, l_{i2}, l_{i3}, l_e\}$ (four outputs) from the coordinates $\{x, y, z\}$ (three inputs), we propose a constraint condition: at most two chambers in a bending segment are actuated at the same time, so that at least one chamber in one bending segment is in initial length. Thus, the point of this method is to figure out which chamber is in initial length.

We also resolve the transformation from $\{x, y, z\}$ to $\{l_{i1}, l_{i2}, l_{i3}, l_e\}$ with the attitudes $\{\kappa_i, \varphi_i, \theta_i\}$. First, we obtain the rotation angle φ_1 from the given inputs $\{x, y, z\}$.

$$
\varphi_1 = -\tan^{-1}\left(\frac{y}{x}\right) \tag{11}
$$

Then we evaluate φ_1 to figure out which two chambers need to be actuated. According to the geometry relationship in **Figure 3d**, we can give an equation where we represent the initial length with the attitudes parameters $\{\kappa_i, \varphi_i, \theta_i\}$. The initial length of chambers can be pre-measured by camera calibration. Here, on the relationship $\kappa_i = {r_i}^{-1}$, we also regarded r_i as attitudes parameter κ_i.

$$
{}^{3}_{0}T = {}^{1}_{0}T \cdot {}^{2}_{1}T \cdot {}^{3}_{2}T
$$

$$
\begin{cases} l_{i1\text{init}} = \theta_1 \cdot \left(r_1 - d\sin\varphi_1\right), when \frac{\pi}{6} \le \varphi_1 < \frac{5\pi}{6} \\ l_{i2\text{init}} = \theta_1 \cdot \left[r_1 + d\cos\left(\varphi_1 - \frac{\pi}{6}\right)\right], when \frac{5\pi}{6} \le \varphi_1 < \frac{3\pi}{2} \\ l_{i3\text{init}} = \theta_1 \cdot \left[r_1 - d\cos\left(\varphi_1 + \frac{\pi}{6}\right)\right], when \frac{3\pi}{2} \le \varphi_1 < 2\pi or 0 \le \varphi_1 < \frac{\pi}{6} \end{cases} \tag{12}
$$

Considering the geometry relationship shown in **Figure 3D**, we derive another equation from the given coordinate:

$$
\frac{x}{2} = r_1 \cdot \cos\varphi_1 \cdot (1 - \cos\theta_1) \tag{13}
$$

In equations (12) and (13), we can found that only r_1 and θ_1 are the unknown quantities. Combining the two equations, we can solve the rest attitudes parameters. Then, we easily obtained the length of all chambers $\{l_{i1}, l_{i2}, l_{i3}, l_e\}$.

$$
\begin{cases} l_{i1} = \theta_i \left(r_i - d\sin\varphi_i\right) \\ l_{i2} = \theta_i \left[r_i + d\cos\left(\varphi_i - \frac{\pi}{6}\right)\right] \\ l_{i2} = \theta_i \left[r_i - d\cos\left(\varphi_i + \frac{\pi}{6}\right)\right] \\ l_e = -2r_1 \sin\theta_1 - z \end{cases} \tag{14}
$$

According to above equations, we obtain specific inverse transformation from $\{x, y, z\}$ to $\{l_{i1}, l_{i2}, l_{i3}, l_e\}$. With the help of the pressure – length calibration (**Figure 4**), we can further transfer from $\{l_{i1}, l_{i2}, l_{i3}, l_e\}$ to the actuating pressure $\{p_{i1}, p_{i2}, p_{i3}, p_e\}$ for our model-based pneumatic control.

Actuation and Control

The current soft manipulator is actuated by pneumatic pressure. We implement a multi-channel pneumatic driving system, shown in **Figure 5**. The system has ten pneumatic channels while each channel can generate pressure independently with maximum of 500 kPa to actuate the chambers in the underwater soft manipulator. The system contains a microcontroller (STM32F103, *STMicroelectronics*, Italy and France), DA convertors (PCF8591, *NXP*, Netherland), proportional valves (ITV0030-2BL, *SMC*, Japan), pressure sensors (ISE30A, *SMC*, Japan), an air compressor, and related software. We apply PID method in the closed-loop control of pressure, which is continuously adjusted according to the data from pressure sensors.

To control the underwater soft manipulator, we program the inverse-kinematics-model-based control algorithm in MATLAB. Calculating pressures from the reference coordinates, the software can conduct the underwater soft manipulator to pick and place object at specific positions. The calculated pressures

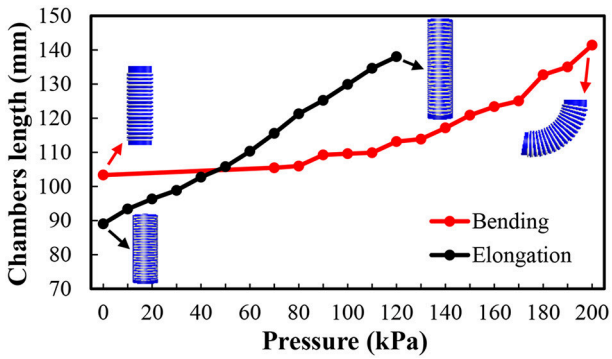

FIGURE 4 | The multi-channel pneumatic actuation system for the underwater soft manipulator. The system contains a microcontroller, power source, DA converter, ten proportional valves, and ten air pressure sensors.

can be sent to actuation system via RS232 communication protocol. By dividing the trajectory path into small segments (0.5 mm) and inserting desired points, we can control the underwater soft manipulator to follow a specific trajectory. In the field application, we also balance the pressures in chambers of the underwater soft manipulator according to the water depth. The balance transformation is shown in the equation (15), where p_d is the pressure applied, p_0 is the pressure calculated, $\rho_{environment}$ is the underwater environment density (1025 kg/m^3 is considered as the sea water density), h_d is the depth where the robot works. It should be noted that the underwater soft manipulator is mainly designed for grasping fragile sea animals, which most of them are suspending in the water and have no load on the underwater soft manipulator. Currently, we have not considered the influence of the gravity and loads on control of the underwater soft manipulator.

$$p_d = p_0 + \rho_{environment} g h_d \tag{15}$$

Laboratory Experiments Setup for Characterizing the Underwater Soft Manipulator

In order to evaluate the capability of the kinematic model, we perform experiments on the model based location error and trajectory planning. We apply a stereo cameras system to capture the motions and trajectories. The underwater soft manipulator is mounted in water and actuated by the multi-channel pneumatic system. The stereo cameras is carefully calibrated, and the error is less than 0.5 mm. Moreover, we rebuild the motions and got the coordinates of marker points from the images of different views. We perform the location error in different directions (φ_i) with the distance (d) ranging from 0mm to 100 mm, 10 mm of step length. We also perform the trajectory planning ability with paths of line and circle. Then, we run the workspace simulation in MATLAB.

RESULTS

Kinematic Model Validation, Trajectory Planning, and Workspace Simulation

The underwater soft manipulator is actuated to move different distances (d), and the average control errors (between the experiments and simulations) of both the distances and rotational angles of the manipulator's base (φ_i) are demonstrated in **Figure 6**. We found that the errors are within the range of 2.7∼13.4 mm when the distances changing from 0mm to 100 mm. This error range is tolerant to the soft gripper while grasping [the tolerant deviation of gripper and objects that led to successful grasp (Hao et al., 2018)]. According to the kinematic model, simulation on the workspace of the soft arm is illustrated as **Figure 7**. The results show that the underwater soft manipulator collected a plate-shaped workspace with a size of approximately 400 mm in diameter and 100 mm height.

Furthermore, we demonstrate the trajectory planning ability of the underwater soft manipulator with paths of line shaped and arc shaped trajectories (**Figure 8**). While performing the line trajectory (**Figure 8A**), the underwater soft manipulator is actuated from the point A (−110, −64, −270) (unit: mm) to the point B (110, 64, −295) at a programmed speed of 32 mm/s. The red circles are tracked points from the experiments; the blue lines are the computer-programmed path. The black lines represent the underwater soft manipulator, and the black dots on the black lines represent the intersections of different segments. The results show that experiment trajectory has a small error from the desired path in 3D space. The tracked points match the programmed path well and the error is less than 6.6 mm (**Figure 8B**). In the arc shaped trajectory, the underwater soft manipulator is actuated from the point A (−55, −35, −285) to the point B (55, 35, −320) with a rotation angle of 120°, radius of 65 mm and programmed speed of 45 mm/s, as shown in **Figure 8C**. We observe a vibration when suddenly changed moving direction of the underwater soft manipulator (**Figure 8D**). Lines and arcs are the fundamental shapes of trajectory; therefore, we hope more complex trajectory tracking can be achieved in the future based on the current work.

Field Test of Underwater Grasping

To examine the capabilities of the underwater soft manipulator, we construct an underwater robot with the underwater soft manipulator (**Figure 1b**), and perform the underwater grasping of fragile marine seafood animals (e.g., sea cucumbers, echini, etc.) in the natural undersea environment. A 4-DOF underwater vehicle is integrated with two cameras, which provide images from near top view for the grasping and large side view for the movement guiding. The movements of the underwater vehicle is under PID control that enable stable swimming and hovering. The underwater robot is powered from a ship floating above the grasping area. Both the underwater soft manipulator and underwater vehicle are under remote control via the real-time underwater cameras (transmitting images via cables). **Figure 9** shows the system architecture applied for the undersea grasping, which is realized in three main steps: (1) The underwater robot is operated to approach the targets area and performs hovering

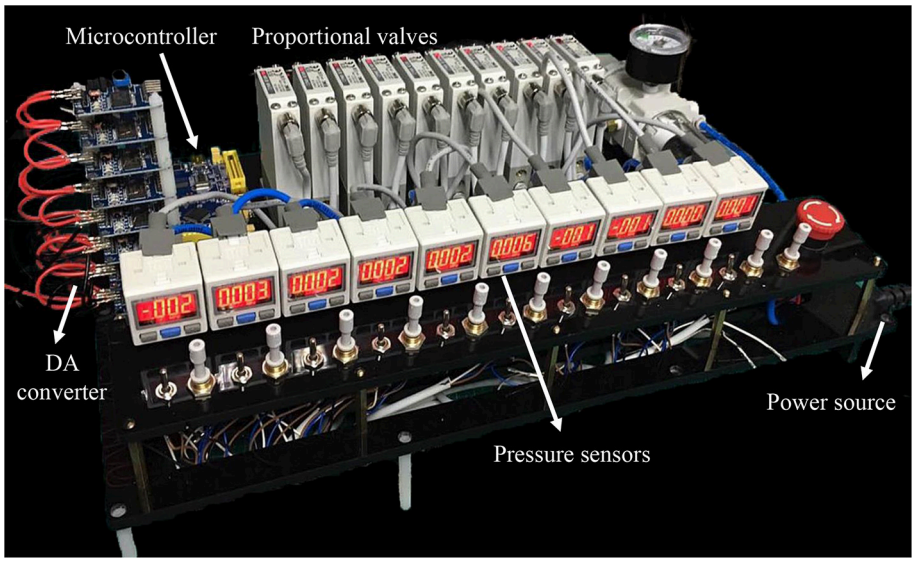

FIGURE 5 | Chamber lengths of the bending segments (red) and elongating segment (black) as a function of the actuation pressure.

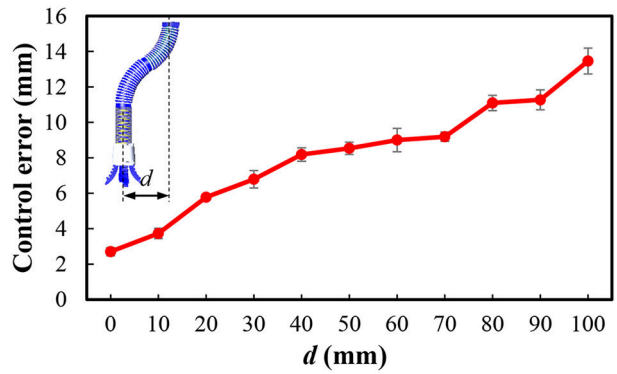

FIGURE 6 | Control location error as a function of operating radius *d* (0 to 100 mm).

and searching the seafood animal targets. (2) The underwater robot sinks to the bottom of the ocean. Then the underwater soft manipulator is controlled via inverse kinematics model to approach the undersea animals with the soft gripper open. (3) The underwater soft manipulator picks the target and places it into the collecting basket. While working underwater, the environment pressure is variable in different operating depth. Thus, the actuating pressures in chambers of the underwater soft manipulator are balanced according to the depth change (see Equation 15).

Figure 10 shows the field grasping in the natural undersea environment (**Figure 10a**), where the depth is 10 m and the speed of current in the ocean bottom is about 2 m/s. The seabed is covered by sand and stones, and the animals spread around and even partially embedded in sand and rocks. Finally, we successfully grasp echini, sea cucumbers, and shells at the depth 10 m undersea within 20 min (**Figures 10b,c**).

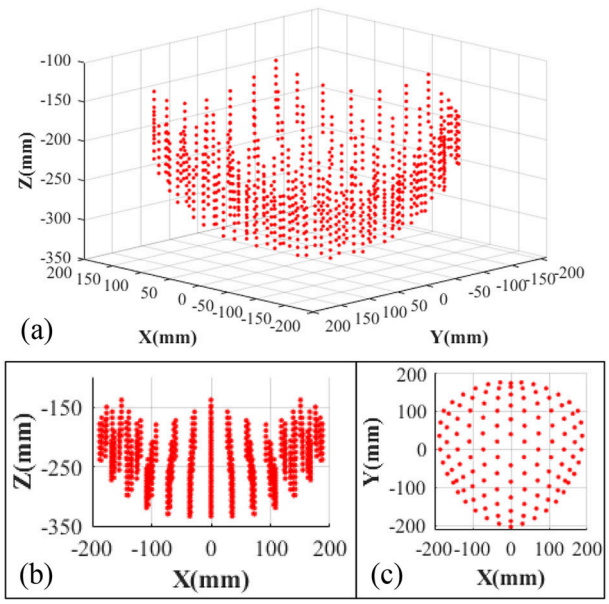

FIGURE 7 | (a) The simulation of operating workspace of the underwater soft manipulator. **(b)** The front view of the workspace. **(c)** The top view of the workspace.

CONCLUSION AND DISCUSSION

In this paper, we construct a soft manipulator and ROV system for seafood grasping in shallow water. The underwater soft manipulator is designed and actuated as opposite-bending-extension condition and can achieve 3-DOF movements in space. It is controllable with a simple but rapid inverse kinematics. The results show that the error is less than 13.4 mm, and we achieve

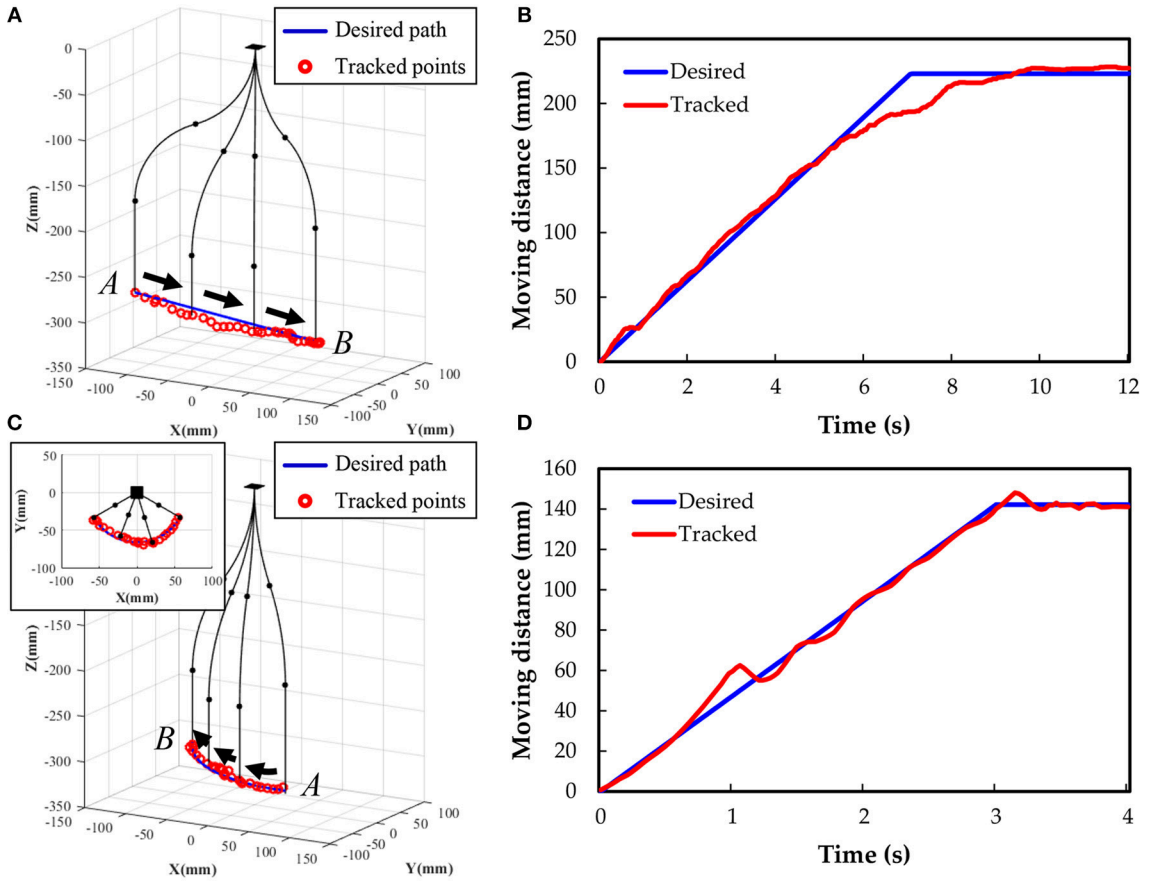

FIGURE 8 | Controlled soft manipulator following trajectories of a line **(A)** and an arc **(C)**. Distance response with time while tracking **(B)** the line trajectory and **(D)** the arc trajectory.

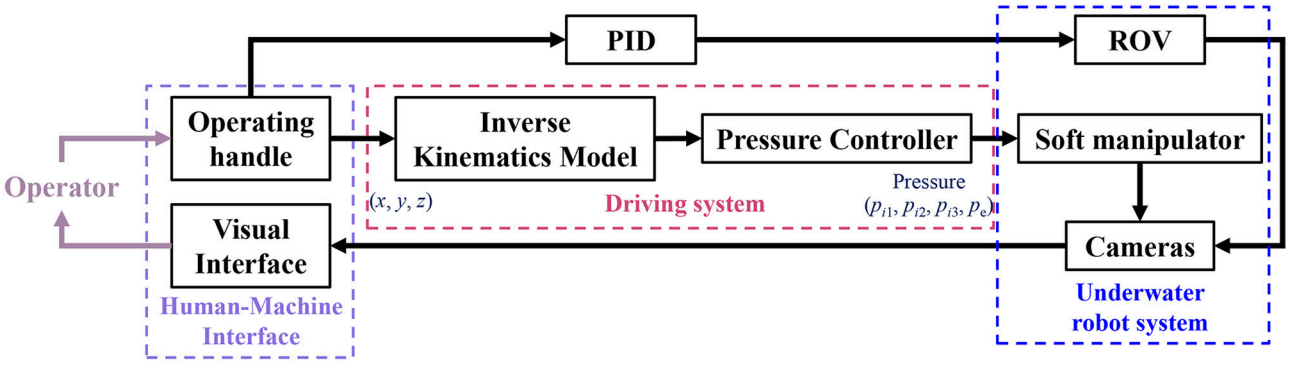

FIGURE 9 | System architecture of the underwater grasping robot. The system contains human-machine Interface, driving system and the underwater robot system. The underwater robot is operated to approach the target seafood animals by the human operator. Then the underwater soft manipulator is controlled pick and place the sea animals via inverse kinematics model. The whole process is monitored by cameras which facilitates the remote control of human operator.

the trajectory planning by tracing the paths of a line and an arc. The experimental tracking points fit the desired position well in both positions and timescale. Finally, we perform the field test—we tested the manipulation capacity of soft arm in the natural undersea environment. The soft arm manipulator successfully grasp sea animals at a sea depth of 10 m via an underwater robot. Hopefully, this robot can be used for dexterous grasping in shallow water environment (0–50 m), and can replace the human divers for safely harvesting the seafood efficiently, without any damage.

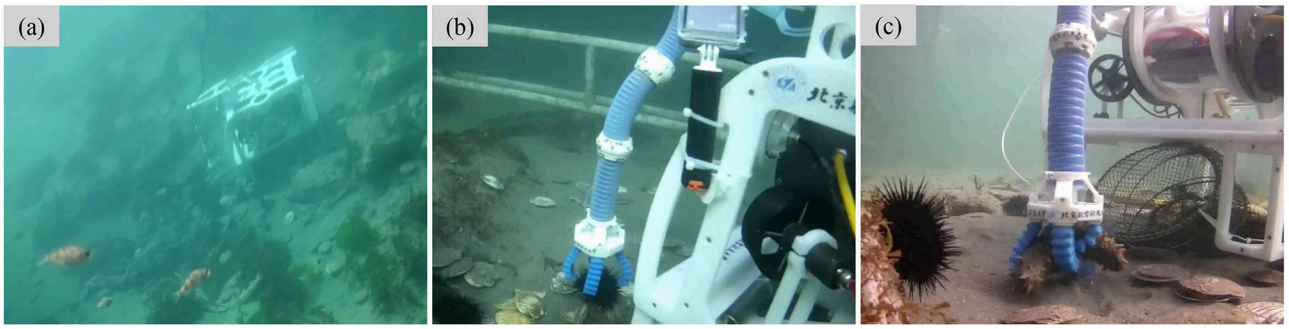

FIGURE 10 | Undersea grasping with the underwater soft manipulator mounted on a small underwater robot. **(a)** The underwater grasping is demonstrated in the natural undersea environment at 10 m depth. **(b,c)** Grasping undersea animals (echini and sea cucumbers) with soft manipulator.

We propose a simple and universal inverse solution for the underwater soft manipulators whose structure and actuation are followed the opposite-bending-extension condition. Distinct from the previous D-H method (Lakhal et al., 2014), machine learning model (Giorelli et al., 2015; Lee et al., 2017), and Jacobian iteration (Marchese and Rus, 2016), this inverse kinematics can be applied for the whole manipulator and does not require heavy computational resources, which enables real-time control in application. This method has also been tested and validated at the natural oceanic environment. The results have proved that reducing the DOFs of the soft manipulator is a possible approach to solve the inverse kinematics problem. The underwater soft manipulator with inverse kinematics can operate in the natural unstructured undersea environment without precise kinematic and force sensory feedback as the rigid manipulators do. Furthermore, the rigid robotic arms and grippers for the underwater manipulations have a huge mass and inertia which impacts their maneuverability. In contrast, soft robots have advantages of compliance and lightweight and may play an important role in underwater manipulation. Compared with the rigid hydraulic manipulators, our soft manipulator has exceptional features of lightweight and low inertia. The underwater soft manipulator has a mass of 0.322 kg (almost zero mass in water), while with a length of 360 mm. The current prototype is significantly lighter than the traditional rigid hydraulic manipulators that commonly has a mass of tens of kilograms, e.g., a hydraulic manipulator with a length of 499 mm has a total mass of 17.2 kg (Fernandez et al., 2013). Thus, locomotion of the underwater soft manipulator has negligible inertial effect for the underwater vehicle than the traditional rigid underwater manipulator.

Previous studies have shown the promising features of soft robots for the deep sea application (Calisti et al., 2011; Cianchetti et al., 2015; Galloway et al., 2016; Licht et al., 2017; Kurumaya et al., 2018; Phillips et al., 2018; Teoh et al., 2018). In this paper, we demonstrate a soft manipulator system with dexterous motions, which aims for the shallow water seafood animal grasping (sea cucumbers, echini, etc.). In the 10 m depth natural, undersea environment, our soft manipulator showed controllable motions under the inverse kinematic model. It can be remotely controlled to pick and place at the specific location coordinated with the underwater cameras, and we achieve more than 80% of succession rate of grasping multiple irregular shaped objects of different sizes and stiffness. Our results show that the underwater soft manipulator has inherent advantages of compliance and is promising for the future underwater manipulation. In addition, the multi-channel pneumatic actuation system and pressure balancing method (equation 15) plays significant roles in the real-world underwater grasping. Thanks to the pressure balancing method, the pressure differential inside and outside of the chambers can be maintained as constant. As a result, the underwater soft manipulator is able to achieve almost identically motions in different operating depth and collect seafood animals in the natural unstructured environment.

In this study, the inverse kinematics method reduce the DOFs to only three. Taking into account the control of the spatial angles of the manipulator tip, which has not been included in this study yet, will further complement the current soft manipulator prototype. Furthermore, pneumatic actuation is applied during current field tests, which results in a slow response time (based on the fact that we used a bunch of long pneumatic tubes) that constrains the manipulator's speed. In future studies, we will employ multi-channel hydraulic actuators with a system that can be mounted on the robot to enhance the grasping efficiency, as well as exploit a fully untethered underwater robot. In order to extend the application of this soft manipulator into the deep sea collection, we will explore the impact of water depth, oceanic current to the locomotion precision and stability in the future study. We will also apply more advanced modeling and control methods (such as the machine learning) to compensate for the system errors, and increase the grasping accuracy and dynamic response under the unstructured environment.

AUTHOR CONTRIBUTIONS

LW conceived the project. ZG accomplished the modeling, actuation, control, and kinematics experiments. ZG, BC, JL, XF, and ZL conducted the underwater robot system and demonstrated the underwater grasping experiments. LW and ZG prepared the manuscript, and all authors provided feedback during subsequent revisions.

FUNDING

This work is supported by the National Science Foundation projects, China, under contracts number 61633004, 61822303, and 61333016.

ACKNOWLEDGMENTS

This article is an extended version of our previous paper on IEEE Robosoft 2018 (Gong et al., 2018b). Permission of reusing the material is authorized by IEEE.

REFERENCES

Calisti, M., Giorelli, M., Levy, G., Mazzolai, B., Hochner, B., and Laschi, C., et al. (2011). An octopus-bioinspired solution to movement and manipulation for soft robots. *Bioinspir. Biomim.* 6:036002. doi: 10.1088/1748-3182/6/3/036002

Cianchetti, M., Calisti, M., Margheri, L., Kuba, M., and Laschi, C. (2015). Bioinspired locomotion and grasping in water: the soft eight-arm octopus robot. *Bioinspir. Biomim.* 10:035003. doi: 10.1088/1748-3190/10/3/035003

Fernandez, J. J., Prats, M., Sanz, P. J., and Garcia, J. C. (2013). Grasping for the seabed: developing a new underwater robot arm for shallow-water intervention. *IEEE Robot. Automat. Magaz.* 20, 121–130. doi: 10.1109/MRA.2013.2248307

Galloway, K. C., Becker, K. P., Phillips, B., Kirby, J., Licht, S., and Tchernov, D., et al. (2016). Soft robotic grippers for biological sampling on deep reefs. *Soft Robot.* 3, 23–33. doi: 10.1089/soro.2015.0019

Giorelli, M., Renda, F., Calisti, M., Arienti, A., Ferri, G., and Laschi, C. (2015). Neural network and jacobian method for solving the inverse statics of a cable-driven soft arm with nonconstant curvature. *IEEE Trans. Robot.* 31, 823–834. doi: 10.1109/TRO.2015.2428511

Gong, Z., Cheng, J., Chen, X., Sun, W., Fang, X., Hu, K., et al. (2018a). A bio-inspired soft robotic arm: kinematic modeling and hydrodynamic experiments. *J. Bion. Eng.* 15, 204–219. doi: 10.1007/s42235-018-0016-x

Gong, Z., Cheng, J., Hu, K., Wang, T., and Wen, L. (2018b). "An inverse kinematics method of a soft robotic arm with three-dimensional locomotion for underwater manipulation," in *2018 IEEE International Conference on Soft Robotics* (Livorno: RoboSoft), 516–521.

Gong, Z., Xie, Z., Yang, X., Wang, T., and Wen, L. (2017). "Design, fabrication and kinematic modeling of a 3D-motion soft robotic arm," in *IEEE International Conference on Robotics and Biomimetics* (Qingdao), 509–514.

Hao, Y., Gong, Z., Xie, Z., Guan, S., Yang, X., Wang, T., et al. (2018). A soft pneumatic robotic gripper with variable effective length. *J. Bion. Eng.* 15, 220–235. doi: 10.1007/s42235-018-0017-9

Jiang, H., Wang, Z., Liu, X., Chen, X., Jin, Y., and You, X., et al. (2017). "A two-level approach for solving the inverse kinematics of an extensible soft arm considering viscoelastic behavior," in *IEEE International Conference on Robotics and Automation* (Singapore), 6127–6133.

Kurumaya, S., Phillips, B. T., Becker, K. P., Rosen, M. H., Gruber, D. F., and Galloway, K. C., et al. (2018). A modular soft robotic wrist for underwater manipulation. *Soft Robot.* 5:399–409. doi: 10.1089/soro.2017.0097<underline

Lakhal, O., Melingui, A., Chibani, A., Escande, C., and Merzouki, R. (2014). "Inverse kinematic modeling of a class of continuum bionic handling arm," in *IEEE/ASME International Conference on Advanced Intelligent Mechatronics* (Besacon), 1337–1342.

Lee, K. H., Fu, D. K., Leong, M. C., Chow, M., Fu, H. C., Althoefer, K., et al. (2017). Nonparametric online learning control for soft continuum robot: anenabling technique for effective endoscopic navigation. *Soft Robot.* 4, 324–337. doi: 10.1089/soro.2016.0065

Licht, S., Collins, E., Mendes, M. L., and Baxter, C. (2017). Stronger at depth: jamming grippers as deep sea sampling tools. *Soft Robot.* 4, 305. doi: 10.1089/soro.2017.0028

Marchese, A. D., and Rus, D. (2016). Design, kinematics, and control of a soft spatial fluidic elastomer manipulator. *Int. J. Robot. Res.* 35, 840–869. doi: 10.1177/0278364915587925

Martín, A., Barrientos, A., and del Cerro, J. (2018). The Natural-CCD algorithm, a novel method to solve the inverse kinematics of hyper-redundant and soft robots. *Soft Robot.* 5, 242–257. doi: 10.1089/soro.2017.0009

Martinez, R. V., Branch, J. L., Fish, C. R., Jin, L., Shepherd, R. F., and Nunes, R. M. D., et al. (2013). Robotic tentacles with three-dimensional mobility based on flexible elastomers. *Adv Mater.* 25, 205–212. doi: 10.1002/adma.201203002

Phillips, B. T., Becker, K. P., Kurumaya, S., Galloway, K. C., Whittredge, G., Vogt, D. M., et al. (2018). A dexterous, glove-based teleoperable low-power soft robotic arm for delicate deep-sea biological exploration. *Sci. Rep.* 8:14779. doi: 10.1038/s41598-018-33138-y

Polygerinos, P., Wang, Z., Overvelde, J. T., Galloway, K. C., Wood, R. J., Bertoldi, K., et al. (2015). Modeling of soft fiber-reinforced bending actuators. *IEEE Trans. Robot.* 31, 778–789. doi: 10.1109/TRO.2015.2428504

Teoh, Z. E., Phillips, B. T., Becker, K. P., Whittredge, G., Weaver, J. C., Hoberman, C., et al. (2018). Rotary-actuated folding polyhedrons for midwater investigation of delicate marine organisms. *Sci. Robot.* 3:eaat5276. doi: 10.1126/scirobotics.aat5276

Webster Iii, R. J., and Jones, B. A. (2010). Design and kinematic modeling of constant curvature continuum robots: a review. *Int. J. Robot. Res.* 29, 1661–1683. doi: 10.1177/0278364910368147

Webster, R. J., Okamura, A. M., and Cowan, N. J. (2007). "Toward active cannulas: miniature snake-like surgical Robots," in *IEEE/RSJ International Conference on Intelligent Robots and Systems*, 2857–2863.

Conflict of Interest Statement: The authors declare that the research was conducted in the absence of any commercial or financial relationships that could be construed as a potential conflict of interest.

frontiers in Robotics and AI

ORIGINAL RESEARCH
published: 30 April 2019
doi: 10.3389/frobt.2019.00030

Design Considerations for 3D Printed, Soft, Multimaterial Resistive Sensors for Soft Robotics

Benjamin Shih[1], *Caleb Christianson*[2], *Kyle Gillespie*[1†], *Sebastian Lee*[1], *Jason Mayeda*[1], *Zhaoyuan Huo*[1] *and Michael T. Tolley*[1*]

[1] Department of Mechanical and Aerospace Engineering, University of California, San Diego, San Diego, CA, United States,
[2] Department of Nanoengineering, University of California, San Diego, San Diego, CA, United States

OPEN ACCESS

Edited by:
Perla Maiolino,
University of Cambridge,
United Kingdom

Reviewed by:
Ioannis Andrea Ieropoulos,
University of the West of England,
United Kingdom
Josie Hughes,
University of Cambridge,
United Kingdom

***Correspondence:**
Michael T. Tolley
tolley@ucsd.edu

†Present Address:
Kyle Gillespie,
Department of Mechanical and Aerospace Engineering, University of California, Los Angeles, Los Angeles, CA, United States

Specialty section:
This article was submitted to Soft Robotics, a section of the journal Frontiers in Robotics and AI

Received: 04 December 2018
Accepted: 08 April 2019
Published: 30 April 2019

Citation:
Shih B, Christianson C, Gillespie K, Lee S, Mayeda J, Huo Z and Tolley MT (2019) Design Considerations for 3D Printed, Soft, Multimaterial Resistive Sensors for Soft Robotics. Front. Robot. AI 6:30. doi: 10.3389/frobt.2019.00030

Sensor design for soft robots is a challenging problem because of the wide range of design parameters (e.g., geometry, material, actuation type, etc.) critical to their function. While conventional rigid sensors work effectively for soft robotics in specific situations, sensors that are directly integrated into the bodies of soft robots could help improve both their exteroceptive and interoceptive capabilities. To address this challenge, we designed sensors that can be co-fabricated with soft robot bodies using commercial 3D printers, without additional modification. We describe an approach to the design and fabrication of compliant, resistive soft sensors using a Connex3 Objet350 multimaterial printer and investigated an analytical comparison to sensors of similar geometries. The sensors consist of layers of commercial photopolymers with varying conductivities. We characterized the conductivity of TangoPlus, TangoBlackPlus, VeroClear, and Support705 materials under various conditions and demonstrate applications in which we can take advantage of these embedded sensors.

Keywords: soft sensor, 3D printed, soft skin, resistive sensor, strain sensor, soft robotics

1. INTRODUCTION

3D printing has enabled many new design and fabrication approaches for robotics (Lipson and Kurman, 2013). In parallel, a new perspective on the role that materials play in robotic design has altered the building blocks and tools with which we create our robotic systems. The ability to print soft and rigid materials simultaneously using a single machine has expanded the realm of possibilities for fabricating robots, including systems that are biomimetic (Pearson et al., 2011; Kumar et al., 2017; Wang et al., 2017b) and ones that have improved resistance to impact through functional gradients (Bartlett et al., 2015).

In the long term, one goal of 3D printing is the ability to print an entire robot in one go and have it walk itself out of the machine upon completion (Lipson, 2015). Recent work has demonstrated this "get up and walk away" concept. Felton et. al. describe a method for building self-folding machines using laminate structures that fold themselves up in multiple stages and can walk away after receiving electronics and a battery (Felton et al., 2014). Similar in overall concept, MacCurdy et. al. used a multimaterial 3D printer to print fluid-filled bellows directly integrated into the transmission of their locomotive robot, which can also walk immediately after attaching a motor and battery without additional mechanical modifications (MacCurdy et al., 2016). However, neither of these robots possess sensing capabilities for feedback control and learning. In addition, robots

that can get up and walk away entirely on their own require a built-in, on-board energy source. The previous robots have batteries added after printing, whereas robots like the EcoBots have a stomach for real digestion that enables them to sustain themselves (Ieropoulos et al., 2010).

Soft robotics is one field that has benefited significantly from 3D printing (Rus and Tolley, 2015). Robot designers can print both the molds for making soft robots (Florez et al., 2014) as well as the soft robots directly (Bartlett et al., 2015). However, a major challenge with soft robots is the development of effective sensors. Soft robots are not constrained to prismatic or revolute motions, and obtaining sensory feedback on these motions requires different types of sensors than those used for rigid robots. In addition, soft robots may require sensors that can be placed on complex surface geometries or embedded within the body.

Much of the soft robot development today has focused on actuation (Conn et al., 2012; Connolly et al., 2017; Miriyev et al., 2017; Kellaris et al., 2018). Sensor design for soft robots is complicated because flexible, compliant robots often have non-planar, complex surfaces that are difficult to cover and sensorize with traditional manufacturing techniques. Proper selection from among the wide range of design parameters (e.g., geometry, material, actuation type, etc.) is critical to the function of soft robots. Conventional rigid sensors can be effective for soft robots with constrained motions (Zhao et al., 2016; Homberg et al., 2018; Scimeca et al., 2018). However, the general case of a soft robot with a high number of degrees of freedom requires capabilities such as out-of-plane twisting. Sensors that are directly integrated into the bodies of soft robots and co-fabricated could help improve both their exteroception and interoception capabilities. We want to move toward highly integrated structural and sensing components as we see in biological human bodies, which may not be possible with discrete, rigid sensors.

Recently, interest in 3D printing soft robots has grown significantly. Previously, research groups have printed various actuators (Drotman et al., 2017; Kalisky et al., 2017) and bodies (Umedachi et al., 2013; Bartlett et al., 2015; MacCurdy et al., 2016) for soft manipulation and locomotion. Alongside the development of soft robot actuators, many groups have become interested in incorporating sensors and closing the control loop for feedback on the robot's interactions with its environment. Felt et. al. designed an inductance-based sensing system to measure and control bellowed continuum joints, by wrapping coils of wires and measuring changes in inductance (Felt et al., 2017). We (Shih et al., 2017) and others (Bilodeau et al., 2015; Farrow and Correll, 2015), have embedded soft sensors for measuring bending into the layers of pneumatic fingers, which enabled the fingers to estimate the shapes of various objects using tactile sensing (Bilodeau et al., 2015; Farrow and Correll, 2015; Zhao et al., 2016; Shih et al., 2017). Homberg et. al. clustered sensor readings from their fingers to identify correspondences to gripper configurations and to classify grasped objects (Homberg et al., 2015), Kim et. al. 3D printed pneumatic pouches and connected

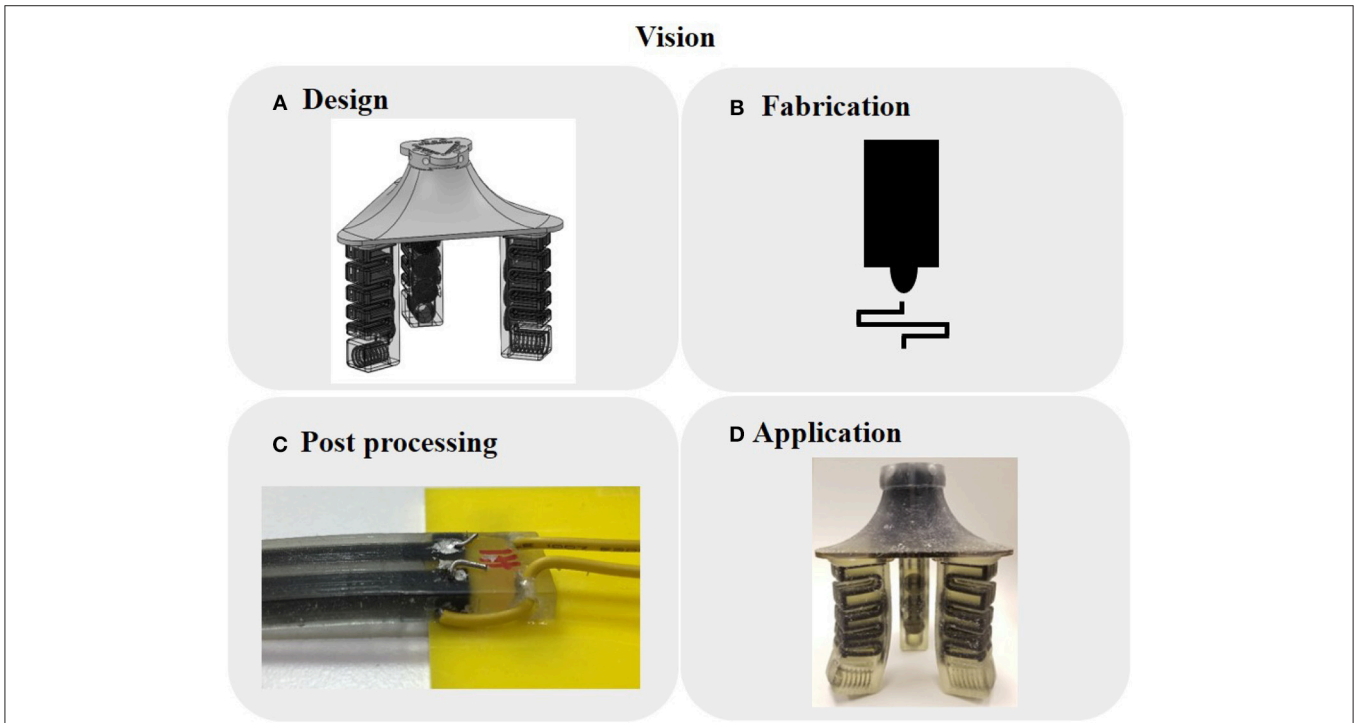

FIGURE 1 | Overall vision of the pipeline for our 3D printed sensors. **(A)** Digitized CAD design with embedded, integrated sensing. **(B)** Multimaterial 3D printer that simultaneously co-fabricates both actuators and sensors. **(C)** Post-processing such as removing support material or wire connections. **(D)** Immediately deployable for real-world applications.

them to pressure sensors to sense when the pouches came into contact with external objects (Kim et al., 2015), and Pearson et. al. demonstrated tactile sensing in both compliant, 3D structures and soft, 3D printed actuators (Pearson et al., 2010).

Many groups have also begun experimenting with various fabrication techniques for soft sensors, particularly in the form of skin-like structures (Cheng et al., 2010; Bauer et al., 2014; Sonar and Paik, 2016; Devaraj et al., 2018). Muth et. al. customized a printer for sensor fabrication which embeds conductive material into a partially-cured silicone elastomer substrate that then fully cures and solidifies (Muth et al., 2014). Frutiger et. al. and White et. al have also 3D printed conductive materials for sensors (Frutiger et al., 2015; White et al., 2017). Inspired by mechanoreceptors found within skin, Lipomi et. al. and Tee et. al. developed skin-like sensors that can detect strain and pressure (Lipomi et al., 2011; Tee et al., 2015), and Yin et. al. fabricated a robotic skin that senses shear force (Yin et al., 2017). Multiple groups have explored using deep learning to understand deformations and changes in a soft robot using embedded, soft sensors (Han et al., 2018; Soter et al., 2018; Thuruthel et al., 2019). However, the integration of these skins into real-world robot systems for sensing remains an open problem (Silvera-Tawil et al., 2015). Having a separate skin also requires the robot designer to affix the sensing elements in a separate manufacturing step, limiting the ability to sensorize the complex, dynamic bodies of soft robots.

In this paper, we present:

- A method for printing multiple, soft materials simultaneously to produce a resistive sensing element using a commercial 3D printer, which enables users to incorporate arbitrary sensor geometries into their soft robots.
- Design considerations for creating sensors based on 3D printable conductive materials.
- A demonstration for how we can embed soft, complex-shaped sensors into compliant grippers.

A surprising aspect of what we present is that many researchers are thinking about how to make soft robots with embedded liquid metals, whereas commercially available systems today already allow us to directly print general conductive traces. We hypothesize that current commercial systems already allow for the fabrication of soft actuators with embedded sensors. Not only can existing systems already perform the manufacturing, but this approach also enables designs that would otherwise be very challenging for existing fabrication techniques, e.g., multilayer sensor or complex structures within a 3D body. With traditional lithographic approaches, it is not obvious how to fabricate such designs.

In section 2, we discuss background for the topic. In section 3, we explain the materials and methods that we used for the experiments. In section 4, we present and discuss the results, including the types of sensors that we printed and parameters that contributed to their conductivity, model of the sensitivity to strain, and experimental characterization of the sensors. In section 5, we present potential applications of the 3D printed sensors. Lastly, in section 6, we discuss conclusions and future work.

2. MATERIALS AND METHODS

2.1. Design and Fabrication of the Resistive Sensors

Many challenges exist with the integration of sensors into the body of soft robots. Current techniques are often unable to

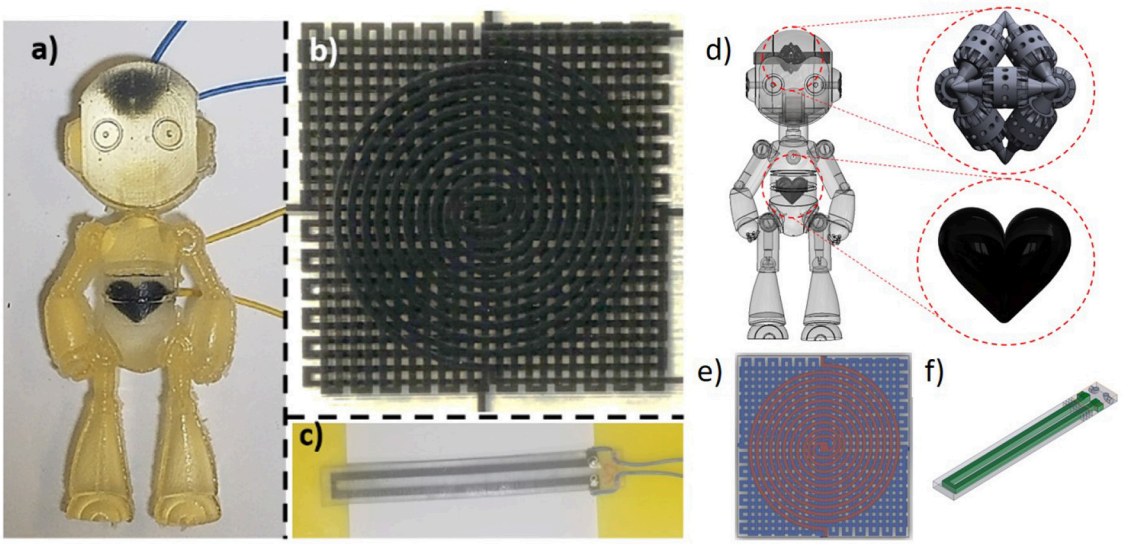

FIGURE 2 | 3D printed, resistive, soft sensors and the correspoding CAD drawings. **(a,d)** Humanoid robot-front view. Enlarged drawings of the embedded heart-and brain-shaped sensors. **(b,e)** Multilayer strain and pressure sensor-top view. **(c,f)** Uniaxial strain sensor with mechanical strain relief and functional gradient to improve wire interface-isometric view.

accommodate the elastic, large deformations of soft robots (i.e., the stretching and bending) that arise in applications such as wearable computing and smart textiles (Majidi, 2014).

We can overcome many of these challenges using a commercially available 3D printer (Stratasys Objet350 Connex3) that has the ability to mix conductive and dielectric materials. Many groups have produced actuatable soft robots with this tool: (Umedachi et al., 2013; Bartlett et al., 2015; Kim et al., 2015; MacCurdy et al., 2016; Drotman et al., 2017; Kalisky et al., 2017; Kumar et al., 2017; Wang et al., 2017b; Shih et al., 2018). We investigated whether this printer can also directly embed sensors into soft robot systems.

Materials that the printer can produce include a flexible, translucent photopolymer (TangoPlus FLX930); a flexible, black photopolymer (TangoBlackPlus FLX980); a rigid, clear photopolymer (VeroClear RGD810); and a flexible, low-yield polymer (SUP705) as support material. The black resin contains carbon particles (Stratasys, 2014b), which provide a small but measurable conductivity, and can serve as conductive traces for sensors. We created the geometry of the sensors using computer-aided design (CAD) software, fabricated our designs using the 3D printer, and secured the wires using silver paste and mechanical strain reliefs (**Figure 1**). **Figures 2**, **3** show the sensor-only designs and the test samples, respectively, that we characterized in this paper.

The commercial material has comparable mechanical strain-to-failure properties as skin: it is reported to have 70–120% elongation at break (Stratasys, 2016). During our tests (section 3) we observed strain-to-failure of approximately 20%. However, even this reduced value may be sufficient for most applications. For comparison, most types of human skin fail after exceeding 15% strain (Kim et al., 2017). The physiological limitation is measured to be at most 45% in areas such as the fully flexed knee or elbow (Wessendorf and Newman, 2012; Kim et al., 2017). Thus, even with relatively low strain-to-failure, the commercial material may still be useful in creating bioinspired and biomimetic designs.

2.2. Removal of Support Material

The printer allows the user to choose between surface finishes that are either glossy or matte, where matte is achieved by coating the entire print in support material. We printed the test blocks with matte coatings to maintain a uniform surface finish. The dimensions of the test blocks were 10 × 10 × 50 mm, with 10 × 10 × 3 mm tabs for the measurement clamps (**Figure 3**). The process we use to remove the support material occurs in multiple stages (**Figure 3**). Because the support material appears to contribute to the conductivity (further evaluated in section 3.4), it is important to thoroughly clean the surface of

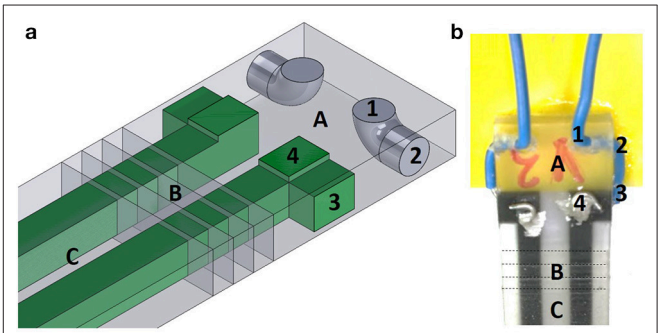

FIGURE 4 | Our method for wire attachment. **(a)** Schematic for the wire attachment procedure - isometric view. We insert the wire at 1, and pass through in order of 1-2-3-4 to both distribute strain on the wire and to improve the electrical conductivity between the solid wire and the photopolymer trace. These numbers are only labeled on half of the sensor shown, for clarity. **(b)** Completed, physical version of the wire attachment - top view.

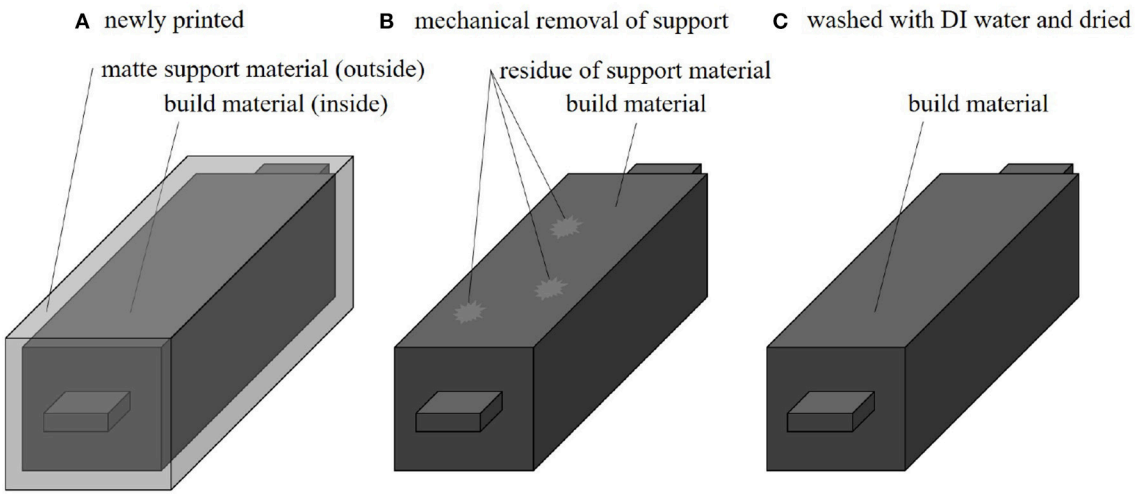

FIGURE 3 | Stages of the process for removing the support material. **(A)** Newly printed block of material for characterization, with a matte surface finish. **(B)** Block of material after we mechanically remove the support material. Some patches of support material can remain on the surface. **(C)** Block of material after we wash it with distilled water and dry the sample.

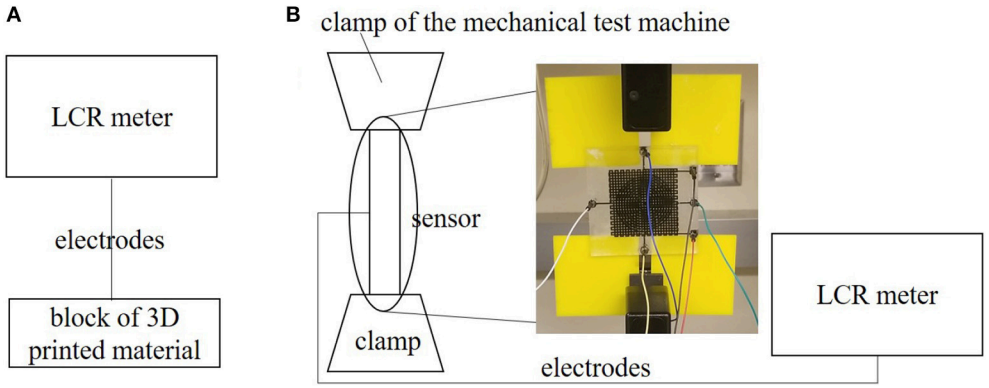

FIGURE 5 | Test setup for characterization. **(A)** Setup to measure conductivity of blocks. **(B)** Setup to simultaneously measure strain and conductivity.

the material or enclose it within a different material. In this process (**Figure 3A**), a fresh block of material comes off the 3D printer with a matte surface finish and is coated in support material. **Figure 3B** depicts the block of material after the support is mechanically scraped off the surface of the block by hand. Finally, as shown in **Figure 3C**, this process ends with the careful cleaning of any remaining support material on the surface of the block, by washing the block with distilled water and drying it.

2.3. Mechanical Strain Relief

As noted in previous work (Mengüç et al., 2014; Shih et al., 2018), attaching solid-core wires to soft materials can be difficult and result in an unstable connection because the wire can tear the soft material or gradually shift around. Thus, our solution for effective electrical connections is to combine: (1) soft insertion points for mechanically securing the wires, and (2) additional mechanical relief using an extra loop of wire to wrap around, which reduce the tearing of the electrodes when the sensor experiences strain.

For this sensor design, we included soft holes within the rigid material to function as a mounting point. The hole in **Figure 4** connecting the points labeled 1 and 2 is filled during the printing process using the dielectric photopolymer (TangoPlus, FLX930), which provides mechanical relief by restricting the motion of the wire. At 3 and 4, we push the bare wire through the black elastomer and coat the wire and photopolymer interface with silver paste to increase electrical conductivity. In **Figure 4**, A represents a rigid photopolymer (VeroClear RGD810, Stratasys), B represents a functional stiffness gradient (consisting of TangoPlus and VeroClear: FLX9050, FLX9070, and FLX9095, Stratasys), and C represents a flexible photopolymer (TangoPlus FLX930, Stratasys).

2.4. Experimental Setup for Measurement and Characterization

We connected the sensors to an inductance, capacitance, and resistance (LCR) meter (Keysight, E4980AL), which provides high precision measurements. We smoothed the sensor readings with an 8 point averaging filter on the LCR meter.

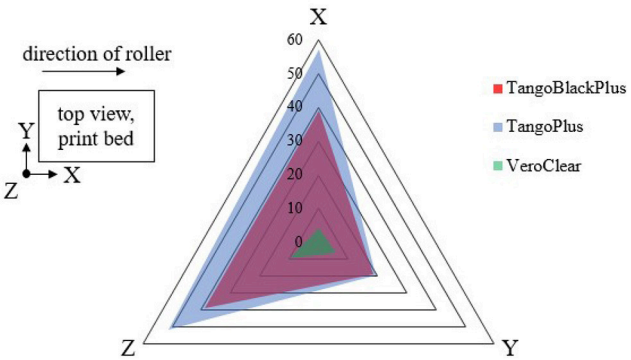

FIGURE 6 | Plot of the impact of anisotropy on the 3D printed material. Number of samples n = 10.

We prescribed the strain using a mechanical testing machine (Instron 5965) (**Figures 5A**, **10**, **11A**). For the multilayer sensor, we tested the pressure by placing a range of standard masses on top of the pressure sensor, which we converted to a pressure using the relationship ($P = \frac{mg}{A}$) (**Figure 11B**).

2.5. Removal of Water Content by Desiccation

Because of the constituent components in the 3D printer material (further explanation in section 3.4), we investigated how much of an impact water content had on mass and conductivity. In the desiccation process, we placed the test blocks in an air-tight, sealed container with packets of silica desiccant (Dry & Dry). Throughout multiple 1 h periods, we removed the blocks and reported the conductivity.

2.6. Preferential Strain Response of the Multi-Dimensional Sensor

We looked at the sensitivity of the multi-directional sensor by connecting it to the LCR meter while simultaneously stretching

the sensor in the Instron. The parameters of the Instron include a strain rate of 0.0025 mm/mm/s (0.25% strain per second) and an auto-stop at 15% extension. **Figure 5B** shows the setup for simultaneously stretching the material while measuring the conductivity.

2.7. Model of Strain Response

For elastomer-like materials, the overall length of the channel increases while the cross-sectional area of the channel decreases when the channel of the sensor experiences axial deformation, leading to an increase in the resistance of the channel (Park et al., 2012). Here, we are ignoring the microscale, bond-level effects (Creton and Ciccotti, 2016) and assuming the change is dominated by macroscopic geometric change.

Assuming rectangular traces, we can represent the resistance of an undeformed sensor as:

$$R_0 = \frac{\rho L}{wh} \tag{1}$$

where R_0 is the resistance in the undeformed state, ρ is the electrical resistivity of the photopolymer, L is the length of the conductive channel, and w and h are the width and height of the cross-section of the conductive material, respectively.

The change in resistance of the stretched material is:

$$\begin{aligned} \Delta R &= R - R_0 \\ &= \rho \frac{L + \Delta L}{(w + \Delta w)(h + \Delta h)} - \rho \frac{L}{wh} \end{aligned} \tag{2}$$

where R is the resistance when the sensor stretches by ΔL.

Next, we can replace Δw with $-\nu \epsilon w$ and Δh with $-\nu \epsilon h$, and substitute $\epsilon = \frac{\Delta L}{L}$ to obtain:

$$\frac{\Delta R}{R_0} = \epsilon \left[\frac{(1 + 2\nu) - \nu^2 \epsilon}{(1 - \nu \epsilon)^2} \right] \tag{3}$$

where ϵ is the strain and ν is the Poisson's ratio.

The Poisson's ratio for this photopolymer material is approximately $\nu = 0.49$ (Slesarenko and Rudykh, 2017), which enables us to further simplify Equation 3 to:

$$\frac{\Delta R}{R_0} = \frac{\epsilon(8.25 - \epsilon)}{(2.04 - \epsilon)^2} \tag{4}$$

2.8. Model of Pressure Response

We modeled the relationship between the change in resistance and contact pressure using linear elastic fracture mechanics (Park et al., 2010). Once again, assuming rectangular traces, we can represent the normalized change in resistance as:

$$\frac{\Delta R}{R_0} = \frac{1}{1 - 2(1 - \nu^2) wP/(Eh)} - 1 \tag{5}$$

where P is the pressure on the sensor and E is the elastic modulus of the material.

3. RESULTS AND DISCUSSION

3.1. Characterization of the Dependence of Conductivity on Orientation of 3D Print

Previous work has shown that 3D printers exhibit anisotropic properties depending on the orientation of the print (Wang et al., 2017a). Thus, we characterized the dependence of the conductivity on the orientation of 3D print. We tested samples of each of the TangoPlus, TangoBlackPlus, and VeroClear materials.

Our results (**Figure 6**) show that there is a difference in resistance measurements between TangoBlackPlus and TangoPlus in the x-axis and z-axis directions of the 3D print. However, in the y-axis direction, the conductivity changes minimally between the two materials. In all three directions of the coordinate frame, there is a substantial difference between the readings for the VeroClear and for the other materials.

This phenomenon may be due to the spacing of the print heads. The commercial 3D printer moves along the x-axis of the bed and sputters droplets of uncured ink onto the print bed. The printer cures each layer of ink with a UV light before incrementing the positioning of the z-axis and moving to the subsequent layer. In addition, the roller component of the 3D printer, which smooths each layer of ink, also acts along the x-axis. This asymmetry in the plot could be due to increased overlapping of the ink in the x direction relative to the y direction. For the remainder of the experiments, we consider only the conductivity of the in-plane x-direction.

3.2. Characterization of the Dependence of Conductivity on Removal of Support Material

To characterize the dependence of conductivity on the amount of support material coating the surface of the blocks of material, we measured the resistance of the materials at various points throughout the process of removing the support material.

We observed that the resistance of the TangoBlackPlus and TangoPlus samples increased, meaning the conductivity

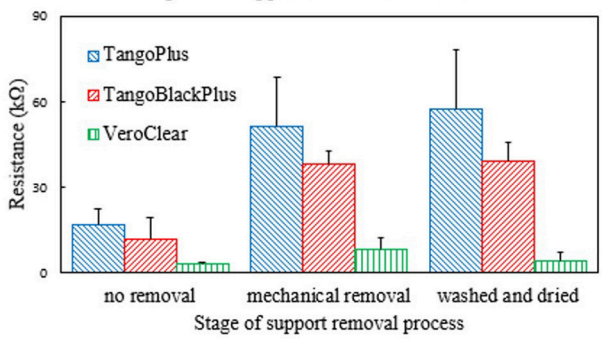

FIGURE 7 | Plot of how the resistance of the 3D printed materials changes depending on how much support material is on the surface. Each group of bars corresponds to the measurement along the various stages in the removal process of the support material (**Figure 3**). Number of samples n = 10.

of the samples decreased overall (**Figure 7**). This observation suggests that the support material contributed toward the conductivity measurement of each material, and indicated that the surface of various materials need to be thoroughly cleaned of support material.

In addition, the data show that the VeroClear material actually exhibited the most conductivity. While this result is interesting, we cannot directly integrate it into soft sensors or soft-bodied robots because of its intrinsic rigid mechanical properties. However, the relatively-lower resistance of VeroClear may be useful for other applications.

3.3. Characterization of the Dependence of Conductivity on Contact Resistance

While measuring the materials and designing the mechanical strain relief, we observed that the contact resistance due to the rigid wire and soft material appeared to play a significant role in the measurement of the conductivity. Thus, we characterized the dependence of conductivity on the contact resistance by comparing the material with and without wires (clamping onto the material directly with the LCR probes). **Figure 8** shows the results of the comparison of the resistance pre- and post- wire attachment. Because the system is soft, it deforms upon clamping. We avoided directly clamping to the soft material by attaching a wire. The resistance measured when clamping directly to the material is less than that measured when a wire is connected to the material with silver paste at the interface because of contact resistance that the wiring introduced.

When the material comes directly into contact with the clamps for measurement, it gradually tears due to a stress concentration at the interface of contact. The mechanical breakdown of the material reinforces the need for a soft-rigid wire interface. By adding wires to the samples, we could reduce variance in the LCR measurements by providing a fixed point of attachment to the soft material. A single, physical point of contact also helped with the consistency of the measurements by reducing the mechanical wear of the LCR electrodes on the samples. Additionally, the mechanically strain relief (section 2.3) further helps with reducing the movement of the wires.

There may be two scales of physical behavior that influence the reading that the LCR meter produces: (1) the physical, geometric deformation of the material at the macro-scale, and (2) the micro-scale separation of the particles in the soft material as the chemical bonds between the particles begin to separate and the material begins to tear (Creton and Ciccotti, 2016).

3.4. Characterization of the Dependence of Conductivity on Water Content

The datasheets for the 3D printed materials indicate that they contain hydrophilic, organic compounds (Stratasys, 2014a,b,c,d). In addition, we noticed that the cleanliness of the surface of the materials, particularly the removal of the support material, had an impact on the measurement of conductivity. These observations indicated that the support material was contributing to the conductivity, possibly because of the ability of the material to absorb and hold onto water.

To further understand how the water content impacts the conductivity of the material, we tested the effects of desiccating the materials. We reduced the water content in the blocks using silica desiccants, and measured the changes in mass due to water content as well as the resulting change in conductivity (**Figure 9**). This procedure is further described in section 2.5.

The mass of the blocks decreased due to the desiccation, which we attribute to the loss of water content. The desiccation process resulted in an overall decrease of –1.00%. The average resistance of the samples from the desiccation process increased by 84.78%,

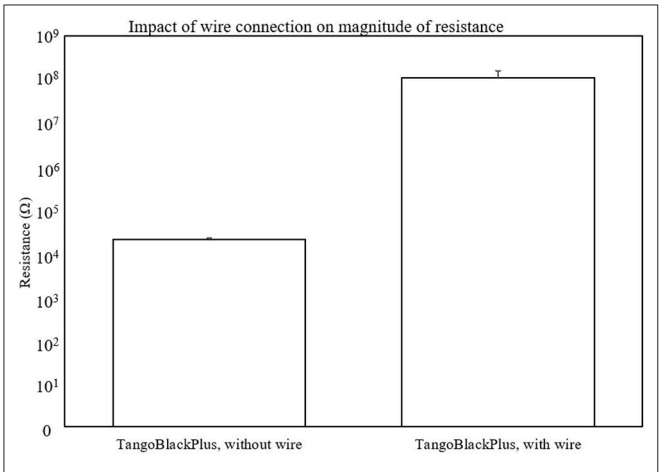

FIGURE 8 | Plot of the dependence of the magnitude of conductivity based on contact resistance. We plot the magnitudes on a logarithmic scale to show the order of magnitude difference that the wire connection results in. Number of samples $n = 3$.

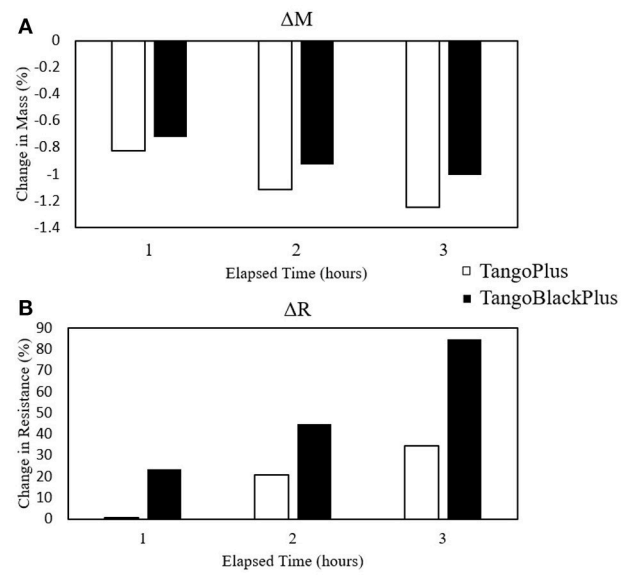

FIGURE 9 | Plots of changes in mass and resistance due to desiccation. **(A)** Percent change in mass. **(B)** Percent change in resistance. Number of samples $n = 6$.

indicating that the samples became less conductive than before the desiccation process and that the presence of moisture can impact the sensor readings.

3.5. Comparison Between Model and Experimental Data

We compared the analytical models of the uniaxial and multilayer sensors (section 2.7) with the measurements from our experimental tests. We characterized our sensors using an LCR meter. We required sensitive measurement equipment because the conductive photopolymer has a carbon black percentage of $< 0.1\%$ by mass (Stratasys, 2014b), resulting in resistances with large magnitudes (in the MΩ range). We filtered the sensor readings with a 32 point averaging window on the LCR meter. **Figure 10** shows the normalized change in resistance vs. strain for the uniaxial strain sensor, **Figure 11A** shows the normalized change in resistance vs. strain along one of the two axes of strain for the multilayer sensor, and **Figure 11B** shows the normalized change in resistance vs. pressure for the multilayer sensor.

To better visualize the trends, we introduced a single constant scale factor of $S_{strain} = 14.25$ for both strain sensors (Equation 6) and another of $S_{pressure} = 3,850$ for the pressure sensor (Equation 7), resulting in the theoretical plots in **Figures 10**, **11**. For the scale factor for strain, we selected its value by simultaneously minimizing the residuals for both the uniaxial and multilayer sensors. The scale factors are included to demonstrate that despite the differences in magnitude, the trend of the measurements behaves similarly to predictions of the sensors with similar geometry of the traces despite differences in the materials for fabricating the sensors.

$$\frac{\Delta R}{R_0} = S_{strain}\epsilon\frac{(8.25-\epsilon)}{(2.04-\epsilon)^2}$$
$$\frac{\Delta R}{R_0} = S_{pressure}\left[\frac{1}{1-2(1-\nu^2)wP/(Eh)}-1\right] \quad (6)$$

One potential reason for the difference in scale is that the resistivity may not be constant as we had previously assumed. During stretching, the geometry of the sensor changes, which can be described with Poisson's ratio. This change in geometry alters the resulting resistance of the trace. However, since our traces are polymers, strain will cause some carbon particles to get closer together while others will separate, depending on the initial distribution of the polymer network within the dielectric (Zhang et al., 2007). This would impact electron mobility, and thus the assumption of constant resistivity might not be valid and requires further investigation.

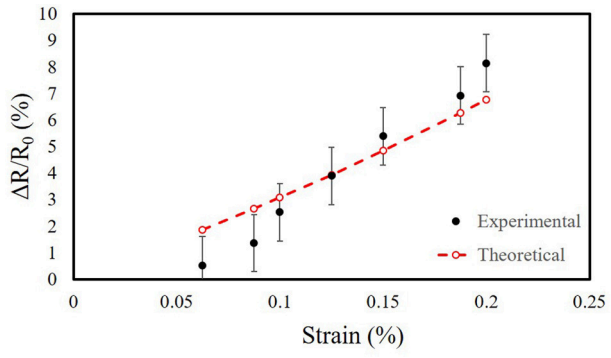

FIGURE 10 | Normalized change in resistance vs. strain for the uniaxial strain sensor. Comparison of analytical model to experimental characterization. The mean is 108 MΩ at rest. Number of samples $n = 3$.

3.6. Multimodal Sensitivity

Analysis of the strain response of the multi-layer sensor helped identify that the patterning of the traces make a difference in the measurement, and demonstrated that the LCR meter could discern between the different directions of strain.

When stretching in the vertically-aligned direction, we observed that the vertically-aligned sensor increased in resistance whereas the horizontally-aligned and pressure sensors decreased in resistance (**Figure 12**). The trend that we observed is consistent with what we expected from Poisson's ratio. However, the magnitudes are not: the vertically-aligned traces experienced less relative change than the horizontally-aligned traces did. This effect could potentially be because the change in resistance is bigger when you compress the material together than when you stretch it apart, as compared to liquid materials such as eGaIn. Modeling this material as a conductor of changing volume is not accurate, but rather the material is more sensitive to compression than extension as shown from these results.

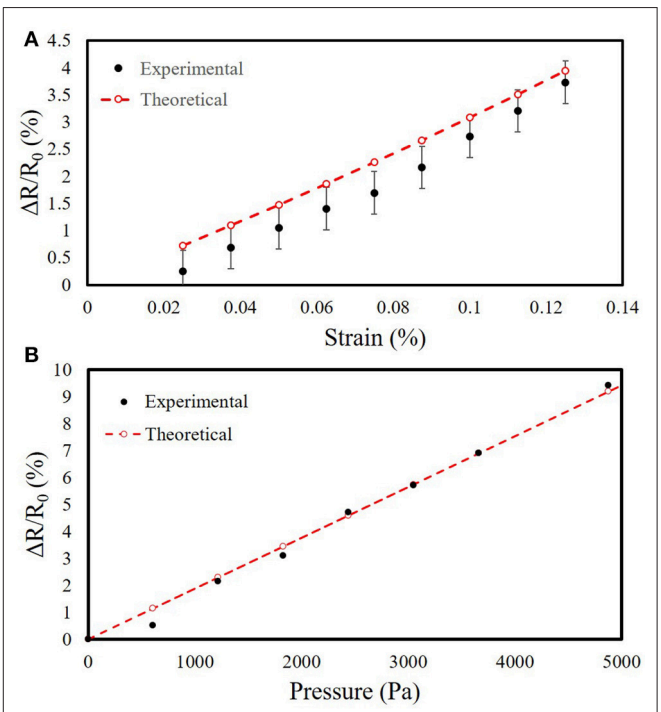

FIGURE 11 | Comparison of analytical model to experimental characterization for the multilayer sensor. **(A)** Normalized change in resistance vs. strain. The mean is 147 MΩ at rest. Number of samples $n = 3$. **(B)** Normalized change in resistance vs. pressure. The mean is 560 MΩ at rest.

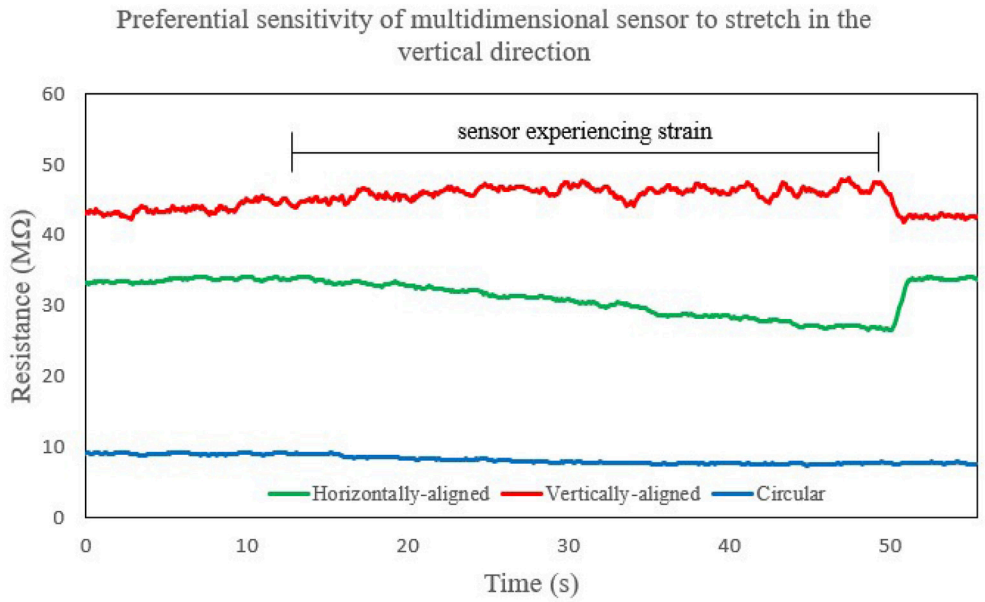

FIGURE 12 | Plot showing the strain response of the multimodal sensor in multiple directions as we stretch it along the vertically-aligned direction. In this situation, the sensor is more sensitive to the serpentine pattern that is horizontally-aligned as opposed to the one that is vertically-aligned, whereas the circular sensor experiences a minimal change in its response relative to the other directions.

3.7. 3D Printed Soft Gripper With Embedded Sensors

We demonstrated the use of this fabrication process to print a soft gripper with embedded sensors by integrating the sensing capabilities directly into a pneumatic gripper (**Figure 13**). In addition, we measured the static sensor readings as the gripper held onto various objects, which we selected from the YCB dataset (Calli et al., 2017) (**Figure 13**). We also measured the dynamic response of the sensors as we actuated the fingers simultaneously (**Figure 14**).

As a proof of concept demonstration, we measured the sensor readings for the various gripper configurations associated with grasping different objects. Each finger is pneumatically actuated, like previously presented pneunets (Mosadegh et al., 2014), and we denoted the corresponding sensors as S1, S2, and S3. We defined holding as the grasp position associated with the configuration of each finger as it conforms around the objects (**Figure 13**) and repeated each grasp 3 times. Previous work has shown that these configurations can be used to identify or classify these object-associated grasps (Homberg et al., 2015). The embedded sensors could be beneficial for detecting touch or helping with state estimation for the gripper, and clusters formed from multiple grasps could be amenable to classification.

4. CONCLUSIONS AND FUTURE WORK

This paper presents the concept of 3D printing resistive sensors using a commercially available printer and material. We characterized the dependence of the 3D printed material's conductivity on a variety of factors and introduce guidelines on how to improve the fabrication method for similar types of sensors. In addition, we studied the mechanical strain response and model the sensors that we fabricated using this process.

The current iteration of the 3D printed material is promising, but there are some limitations to consider when working with it. To begin with, the company did not intentionally design the material as a conductor, and thus the resistance has a large magnitude. Measurement of the sensor values requires high-sensitivity electronics and the high impedance and limited conductivity could limit sensitivity. The readings also experience drift and oscillations due to the macro- and micro-scale deformations of the material. In addition, this photopolymer material experiences limited strain compared to materials for "traditional" soft sensors like silicone elastomers, which could limit its use for soft robots.

Future work includes studying the other modes of sensors that this method may enable, such as printing capacitive and inductive sensors. Finding a method to reduce the drift of the readings over time would help improve the potential for deploying this material for real-world applications. In addition, knowledge of the mechanical and chemical properties of the materials can inform and optimize the design of 3D printed sensors for future applications. The ability to embed sensors into soft robots using accessible, commercial 3D printers would 1 day play a role in printing an entire robot along with all of its components.

This work is a step toward the direct printing of sensorized soft robots using commercially available systems. Simultaneously,

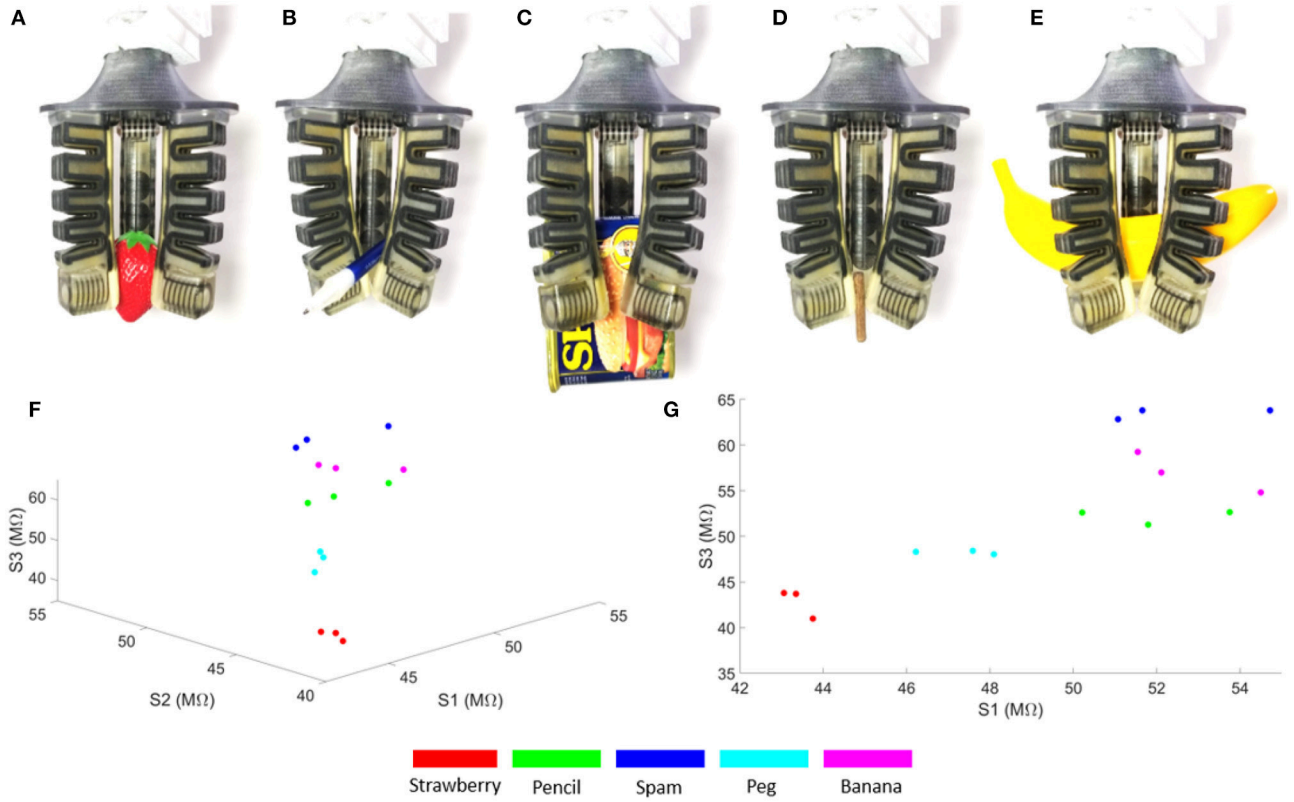

FIGURE 13 | Pneumatic gripper with embedded strain sensors and the static sensor readings of the gripper corresponding to the configuration of the fingers while holding various objects. S1, S2, and S3 are the sensor readings from each of the three fingers. **(A)** Plastic strawberry. **(B)** Pencil. **(C)** Can of spam. **(D)** Toy peg. **(E)** Plastic banana. **(F)** 3D perspective of the scatter plot. **(G)** 2D perspective of the scatter plot.

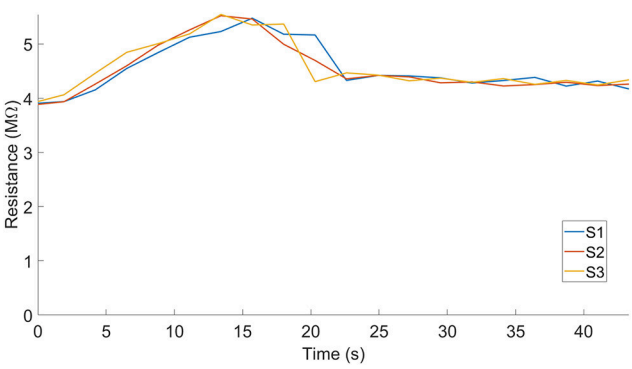

FIGURE 14 | Dynamic sensor readings of the gripper as the fingers close, without an object. S1, S2, and S3 represent each of the sensor readings that the fingers in the gripper produced.

embedded printing of sensors is a powerful process that could enable and enhance seamless integration of sensors into soft robots, but there does not yet exist a suitable, commercially available, easy-to-use platform that allows users to simultaneously print soft actuators and sensors. Because we expect the availability of conductive, commercial 3D printed materials to increase in the future, our focus for the future can shift to further exploring applications that this approach enables. As 3D printing technology improves and decreases in cost, multimaterial and conductive printing will grow increasingly ubiquitous and accessible, further enabling novel methods for integrating sensors into complex bodies.

Multimaterial digital manufacturing has the potential to enable robot designs with not only varying mechanical properties, but also varying electrical properties. This capability enables a whole new design space of sensors embedded in the bodies of soft robots. However, there are currently several practical challenges to applying this method, including interfacing and characterization of material properties. In this paper, we explored some of the above challenges and demonstrated how we can fabricate soft, fully 3D printable machines with embedded sensing.

AUTHOR CONTRIBUTIONS

BS conceptualized the project, designed the experiments, performed characterizations, analyzed the model, interpreted the results, and wrote the paper. CC conceptualized the project, performed characterizations, designed the experiments, and interpreted the results. KG, SL, JM, and ZH refined the

fabrication process and helped with experiments. MT oversaw all activities.

FUNDING

This work was supported by the Office of Naval Research grant number N000141712062 and the National Science Foundation Graduate Research Fellowship Grant No. DGE-1144086.

ACKNOWLEDGMENTS

The authors thank Professor Shengqiang Cai, Zhaoqiang Song, and Qiguang He for instruction and use of the Instron machine; Professor Tina Ng and Dr. Moran Amit for helpful discussion regarding experimental setups for sensor measurements; GrabCAD users Ganagalla Korlayya, Sudhir Gill, and praveen for their open-source drawings; and IEEE for permission to reuse figures and content.

REFERENCES

Bartlett, N. W., Tolley, M. T., Overvelde, J. T., Weaver, J. C., Mosadegh, B., Bertoldi, K., et al. (2015). A 3d-printed, functionally graded soft robot powered by combustion. *Science* 349, 161–165. doi: 10.1126/science.aab0129

Bauer, S., Bauer-Gogonea, S., Graz, I., Kaltenbrunner, M., Keplinger, C., and Schwödiauer, R. (2014). 25th anniversary article: a soft future: from robots and sensor skin to energy harvesters. *Adv. Mater.* 26, 149–162. doi: 10.1002/adma.201303349

Bilodeau, R. A., White, E. L., and Kramer, R. K. (2015). "Monolithic fabrication of sensors and actuators in a soft robotic gripper," in *Intelligent Robots and Systems (IROS), 2015 IEEE/RSJ International Conference on* (Hamburg: IEEE), 2324–2329.

Calli, B., Singh, A., Bruce, J., Walsman, A., Konolige, K., Srinivasa, S., et al. (2017). Yale-cmu-berkeley dataset for robotic manipulation research. *Int. J. Rob. Res.* 36, 261–268. doi: 10.1177/0278364917700714

Cheng, M. Y., Lin, C. L., Lai, Y. T., and Yang, Y. J. (2010). A polymer-based capacitive sensing array for normal and shear force measurement. *Sensors* 10, 10211–10225. doi: 10.3390/s101110211

Conn, A. T., Pearson, M. J., Pipe, A. G., Welsby, J., and Rossiter, J. (2012). "Dielectric elastomer vibrissal system for active tactile sensing," in *Electroactive Polymer Actuators and Devices (EAPAD) 2012*, Vol. 8340 (San Diego, CA: International Society for Optics and Photonics), 83400F.

Connolly, F., Walsh, C. J., and Bertoldi, K. (2017). Automatic design of fiber-reinforced soft actuators for trajectory matching. *Proc. Natl. Acad. Sci. U.S.A.* 114, 51–56. doi: 10.1073/pnas.1615140114

Creton, C., and Ciccotti, M. (2016). Fracture and adhesion of soft materials: a review. *Rep. Progr. Phys.* 79:046601. doi: 10.1088/0034-4885/79/4/046601

Devaraj, H., Giffney, T., Petit, A., Assadian, M., and Aw, K. (2018). The development of highly flexible stretch sensors for a robotic hand. *Robotics* 7, 54. doi: 10.3390/robotics7030054

Drotman, D., Jadhav, S., Karimi, M., and Tolley, M. T. (2017). "3d printed soft actuators for a legged robot capable of navigating unstructured terrain," in *Robotics and Automation (ICRA), 2017 IEEE International Conference on* (Singapore: IEEE), 5532–5538.

Farrow, N., and Correll, N. (2015). "A soft pneumatic actuator that can sense grasp and touch," in *Intelligent Robots and Systems (IROS), 2015 IEEE/RSJ International Conference on* (Hamburg: IEEE), 2317–2323.

Felt, W., Telleria, M. J., Allen, T. F., Hein, G., Pompa, J. B., Albert, K., et al. (2017). An inductance-based sensing system for bellows-driven continuum joints in soft robots. *Robotics* 43, 435–448. doi: 10.1007/s10514-018-9769-7

Felton, S., Tolley, M., Demaine, E., Rus, D., and Wood, R. (2014). A method for building self-folding machines. *Science* 345, 644–646. doi: 10.1126/science.1252610

Florez, J. M., Shih, B., Bai, Y., and Paik, J. K. (2014). "Soft pneumatic actuators for legged locomotion," in *Robotics and Biomimetics (ROBIO), 2014 IEEE International Conference on* (Bali: IEEE), 27–34.

Frutiger, A., Muth, J. T., Vogt, D. M., Mengüç, Y., Campo, A., Valentine, A. D., et al. (2015). Capacitive soft strain sensors via multicore–shell fiber printing. *Adv. Mater.* 27, 2440–2446. doi: 10.1002/adma.201500072

Han, S., Kim, T., Kim, D., Park, Y.-L., and Jo, S. (2018). Use of deep learning for characterization of microfluidic soft sensors. *IEEE Rob. Autom. Lett.* 3, 873–880. doi: 10.1109/LRA.2018.2792684

Homberg, B. S., Katzschmann, R. K., Dogar, M. R., and Rus, D. (2015). "Haptic identification of objects using a modular soft robotic gripper," in *Intelligent Robots and Systems (IROS), 2015 IEEE/RSJ International Conference on* (IEEE), 1698–1705.

Homberg, B. S., Katzschmann, R. K., Dogar, M. R., and Rus, D. (2018). Robust proprioceptive grasping with a soft robot hand. *Auton. Robots* 43, 681–696. doi: 10.1007/s10514-018-9754-1

Ieropoulos, I., Greenman, J., Melhuish, C., and Horsfield, I. (2010). "Ecobot-iii-a robot with guts," in *ALIFE. Proceedings of the Twelfth International Conference on the Synthesis and Simulation of Living Systems*. 733–740.

Kalisky, T., Wang, Y., Shih, B., Drotman, D., Jadhav, S., Aronoff-Spencer, E., et al. (2017). "Differential pressure control of 3d printed soft fluidic actuators," in *Intelligent Robots and Systems (IROS), 2017 IEEE International Conference on* (Vancouver, BC: IEEE).

Kellaris, N., Venkata, V. G., Smith, G. M., Mitchell, S. K., and Keplinger, C. (2018). Peano-hasel actuators: Muscle-mimetic, electrohydraulic transducers that linearly contract on activation. *Sci. Rob.* 3:eaar3276. doi: 10.1126/scirobotics.aar3276

Kim, J., Alspach, A., and Yamane, K. (2015). "3d printed soft skin for safe human-robot interaction," in *Intelligent Robots and Systems (IROS), 2015 IEEE/RSJ International Conference on* (Hamburg: IEEE), 2419–2425.

Kim, Y.-S., Lu, J., Shih, B., Gharibans, A., Zou, Z., Matsuno, K., et al. (2017). Scalable manufacturing of solderable and stretchable physiologic sensing systems. *Adv. Mater.* 29:1701312. doi: 10.1002/adma.201701312

Kumar, K., Liu, J., Christianson, C., Ali, M., Tolley, M. T., Aizenberg, J., et al. (2017). A biologically inspired, functionally graded end effector for soft robotics applications. *Soft Rob.* 4, 317–323. doi: 10.1089/soro.2017.0002

Lipomi, D. J., Vosgueritchian, M., Tee, B. C., Hellstrom, S. L., Lee, J. A., Fox, C. H., et al. (2011). Skin-like pressure and strain sensors based on transparent elastic films of carbon nanotubes. *Nat. Nanotechnol.* 6, 788–792. doi: 10.1038/nnano.2011.184

Lipson, H. (2015). A grand challenge for additive manufacturing: can we print a robot that will walk out of the printer? *3D Print. Addit. Manuf.* 2, 41. doi: 10.1089/3dp.2015.29000.hli

Lipson, H., and Kurman, M. (2013). *Fabricated: The New World of 3D Printing*. Indianapolis, IN: John Wiley & Sons.

MacCurdy, R., Katzschmann, R., Kim, Y., and Rus, D. (2016). "Printable hydraulics: a method for fabricating robots by 3d co-printing solids and liquids," in *Robotics and Automation (ICRA), 2016 IEEE International Conference on* (Stockholm: IEEE), 3878–3885.

Majidi, C. (2014). Soft robotics: a perspective-current trends and prospects for the future. *Soft Rob.* 1, 5–11. doi: 10.1089/soro.2013.0001

Mengüç, Y., Park, Y.-L., Pei, H., Vogt, D., Aubin, P. M., Winchell, E., et al. (2014). Wearable soft sensing suit for human gait measurement. *Int. J. Rob. Res.* 33, 1748–1764. doi: 10.1177/0278364914543793

Miriyev, A., Stack, K., and Lipson, H. (2017). Soft material for soft actuators. *Nat. Commun.* 8, 596. doi: 10.1038/s41467-017-00685-3

Mosadegh, B., Polygerinos, P., Keplinger, C., Wennstedt, S., Shepherd, R. F., Gupta, U., et al. (2014). Pneumatic networks for soft robotics that actuate rapidly. *Adv. Funct. Mater.* 24, 2163–2170. doi: 10.1002/adfm.201303288

Muth, J. T., Vogt, D. M., Truby, R. L., Mengüç, Y., Kolesky, D. B., Wood, R. J., et al. (2014). Embedded 3d printing of strain sensors within highly stretchable elastomers. *Adv. Mater.* 26, 6307–6312. doi: 10.1002/adma.201400334

Park, Y.-L., Chen, B.-R., and Wood, R. J. (2012). Design and fabrication of soft artificial skin using embedded microchannels and liquid conductors. *IEEE Sens. J.* 12, 2711–2718. doi: 10.1109/JSEN.2012.2200790

Park, Y.-L., Majidi, C., Kramer, R., Bérard, P., and Wood, R. J. (2010). Hyperelastic pressure sensing with a liquid-embedded elastomer. *J. Micromech. Microeng.* 20:125029. doi: 10.1088/0960-1317/20/12/125029

Pearson, M. J., Mitchinson, B., Sullivan, J. C., Pipe, A. G., and Prescott, T. J. (2011). Biomimetic vibrissal sensing for robots. *Philos. Trans. R. Soc.* 366, 3085–3096. doi: 10.1098/rstb.2011.0164

Pearson, M. J., Mitchinson, B., Welsby, J., Pipe, T., and Prescott, T. J. (2010). "Scratchbot: Active tactile sensing in a whiskered mobile robot," in *International Conference on Simulation of Adaptive Behavior* (Paris: Springer), 93–103.

Rus, D., and Tolley, M. T. (2015). Design, fabrication and control of soft robots. *Nature* 521, 467–475. doi: 10.1038/nature14543

Scimeca, L., Maiolino, P., and Iida, F. (2018). "Soft morphological processing of tactile stimuli for autonomous category formation," in *2018 IEEE International Conference on Soft Robotics (RoboSoft)* (Livorno: IEEE), 356–361.

Shih, B., Drotman, D., Christianson, C., Huo, Z., White, R., Christensen, H. I., et al. (2017). "Custom soft robotic gripper sensor skins for haptic object visualization," in *Intelligent Robot and Systems (IROS), 2017 IEEE International Conference on* (Vancouver, BC: IEEE).

Shih, B., Mayeda, J., Huo, Z., Christianson, C., and Tolley, M. T. (2018). "3d printed resistive soft sensors," in *2018 IEEE International Conference on Soft Robotics (RoboSoft)* (Livorno: IEEE).

Silvera-Tawil, D., Rye, D., and Velonaki, M. (2015). Artificial skin and tactile sensing for socially interactive robots: a review. *Rob. Auton. Syst.* 63, 230–243. doi: 10.1016/j.robot.2014.09.008

Slesarenko, V., and Rudykh, S. (2017). Towards mechanical characterization of soft digital materials for multimaterial 3d-printing. *Int J Eng Sci.* 123, 62–72. doi: 10.1016/j.ijengsci.2017.11.011

Sonar, H. A., and Paik, J. (2016). Soft pneumatic actuator skin with piezoelectric sensors for vibrotactile feedback. *Front. Rob. AI* 2:38. doi: 10.3389/frobt.2015.00038

Soter, G., Conn, A., Hauser, H., and Rossiter, J. (2018). "Bodily aware soft robots: integration of proprioceptive and exteroceptive sensors," in *2018 IEEE International Conference on Robotics and Automation (ICRA)* (Brisbane, QLD: IEEE), 2448–2453.

Stratasys (2014a). *Objet Support705 sup705 Data Sheet*. Available online at: https://www.stratasys.com/~/media/Main/Files/SDS/Support-Materials/SDS_Objet-Support-SUP705-US.pdf

Stratasys (2014b). *Objet Tangoblackplus flx980 Data Sheet*. Available online at: http://usglobalimages.stratasys.com/Main/Secure/MSDS/Rubber-like%20Materials/DOC-06133-Objet-TangoBlackPlus-FLX980-US.pdf

Stratasys (2014c). *Objet Tangoplus flx980 Data Sheet*. Available online at: http://usglobalimages.stratasys.com/Main/Secure/MSDS/Rubber-like%20Materials/DOC-06128-Objet-TangoPlus-FLX930-US.pdf

Stratasys (2014d). *Objet Veroclear Rgd810 Data Sheet*. Available online at: http://usglobalimages.stratasys.com/Main/Secure/MSDS/Transparent%20Materials/DOC-06119-Objet-VeroClear-RGD810-EU.pdf

Stratasys (2016). *Polyjet Materials Data Sheet*. Available online at: usglobalimages.stratasys.com/Main/Files/Material_Spec_Sheets/MSS_PJ_PJMaterialsDataSheet.pdf

Tee, B. C.-K., Chortos, A., Berndt, A., Nguyen, A. K., Tom, A., McGuire, A., et al. (2015). A skin-inspired organic digital mechanoreceptor. *Science* 350, 313–316. doi: 10.1126/science.aaa9306

Thuruthel, T. G., Shih, B., Laschi, C., and Tolley, M. T. (2019). Soft robot perception using embedded soft sensors and recurrent neural networks. *Sci. Rob.* 4:eaav1488. doi: 10.1126/scirobotics.aav1488

Umedachi, T., Vikas, V., and Trimmer, B. A. (2013). "Highly deformable 3-d printed soft robot generating inching and crawling locomotions with variable friction legs," in *Intelligent Robots and Systems (IROS), 2013 IEEE/RSJ International Conference on* (Tokyo: IEEE), 4590–4595.

Wang, X., Jiang, M., Zhou, Z., Gou, J., and Hui, D. (2017a). 3d printing of polymer matrix composites: a review and prospective. *Composites B* 110, 442–458. doi: 10.1016/j.compositesb.2016.11.034

Wang, Y., Yang, X., Chen, Y., Wainwright, D. K., Kenaley, C. P., Gong, Z., et al. (2017b). A biorobotic adhesive disc for underwater hitchhiking inspired by the remora suckerfish. *Sci. Rob.* 2:eaan8072. doi: 10.1126/scirobotics.aan8072

Wessendorf, A. M., and Newman, D. J. (2012). Dynamic understanding of human-skin movement and strain-field analysis. *IEEE Trans. Biom. Eng.* 59, 3432–3438. doi: 10.1109/TBME.2012.2215859

White, E. L., Yuen, M. C., Case, J. C., and Kramer, R. K. (2017). Low-cost, facile, and scalable manufacturing of capacitive sensors for soft systems. *Adv. Mater. Technol.* 2:1700072. doi: 10.1002/admt.201700072

Yin, J., Santos, V. J., and Posner, J. D. (2017). Bioinspired flexible microfluidic shear force sensor skin. *Sens. Actuators A Phys.* 264, 289–297. doi: 10.1016/j.sna.2017.08.001

Zhang, W., Dehghani-Sanij, A. A., and Blackburn, R. S. (2007). Carbon based conductive polymer composites. *J. Mater. Sci.* 42, 3408–3418. doi: 10.1007/s10853-007-1688-5

Zhao, H., O'Brien, K., Li, S., and Shepherd, R. F. (2016). Optoelectronically innervated soft prosthetic hand via stretchable optical waveguides. *Sci. Rob.* 1:eaai7529. doi: 10.1126/scirobotics.aai7529

Conflict of Interest Statement: The authors declare that the research was conducted in the absence of any commercial or financial relationships that could be construed as a potential conflict of interest.

frontiers in Robotics and AI

TECHNOLOGY REPORT
published: 14 May 2019
doi: 10.3389/frobt.2019.00034

PolyJet-Printed Bellows Actuators: Design, Structural Optimization, and Experimental Investigation

Gabriel Dämmer[1,2]*, *Sven Gablenz*[2], *Alexander Hildebrandt*[2] and *Zoltan Major*[1]

[1] Institute of Polymer Product Engineering, Johannes Kepler University Linz, Linz, Austria, [2] Advanced Mechatronic Systems, Festo AG & Co. KG, Esslingen am Neckar, Germany

Pneumatic bellows actuators are exceptionally suitable for Additive Manufacturing (AM) as the required geometrical complexity can easily be obtained and their functionality is not affected by rough surfaces and small dimensional accuracy. This paper is an extended version of a previously published contribution to the RoboSoft2018 conference in Livorno, Italy. The original paper (Dämmer et al., 2018) contains a simulation-driven design approach as well as experimental investigations of the structural and fatigue behavior of pneumatic multi-material PolyJet™ bellows actuators. This extended version is enhanced with investigations on the relaxation behavior of PolyJet bellows actuators. The presented results are useful for researchers and engineers considering the application of PolyJet bellows actuators for pneumatic robots.

Keywords: additive manufacturing, pneumatic actuator, printed robotics, pneumatic robot, multi-material 3D printing, visco-elastic, design for additive manufacturing (DfAM), structural optimization

OPEN ACCESS

Edited by:
Helmut Hauser,
University of Bristol, United Kingdom

Reviewed by:
Giuseppe Quaglia,
Polytechnic University of Turin, Italy
Alvo Aabloo,
University of Tartu, Estonia

***Correspondence:**
Gabriel Dämmer
gabriel.daemmer@festo.com

Specialty section:
This article was submitted to Soft Robotics, a section of the journal Frontiers in Robotics and AI

Received: *25 November 2018*
Accepted: *15 April 2019*
Published: *14 May 2019*

Citation:
Dämmer G, Gablenz S, Hildebrandt A and Major Z (2019) PolyJet-Printed Bellows Actuators: Design, Structural Optimization, and Experimental Investigation. Front. Robot. AI 6:34. doi: 10.3389/frobt.2019.00034

INTRODUCTION

The design of future robotic systems will be shaped by the demand for a large product variety and short lead times but may at the same time benefit from the constant progress in manufacturing technologies. In this context, multiple opportunities arise from the combination of AM and pneumatic actuation.

A possible approach to increase flexibility in future production processes are human-robot collaboration scenarios, characterized by the immediate proximity of humans and robots. The elimination of safety cages is accompanied by the obligatory demand of physical integrity of human co-workers. By minimizing manipulator link inertia and adding compliant elements in the kinematic chain, hazards inherent to robotic systems can be reduced (Zinn et al., 2004; DIN ISO/TS 15066:2017-04, 2017; Dämmer et al., 2018). AM technologies allow manufacturing of very complex geometries (Clausen et al., 2016) as those obtained by topology optimization, resulting in very light-weight parts. In electro-mechanical drive systems, inherent compliance comes at the cost of a significant increase in mechanical complexity (Lens et al., 2010). This applies in particular to inherently adjustable compliant systems (Grebenstein et al., 2011; Dämmer et al., 2018). Due to the compressibility of air, pneumatic actuators are inherently compliant and can easily be arranged to antagonistic pairs with adjustable compliance (Vanderborght et al., 2013; Baiden and Ivlev, 2014; Veale and Xie, 2016). Recently, the strive for double-acting pneumatic actuators has lead to novel designs that might result in very compact future products (Ferraresi et al., 2014). Moreover, functional integration enabled by AM (Paz et al., 2016) and mechanical simplicity of pneumatic actuators (Hildebrandt, 2009) may result in a reduced number of parts, therefore minimizing efforts

for assembly and logistics. Additionally, in tool-less manufacturing technologies, such as AM, quantities have a reduced effect on manufacturing cost and therefore enhance flexible processes and low batch sizes. However, for the investigation of the expected benefits, suitability of future robotic components for AM is mandatory.

From the perspective of additive manufacturability, bellows actuators are very promising for two reasons. First: Good surface quality and dimensional accuracy that can hardly be achieved by AM technologies (MacCurdy et al., 2016) are not required for the bellows working principle. Second: The complex folded structure exploits the geometrical freedom inherent to AM and actuators performance can easily be modified by shape and material variations. An excellent example of functional integration by additive manufacturing is the Bionic Handling Assistant (Grzesiak et al., 2011) in which additively manufactured bellows structures accommodate external loads and move the robot.

For AM of bellows structures, various technologies have been used, such as selective laser sintering (SLS) (Grzesiak et al., 2011), PolyJet™ printing (PJP) (MacCurdy et al., 2016; Drotman et al., 2017) and Digital Mask Projection Stereolithography (DMP-SL) (Peele et al., 2015). AM of molds for silicone molding of bending actuators was demonstrated in numerous publications (e.g., Mosadegh et al., 2014). Also, detailed reviews of bellows actuators in the context of articulated robotic systems (Gaiser et al., 2012), 3D printing (Zolfagharian et al., 2016) and soft robotics (Polygerinos et al., 2017) have been published.

In the EU founded research project "Digital Materials for 3D Printing" (DIMAP), novel functional materials for PolyJet™ printing were developed (http://www.dimap-project.eu). As an application showcase, PolyJet-printable highly integrated robot components—including bellows actuators—were designed. However, despite of several examples of AM bellows actuators in the context of robotics, there is a lack of knowledge on the achievable performance and simulation-driven design strategies. In addition to that, repeated loadings have recently been related to a significant decrease of the sustainable strains in PolyJet elastomers (Moore et al., 2015).

In the conference paper (Dämmer et al., 2018), pneumatic multi-material PolyJet bellows actuators are presented. Their structural behavior is investigated and compared to structural simulations. In order to improve the actuators performance, bellows design is interpreted as a shape optimization problem with strain minimization as the main objective. Finally, endurance runs are performed to investigate the effects of shape optimization and two different materials on the number of load cycles to failure. Because force responses to imposed displacements were observed to be significantly time dependent, this extended version is enhanced with relaxation tests of elastomeric bellows structures. The relevance of the presented results for the development of a multi-material light-weight gripper is presented demonstrated in another extended version paper (Dämmer et al., 2019). The presented results contribute to the general knowledge concerning the use of PolyJet elastomers for pneumatic actuators and robots.

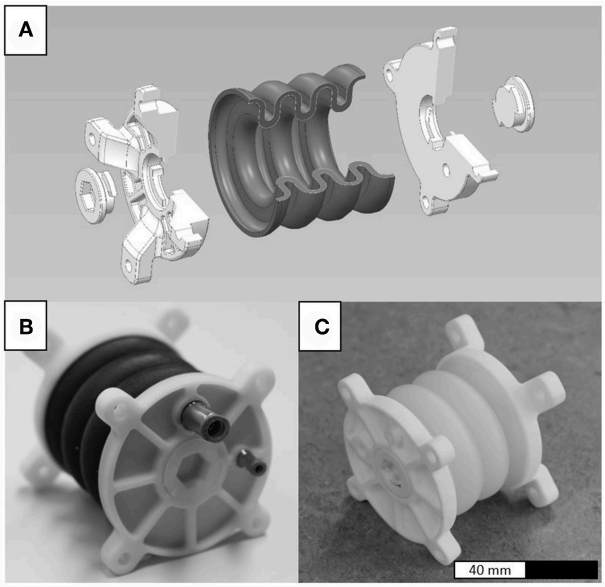

FIGURE 1 | Linear bellows actuators **(A)** obtained by simultaneously printing hard and soft materials. The soft materials TangoBlackPlus™ **(B)** and Agilus30™ **(C)** were used. The total length of the actuators is 78 mm and the outer diameter of the bellows structure is 64.2 mm.

DESIGN

The performance requirements (e.g., force, deflection) and available space for a bellows actuator may vary significantly depending on the intended application and specific design of surrounding components. The bellows actuators described in the following are not intended for the use in a real-life application, but for the understanding of fundamental principles that may be transferred to arbitrary applications. Therefore, PolyJet printable linear bellows actuators (**Figure 1**) were designed that comprise a soft, elastomeric bellows structure and hard, thermosetting flanges. Holes were placed in the flanges to be able to remove the waxlike material that supports overhangs during the printing process (**Figure 1A**).

The bellows structure and flanges are manufactured in one multi-material piece and complemented with closing caps and pneumatic connectors. In this paper, the standard soft material TangoBlackPlus™ (TB+) (**Figure 1B**) and novel soft material Agilus30™ (A30) (**Figure 1C**) are compared. For the flanges, the standard hard material VeroWhitePlus™ (VW+) was used. Actuators containing TB+ (**Figure 1B**) were printed by cirp GmbH (Römerstraße 8, 71296 Heimsheim, Germany), actuators containing A30 (**Figure 1C**) by Stratasys® Ltd. (Haim Holtsman St. 1, 7612401 Rehovot, Israel).

FINITE ELEMENTS ANALYSIS

Preliminary Considerations

In general, linear actuators are used to transform different sources of energy (e.g., electric, pneumatic) into mechanical

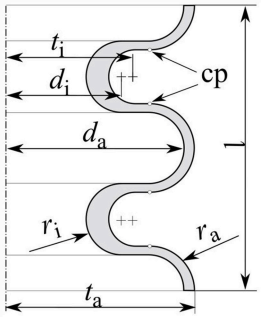

Param	V1/mm	V2/mm
d_a	30	30
r_i	7.5	5.0
r_a	7.5	6.5
t_a	32.0	32.1
t_i	24.5	21.4
d_i	24.5	20.5
l	52	52

FIGURE 2 | Left: parameterization of a u-shaped bellows structure with non-constant wall thickness. Displacements are read out at the control points (cp) to evaluate the distances to adjacent half-waves. Right: parameter values in mm for an initial (V1) and optimized version (V2). Thereby d_a and l are kept constant for comparative analysis of V1 and V2.

energy i.e., create force and translational motion. The usable force (referred to as "effective force") F_{eff} and linear deflection x of a pneumatic bellows actuator are dependent on the bellows geometry and material as well as the pneumatic and mechanical components of the complete actuation system. Assuming quasi-static conditions and frictionless guiding, F_{eff} can be expressed as a function (1) of the pressure force F_p and the structural force F_s. Thereby F_s is caused by the bellows deformation.

$$F_{\text{eff}} = F_p - F_s \tag{1}$$

F_p can easily be determined ($F_p = (\Delta p) \cdot A_{\text{eff}}$) by multiplying the relative pressure Δp ($\Delta p = p_i - p_a$) and the effective area A_{eff} of the actuators flange. The structural force F_s however, is a function of x and Δp (and $\dot{x}$, t if visco-elasticity is considered) and can hardly be computed analytically. Therefore, the following sections describe a geometrical representation and a material model for elastomeric bellows structures for the implementation in finite elements analysis (FEA).

Geometry Representation

The elastic modulus of the flange material is in the range >1,000 MPa (Sheikhnejad et al., 2016), compared to 0,5 MPa for the elastic modulus of the bellows structure (Reiter and Major, 2011). Therefore, deformation of the flange is neglected in the following FEA i.e., the flange is solely represented by boundary conditions at the relevant nodes of the bellows structures mesh. For the bellows structure, an axisymmetric u-shaped design—comprised of parallel lines and semicircles—is chosen. The entire bellows structure with non-constant wall thickness can therefore be unambiguously defined by a planar sketch comprised of 7 design parameters (**Figure 2**, left). Parameter values (in mm) for an initial and optimized version are given in **Figure 2** (right) and will be referred to in the subsequent paragraphs.

Material Model

The structural force F_s, exerted by the deformed bellows structure, originates in the strive of the molecular chains to return to their initial configuration. On a macroscopic level, entropic elasticity in elastomers is typically described by a strain energy function U (Ogden, 1997). In the polynomial form (Equation 2) (Dassault Systemes Simulia Corp., 2014), U is expressed as a function of the first and second invariant (I_1, I_2) of the left Cauchy-Green deformation tensor and—in case of compressibility—of the elastic volume strain J_{el} as

$$U = \sum_{i+j=1}^{N} C_{ij}(I_1 - 3)^i (I_2 - 3)^j + \sum_{i=1}^{N} \frac{1}{D_i}(J_{\text{el}} - 1)^{2i}. \tag{2}$$

Thereby, the material constants C_{ij} and D_i are related to the deviatoric and volumetric material behavior, respectively. For the FE simulations described below, the general polynomial form (Equation 2) is reduced to the first order ($N = 1$) Mooney-Rivlin form for compressible materials (Dassault Systemes Simulia Corp., 2014) in the form of

$$U = C_{10}(I_1 - 3) + C_{01}(I_2 - 3) + \frac{1}{D_1}(J_{\text{el}} - 1)^2. \tag{3}$$

The material constants that are used in the following ($C_{10} = 0.11$ MPa, $C_{01} = 4.52$ MPa, $D_1 = 2.28$ MPa) were determined by fitting the model (Equation 3) to uniaxial tensile and compression test data of TB+ using Abaqus' (Dassault Systèmes) fitting procedure.

EXPERIMENTAL VERIFICATION

In order to validate the FEA of the bellows geometry, an actuator test bench was set up that allows to measure the effective force F_{eff} for given pressures Δp and deflections x. **Figure 3** shows a bellows actuator mounted to the actuator test bench at three displacement states. The applied pressure difference Δp is controlled by a Festo VPPM pressure control valve (0–2 bar), F_{eff} is measured using a Burster 8523-50 force sensor (+/- 0-50 N) and the displacement x is controlled by a Festo EGSA-50-100 linear axis.

In the procedure, displacements were varied between −20 and 30 mm and relative pressures Δp were varied from 0 to 140 mbar in 20 mbar steps. In **Figure 4** the experimental ("Exp.") and simulated ("FEA") force-pressure-deflection characteristics are compared. The effective force was observed to increase for almost 30 s after the final displacements were reached. Therefore, measurements were taken after 30 s (relaxation is investigated closely in paragraph Investigating Relaxation in PolyJet Bellows Actuators). As expected, the effective force F_{eff} exerted by the actuator increases with an increase in relative pressure Δp but decreases (in general) with an increase in deflection x. For negative deflections ($x < 0$), the effective force F_{eff} remains almost constant.

Noticeably, none of the lines covers the full range from −20 up to 30 mm deflection. Extension is limited at lower pressures due to a shift in the static force equilibrium (Equation 1). Compression is limited at higher pressures because the waves of the bellows geometry tend to touch adjacent waves ("self-contact"). Whereas, results from FEA are generally in good accordance with the experimental results, **Figure 4** indicates, that deviations increase as a result of high pressures or elongations.

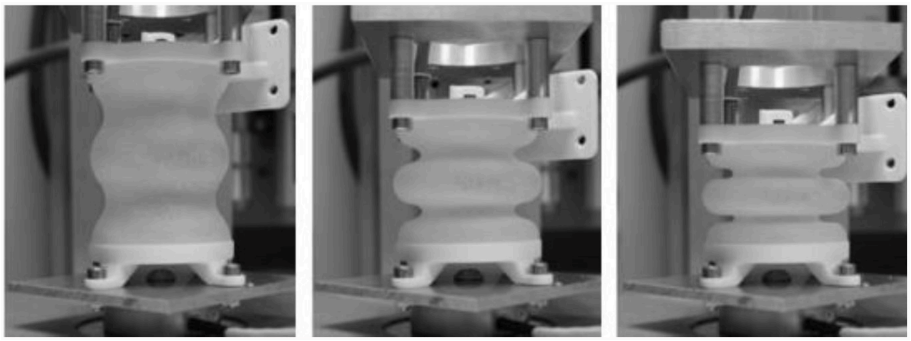

FIGURE 3 | Measuring the effective force F_{eff} of a linear bellows actuator. Three displacement states were tested i.e., extension (left), initial (middle) and compression (right) state. Excessive extensions lead to large strains and structural failure, compression is limited due to self-contact of adjacent half-waves.

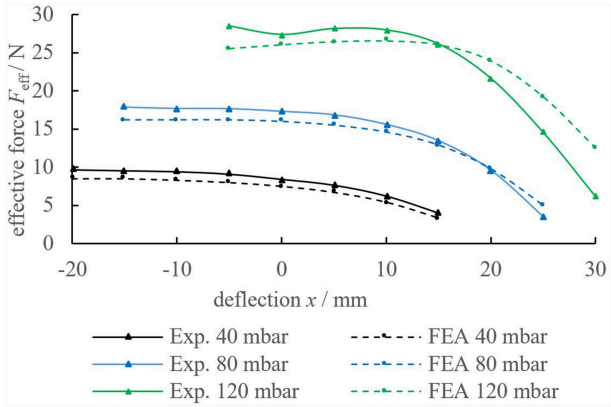

FIGURE 4 | Comparison of the experimental (solid lines) and simulated (dotted line) results of the pressure and displacement dependent effective force F_{eff}. Simulations are generally in good agreement with the experimental results. Note, that lines between measuring points are interpolated.

This is most possibly due to the fitting range of the constitutive model. For improved accordance of simulation and experiment, material tests covering multi-axial states of stress and time-dependency are advised.

OPTIMIZATION OF BELLOWS GEOMETRY

Bellows Optimization Problem

In the following paragraph an exemplary problem is solved but the shown methods are easily modifiable to other problems. In the experiments described above, repeated loadings lead to cracks in the bellows structure which can be explained by fatigue. In repeatedly strained elastomers (Gent et al., 1964; Lake and Lindley, 1964) material imperfections—also typical for AM materials (Moore et al., 2015)—cause local strain peaks that lead to the formation and propagation of microscopic cracks and eventually result in fatigue failure. To find an improved bellows design (V2), that reaches similar effective force F_{eff} and deflection x as the initial geometry (V1) but sustains an increased number of load cycles, a numerical optimization routine was developed. Thereby, maximum (logarithmic) principal strain $\varepsilon_{\text{ln, max}}$ was considered as a fatigue life indicator (Zhou, 2016) in the strain objective function

$$Q_{\varepsilon}(x) = (\varepsilon_{\text{ln, max}}(x) - \varepsilon_{\text{max}})^2. \tag{4}$$

Designs x that lead to simulated strains $\varepsilon_{\text{ln, max}}$ larger than a reference strain ε_{max} are penalized with large objective function values. To achieve a required deflection while avoiding self-contact, the penalty functions $Q_{\text{ld}}(x)$ and $Q_{\text{sc}}(x)$ were stated analogous to $Q_{\varepsilon}(x)$ and added up to a multi-criteria objective function

$$Q(x) = w_{\varepsilon} \cdot Q_{\varepsilon}(x) + w_{\text{ld}} \cdot Q_{\text{ld}}(x) + w_{\text{sc}} \cdot Q_{\text{sc}}(x) \tag{5}$$

with w_{ε}, w_{ld}, and w_{sc} being associated weighting factors for the compensation of units. The required effective force F_{eff} is implemented as a hard constraint which requires Δp to be variable. The bellows structures length and effective area of the flanges were kept constant to be able to compare the effect of the optimization. A bellows design is therefore fully described by the design vector

$$x = [r_{\text{i}} \; r_{\text{a}} \; t_{\text{i}} \; t_{\text{a}} \; d \; \Delta p]^{\text{T}} \tag{6}$$

In addition, an (even) integer parameter n_{hw} is defined to quantify the number of half-waves that describe the bellows structure. Bounds and secondary constraints are defined (their exhaustive description is beyond the scope of this paper) in a constraint vector $g(n_{hw}, x)$ to exclude infeasible geometries. Therefore, and following (Mahl, 2015) the constraint mixed integer bellows optimization problem is

$$\min_{n_{\text{hw}}} \left\{ \min_{x} \left\{ Q(n_{\text{hw}}, x) \middle| g(n_{\text{hw}}, x) \leq 0 \right\} \right\}. \tag{7}$$

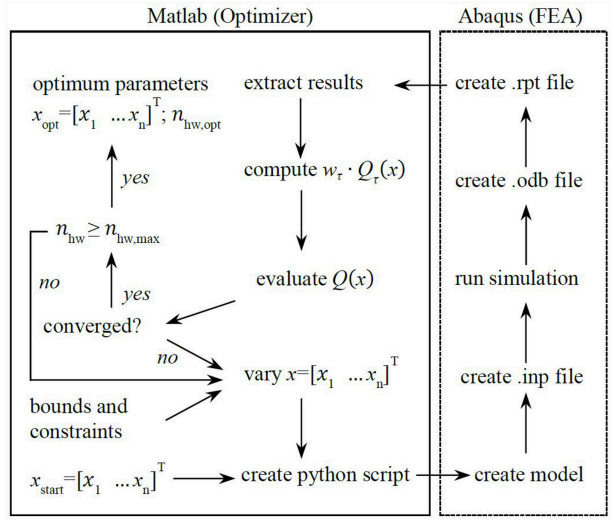

FIGURE 5 | Optimization routine for the optimization of linear bellows actuators. The routine finds optimum geometry parameters and relative pressure to generate a required effective force at required displacement while minimizing the maximum principal strain in the bellows structure.

Optimization Results and Verification

An optimization routine was realized to solve the above stated optimization problem based on the structural simulation and parameterization described above. Matlab (MathWorks) and Abaqus (Dassault Systèmes) were connected and software communication was realized by python scripts (**Figure 5**). The routine starts with the initial parameters x_{start} and $n_{hw,\,start}$ and terminates with the optimum parameters x_{opt} and $n_{hw,\,opt}$. The gradient based Matlab optimization function *fmincon* (default settings) was chosen for convenient implementation of bounds and secondary constraints. The optimization routine was run considering a maximum strain reference of $\varepsilon_{max} = 0.2$ and a force requirement of 12 N at 30 mm linear deflection.

Figure 6 illustrates the simulated max. principal strain distribution of the initial (V1) and the optimized bellows geometry (V2). The corresponding shape parameters are given in **Figure 2** (right). The initial geometry (V1) is described by four half-waves with constant wall thickness. To reach an effective force of 12 N at 30 mm deflection, 140 mbar are required that induce a (simulated) maximum principal strain of 65%. The optimized geometry (V2) consists of six instead of four half-waves and a non-constant wall thickness. At a linear deflection of 30 mm and an applied pressure of 100 mbar, the effective force is above 12 N and the simulated max. principal strain 24%.

In **Figure 7** the pressure-force-deflection characteristics of the initial (V1) and optimized (V2) geometry are compared. For the optimized geometry (dotted lines), the effective force is significantly less dependent on the deflection, i.e., lower pressures are sufficient to generate comparatively high forces at large displacements. Considering **Figure 6** in conjunction with Equation (1), it can be concluded, that the loss of effective force for increasing deflections is caused by the increasing strain in the material.

The optimized geometry (V2) satisfies the force-displacement requirements of 12 N at 30 mm. Moreover, the significant reduction of the simulated maximum principal strain (24% instead of 64%) in conjunction with fatigue data from literature (Moore et al., 2015) gives rise to assume an increased fatigue life of the new bellows geometry (V2) compared to the initial geometry (V1).

ENDURANCE RUN

Endurance runs were performed to validate the hypothesis predicting increased fatigue life of the optimized geometry and for comparison of TB+ with a novel material. Agilus30™ (A30) is a recently released PolyJet elastomer with similar hardness range (Shore A 30–35 compared to 26–28 for TB+) as well as an increased elongation at break and tear resistance (Stratasys, Ltd.). Due to superior properties in the data-sheet (Stratasys, Ltd.), an increased fatigue life, compared to TB+, was expected. It is pointed out that the same geometries and material parameters were used for both the TB+ and A30 bellows because no sufficient material data of A30 was available at this time. Therefore, A30 results should be interpreted with care and are presented for comparative purposes.

Figure 8 illustrates a bellows actuator mounted to the endurance test bench. During the test, the left side of the bellows actuator can move freely in horizontal direction and is guided by four PTFE-lubricated guiding bolts. In the endurance runs, a pressure of 140 mbar for V1 and 100 mbar for V2 was applied for 30 s. The resulting deflection was mechanically restrained to 30 mm.

Pressure was then released for another 30 s before the procedure was repeated. Volume flow was measured during the 30 s period to detect possible damage of the bellows and the experiment was stopped in case a threshold value of 2 Nl/min was exceeded.

Figure 9 contains the load cycles to failure that were reached by the bellows actuators. Cycles to failure range from below 20 (TB+, V1) to more than 30,000 (A30, V2). In average, A30 bellows with the initial geometry (V1) endured 143 load cycles and with the optimized geometry (V2) 24,104 load cycles. Even without statistical significance, the results strongly indicate that the optimized geometry (V2) sustains significantly more load cycles until failure compared to the initial geometry (V1). Moreover, we can assume that bellows made from A30 endure significantly more load cycles to failure compared to ones manufactured from TB+.

Noticeably, different geometries lead to different but consistent modes and locations of failure. Thereby, two categories can be made for failures as shown in **Figure 10**. All specimens of the initial geometry (V1) failed at the inner wave due to cracks in axial direction (**Figure 10**, left). In the corresponding FEA max. principal strains are oriented in tangential direction at the inner diameter i.e., perpendicular to the cracks. Specimens of the optimized geometry (V2) consistently failed in tangential direction (i.e., perpendicular

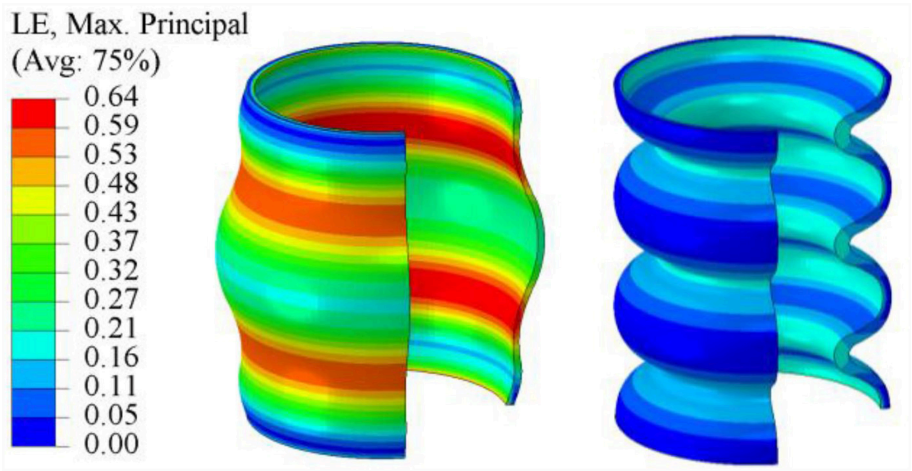

FIGURE 6 | Simulated max. principal strain distribution of the initial geometry V1 (left) and optimized geometry V2 (right).

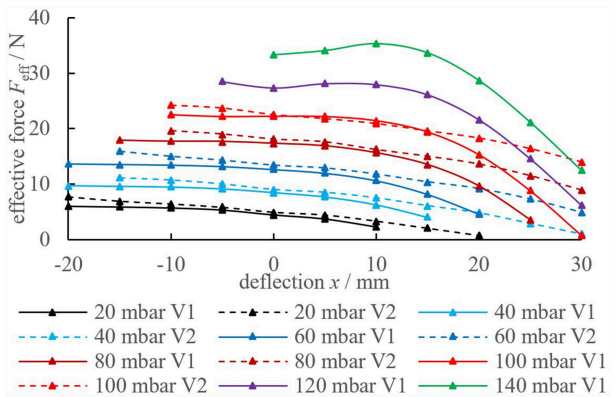

FIGURE 7 | Comparison of the experimental pressure-force-deflection characteristics of the initial (V1, solid lines) vs. the optimized (V2, dotted lines) geometry. The optimized geometry (V2) requires less pressure to produce the required forces at large deflections which is a result of max. principal strain minimization. Lines between measuring points are interpolated.

to axial strains) near to the flanges as illustrated in **Figure 10** (right). Location and direction of failure are consistent with the simulated max. principal strain distribution obtained from FEA.

There are multiple possibilities to further increase the fatigue life of the bellows actuators described above. The specific geometric representation as described in **Figure 2** presents a compromise between the dimensions (and size) of the solution space and cost (time for development of the routine itself and computation time). Further optimization could be realized by choosing a more complex parameterization. Note, that the rotationally symmetric design was chosen here in order to minimize the dimensions of the optimization problem. If this simplification is omitted, the effective flange area could be increased without an increase in the main dimensions of the actuator.

INVESTIGATING RELAXATION IN POLYJET BELLOWS ACTUATORS

Motivation for Investigating the Relaxation in PolyJet Bellows Actuators

The accuracy of a pneumatic robotic system depends in many cases on the accuracy with which its actuators are modeled. This is, because in state-of-the-art model-based controllers a physical model of the system is utilized to compute the desired pressures. In bellows actuators, the pressurization or forced motion of the actuator implies a deformation of the bellows structure i.e., different pressure or motion profiles result in different strains/strain rates in the bellows material. Depending on the specific application or task of a light-weight robot, cycle times may range from fractions of a second to several seconds or minutes. During the experiments described in the previous paragraphs we experienced that the PolyJet printed bellows react significantly time dependent to applied pressures and forced deformations. In paragraph Experimental Verification, this fact was accounted for by waiting until the force responses of the structures had stabilized (i.e., 30 s in **Figures 4**, **7**) before measurements were taken. However, this procedure is impractical for an actual robotic application and implications for structural simulation have to be evaluated. Thereby, time dependent mechanical behavior is typical for elastomeric structures (Saccomandi and Ogden, 2004; Bergström, 2015) and originates mainly from the rearrangement of the molecular chains (entropic elasticity) induced by deformation. Several publications confirm our qualitative experiences concerning the time dependency of PolyJet materials in general (Blanco et al., 2014; Zhang and Albert, 2016) and—most important—the PolyJet elastomers TangoBlack™ (a predecessor of TB+) (Kundera and Bochnia, 2014), and A30 (Akbari et al., 2018). However, to our knowledge no closer investigations on the time dependent behavior of A30 bellows structures were published yet. Therefore, in the following paragraphs the relaxation behavior of A30 bellows structures is investigated. Results are intended to

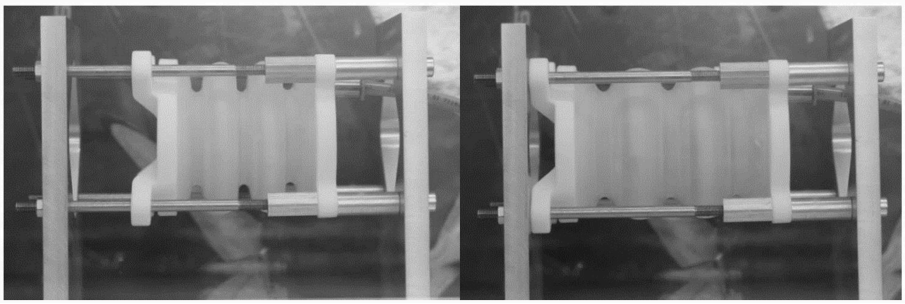

FIGURE 8 | Endurance runs with bellows actuators. Initial state (left) and extension state (right). Extension is mechanically limited to 30 mm. The experiment was stopped in case a threshold volume flow was reached.

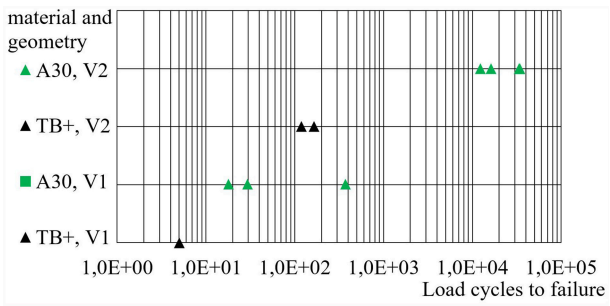

FIGURE 9 | Load cycles to failure of different bellows actuators. Best results are obtained from the combination of Agilus30™ (A30) and geometry variant 2 (V2). Each data corresponds to a single endurance run.

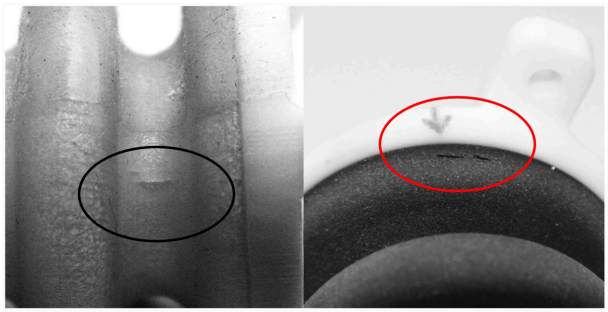

FIGURE 10 | Cracks in the bellows structure are oriented in axial direction at the inner diameter of the initial geometry "V1" (left) and tangential direction next to the flange of the optimized geometry "V2" (right) which is in accordance with the locations and perpendicular to the directions of max. principal strain in the corresponding FEA.

make an initial assessment of the significance of time dependency for (soft) robotic applications and will be used for the validation of visco-elastic material models in the future.

Redesign of Bellows Actuators for Relaxation Testing

In order to increase cost-efficiency, new test geometries (**Figure 11**) were designed that are considerably smaller (total length of 22 mm instead of 78 mm) than the ones described in Design. Regarding future research, a simple bellows geometry with two halve waves was chosen that can also be molded using a two-part core (e.g., for silicone molding).

The soft bellows structure (yellow) is printed together with two rigid square shaped flanges (white). Circular end caps (white) are printed separately and mounted after the support material is removed from the bellows chamber. The bellows actuators were printed by cirp GmbH (Römerstraße 8, 71296 Heimsheim, Germany). All parts investigated in paragraph Investigating Relaxation in PolyJet Bellows Actuators were printed with matte finish and oriented with the main axis parallel to the printing platform.

Experimental Setup and Relaxation Testing Procedure

Two load cases were applied, in order to investigate the relaxation behavior of the bellows actuators (**Figure 11**).

Load case "Deflection": starting from the initial length of the actuator (22 mm), the upper flange was pulled with a rate of 8 mm/s until a linear deflection of 4 mm was reached. The deflection was maintained for 90 s and the (retracting) force exerted by the deflected actuator was monitored. No pressure differential was applied in load case "Deflection".

Load case "Pressurization": starting from ambient pressure in the bellows actuator, a pressure step of +0.4 bar was applied by quickly opening a shut-off valve. Deflection was completely suppressed and the increased relative pressure was maintained for at least 90 s. The exerted force of the pressurized actuator was monitored. In order to apply the described loads and monitor the applied and resulting parameters, a test setup (**Figure 12**, left) was build up. Pneumatic hoses were attached to the actuators (**Figure 12**, right) to connect the pressure supply and sensor.

The test bench (Bose Corp., ElectroForce Systems Group, MN, US) comprises a linear actuator for monotonic tests, a WMC-25 load cell (Interface Inc. AZ, US) and a controller unit and workstation. WinTest® DMA software (Bose Corp.) was utilized to perform and analyze the experiments. For presetting and applying the preselected pressure, a Festo LRP-1/4-4 precision pressure (Festo AG & Co. KG, GER) regulator and a manual Festo shut-off valve were used. Pressure was measured using a Keller 21 PY (Keller AG, CH) pressure transmitter.

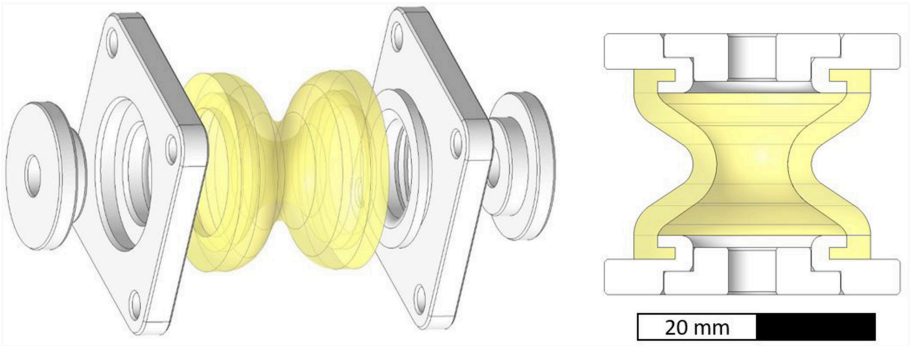

FIGURE 11 | Exploded (left) and sectional (right) view of PolyJet printed bellows structure for relaxation testing. The bellows (yellow) and square shaped flanges (white) are printed into one multi-material part.

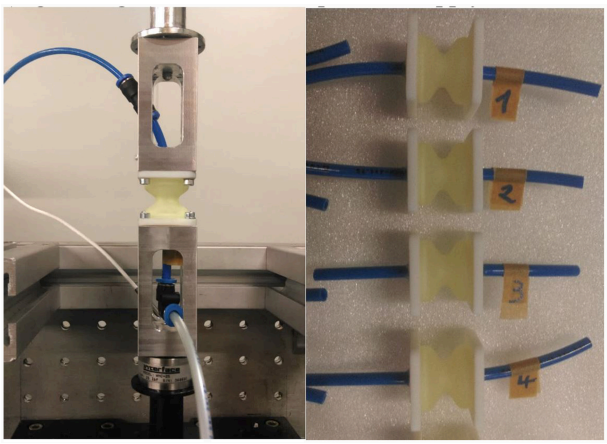

FIGURE 12 | Relaxation tests with A30 bellows actuators. Left: pneumatic actuator mounted to the test bench, air hoses for pressure supply/sensor and load cell. Right: bellows actuators tested for this publication.

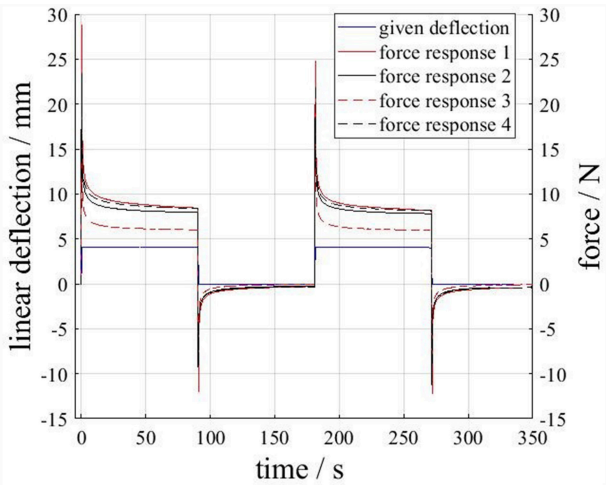

FIGURE 13 | Actuator force responses due to an applied deflection. The applied deflection profile is plotted (blue) for the first test run only, but is virtually the same for the other test runs.

TABLE 1 | Sequence of relaxation tests.

Nr.	Test 1	Test 2	Test 3	Test 4
1	Pressurization	Pressurization	Deflection	Deflection
2	Pressurization	Pressurization	Deflection	Deflection
3	Deflection	Deflection	Pressurization	Pressurization
4	Deflection	Deflection	Pressurization	Pressurization

A total of four equal specimen was tested. Thereby, each specimen was tested two consecutive times in one load case. The testing sequence was varied according to **Table 1** in order to account for possible irreversible effects, such as plastic deformation or cracks.

Results and Interpretation

Figure 13 displays the given deflection and force responses of the four actuators in the load case "Deflection". As can be seen, the rapidly applied displacement (4 mm in 0,5 s) leads to pronounced peak forces for all actuators. During times of constant displacement, the amount of the actuator forces decreases and asymptotically approaches a plateau. The retraction of the test bench to the initial length causes an opposed force. Whereas, the force responses of the actuators 1,2 and 4 are similar, the force response of actuator 3 differs significantly in amplitude.

In **Figure 14** the force responses of the four actuators in the load case "pressurization" are displayed. The rapidly applied pressure step (+0.4 bar; plotted for the test with the first actuator only) leads to a nominal increase in actuator force. During the intervals of constant pressure, the force responses asymptotically approach a plateau. The force response of actuator 3 is significantly larger (in amount) than the other responses. The reason for this deviation is not known. However, in combination with the results from **Figure 13** it can be concluded, that actuator 3 poses less resistance to applied loads (i.e., has a "softer" structure) which results in a lower measured force under deflection but a

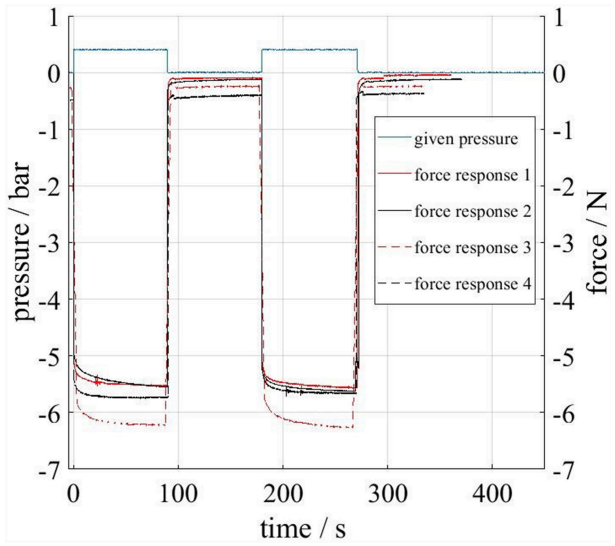

FIGURE 14 | Actuator force responses due to an applied pressure. For the sake of clarity, the applied pressure profile is plotted (blue) for the test run with the first actuator only.

larger measured force amount under pressurization. Further investigations including larger numbers of specimen have to clarify this.

Nevertheless, two interesting observations can be made from **Figures 13**, **14**. First: all force responses are significantly time dependent, e.g., peak forces in **Figure 13** reach over 20 N but decrease quickly below 10 N. Second: the deliberate pre-stretching during the loadcases applied in our tests seems to have little effect on the structures stiffnesses in subsequent tests. This can be concluded from the fact that consecutive tests lead to similar force responses (**Figures 13**, **14**) and that no clear distinction can be made between pre-stretched and non-pre-stretched actuators in **Figure 13**. The observed time dependency is typical for elastomers and in line with our qualitative expectations. However, the described results may be used to build mathematical models of the actuators time dependent behavior and serve as a starting point for standardized cyclic and rate dependent tests for the calibration of visco-elastic material models.

For the FEA and optimization of the bellows actuators in paragraphs Finite Elements Analysis–Optimization of Bellows Geometry, the constitutive behavior was modeled as time independent which represents a major simplification considering the results presented in this paragraph. In this context it is also important to note, that all presented data regarding strain is simulative and we have no evidence of the actual level of strains in the structure. However, the results of the endurance runs in paragraph Endurance Run proof, that the shape optimization lead to an significantly increased fatigue life. Moreover, the comparison of simulative strain maxima (**Figure 6**) and experimental failure modes and locations (**Figure 10**) indicates a good significance of the FEA considering the qualitative strain distribution in the structure.

CONCLUSION

Additively manufactured bellows actuators pose an interesting option for the actuation of future robotic systems as their structural behavior is highly tunable by shape and material. This paper contains the design, shape optimization and experimental investigations of pneumatic PolyJet bellows actuators. First, multi-material bellows actuators were designed using VeroWhitePlus^{TM} material for the rigid flanges and TangoBlackPlus^{TM} (TB+)/Agilus30^{TM} (A30) for the soft bellows structure. Then, the bellows structural behavior was analyzed by finite elements analysis. A numerical optimization strategy was developed and the effect of geometry optimization and material selection on the sustainable number of load cycles was investigated. Results strongly indicate that the proposed design strategy—based on a multi-criteria optimization routine—leads to significantly improved fatigue life. Moreover, A30 bellows withstood significantly higher numbers of repeated loadings than TB+ bellows. Modes and locations of failure largely correspond with finite elements analysis. In this extended version, the better performing material (A30) was investigated more closely. Therefore, relaxation test were carried out using redesigned test structures. The findings confirm the significance of time dependency of A30 material behavior. Results contribute to the understanding of the mechanical behavior of PolyJet elastomers under static, dynamic and repeated loadings, such as present in printed robots.

AUTHOR CONTRIBUTIONS

GD coordinated the activities at Festo regarding mechanics in the DIMAP project. This included literature research, coordinating the tests, interpreting the results as well as planning and writing the conference paper and extended version. SG realized the shape optimization routine and component tests for the conference paper. AH supported the DIMAP project at Festo and coordinated the activities regarding feedback control for the paper. ZM initiated the DIMAP project at IPPE and coordinated all material and component tests at IPPE.

ACKNOWLEDGMENTS

The authors thank for the opportunity to be involved in the DIMAP project funded as part of the Horizon 2020 program (GA 685937). Moreover, we thank the responsible persons of the 2018 IEEE International conference on Soft Robotics (RoboSoft) for the permission to reuse the content of the conference paper (Dämmer et al., 2018). We thank Michael Lackner and Gerhard Wurzinger from the Institute of Polymer Product Engineering (IPPE) for realizing the experiments described in paragraph Investigating Relaxation in PolyJet Bellows Actuators at the JKU, Linz.

REFERENCES

Akbari, S., Sakhaei, A. H., Kowsari, K., Yang, B., Serjouei, A., Yuanfang, Z., et al. (2018). Enhanced multimaterial 4D printing with active hinges. *Smart Mater. Struct.* 27:065027. doi: 10.1088/1361-665X/aabe63

Baiden, D., and Ivlev, O. (2014). "Independent torque and stiffness adjustment of a pneumatic direct rotary soft-actuator for adaptable human-robot-interaction," in *Proc. 23rd International Conference on Robotics in Alpe-Adria-Danube Region (RAAD)* (Smolenice).

Bergström, J. S. (2015). *Mechanics of Solid Polymers: Theory and Computational Modeling*. William Andrew Publishing.

Blanco, D., Fernandez, P., and Noriega, A. (2014). Nonisotropic experimental characterization of the relaxation modulus for PolyJet manufactured parts. *J. Mater. Res.* 29, 1876–1882. doi: 10.1557/jmr.2014.200

Clausen, A., Aage, N., and Sigmund, O. (2016). Exploiting additive manufacturing infill in topology optimization for improved buckling load. *Engineering.* 2, 250–257. doi: 10.1016/J.ENG.2016.02.006

Dämmer, G., Gablenz, S., Hildebrandt, A., and Major, Z. (2018). "Design and shape optimization of PolyJet bellows actuators," in *Proceedings of 2018 IEEE International Conference on Soft Robotics (RoboSoft)* (Livorno).

Dämmer, G., Gablenz, S., Hildebrandt, A., and Major, Z. (2019). Design of an Additively Manufacturable Multi-Material Light-Weight Gripper with integrated Bellows Actuators. *Advances in Science, Technology and Engineering Systems Journal* 4, 23–33. doi: 10.25046/aj040204

Dassault Systemes Simulia Corp. (2014). *Abaqus Theory Guide*. Version 6.14.

DIN ISO/TS 15066:2017-04 (2017). *Robots and Robotic Devices–Collaborative Robots.* Geneva: International Organization for Standardization.

Drotman, D., Jadhav, S., Karimi, M., Tolley, M. T., et al. (2017). "3D printed soft actuators for a legged robot capable of navigating unstructured terrain," in *Proc. 2017 IEEE International Conference on Robotics and Automation (ICRA)* (Singapore), 5532-5538.

Ferraresi, C., Franco, W., and Quaglia, G. (2014). A novel bi-directional deformable fluid actuator. *J. Mech. Eng. Sci.* 228, 2799–2809. doi: 10.1177/0954406214522022

Gaiser, I., Andres, A., Bretthauer, G., Breitwieser, H., Ivlev, O., Wiegand, R., et al. (2012). *Compliant Robotics and Automation With Flexible Fluidic Actuators and Inflatable Structures*. London: INTECH Open Access Publisher. doi: 10.5772/51866

Gent, A. N., Lindley, P. B., and Thomas, A. G. (1964). Cut growth and fatigue of rubbers. I. The relationship between cut growth and fatigue. *J. Appl. Polym. Sci.* 8, 455–466. doi: 10.1002/app.1964.070080129

Grebenstein, M., Albu-Schäffer, A., Bahls, T., Chalon, M., Eiberger, O., Friedl, W., et al. (2011). "The DLR hand arm system," in *Proc. 2011 IEEE International Conference on Robotics and Automation (ICRA)* (Shanghai), 3175–3182.

Grzesiak, A., Becker, R., and Verl, A. (2011). The bionic handling assistant: a success story of additive manufacturing. *Assem. Autom.* 31, 329–333. doi: 10.1108/01445151111172907

Hildebrandt, A. (2009). *Regelung und Auslegung servopneumatischer Aktuatorsysteme*. Dissertation, University of Stuttgart.

Kundera, C., and Bochnia, J. (2014). Investigating the stress relaxation of photopolymer O-ring seal models. *Rapid Prototyp. J.* 20, 533–540. doi: 10.1108/RPJ-04-2013-0043

Lake, G. J., and Lindley, P. B. (1964). Cut growth and fatigue of rubbers. II. Experiments on a noncrystallizing rubber. *J. Appl. Polym. Sci.* 8, 707–721. doi: 10.1002/app.1964.070080212

Lens, T., Kunz, J., Von Stryk, O., Trommer, C., and Karguth, A. (2010). "Biorob-arm: A quickly deployable and intrinsically safe, light-weight robot arm for service robotics applications," in *Proc. 41st International Symposium on Robotics (ISR) and 6th German Conference on Robotics (ROBOTIK)* (Berlin), 905–910.

MacCurdy, R., Katzschmann, R., Youbin, K., and Rus, D. (2016). "Printable hydraulics: a method for fabricating robots by 3D co-printing solids and liquids," in *Proc. 2016 IEEE International Conference on Robotics and Automation (ICRA)*.

Mahl, T. (2015). *Strukturmechanische Optimierung, Modellierung und Regelung pneumatisch aktuierter kontinuierlicher Roboter*. Dissertation, University of Stuttgart.

Moore, J., P., and Williams, C. B. (2015). Fatigue properties of parts printed by PolyJet material jetting. *Rapid Prototyp. J.* 21, 675–685. doi: 10.1108/RPJ-03-2014-0031

Mosadegh, B., Polygerinos, P., Keplinger, C., Wennstedt, S., Shepherd, R., and, F., et al. (2014). Pneumatic networks for soft robotics that actuate rapidly. *Adv. Funct. Mater.* 24, 2163–2170. doi: 10.1002/adfm.201303288

Ogden, R. W. (1997). *Non-linear Elastic Deformations*. Mineola, NY: Dover Publications, Inc.

Paz, R., Monzón, M. D., Benítez, A., N., and González, B. (2016). New lightweight optimisation method applied in parts made by selective laser sintering and Polyjet technologies. *Int. J. Comput. Integr. Manufac.* 29, 462–472. doi: 10.1080/0951192X.2015.1066033

Peele, B. N., Wallin, T., J., Zhao, H., and Shepherd, R. F. (2015). 3D printing antagonistic systems of artificial muscle using projection stereolithography. *Bioinspiration Biomim.* 10:055003. doi: 10.1088/1748-3190/10/5/055003

Polygerinos, P., Correll, N., Morin, S., A., Mosadegh, B., Onal, C. D., et al. (2017). Soft robotics: review of fluid-driven intrinsically soft devices; manufacturing, sensing, control, and applications in human-robot interaction. *Adv. Eng. Mater.* 19:1700016. doi: 10.1002/adem.201700016

Reiter, M., and Major, Z. (2011). A combined experimental and simulation approach for modelling the mechanical behaviour of heterogeneous materials using rapid prototyped microcells. *Virtual Phys. Prototyp.* 6, 111–120. doi: 10.1080/17452759.2011.586949

Saccomandi, G., and Ogden, R. W. (2004). *Mechanics and Thermomechanics of Rubberlike Solids*. Wien: Springer-Verlag Wien GmbH.

Sheikhnejad, O., Hiptmair, F., and Major, Z. (2016). "Finite element simulation and mechanical modelling of nanoparticles reinforced composite," in *Proc. 6th International Conference on Additive Technologies* (Nürnberg).

Stratasys, Ltd. (2017). *PolyJet Materials DataSheet*. Available online at: http://usglobalimages.stratasys.com/Main/Files/Material_Spec_Sheets/MSS_PJ_PJMaterialsDataSheet.pdf?v=635785205440671440 (accessed February 26, 2018).

Vanderborght, B., Albu-Schäffer, A., Antonio, A., Burdet, E., Caldwell, D., and, G., et al. (2013). Variable impedance actuators: a review. *Robot. Autonom. Syst.* 61, 1601–1614. doi: 10.1016/j.robot.2013.06.009

Veale, A. J., and Xie, S. Q. (2016). Towards compliant and wearable robotic orthoses: a review of current and emerging actuator technologies. *Med. Eng. Phys.* 38, 317–325. doi: 10.1016/j.medengphy.2016.01.010

Zhang, P., and Albert, A. C. (2016). Transversely isotropic hyperelastic-viscoplastic model for glassy polymers with application to additive manufactured photopolymers. *Int. J. Plast.* 80, 56–74. doi: 10.1016/j.ijplas.2015.12.012

Zhou, Y. (2016). *Fatigue Properties of Magnetorheological Elastomers and The Design of Interfacial Layers to Improve Fatigue Life*. Ph.D. thesis, Dublin Institute of Technology.

Zinn, M., Roth, B., Khatib, O., and Salisbury, J. K. (2004). A new actuation approach for human friendly robot design. *Int. J. Robot. Res.* 23, 379–398. doi: 10.1177/0278364904042193

Zolfagharian, A., Kouzani, A., Z., Khoo, S., Y., Moghadam, A. A., et al. (2016). Evolution of 3D printed soft actuators. *Sensors Actuators.* 250, 258–272. doi: 10.1016/j.sna.2016.09.028

Conflict of Interest Statement: During the period in which the described work was done, GD, SG, and AH were employed by Festo AG. & Co. KG., Esslingen, Germany and ZM was employed by Johannes Kepler University, Linz, Austria. Stratasys, PolyJet, TangoBlackPlus, TangoBlack, VeroWhitePlus, and Agilus30 are trademarks of the company Stratasys Ltd. (Rehovot, Israel) in some countries.

frontiers in Robotics and AI

ORIGINAL RESEARCH
published: 24 May 2019
doi: 10.3389/frobt.2019.00040

Evaluation of 3D Printed Soft Robots in Radiation Environments and Comparison With Molded Counterparts

Osman Dogan Yirmibeşoğlu[1], Tyler Oshiro[2], Gina Olson[1], Camille Palmer[2] and Yigit Mengüç[1]*

[1] Collaborative Robotics and Intelligent Systems Institute, Oregon State University, Corvallis, OR, United States, [2] School of Nuclear Science and Engineering, Oregon State University, Corvallis, OR, United States

Robots have an important role during inspection, clean-up, and sample collection in unstructured radiation environments inaccessible to humans. The advantages of soft robots, such as body morphing, high compliance, and energy absorption during impact, make them suitable for operating under extreme conditions. Despite their promise, the usefulness of soft robots under a radiation environment has yet to be assessed. In this work, we evaluate the effectiveness of soft robots fabricated from polydimethylsiloxane (PDMS), a common fabrication material, under radiation for the first time. We investigated gamma-induced mechanical damage in the PDMS materials' mechanical properties, including elongation, tensile strength, and stiffness. We selected three radiation environments from the nuclear industry to represent a wide range of radiation and then submerged a 3D printed hexapus robot into a radiation environment to estimate its operation time. Finally, to test the reliability of the 3D printed soft robots, we compared their performances with molded counterparts. To analyze performance results in detail, we also investigated dimensional errors and the effects of fabrication methods, nozzle size, and print direction on the stiffness of PDMS material. Results of this study show that with increasing exposure to gamma irradiation, the mechanical properties of PDMS decrease in functionality but are minimally impacted up to 20 kGy gamma radiation. Considering the fractional changes to the PDMS mechanical properties, it is safe to assume that soft robots could operate for 12 h in two of the three proposed radiation environments. We also verified that the 3D printed soft robots can perform better than or equal to their molded counterparts while being more reliable.

Keywords: 3D printing, additive manufacturing, soft robotics, radiation environments, soft actuators, nuclear robotics, silicone elastomer

OPEN ACCESS

Edited by:
S. M. Hadi Sadati, University of Bristol, United Kingdom

Reviewed by:
Massimo Mastrangeli, Delft University of Technology, Netherlands
Deepak Trivedi, General Electric, United States

****Correspondence:***
Osman Dogan Yirmibeşoğlu
yirmibeo@oregonstate.edu

Specialty section:
This article was submitted to Soft Robotics, a section of the journal Frontiers in Robotics and AI

Received: *17 November 2018*
Accepted: *03 May 2019*
Published: *24 May 2019*

Citation:
Yirmibeşoğlu OD, Oshiro T, Olson G, Palmer C and Mengüç Y (2019) Evaluation of 3D Printed Soft Robots in Radiation Environments and Comparison With Molded Counterparts. Front. Robot. AI 6:40. doi: 10.3389/frobt.2019.00040

INTRODUCTION

Robotics research has a significant role when utilizing robots for inspection, clean-up, and sample collection in hazardous environments inaccessible to humans. Especially when it comes to radiation environments, their deployment minimizes unnecessary exposure of workers to the harmful effects of radiation (Moore, 1985). Accordingly, robots have a long history in the nuclear field, from the incident at Three Mile Island, Reactor 2 (TMI-2) in 1979 to the 2011 disaster at Fukushima Daiichi

Nuclear Power Plant (Urabe and Stapczynski, 2017). At TMI-2, robots performed surveillance, inspection, and decontamination tasks following the meltdown (Hess and Metzger, 1985; Lovering, 2009). Soon after the nuclear power plant accident in Fukushima, Japan, the existing Quince robot was modified to perform inspection and sampling tasks in two of the affected units (Nagatani et al., 2011a). This robot completed several objectives before becoming irretrievably lost (Nagatani et al., 2011b). Recently, equipment specifically designed to operate within Fukushima, including Toshiba's Scorpion and Sunfish models, have been introduced to perform additional surveillance (Fackler, 2017). However, most of the deployed robots faced a similar problem: getting stuck or tangled in debris. They also suffered from circuit malfunctions due to high doses of radiation, especially if hardened parts were not used in fabrication (Fackler, 2017). The contaminated and malfunctioning robots were abandoned inside the reactor, at a total loss of the equipment's capital cost (Mary-Ann, 2015; Sheldrick and Funakoshi, 2016; McCurry, 2017). These circumstances raised a central question: Can we use low-cost soft robots in radiation environments? Soft robots provide advantages over rigid robots in terms of body morphing (Laschi et al., 2016), absorbing the energy of an impact or collision (Lee et al., 2017), high compliance (Rus and Tolley, 2015), and cheaper fabrication costs (Hill et al., 2000). The most significant of these advantages is the robot's ability to conform to different obstacles and terrains in various radiation environments, especially during passage through non-traditional entryways when doors and access points are blocked. Moreover, millimetric (Hu et al., 2018; Ranzani et al., 2018) scale soft robots may also provide considerable advantages under radiation environments.

In order to evaluate the effectiveness of soft robots under radiation, the convenience of the fabrication material for the environment plays a crucial role. The earliest investigations of the effect of gamma radiation on polydimethylsiloxane (PDMS) were performed by Charlesby (Charlesby, 1955) and Miller (Miller, 1960) in the late 1950s. They determined that the degree of crosslinking induced by radiation is a function of dose and demonstrates a direct-response relationship. Charlesby calculated a 32-eV energy absorption requirement per crosslink and Miller calculated a crosslinking yield of 3.0% for irradiation by electrons. Notably, both studies were performed on the liquid form of PDMS rather than the cured form considered in soft robotic applications. Therefore, to fill this research gap, and to estimate fabricated soft robots' operation time under radiation, we investigated gamma-induced mechanical damage in PDMS and sent a 3D printed soft robot into an underwater radiation environment. The main reasons for selecting the 3D printing method over molding to fabricate soft robots will be detailed in the following paragraphs.

To send a soft robot in an unstructured radiation environment for inspection purposes or delivery tasks, it must offer significant dexterity and mechanical compliance, with minimum control requirements. However, disadvantages of soft robots such as limited afforded strength and payload (Lee et al., 2017), limited control and autonomy (Trivedi et al., 2008; Singh and Krishna, 2014), need for tethering (Majidi, 2014; Schmitt et al., 2018), and limited sensory equipment (Rus and Tolley, 2015; Lee et al., 2017) still need to be overcome. To meet some of these demands, the soft actuators within the soft robot must enhance their functionality, which is limited by fabrication techniques (Marchese et al., 2015). Since conventional soft robot manufacturing techniques such as lamination casting (also known as soft lithography) (Xia and Whitesides, 1998; Tolley et al., 2014), retractable pin casting (Marchese et al., 2014, 2015), lost wax casting (Sias, 2005; Marchese et al., 2015), and rotomolding (Zhao et al., 2015) restrict possible geometries, shapes, complexity, and scale of the manufactured soft robots, we choose to focus on additive manufacturing (AM) methods (Truby and Lewis, 2016; Walker et al., 2019). However, the most commonly used AM techniques, such as stereolithography (SLA) (Peele et al., 2015), fused filament fabrication (FFF) (Yap et al., 2016), and PolyJet (Drotman et al., 2017) are not suitable for 3D printing PDMS material for fabricating soft robots (Trimmer et al., 2015; Laschi et al., 2016; Kastor et al., 2017).

One of the first examples of a 3D printed soft actuator (Peele et al., 2015) failed at around 40% strain (after approximately nine cycles) due to photopolymer SLA materials while their molded counterparts fabricated with the PDMS materials were able to undergo more than 600% strain (Mosadegh et al., 2014). Alternatively, another 3D printed soft actuator manufactured through FFF methods was limited to the NinjaFlex (NinjaTek, PA) thermoplastic material with a Shore hardness of 85A (Yap et al., 2016). More recent 3D printed soft robots were manufactured with PolyJet technology which allowed researchers to (1) manufacture a quadrupedal robot with soft legs capable of two axis rotation (Drotman et al., 2017), (2) create a material stiffness gradient within the soft robot body (Bartlett et al., 2015), and (3) 3D co-print solids (flexible, rigid) and liquids to fabricate hydraulically actuated components (MacCurdy et al., 2016). However, the commercially available materials (Stratasys, MN) used in this process were limited by Shore hardness (ranging between 27A and 95A).

To overcome strain limitations and use PDMS materials within AM, researchers focused on direct ink writing (DIW) techniques. Ober et al. analyzed the behavior of complex fluids and developed a micro-scale active mixing system for two-part materials, and successfully 3D printed PDMS objects (Hardin et al., 2015; Ober et al., 2015), but they did not demonstrate the fabrication of soft actuators or robots. Instead of using two-part PDMS materials, Plott et al. used moisture-cured silicone elastomer to successfully 3D print finger pneumatic actuators (Plott and Shih, 2017). Unfortunately, their printing technique restricted the achievable geometry as it required near voidless construction.

Considering the limitations of current state-of-the-art PDMS printing, the soft robotics community has yet to match the performance of the molded functional soft robots made from PDMS materials with 3D printing technology. In prior work (Yirmibesoglu et al., 2018), we developed a 3D printer to address this research gap. Here by modifying the previous printer design, we improved the complexity and increased the scale of the fabricated soft robots, which enabled us to 3D print a

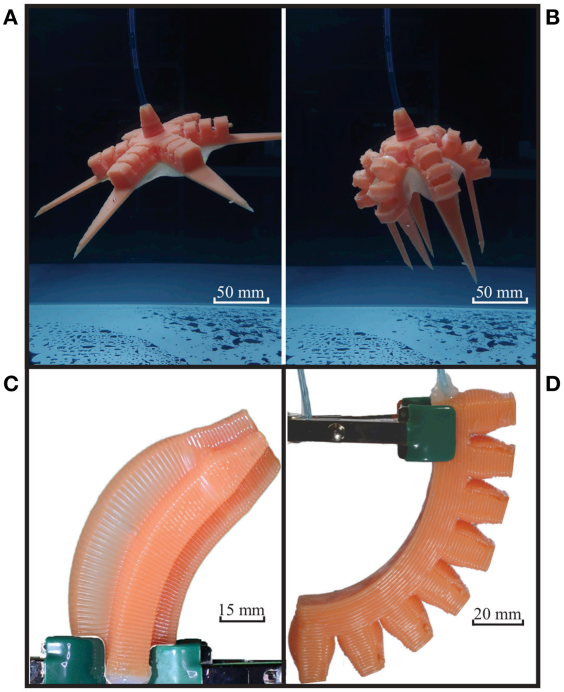

FIGURE 1 | 3D printed soft robots. **(A)** Hexapus nominal state. **(B)** Hexapus actuated state. **(C)** 4 channel tentacle (Yirmibesoglu et al., 2018). **(D)** Pneu-net actuator (Yirmibesoglu et al., 2018).

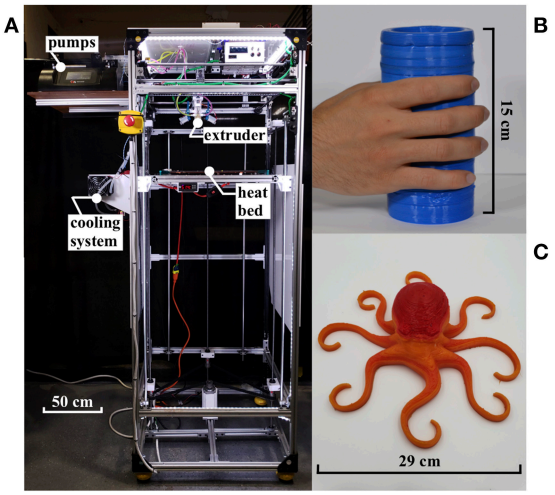

FIGURE 2 | (A) 3D silicone printer. **(B)** 15 cm tall cylinder, 3D printed in 5 h without collapsing. **(C)** Soft octopus sculpture (0.79 kg), 3D printed in 18 h.

hexapus robot (**Figures 1A,B**) for testing soft robots under a radiation environment.

In this work, in order to assess the usefulness of soft robotics under radiation, we selected 3 radiation environments to provide a wide scope of operation. To estimate fabricated soft robots' operation time in these radiation environments, we measured gamma-induced changes in mechanical properties such as elongation, tensile strength, and compression of the PDMS material. The viability of the soft robots under 3 selected radiation environments was analyzed based on PDMS behavior after irradiation. Later, a 3D printed soft hexapus robot (Frame et al., 2018) was operated in a radiation environment, and its absorbed dose rate was measured to estimate its operation time. By using 3D printing as the fabrication method, we increased design complexity of the hexapus robot, which enabled us to test its operation time under radiation environment. Finally, to ensure the reliability of the 3D printed soft robots we investigated the effects of fabrication methods, nozzle size, and print direction on the stiffness of the PDMS material.

This paper is organized as follows. In section 3D printing of silicone material, we introduced the improvements to the 3D silicone printer that enabled us to 3D print a hexapus robot. In section Materials and methods, we detailed the protocols to measure the effect of gamma irradiation on PDMS material and select radiation environments. Also, experimental methods and setups for radiation experiments and robot performance comparisons are detailed. In section Results and discussion, we analyzed the changes in the mechanical properties of PDMS samples after gamma irradiation and we measured the gamma irradiation absorbed by the 3D printed hexapus robot submerged into bulk shield tank while repeating pull and push motions. After that, we conducted blocked force and bend angle experiments to compare the performance differences between our 3D printed soft robots (4 channel tentacle **Figure 1C** and Pneu-net actuator **Figure 1D**) and their molded counterparts. We also measured the effects of fabrication methods, nozzle sizes, and print directions on the stiffness of the fabricated PDMS material. Finally, in section Conclusion, conclusions and future work are presented. Authors also provided a table of the acronyms (**Supplementary Table 1**) used throughout the paper to help readers.

3D PRINTING OF SILICONE MATERIAL

In this section, we describe improvements to the previous 3D silicone printer design that enabled us to 3D print a hexapus robot (**Figure 1A**) capable of swimming in an underwater radiation environment. For additional instrument design details, please refer to the original paper (Yirmibesoglu et al., 2018). The major changes in the 3D printer setup (**Figure 2A**) include new material, modified extruder, and new print parameters. A detailed explanation of the 3D printer including a preliminary benchmark study for AM of soft materials is provided in the **Supplementary Material**.

Print Material

The print material we used was Dragon Skin 10 (DS10) very fast, a two-part platinum cure silicone (Smooth-On, PA), in combination with 1 wt % Thi-Vex (Smooth-On, PA), a viscosifying agent used to thicken the formulation to improve print fidelity based on our previous paper (Yirmibesoglu et al., 2018). However, due to high loads on the syringe pumps at

75 cm tube length (**Supplementary Figure 1**), we added 10 wt % silicone thinner (Smooth-On, PA) into the formula, based on the findings of a recent study (Walker et al., 2018). With the improved formula, the accumulated load decreased from 351 N down to 252 N. The high viscosity print material also prevented bubble formation at the macro level.

Extruder Mechanism

We improved the extruder mechanism from previous works (Ober et al., 2015; Morrow et al., 2017; Yirmibesoglu et al., 2018) in several ways to print taller soft objects (**Figure 2B**) and to achieve extended print times (**Figure 2C**). First, we decreased the mixer chamber volume. In the old design, the cross section diameter of the mixer chamber was 10.8 mm, resulting in 8.1 times the volume to be initially filled by the mixed material before extrusion, compared to the new mixer chamber design. With a bigger volume, the amount of the time that the material mix stayed inside the mixer was longer. Since the heat bed (**Figure 2A**) and convective heating (**Figure 3A**) created a hot environment around the mixer chamber, this resulted in an increase in the crosslinking rate of the mixed material. With higher crosslinking, the material became more viscous and was unable to pass through smaller nozzle sizes resulting in a clogged mixer. The smaller chamber volume decreased the amount of time required to discharge the mixed material from the mixer chamber before the crosslinking turns the material into a highly viscous state.

Second, by adding the water jacket system (**Figure 3B**), we circulated cold water around the mixer chamber using a commercially available pump (Water cooling kit, E3D-online, UK) to maintain the temperature of the mixed material below 25°C while the surrounding environment was between 45° and 80°C. The combination of the smaller volume mixer chamber and water jacket systems, kept the crosslinking rate of the mixed material low enough, so that discharge of the mixed material completed before the mixer got clogged resulting in extended print times. Our longest print took 18 h using a 0.839 mm nozzle and weighed 0.79 kg (**Figure 2C**). Achieving extended print times was the key to fabricate the hexapus robot for radiation tests, which was 3D printed in 11 h with DS10-fast composition. The step-by-step guide to manufacturing the initial version of this extruder mechanism is publicly available on the Soft Robotics Toolkit[1].

Print Parameters and Limitations

After modifying the extruder to print taller silicone objects and extend print times, to achieve high resolution with prints we followed a recent strategy (Yuk and Zhao, 2018) that benefits from the deformation of viscoelastic inks. With the guidance of this study, by mainly tuning print parameters such as print speed, flow rate, and layer height we deposited lines between die-swelling, equi-dimensional, and thinning print modes (Yuk and Zhao, 2018). The transition between the modes was achieved by changing the print speed or flow rate. Our latest list of parameters for a successful print is available in **Supplementary Table 3**. Moreover, there are a couple of design limitations observed in robot fabrication. A list of design limitations with the recommended parameters is available in **Supplementary Table 4**. By considering the printer modifications, improved print parameters and design limitations detailed in this section, we achieved the AM of the hexapus robot.

[1]https://softroboticstoolkit.com/3d-silicone-printer (accessed April 2019)

MATERIALS AND METHODS

In this section, we first detail the protocols to measure the effect of gamma irradiation on the mechanical properties of the PDMS material. We then describe the selection of radiation environments for soft robot operation and how to measure the irradiation dose of the hexapus robot. Second, we describe the comparison methods for measuring performance and ensuring the reliability of the 3D printed soft robots compared to their molded counterparts. Finally, we describe experimental methods to identify the causes of performance differences between 3D printed and molded soft robots.

Mechanical Testing of Gamma-Induced PDMS Samples

In order to evaluate soft robot reliability in gamma radiation environments, samples of PDMS were irradiated in a GammaCell 220 to a high dose rate from a Co-60 source (a radioactive isotope of the element cobalt). We prepared 27 dumbbell test pieces and 20 disc-shaped compression samples were prepared from DS10-fast silicone. The sample dimensions were 29.0 mm in diameter and 12.5 mm in thickness. To create samples of both kinds, equal parts by weight of DS10-fast part A and B were mixed and poured into molds and placed under −100 kPa vacuum for 5 min. Then these samples were placed in a 60°C oven for 15 min and were allowed to rest to reach the final mechanical properties. Finally, samples were irradiated at six increments of gamma-only doses from 7 to 400 kGy, with at least three samples tested at each cumulative dose. A total of 6 samples were reserved as a control group.

After gamma irradiations were completed, samples were subjected to mechanical tests in a motorized tension/compression stand (ESM1500, Mark-10, NY) **(Figures 4A,B)**. For the tensile tests, the length of the narrow portion of the sample (L1), was increased by separating the sample ends at a rate of 250 mm/min. The samples were stretched until failure while measuring L1 and the tensile force to determine the "tensile strength at break" and "elongation at break" according to ASTM D412-16. For compression testing, the height of the sample was decreased at a rate of 50 mm/min to 75% of the original value, then released.

Selecting Radiation Environments for Soft Robot Operation

To provide context for this assessment, three radiation environments were considered to represent the general diversity of potential applications. Environments in the nuclear power industry are used because they are well-characterized and

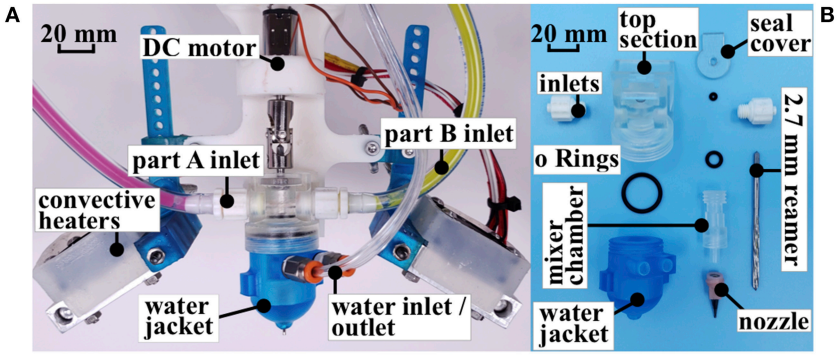

FIGURE 3 | (A) Extruder mechanism with water jacket addition. **(B)** Mixer assembly.

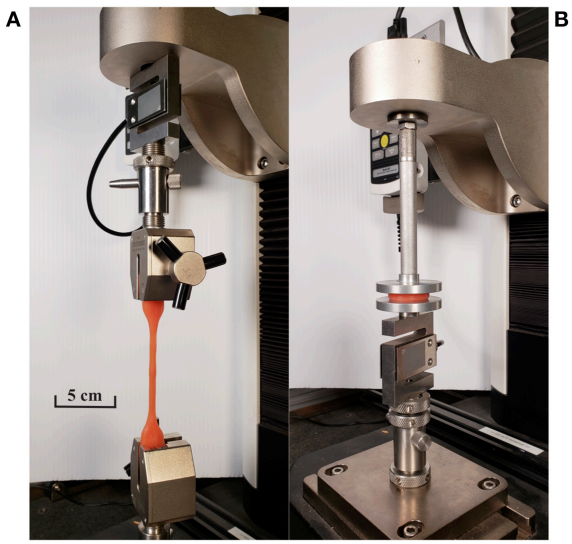

FIGURE 4 | Testing irradiated dumbbell and disc samples with Mark-10 motorized test stand (Oshiro, 2018). **(A)** Tensile strength and elongation testing setups. **(B)** Compression testing setup.

encompass real-life scenarios of various dose rates. The three radiation environments are selected from a guide (Sharp and Garlick, 1994): (1) Spent fuel storage pools, (2) Vitrified waste and the vitrification process, and (3) Deactivation of a generic pressurized water reactor (PWR). Available dose rate ranges and averages from these documented environments were used to calculate a cumulative dose assuming as 12 h robot task time. In all cases, the most conservative (highest documented dose rate) was assumed, which resulted in a 12 h cumulative dose of 120 kGy for spent fuel storage pools, 21.6 kGy for vitrified waste and the vitrification process, and 12 kGy for deactivation of a generic PWR. The cumulative dose, rather than the dose rate, is applicable here because past research on PDMS (Comstock, 1989) suggests that radiation is a function of cumulative dose and is not heavily dependent on dose rate.

Measuring the Irradiation Dose of the Hexapus Robot in the Bulk Shield Tank

To estimate the 3D printed soft robots' operation time we submerged the hexapus robot into a radioactive bulk shield tank. The hexapus robot was 46 mm tall and 286 mm in diameter. Six actuation arms consisted of Pneu-net structures were place 60° apart from each other. Tap water was pumped and withdrawn in consecutive cycles into the hexapus by using a 60 ml syringe attached to a syringe pump (NE-4000, New Era, NY) at the max pump speed of 95.99 ml/min. We switched from pneumatic to hydraulic to avoid the hexapus robot floating on the surface. The hexapus and the pump were connected by 6 meters of soft tubing with an inner diameter of 3.2 mm (**Supplementary Figure 3**). Later, the hexapus was submerged into a radioactive bulk shield tank (2.7 × 2.4 × 3.7 m–width x height × depth), (**Supplementary Video 1**). The tank was under the effect of two main gamma irradiation sources: (1) a used graphite reflector, and (2) radiation flux coming from the neighboring operating nuclear reactor. An underwater ion chamber (CPMU, Technical Associates, CA) was used to measure the dose rate next to the hexapus (**Supplementary Figure 4**). In addition, we were unable to measure the performance change of the hexapus' pull and push motions with absorbed dose rate (**Supplementary Video 1**) as our underwater camera equipment was not suitable for radiation environments.

Measuring the Performance of the 3D Printed and Molded Soft Robots

Reliable operation of a soft robot is a vital step before evaluating the effectiveness of soft robots under radiation. To ensure the reliability of the 3D printed soft robots and verify their performances we compared them with the molded counterparts. However, we did not fabricate a molded version of the hexapus robot because of the laborious and time intensive (up to 3 days) manufacturing steps which are beyond the scope of the current work. Instead, we fabricated 4 channel tentacles and Pneu-net actuators that are part of the hexapus actuation design.

The blocked force and bend angle experiments were used to measure the performance of each robot in response to given pressure (Holland et al., 2014). Fabricated 4 channel

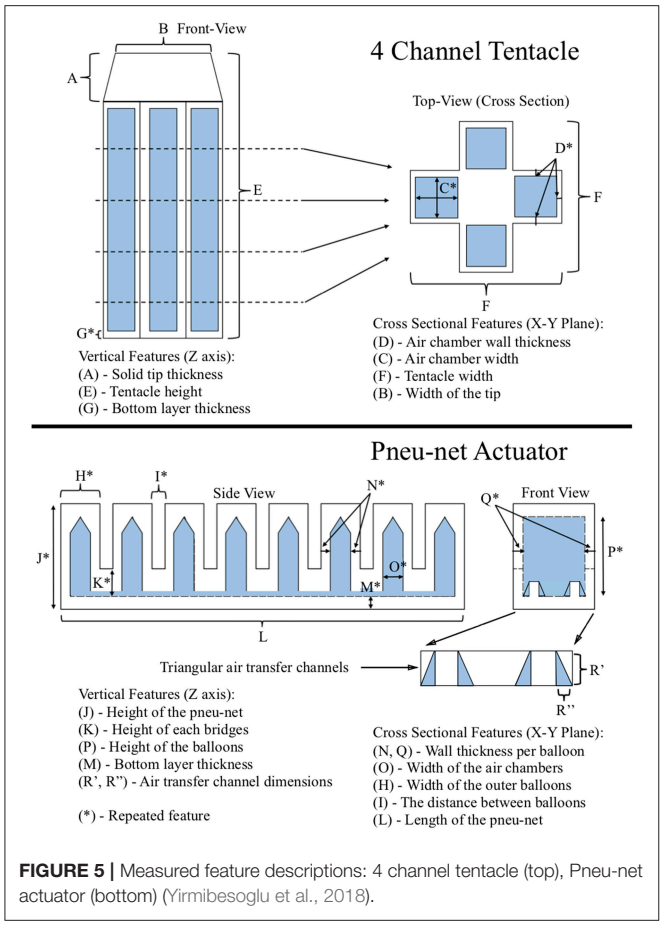

FIGURE 5 | Measured feature descriptions: 4 channel tentacle (top), Pneu-net actuator (bottom) (Yirmibesoglu et al., 2018).

tentacles (Marchese and Rus, 2016) were used for identifying the effects of 3D printing compared to lost wax casting on robots' performance. Next, fabricated Pneu-net actuators (Ilievski et al., 2011; Mosadegh et al., 2014) were used for identifying the effects of 3D printing compared to lamination casting on robots' performance. We selected our robot designs based on the most common (excluding the use of fabric) bending principles: eccentric void asymmetry (4 channel tentacle) and corrugated membrane asymmetry (Pneu-net actuator, hexapus) (Gorissen et al., 2017). Differences between fabrication steps of the tested robots are provided in **Supplementary Table 5**, and the experimental setup used for the performance comparison tests can be seen in **Supplementary Figure 5.**

In order to understand any performance differences in the blocked force and bend experiments, we initially calculated dimensional errors. Features measured and compared against CAD models were shown in **Figure 5** for both the 4-channel tentacle [Top] and Pneu-net actuator [Bottom]. The cross-sectional features (those in the X-Y plane) and the vertical features (those in the Z-axis) were measured. We consolidated features together by averaging their mean values. Each variable was measured at four random locations on the soft robots with a digital caliper and percent error deviations calculated.

Measuring the Effects of Fabrication Methods, Nozzle Size, and Print Direction

To further investigate performance differences, we analyzed the stiffness change of the PDMS material caused by used fabrication methods. Sixty six dumbbell test samples were prepared and divided into 11 subgroups in order to measure the effects of fabrication methods, nozzle size and print direction on the Young's modulus of the used PDMS material. Twenty four of the samples were molded and 42 of them were 3D printed by following the ASTM D412 type C dimensions. Molded test samples were divided into 4 subgroups depending on their cure time: DS10-slow, DS10-medium, DS10-fast, and DS10-very-fast. 3D printed samples were fabricated only with DS10-very-fast and were divided into 7 subgroups depending on their print directions and nozzle sizes: perimeters, longitudinal, transverse, cross, crisscross with 0.417, 0.839, and 1.019 mm (**Figure 6**). Per each subgroup 6 samples were fabricated and defective ones were eliminated; at maximum 3 samples were eliminated from each subgroup. For all the test samples, the main composition (DS10-very-fast with 1 wt % Thi-Vex additive) was mixed with 10 wt % thinner (Walker et al., 2018) and none of the samples were degassed. Print parameters for the dumbbell test samples can be seen in **Supplementary Table 3**.

After waiting overnight to ensure samples reached their final mechanical properties, prepared samples were attached to a Mark-10 motorized test stand including 1000N load cell (MR01-200-1, Mark-10, NY) for measurements (**Figure 4A**). Dumbbell pieces were pulled up with a speed of 60 mm/min until failure. Due to sensor resolution, a systematic error of $\pm$0.5N was introduced into all test results. The Young's modulus was calculated by fitting a 100% tensile modulus line into the experimental data (**Supplementary Figure 6**).

RESULTS AND DISCUSSION

In this section, first, we present the changes in the mechanical properties of PDMS samples after gamma irradiation and analyze the potential of the soft robots under radiation environments. Then, we verify the viability of soft robots under 3 selected radiation environments based on potential tasks in the nuclear industry. Later, we present the absorbed gamma irradiation by the 3D printed hexapus robot and its estimate operation time. We fabricated the hexapus robot by taking advantage of AM to avoid many fabrication challenges inherent to the molding techniques due to the complex design of the robot. To verify the 3D printed robot's reliability, we present their performance differences with molded counterparts. Finally, to explain performance differences, we show the effects of fabrication methods, nozzle sizes, and print directions on the stiffness of the fabricated PDMS material.

Changes in the Mechanical Properties of PDMS After Gamma Irradiation

The measured changes in elongation at break, tensile strength, and compression were plotted as a function of cumulative dose in **Figure 7**. Results indicate that increased cumulative gamma dose leads to decreased elongation at break (**Figure 7A**). However, the

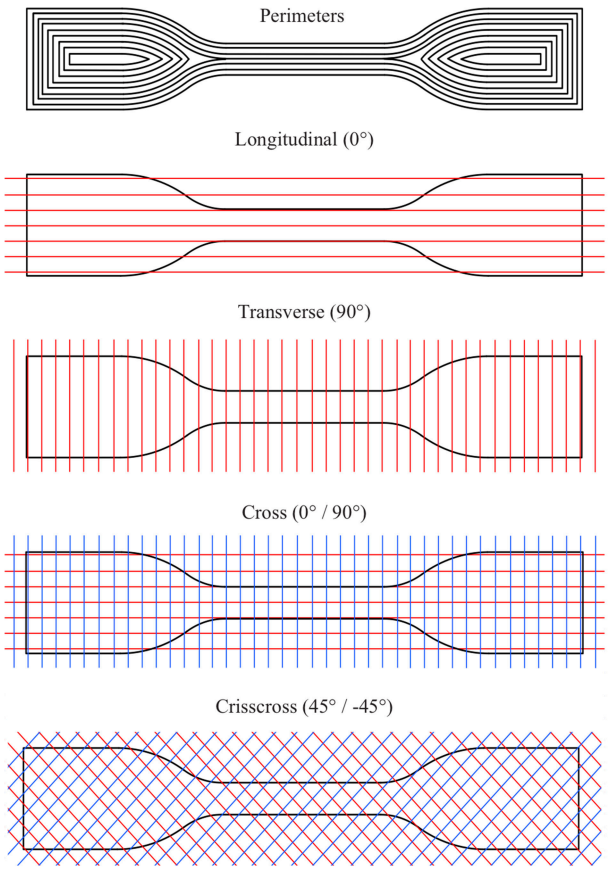

FIGURE 6 | The print direction of the dumbbell test pieces fabricated from PDMS.

relationship is not strictly linear. From 7 to 21.6 kGy, elongation at break decreases slowly, remaining nearly constant. Above 21.6 kGy, there is a steep decrease in elongation at break up to the highest measured dose, 400 kGy. This agrees with past literature, which shows either a small initial increase (Warrick, 1955) or slight decrease (Van de Voorde and Restat, 1972; McCarthy and Mark, 1998) followed by an eventual decrease in elongation at break at higher doses. For the tensile strength property of the material, results showed a slight initial increase from 0 to 21.6 kGy followed by an overall decrease in tensile strength (**Figure 7B**). This includes a steep drop in tensile strength at 55 kGy followed by a recovery back to the general decrease trend from 120 to 400 kGy. The overall trend, not including the 55 kGy drop, agrees with results from a CERN technical report. Past results do not agree on the overall effects of gamma radiation on tensile strength; Warrick (Warrick, 1955) showed an initial increase followed by a sharp decrease while McCarthy and Mark (1998) showed a constant tensile strength over the range of 200–400 kGy. This may be explained by the difference in the experimental aims of the past two studies and this current one. Where Warrick and McCarthy sought an optimum dose to vulcanize the rubber, this study focuses on already cured, solid silicone rubbers. This suggests that gamma irradiation improves the tensile strength of the uncured or incompletely cured material until it achieves a maximum, after which the molecular-level effects become detrimental rather than curative. Thus, the silicone rubber studied here improves to its maximum at roughly 12 kGy then degrades as dose increases above 20 kGy. We anticipate that these results would apply for common cured PDMS materials. However, further testing is required to verify. The results from the CERN technical report fit this profile and support this conclusion (Voorde and Restat, 1972). Since the overall effects of gamma radiation on PDMS in this experiment are decreased elongation at break and decreased tensile strength, it indicates molecular crosslinking is likely the dominant effect within the PDMS matrix as doses are increased. While this experiment did not include investigation on a molecular level and therefore cannot confirm this overall trend with certainty, it does agree with past research by Hill which suggests that irradiation of PDMS results in a higher crosslinking yield than scission yield (Hill et al., 2000). However, an explanation of molecular effects is not necessary to extend the mechanical results and their influence on potential usage areas.

The compression tests of the cylindrical samples determined stiffness by measuring the force required to compress the disc to 75% of its original height, shown in **Figure 7C**. These results point to an increase in stiffness as cumulative dose increases. This increase in stiffness is likely due to a direct response relationship between radiation exposure and cross-linking. This agrees with Basfar's research that shows beta radiation at similar doses results in increased crosslinking and increased resistance to compression (Basfar, 1997). While Basfar's experiment sought to determine the dose required to completely cure a liquid silicone rubber to solid state using radiation, it still indicates that the dominant effect of cumulative radiation is increased crosslinking, which is consistent with the current evaluation of PDMS. Regarding any thickness dependent variations in property degradation of both dumbbell and compression samples, based on the 1.25 MeV photon energy of the Co-60 irradiator, it is safe to assume the dose is uniformly distributed. 10 cm of PDMS reduces the absorbed dose by ∼25%. 3.8 cm is required to alter the absorbed dose rate by 10%, which indicates our hexapus design is also safe. Higher energy photons would require larger thicknesses, up to 18 cm for 10 MeV photons.

The effect of temperature on PDMS has been previously evaluated in the literature (Camino et al., 2001, 2002) and is known to have an influence and was not considered in this study as all irradiations were performed at room temperature. Based on the differences in damage mechanisms between thermal and radiation exposure, it is not anticipated that these effects would interact; however, this has not been evaluated.

Overall, with increasing exposure to high dose gamma radiation, the mechanical properties of PDMS decrease in functionality, as expected. The results of the elongation at break tests suggest that material performance is not greatly impacted up to 20 kGy, at which point it begins to lose its ability to extend more drastically. Similarly, the results of the tensile strength tests suggest that performance is minimally impacted up to roughly 20 kGy followed by a gradual decrease at higher doses. The

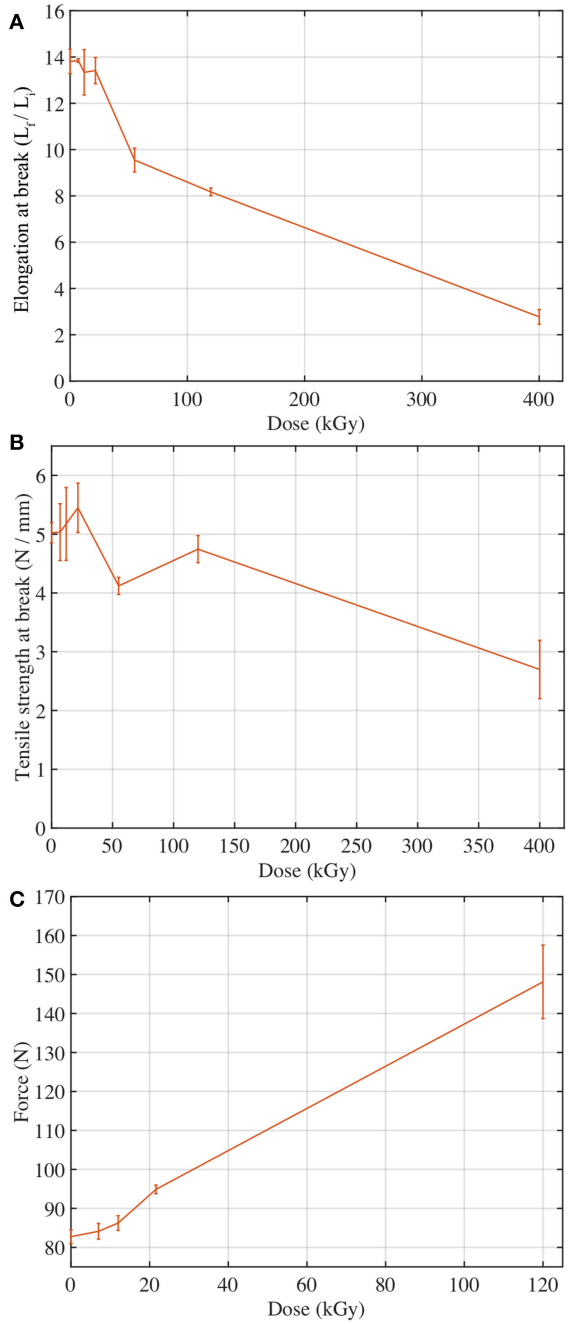

FIGURE 7 | Changes in the mechanical properties of PDMS after gamma irradiation (Oshiro, 2018). **(A)** PDMS elongation decreases with increasing gamma dose. **(B)** PDMS tensile strength for increasing gamma dose. **(C)** Force at 25% compressive strain with increasing gamma dose.

stiffness of the material increases steadily as the cumulative dose increases. These results are consistent with the theory (Hill et al., 2000) that both scission and crosslinking occur initially while crosslinking becomes the dominant effect of gamma radiation on PDMS beyond 20–50 kGy. The major concerns for soft robots and their manipulators at these higher doses is that more pressure will likely to be needed to maintain the range of motion.

Viability of Soft Robots Under Selected Radiation Environments

In order to translate the functionality of soft robotics for potential tasks in the nuclear industry, the cumulative dose at each radiation environment was evaluated for its resultant change to the material properties of PDMS. This study provides a preliminary evaluation of the properties of PDMS under certain irradiation conditions. A fully functional test of the robot under inflation or with a load was not possible in the available irradiation facilities. Additionally, any electronics required for actuation of the robot would not survive these doses (up to 400 kGy) and were therefore not used. The main reason for testing a very high dose rate (400 kGy) is to represent very long time effect on property degradation.

A complex soft robot geometry with external loads could have a state of strain that is a combination of uniaxial, biaxial, shear, and volumetric strains, and full failure characterization requires a suite of tests. However, due to the limitations of this study, mentioned above, detailed failure characterization including equibiaxial strain tests at the inflation state could not be performed. Instead, elongation at break and stiffness were used as measures of mechanical changes due to their predictable effects and direct relation to the functionality of the material. As a function of dose, the fractional change to each property was measured by taking the difference between the irradiated and control sample values and dividing by the control sample value. As shown in **Figure 8**, compression changed by more than 50% in the used fuel pool, and elongation at break in the used fuel pool changed by more than 25%. A similar polymer radiation study considered 50% change as a benchmark to assess the viability of a material (Bonin et al., 2004). By this rubric, soft robotic systems made out of PDMS materials are viable in most radiation environments, which is promising. Changes to the mechanical properties will result in some corresponding loss of function but understanding these mechanical changes as a function of exposure may allow for control systems to compensate for reliable and consistent performance of the soft robots.

Operation Time Estimation and Absorbed Gamma Dose Rate of 3D Printed Hexapus Robot Under Radiation

After submerging the 3D printed hexapus robot to estimate the operation time, the underwater ion chamber was also submerged directly next to it and measured the gamma dose rate as 1 Gy/h. This measured dose rate does not account for the neutron flux coming from the neighboring reactor, which cannot be directly measured under water. A conservative estimate assumes the 1 Gy/h dose rate in which the robot was exposed for 30 min while cycling through its push and pull motions, receiving a total dose of 0.5 Gy. A benchmark of 50% change in material properties is used in polymer radiation experiments to assess the viability of the material (Bonin et al., 2004). While the stiffness changes

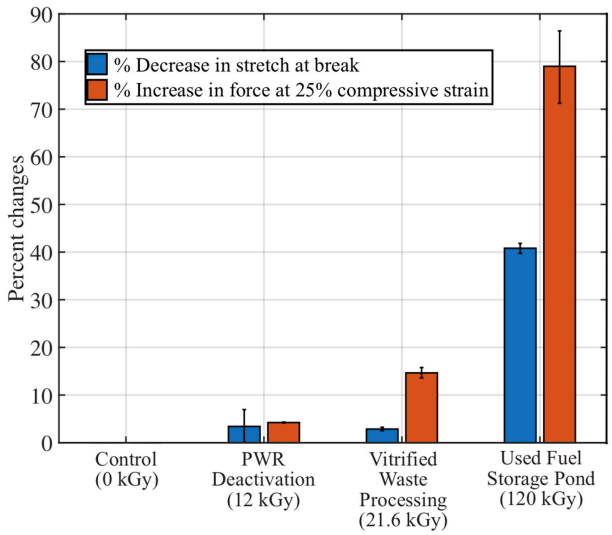

FIGURE 8 | Fractional changes to PDMS mechanical properties compared to representative gamma environments (Oshiro, 2018).

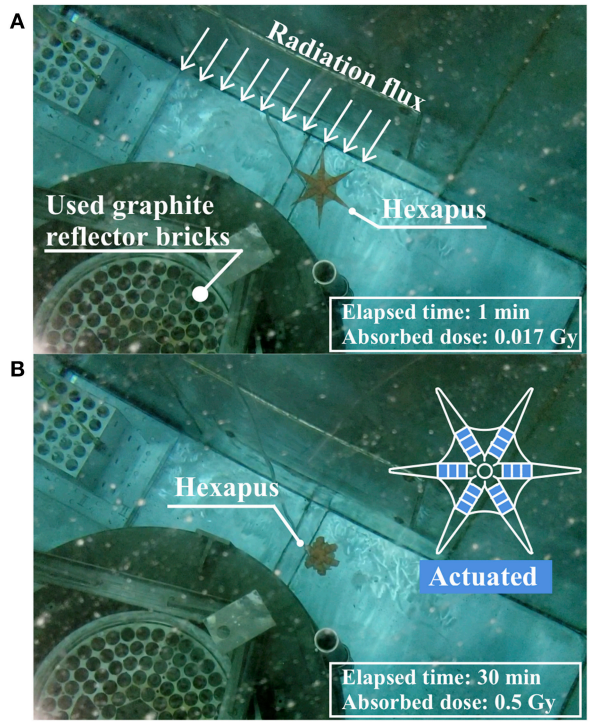

FIGURE 9 | Actuation of the hexapus robot while absorbing gamma irradiation inside bulk shield tank for 30 min. **(A)** Hexapus nominal state. **(B)** Hexapus actuated state.

around 50% at 70 kGy, elongation does not reach the 50% change metric until 120 kGy and the tensile strength is even less susceptible to change. Therefore, it is speculated that the hexapus robot could operate around 70,000 h in the radiation environment shown in **Figure 9** before its stiffness changed more than 50%, assuming with a dose rate of 1 Gy/h. Also considering the fractional changes to the PDMS mechanical properties in **Figure 8**, the robot could operate for the 12-h task time in two of the three proposed radiation environments. The highest dose rate environment, the used fuel storage pond, would have a reduced task time on the order of 7 h in which the stiffness changes by ∼50%. These estimates assume the rest of the robot's control system and pumps continue to perform.

Robot Performance Comparison: 3D Printed vs. Molded

The results of the blocked force and bend angle tests are shown in **Figure 10**. Plotted values reflect the average of the experimental data while the shadowed regions represent one standard deviation. For the 4 channel actuator, we collected data from each channel ($n = 4$), and for Pneu-net actuator, we collected data from 3 trials ($n = 3$). The results of the blocked force tests for the 4 channel tentacles (**Figure 10A**) showed that the force applied by the molded version varies more with increased pressure. Moreover, when the tentacle attachment height above the sensor surface increased, for a fixed inflation volume, the measured maximum blocked force increased from 1 to 2 N (**Supplementary Figure 7**). At a 15 mm height, the 3D printed 4 channel tentacle was able to apply more force than its molded counterpart. When we investigated accumulated pressure levels inside the channels, an injection of 120 ml of air resulted in a pressure of 88 kPa for 3D printed tentacle, but only a 67.5 kPa pressure for the molded tentacle.

The results of the blocked force tests for Pneu-net actuators (**Figure 10B**) showed that both the 3D printed and molded actuators applied the same amount of force (with a 0.03 N difference in between). However, the blocked force values of the molded version again varied more with increased pressure. Also, when we analyzed the data regarding the pressure levels, the molded actuator applied the same amount of force but with 10 kPa less accumulated pressure. The molded actuator did incur a failure at the seam position and was repaired to continue with the experiments.

The results of the bend angle tests for 4 channel tentacles (**Figure 10C**) showed that both tentacles bend to around the same angle. However, it can be seen that the internal channel pressure of the molded actuator jump by 20 kPa when 80 ml of air is injected. The results of the bend angle tests for Pneu-net actuators (**Figure 10D**) showed that after 60 ml of airflow, the angle difference between actuators increased to 23.7°, with molded actuator achieving a higher bend angle. However, this time the bend angle results of both actuators varied less in between experiments.

To explain and discuss the performance differences between the 3D printed and molded soft robots, first, we conducted dimensional error analyses. Results are shown in **Figure 11** with the consolidated feature groups for both the 4 channel tentacles and the Pneu-net actuators in terms of percent error deviations. The 3D printed, 4 channel tentacle and the Pneu-net actuator deviated on average less from the original dimensions provided

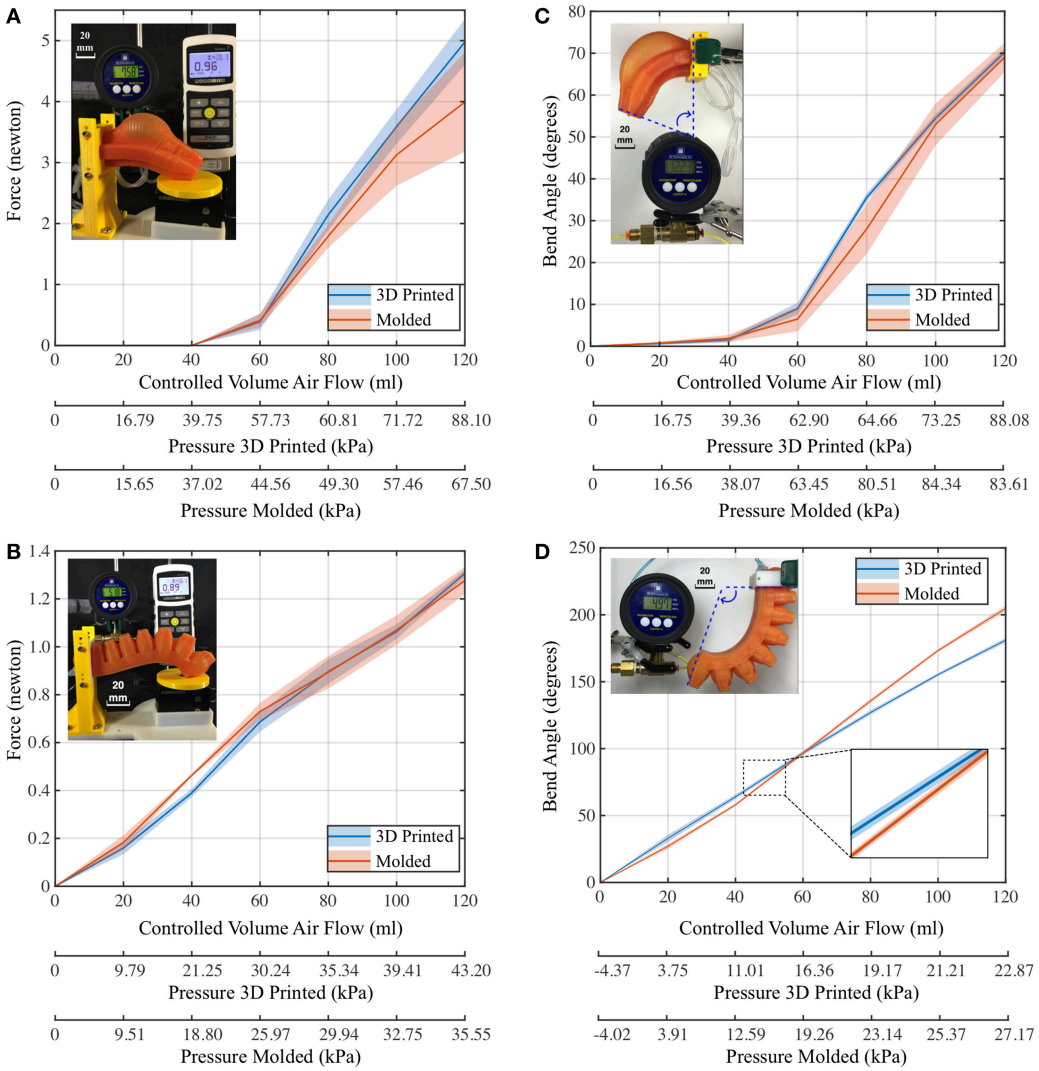

FIGURE 10 | Performance comparison results (Yirmibesoglu et al., 2018). **(A)** Blocked force comparison (4 channel tentacles). **(B)** Blocked force comparison (Pneu-net actuators). **(C)** Bend angle comparison (4 channel tentacles). **(D)** Bend angle comparison (Pneu-net actuators).

from the CAD file compared to their molded counterparts. The 3D printed tentacle has a smaller standard deviation than the molded one for cross-sectional features, while the standard deviations for vertical features for both robots are about the same. The difference in applied force across the two fabrication methods could potentially be caused by a change in stiffness resulting from each fabrication method. Therefore, we analyzed the effects of the fabrication method on the stiffness of the PDMS material, reported in the next section. The observed difference in the accumulated pressure levels inside the channels is likely the result of the inward warping of the wax cores used to create the long channels in the molded tentacle (**Supplementary Figure 8**). Also, since we do not have a force plate blocking the motion in the bend angle tests, compared to the blocked force tests, we believe that an uneven geometry of the channel cross-sections may have caused the 20 kPa jump (**Supplementary Figure 8**).

Regarding the Pneu-net actuators, both the 3D printed and molded actuator's cross-sectional errors were comparable. However, for both the z-axis error and the air transfer channel errors, the molded Pneu-net performed poorly because these dimensions were significantly affected by the manual process of adhering the top and bottom layers of the actuator (lamination casting). This manual process caused uneven geometry at the lamination layer. The bottom section of the molded Pneu-net actuator was thinner compared to the 3D printed actuator. As a result, we observed a 23.7° bend angle difference between the two actuators.

Overall, performance results of the 3D printed 4 channel tentacle and Pneu-net actuator varied less compared to their molded counterparts. The dimensional error results in the cross-sectional areas, which directly affect the performance, were similar for both the molded and 3D printed robots. Moreover, the

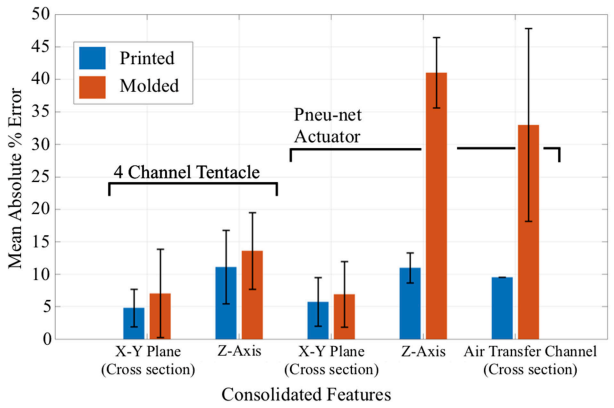

FIGURE 11 | Dimensional quality comparison (Yirmibesoglu et al., 2018).

wall thicknesses of the molded actuators were thicker than the 3D printed ones because the elastomer expands with the mold during the curing process. The dimensional comparison results suggested that the 3D printed soft robots should expand more, as they had thinner walls compared to the molded counterparts, but the experiments showed the opposite. Due to these observations, the following section describes a stiffness analysis that was performed to resolve this discrepancy.

Effects of Fabrication Methods, Nozzle Size, and Print Direction on the Stiffness of PDMS Material

In this section, we first focused on the effects of fabrication methods (molding vs. 3D printing) on the stiffness of PDMS material which is directly related to the performance differences observed in the previous section. We then investigated the effects of nozzle size and print direction (**Figure 6**) on the stiffness of PDMS material to understand if the stiffness property of the PDMS can be changed by these specific parameters.

In **Table 1** we compared the effects of fabrication methods with different available cure times[2] on the Young's modulus of the same material (DS10). For the molding method, we compared the effects of slow, medium, fast and very fast cure times on the stiffness of DS10. For 3D printing method, we only used very fast cure time and compared the stiffness result with its molded counterpart. The results for the molding method with different cure times (**Table 1**) show that DS10-slow has the highest Young's modulus. However, the wait time for the material to settle to its final mechanical properties is 7 h. In contrast to the molding method, the use of 3D printing method to fabricate the same object with DS10-very-fast provides equivalent or better stiffness results with faster fabrication times.

Even though we used the same materials for the different fabrication techniques of the 4 channel tentacles and Pneu-net actuators, there was only one difference that we neglected in our previous work (Yirmibesoglu et al., 2018). Since DS10-very-fast material's pot-life was 4 min, it was not possible to mold the actuator designs. Despite our molding experience, the material would begin to cure before fully filling the mold and settling. Due to this fact, and the indication from the manufacturer that DS10 product lines have the same mechanical properties, we used DS10-slow for fabricating the molded counterparts. With the results on cure time from **Table 1**, we verified that the use of DS10-slow or very-fast materials with the molding method does not necessarily change the overall actuator stiffness. The Young's modulus measurements for DS10-slow and DS10-very-fast are within a standard deviation of each other. However, the use of DS10-very-fast with the 3D printing method might have increased the stiffness of the fabricated soft robots due to a small region of overlap (135.5–140.2 kPa) between the Young's modulus measurements. The maximum Young's modulus of the molded DS10-slow material was 140.2 kPa whereas the maximum Young's modulus for the 3D printed DS10-very-fast material was 158.5 kPa. The 3D printed actuators had a higher stiffness, resulting in the observed performance differences reported in the previous section. The molded 4 channel tentacle could not apply the same force as the 3D printed counterpart because it was less stiff, and in the case of Pneu-net actuator, since the molded actuator is less stiff than the 3D printed one, it achieved higher bend angle.

TABLE 1 | Effects of fabrication method on Young's modulus with different available cure times.

Dragon Skin 10 product line and fabrication method	Cure time[2] (h)	Young's modulus (kPa)	Standard deviation (kPa)
Slow (molded)	7	135.9	4.3
Medium (molded)	5	108.3	5.4
Fast (molded)	1.25	100.0	12.3
Very fast (molded)	0.5	128.9	10.1
Very fast (3D printed–crisscross–0.839 mm nozzle)	0.5	147.0	11.5

The results illustrated in **Table 2** clearly indicate that when the nozzle size decreases the printed material becomes stiffer. The increase in stiffness could be due to preferential polymer chain alignments caused by the decrease in nozzle diameter, but these effects were not studied as they were not within the scope of the work. The amount of micro air bubbles introduced into the material and the total weight of each printed test samples may play a role in the final results as well. We recorded the weights of each dumbbell test samples to make sure that there was not an outlier in each category shown in **Supplementary Table 6**. At the moment, we cannot compare the significance of these 3 variables: polymer chain alignment, air bubbles, and the total weight of the samples on the final results seen in **Table 2**.

Young's modulus results for different print directions with a fixed nozzle size are shown in **Table 3**. The standard deviation ranges for each category overlap the measured values; thus, we cannot distinguish the effects of different print directions on the stiffness of the test pieces. Unlike the thermoplastic

[2]https://www.smooth-on.com/product-line/dragon-skin/ (accessed: April 2019)

TABLE 2 | Effects of nozzle size on Young's modulus.

Nozzle size (mm)	Young's modulus (kPa)	Standard deviation (kPa)
0.417	160.8	6.5
0.839	147.0	11.5
1.019	96.5	5.1

TABLE 3 | Effects of print direction on Young's modulus.

Print directions (at 0.839 mm nozzle size)	Young's modulus (kPa)	Standard deviation (kPa)
Perimeters	147.7	4.1
Longitudinal	140.5	11.0
Transverse	152.1	15.6
Cross (0°/90°)	145.3	4.8
Crisscross (45°/−45°)	147.0	11.5

polyurethane (TPU) material which causes 3D printed actuators to have anisotropic properties (Fernandez-Vicente et al., 2016; Yap et al., 2016), thermoset PDMS material seems to maintain its isotropy in the 3D printing process. Therefore, contrary to TPU material, print direction does not significantly affect the stiffness of the final PDMS product at to 0.839 mm nozzle size. It can be assumed that down to 0.839 mm nozzle size, use of different print directions will not affect the stiffness of the final PDMS product. However, when the nozzle size further decreases the preferential alignment of the polymer chains of the PDMS material may cause print directions to change stiffness. This result also provides an opportunity to choose an appropriate print direction to increase the surface finish quality of the fabricated parts without compromising the stiffness (**Supplementary Figure 9**).

In summary, sections Robot performance comparison: 3D printed vs. molded and Effects of fabrication methods, nozzle size, and print direction on the stiffness of PDMS material support that the 3D printing method with the use of small nozzle sizes increased the stiffness of the fabricated soft robots and maintained more accurate dimensions as defined in the CAD models. These results lead 3D printed soft robots to perform better than or equal to their molded counterparts while being more reliable and robust. Verifying the reliable operation of the 3D printed soft robots will allow more soft robotic applications to emerge under radiation environments.

CONCLUSION

In order to assess the usefulness of soft robots in radiation environments, changes in the mechanical properties such as elongation, tensile strength, and compression of the PDMS material were measured after gamma irradiation. We analyzed the viability of soft robots under 3 radiation environments selected from the nuclear power industry. Finally, we submerged and operated a 3D printed soft robot in a radiation environment and measured the absorbed dose rate to estimate its operation time. To ensure the reliability of the 3D printed soft robots and verify their performances, we compared them with their molded counterparts; the blocked force and the bend angle experiments were tested on four channel tentacle and Pneu-net actuators. To analyze performance results in detail, we also investigated dimensional errors and the effects of fabrication methods, nozzle size, and print direction on the stiffness of PDMS material.

The preliminary evaluation of the properties of PDMS under certain irradiation conditions concludes that with increasing exposure to gamma irradiation, the mechanical properties of PDMS decreased in functionality. However, up to 20 kGy gamma radiation, the elongation and tensile strength of the material are minimally impacted. Considering the fractional changes to the PDMS mechanical properties, it is safe to assume that soft robots could operate for the 12-h task time in two of the three proposed radiation environments. Also, the 3D printing method increased the stiffness of the fabricated soft robots and maintained more accurate dimensions as defined in the CAD models. Therefore, 3D printed soft robots performed better than or equal to their molded counterparts while being more reliable and robust.

The main limitation of this study was due to the difficulties of experimenting under gamma irradiation. We were unable to quantify the performance change of the hexapus robot due to lack of camera equipment that can work in underwater radiation environments. Additionally, any electronics required for actuation of the robot would not survive doses up to 400 kGy; thus detailed failure characterization including equibiaxial strain tests at the inflation state could not be performed. Instead, elongation at break and stiffness were used as measures of mechanical changes due to their predictable effects and direct relation to the functionality of the PDMS material. Even with these limitations, this study provides a preliminary method for assessing the potential of soft robots in radiation environments. While full functional tests will be required to deploy soft robots in nuclear environments, current findings show great promise for soft robots in high dose radiation environments. Future work will focus on quantifying the functionality of a 3D printed soft robot outside of an aquatic environment under radiation with radiation hardened test equipment.

The authors believe that soft robots under radiation environments warrant further study since the mechanical properties of the PDMS material studied showed great promise under radiation. Advantages provided by 3D printing of PDMS will give the opportunity to design and fabricate more complex robots for the soft robotics community. Future developments in this field will allow researchers to broaden the application fields of soft robotics.

AUTHOR CONTRIBUTIONS

OY is the main author who designed and developed the 3D silicone printer and carried on the experiments, sample preparations, 3D printing soft robots, and their analysis. He prepared the draft as the main author. Also, he conducted the irradiation experiment for the hexapus robot. TO is the second author who prepared radiation test samples, conducted irradiation tests and interpreted results for the

radiation environments. Sections from his thesis are used as subsections of the manuscript. GO is the third author who assisted with experiment design and interpretation of the results. CP supervised radiation research studies and provided helpful comments. YM supervised the research, guided its progress, provided helpful comments as main author's Ph.D. supervisor.

FUNDING

3D silicone printing project was supported by the Office of Naval Research Young Investigator Program (ONR YIP N00014-16-1-2529; P.O. Tom McKenna), the DARPA Robotics Fast Track (RFT) Program, and the New Device Group at Intel (Dr. Jeremy Parra, Director of Human Health and Performance). Analysis of the mechanical property changes of PDMS material under radiation was sponsored by NNSA NA-241 Human Capital Development through Idaho National Laboratory.

ACKNOWLEDGMENTS

Special thanks to Dr. Leah Minc, for her assistance with the activation analysis of the neutron-irradiated samples and her capacity for radioisotope identification; Dr. Scott Menn, for his assistance with the radiation safety aspects of all the experiments performed, especially with the GammaCell 220 experiments; Dr. Steven Reese, for his assistance with utilizing the Oregon State University's TRIGA research reactor for neutron irradiations of the PDMS samples; Robert Schickler for his assistance inside the radiation center experiment setup preparations. Also, we would like to thank Callie Branyan for her assistance on proofreading. Finally, the authors would like to thank our undergraduate assistants Grant T. Ballard, Hansung Kim, and Anushka Pandey for their assistance on print material preparations and force calculation experiments.

This work is an extended version of our previous conference paper: © [2018] IEEE. Reprinted, with permission, from Yirmibesoglu et al. (2018) License number for text extract: 4455580625594 and the license number for figures: 4455580955238

Radiation environment studies are extended based on the second author's thesis: (Oshiro, 2018).

SUPPLEMENTARY MATERIAL

The Supplementary Material for this article can be found online at: https://www.frontiersin.org/articles/10.3389/frobt.2019.00040/full#supplementary-material

REFERENCES

Bartlett, N. W., Tolley, M. T., Overvelde, J. T., Weaver, J. C., Mosadegh, B., Bertoldi, K., et al. (2015). A 3D-printed, functionally graded soft robot powered by combustion. *Science* 349, 161–165. doi: 10.1126/science.aab0129

Basfar, A. A. (1997). Hardness measurements of silicone rubber and polyurethane rubber cured by ionizing radiation. *Radiat. Phys. Chem.* 50, 607–610. doi: 10.1016/S0969-806X(97)00123-0

Bonin, H. W., Walker, M. W., and Bui, V. T. (2004). Application of polymers for the long-term storage and disposal of low- and intermediate-level radioactive waste. *Nucl. Tech.* 38, 82–101. doi: 10.13182/NT04-A3462

Camino, G., Lomakin, S. M., and Lageard, M. (2002). Thermal polydimethylsiloxane degradation. Part 2. The degradation mechanisms. *Polymer* 43, 2011–2015. doi: 10.1016/S0032-3861(01)00785-6

Camino, G., Lomakin, S. M., and Lazzari, M. (2001). Polydimethylsiloxane thermal degradation part 1. Kinetic aspects. *Polymer* 42, 2395–2402. doi: 10.1016/S0032-3861(00)00652-2

Charlesby, A. (1955). Changes in silicone polymeric fluids due to high-energy radiation. *Proc. R. Soc.* 230, 120–135. doi: 10.1098/rspa.1955.0116

Comstock, M. J. (1989). "The effects of radiation on hightechnology polymers," in *ACS Symposium Series*, Vol. 381, eds E. Reichmanis and J. H. O'Donnell (Washington, DC: American Chemical Society), 1–13.

Drotman, D., Jadhav, S., Karimi, M., deZonia, P., and Tolley, M. T. (2017). "3D Printed Soft Actuators for a Legged Robot Capable of Navigating Unstructured Terrain." in *2017 IEEE International Conference on Robotics and Automation*, (Singapore: IEEE), 5532–5538. doi: 10.1109/ICRA.2017.7989652

Fackler, M. (2017). *Six Years After Fukushima, Robots Finally Find Reactors' Melted Uranium Fuel*. The New York Times. (2017). Available online at: https://www.nytimes.com/2017/11/19/science/japan-fukushima-nuclear-meltdown-fuel.html (accessed April 2019).

Fernandez-Vicente, M., Calle, W., Ferrandiz, S., and Conejero, A. (2016). Effect of infill parameters on tensile mechanical behavior in desktop 3D printing. *3D Print. Additive Manufact.* 3, 183–192. doi: 10.1089/3dp.2015.0036

Frame, J., Lopez, N., Curet, O., and Engeberg, E. D. (2018). Thrust force characterization of free-swimming soft robotic Jellyfish. *Bioinspir. Biomimet.* 13:064001. doi: 10.1088/1748-3190/aadcb3

Gorissen, B., Reynaerts, D., Konishi, S., Yoshida, K., Kim, J. W., De Volder, M., et al. (2017). Elastic inflatable actuators for soft robotic applications. *Adv. Mater.* 29:1604977. doi: 10.1002/adma.201604977

Hardin, J. O., Ober, T. J., Valentine, A. D., and Lewis, J. A. (2015). Microfluidic printheads for multimaterial 3D printing of viscoelastic inks. *Adv. Mater.* 27, 3279–3284. doi: 10.1002/adma.201500222

Hess, C. J., and Metzger, S. W. (1985). Steady progress at TMI-2. *Int. Atomic Energy Agency Bull.* 17, 16–22.

Hill, D. J. T., Preston, C. M. L., Whittaker, A. K., and Hunt, S. M. (2000). The radiation chemistry of Poly(Dimethyl-Siloxane). *Macromolecul. Sympos.* 156, 95–102. doi: 10.1002/1521-3900(200007)156:1<95::AID-MASY95>3.0.CO;2-E

Holland, D. P., Park, E. J., Polygerinos, P., Bennett, G. J., and Walsh, C. J. (2014). The soft robotics toolkit: shared resources for research and design. *Soft Robot.* 1, 224–230. doi: 10.1089/soro.2014.0010

Hu, W., Lum, G. Z., Mastrangeli, M., and Sitti, M. (2018). Small-scale soft-bodied robot with multimodal locomotion. *Nature* 554, 81–85. doi: 10.1038/nature25443

Ilievski, F., Mazzeo, A. D., Shepherd, R. F., Chen, X., and Whitesides, G. M. (2011). Soft robotics for chemists. *Angew. Chem. Int. Edn.* 50, 1890–1895. doi: 10.1002/anie.201006464

Kastor, N., Vikas, V., Cohen, E., and White, R. D. (2017). A definition of soft materials for use in the design of robots. *Soft Robot.* 4, 181–182. doi: 10.1089/soro.2017.29012.nka

Laschi, C., Mazzolai, B., and Cianchetti, M. (2016). Soft robotics: technologies and systems pushing the boundaries of robot abilities. *Sci. Robot.* 1:eaah3690. doi: 10.1126/scirobotics.aah3690

Lee, C., Kim, M., Kim, Y. J., Hong, N., Ryu, S., Kim, H. J., et al. (2017). Soft robot review. *Int. J. Control Automat. Syst.* 15, 3–15. doi: 10.1007/s12555-016-0462-3

Lovering, D. (2009). *Radioactive Robot: the Machines that Cleaned Up three Mile Island - Scientific American*. Scicence American (2009). Available online at: https://www.scientificamerican.com/article/three-mile-island-robots/ (accessed April 2019).

MacCurdy, R., Katzschmann, R., Kim, Y., and Rus, D. (2016). "Printable hydraulics: a method for fabricating robots by 3D Co-printing solids and liquids." in *2016 IEEE International Conference on Robotics and Automation (ICRA)*, (Stockholm: IEEE), 3878–3885. doi: 10.1109/ICRA.2016.7487576

Majidi, C. (2014). Soft robotics: a perspective—current trends and prospects for the future. *Soft Robot.* 1, 5–11. doi: 10.1089/soro.2013.0001

Marchese, A. D., Katzschmann, R. K., and Rus, D. (2014). "Whole arm planning for a soft and highly compliant 2D robotic manipulator." in *2014 IEEE/RSJ International Conference on Intelligent Robots and Systems*. (Chicago, IL: IEEE), 554–60 doi: 10.1109/IROS.2014.6942614

Marchese, A. D., Katzschmann, R. K., and Rus, D. (2015). A recipe for soft fluidic elastomer robots. *Soft Robot.* 2, 7–25. doi: 10.1089/soro.2014.0022

Marchese, A. D., and Rus, D. (2016). Design, kinematics, and control of a soft spatial fluidic elastomer manipulator. *Int. J. Robot. Res.* 35, 840–869. doi: 10.1177/0278364915587925

Mary-Ann, R. (2015). *Fukushima: Robot 'dies' 3 Hours After Entering Japan's Radioactive Reactor*. International Business Times. (2015). Available online at: https://www.ibtimes.co.uk/fukushima-robot-dies-3-hours-after-entering-japans-radioactive-reactor-1496126 (accessed April 2019).

McCarthy, D. W., and Mark, J. E. (1998). "Poly(Dimethylsiloxane) elastomers from aqueous emulsions: III. Effects of blended silica fillers and gamma-radiation-induced crosslinking. *Rubber Chem. Tech.* 71, 941–948. doi: 10.5254/1.3538519

McCurry, J. (2017). *Dying Robots and Failing Hope: Fukushima Clean-up Falters Six Years after Tsunami*. The Guardian. (2017). Available online at: https://www.theguardian.com/world/2017/mar/09/fukushima-nuclear-cleanup-falters-six-years-after-tsunami (accessed April 2019).

Miller, A. A. (1960). Radiation chemistry of polydimethylsiloxane. I. crosslinking and gas yields. *J. Am. Chem. Soc.* 82, 3519–3523. doi: 10.1021/ja01499a011

Moore, T. (1985). Robots for nuclear power plants. *Int. Atomic Energy Agency Bull.* 17, 31–38.

Morrow, J., Hemleben, S., and Menguc, Y. (2017). Directly fabricating soft robotic actuators with an open-source 3-D printer. *IEEE Robot. Automation Lett.* 2, 277–281. doi: 10.1109/LRA.2016.2598601

Mosadegh, B., Polygerinos, P., Keplinger, C., Wennstedt, S., Shepherd, R. F., Gupta, U., et al. (2014). Pneumatic networks for soft robotics that actuate rapidly. *Adv. Funct. Mater.* 24, 2163–2170. doi: 10.1002/adfm.201303288

Nagatani, K., Kiribayashi, S., Okada, Y., Otake, K., Yoshida, K., Tadokoro, S., et al. (2011a). "Gamma-ray irradiation test of electric components of rescue mobile robot quince - toward emergency response to nuclear accident at fukushima daiichi nuclear power station on March 2011." in *9th IEEE International Symposium on Safety, Security, and Rescue Robotics,* SSRR 2011, (Kyoto: IEEE), 56–60. doi: 10.1109/SSRR.2011.6106756

Nagatani, K., Kiribayashi, S., Okada, Y., Tadokoro, S., Nishimura, T., Yoshida, T., et al. (2011b). "Redesign of rescue mobile robot quince." in *2011 IEEE International Symposium on Safety, Security, and Rescue Robotics*, (Kyoto: IEEE), 13–18 doi: 10.1109/SSRR.2011.6106794

Ober, T. J., Foresti, D., and Lewis, J. A. (2015). Active mixing of complex fluids at the microscale. *Proc. Natl. Acad. Sci. U. S. A.* 112, 12293–12298. doi: 10.1073/pnas.1509224112

Oshiro, T. (2018). *Soft Robotics in Radiation Environments : A Prospective Study of an Emerging Automated Technology for Existing Nuclear Applications*. Corvallis, OR: Oregon State University. Available online at: https://ir.library.oregonstate.edu/concern/graduate_thesis_or_dissertations/9c67wt10b?locale=en (accessed April 2019).

Peele, B. N., Wallin, T. J., Zhao, H., and Shepherd, R. F. (2015). 3D printing antagonistic systems of artificial muscle using projection stereolithography. *Bioinspir. Biomimet.* 10:055003. doi: 10.1088/1748-3190/10/5/055003

Plott, J., and Shih, A. (2017). The extrusion-based additive manufacturing of moisture-cured silicone elastomer with minimal void for pneumatic actuators. *Addit. Manufact.* 17, 1–14. doi: 10.1016/j.addma.2017.06.009

Ranzani, T., Russo, S., Bartlett, N. W., Wehner, M., and Wood, R. J. (2018). Increasing the dimensionality of soft microstructures through injection-induced self-folding. *Adv. Mater.* 30:1802739. doi: 10.1002/adma.201802739

Rus, D., and Tolley, M. T. (2015). Design, fabrication and control of soft robots. *Nature* 521, 467–475. doi: 10.1038/nature14543

Schmitt, F., Piccin, O., Barbé, L., and Bayle, B. (2018). Soft robots manufacturing: a review. *Front. Robot. AI* 5:84. doi: 10.3389/frobt.2018.00084

Sharp, R. E., and Garlick, D. R. (1994). *Radiation Effects on Electronic Equipment: A Designers'/Users' Guide for the Nuclear Power Industry*. Available online at: https://inis.iaea.org/search/search.aspx?orig_q=RN:25067411 (accessed April 2019).

Sheldrick, A., and Funakoshi, M. (2016). *Fukushima's Ground Zero: No Place for Man or Robot*. Reuters. (2016). Available online at: https://www.reuters.com/article/us-japan-disaster-decommissioning/fukushimas-ground-zero-no-place-for-man-or-robot-idUSKCN0WB2X5 (accessed April 2019).

Sias, F. R. (2005). *Lost-Wax Casting: Old, New, and Inexpensive Methods*. Woodsmere Press. https://books.google.com/books/about/Lost_wax_Casting.html?id=e_09Enaf4tIC (accessed April 2019).

Singh, P. K., and Krishna, M. C. (2014). Continuum arm robotic manipulator: a review. *Univ. J. Mech. Eng.* 2, 193–198. doi: 10.13189/ujme.2014.020603

Tolley, M. T., Shepherd, R. F., Mosadegh, B., Galloway, K. C., Wehner, M., Karpelson, M., et al. (2014). A resilient, untethered soft robot. *Soft Robot.* 1, 213–223. doi: 10.1089/soro.2014.0008

Trimmer, B., Lewis, J. A., Shepherd, R. F., and Lipson, H. (2015). 3D printing soft materials: what is possible? *Soft Robot*. 2, 3–6. doi: 10.1089/soro.2015.1502

Trivedi, D., Rahn, C. D., Kier, W. M., and Walker, I. D. (2008). Soft robotics: biological inspiration, state of the art, and future research. *Appl. Bionics Biomech.* 5, 99–117. doi: 10.1155/2008/520417

Truby, R. L., and Lewis, J. A. (2016). Printing soft matter in three dimensions. *Nature* 540, 371–378. doi: 10.1038/nature21003

Urabe, E., and Stapczynski, S. (2017). *Fukushima Fuel-Removal Quest Leaves Trail of Dead Robots*. The Japan Times. (2017). Available online at: https://www.japantimes.co.jp/news/2017/02/17/national/fukushima-fuel-removal-quest-leaves-trail-dead-robots/ (accessed April 2019).

Voorde, M. H. V., and Restat, C. (1972). *Selection Guide to Organic Materials for Nuclear Engineering*. Geneva: CERN.

Walker, S., Daalkhaijav, U., Thrush, D., Branyan, C., Dogan Yirmibesoglu, O., Olson, G., et al. (2018). "Zero-support 3D printing of thermoset silicone via simultaneous control of both reaction kinetics and transient rheology," in *3D Printing and Additive Manufacturing Accepted* (Corvallis, OR), 1–9. doi: 10.1089/3dp.2018.0117

Walker, S., Yirmibeşoglu, O. D., Daalkhaijav, U., and Mengüç, Y. (2019). "Additive Manufacturing of Soft Robots." in *Robotic Systems and Autonomous Platforms*, eds S. M. Walsh and M. S. Strano (Corvallis, OR: Elsevier), 335–59. doi: 10.1016/B978-0-08-102260-3.00014-7

Warrick, E. L. (1955). Effects of radiation on organopolysiloxanes. *Indus. Eng. Chem.* 47, 2388–2393. doi: 10.1021/ie50551a053

Xia, Y., and Whitesides, G. M. (1998). Soft lithography. *Angew. Chem. Int. Edn.* 37, 550–575. doi: 10.1002/(SICI)1521-3773(19980316)37:5<550::AID-ANIE550>3.0.CO;2-G

Yap, H. K., Ng, H. Y., and Yeow, C. H. (2016). High-force soft printable pneumatics for soft robotic applications. *Soft Robot.* 3, 144–158. doi: 10.1089/soro.2016.0030

Yirmibesoglu, O. D., Morrow, J., Walker, S., Gosrich, W., Canizares, R., Kim, H., et al. (2018). "Direct 3D printing of silicone elastomer soft robots and their performance comparison with molded counterparts," in *2018 IEEE International Conference on Soft Robotics (RoboSoft)*, Livorno: IEEE, 295–302. doi: 10.1109/ROBOSOFT.2018.8404935

Yuk, H., and Zhao, X. (2018). A New 3D printing strategy by harnessing deformation, instability, and fracture of viscoelastic inks. *Adv. Mater.* 30:1704028. doi: 10.1002/adma.201704028

Zhao, H., Li, Y., Elsamadisi, A., and Shepherd, R. (2015). Scalable manufacturing of high force wearable soft actuators. *Extreme Mech. Lett.* 3, 89–104. doi: 10.1016/j.eml.2015.02.006

Conflict of Interest Statement: The authors declare that the research was conducted in the absence of any commercial or financial relationships that could be construed as a potential conflict of interest.

frontiers in Robotics and AI

ORIGINAL RESEARCH
published: 20 June 2019
doi: 10.3389/frobt.2019.00045

Characterization of the Growing From the Tip as Robot Locomotion Strategy

Emanuela Del Dottore, Alessio Mondini, Ali Sadeghi and Barbara Mazzolai**

Center for Micro-BioRobotics, Istituto Italiano di Tecnologia, Pontedera, Italy

Growing robots are a new class of robots able to move in the environment exploiting a growing from the tip process (movement by growing). Thanks to this property, these robots are able to navigate 3D environments while negotiating confined spaces and large voids by adapting their body. During the exploration of the environment, the tip of the robot is able to move in any direction and can be kinematically considered as a non-holonomic mobile system. In this paper, we show the kinematics of robot growing at its tip level. We also present the affordable workspace analyzed by an evaluation of feasible trajectories toward target poses. The geometrical key parameters imposing constraints on growing robots' workspace are discussed, in view of facing different possible application scenarios. The proposed kinematics was applied to a plant-inspired growing robot moving in a 3D environment in simulation, obtaining ∼2 cm error after 1 m of displacement. With appropriate parametrization, the proposed kinematic model is able to describe the motion from the tip in robots able to grow.

Keywords: growing robot, kinematics, 3D navigation, bioinspiration, soft robotics

OPEN ACCESS

Edited by:
S. M. Hadi Sadati,
University of Bristol, United Kingdom

Reviewed by:
Surya Girinatha Nurzaman,
Monash University Malaysia, Malaysia
Chongjing Cao,
University of Bristol, United Kingdom

****Correspondence:***
Emanuela Del Dottore
emanuela.deldottore@iit.it
Barbara Mazzolai
barbara.mazzolai@iit.it

Specialty section:
This article was submitted to Soft Robotics, a section of the journal Frontiers in Robotics and AI

Received: *08 December 2018*
Accepted: *31 May 2019*
Published: *20 June 2019*

Citation:
Del Dottore E, Mondini A, Sadeghi A and Mazzolai B (2019) Characterization of the Growing From the Tip as Robot Locomotion Strategy. Front. Robot. AI 6:45. doi: 10.3389/frobt.2019.00045

INTRODUCTION

The ability of robots to move and interact with the environment is of fundamental importance for the accomplishment of demanded tasks in out-of-factory scenarios. Several kind of locomotion have been studied and adopted for different applications: in-pipe inspection (Mirats Tur and Garthwaite, 2010), medical (Phee et al., 1997; Dario and Mosse, 2003), aerial (Colomina and Molina, 2014), terrestrial (Siegwart et al., 2011), or marine (Seto, 2013) exploration. Among many solutions, animal-like locomotion strategies have been implemented in several different robotic platforms to improve performance and compliancy with the environment (Sfakiotakis et al., 1999; Armour et al., 2007; Bachmann et al., 2009; Cianchetti et al., 2015; Aguilar et al., 2016; Hooper and Büschges, 2017). More recently, plants have been explored in robotics leading to a new paradigm of locomotion, which is moving by growing (Sadeghi et al., 2013, 2014, 2017; Del Dottore et al., 2018b). This new class of robots can navigate the environment taking inspiration from the plants' feature to continuously increase the mass by adding new cellular material at their growing extremities, i.e., at shoot and root apexes (Verbelen et al., 2006). From an artificial perspective, this movement strategy can be exploited by additive manufacturing techniques (Sadeghi et al., 2017; Kayser et al., 2019) or skin eversion (Tsukagoshi et al., 2011; Sadeghi et al., 2013; Hawkes et al., 2017). This way, the robot is able to orient itself without the need of moving its entire body but confining the movement at its tip, while dynamically creating the robot's body and adapting its morphology to the environmental conditions and physical constraints. This feature qualifies robots able to grow for applications where the environment is not necessarily predefined or predictable, and high body adaptability is required (Laschi et al., 2016).

Being growth a new topic in robotics, the kinematics of such kind of movement is still poorly described in literature. Yet, to a certain extent, particularly from a kinematics point of view, a growing robot shows some similarities with systems implementing a follow-the-leader strategy, similarly to serpentine or hyper-redundant manipulators (Choset and Henning, 1999; Neumann and Burgner-Kahrs, 2016). This strategy of motion enables the extension of the backbone curve from the end effector location, while the antecedent part of the body follows the head direction. Such growth-like movement can be achieved either by propagating the curve forward from the base with the extension of discrete manipulator segments (Neumann and Burgner-Kahrs, 2016), and from the head down to the body (Choset and Henning, 1999), or with an extension from the tip with the release of a nested module (Gilbert et al., 2015; Kang et al., 2016). However, a follow-the-leader robot typically slides all its body, or a consistent part of it, during tip advancement, instead a growing robot permits to moves only its tip, while the consolidated structural body is fixed respect to the environment, reducing external friction and, thus, the energy required for moving (Sadeghi et al., 2013, 2014). Moreover, systems implementing follow-the-leader strategy are normally discretized, with a fixed number of segments (and joints) and a defined maximum length (and workspace in case of manipulators). On the contrary, a growing robot has not a predefined body, since this mainly depends by the added feeding material, and the robot can assume, in theory, an infinite number of configurations.

In the scenario of a robot growing at the tip and moving in space, the main question to be addressed is related to the path that the robot can take toward the target point, rather than the trajectory that the end effector makes to reach a specific point. In this view, we can compare the motion of this growing robot to that of a mobile robot able to navigate in a three dimensional space. To this end, it is important to describe the geometric configurations, or poses, of a growing robot and the potential environments that it can be able to navigate. Another important consideration is that a growing robot at the tip is a non-holonomic system, having a total of five DoF in configuration space (tip position in 3D space, and heading, and pitch angles) but only three controllable DoF at joint space, which are: two degrees of steerability (for tip orientation), plus one degree of mobility (the system velocity - in this case called growth velocity). These three degrees of maneuverability define together the space of possible configurations of a growing robot in 3D. For mobile robots, analyzing the workspace includes definition of how the robot moves between different poses, as well as of possible trajectories that the robot takes to reach a desired position with a specific orientation. The kinematic control of a system moving from a pose to another along a desired trajectory is often done by dividing the path in motion segments composed by straight lines and segments of a circle (Siegwart et al., 2011). When considering mechanical constraints, Dubin's path generation approaches (Dubins, 1957) are often used and adapted for the definition of feasible trajectories in 3D space (Ambrosino et al., 2009; Babaei and Mortazavi, 2010; Yu et al., 2015; Makdah et al., 2016).

In Del Dottore et al. (2018a), we provided a plant-inspired kinematic model, described in joint space, of a growing robot able to deposit new material from its tip in order to incrementally build its body (Sadeghi et al., 2017) and consequently move its exploratory tip forward. In that work we evaluated the error between target positions achieved in simulation and with the real robot after three different paths (2D curvilinear trajectories with arcs radius of 12.5, 17.5, and 22.5 cm), finding the maximal error of about 7% in 10 cm traveled in air. Here, we go forward providing a more thorough formalization of the kinematics, extending the description from joint to configuration space, and analyzing the space of maneuverability following the approach of non-holonomic systems. We present a strategy for defining suboptimal trajectories, with Dubin's path, for growing robots moving in 3D space and we describe the movements of the robot with our proposed kinematics. We also tested and evaluated our kinematic control in simulation parametrizing the model *in primis* with our plant-inspired growing robot, then testing robustness introducing different level of perturbations during growth, and finally with different settings of robot size and velocity.

In the following, we first describe the kinematics and the key design parameters affecting the behavior of growing robots (section Methods); then, we present the strategy proposed for defining 3D trajectories (section Results); and, finally, we discuss results of the simulations (section Discussions), followed by conclusive remarks (section Conclusions).

METHODS

Kinematics of Growing Robots

The characterization of the motion of a robot requires the definition of its kinematics and strategy to move from a point A to a point B in its configuration space. Based on the Chasles' theorem, any robot starting from (point) A, with a certain orientation, can reach (point) B, with another orientation, by means of a translation followed by a rotation of the body about its initial position (Siciliano and Khatib, 2008).

In Del Dottore et al. (2018a) there is an introduction of the forward kinematics, inspired by plant growth, describing the motion from the tip in 3D space through homogeneous transformation matrices. Starting from that, we can generalize the formulation by describing i as a moving coordinate frame, integral with the robot's tip, and j as the inertial frame (**Figure 1A**) (the entire dictionary of the symbols used throughout the paper is available in **Supplementary Material**). The origin of coordinate frame i relative to coordinate frame j can be denoted by the 3×1 vector:

$$ {}^{j}p_i = \begin{pmatrix} {}^{j}x_i \\ {}^{j}y_i \\ {}^{j}z_i \end{pmatrix}. \tag{1} $$

A generic point ${}^{i}r \in \mathbb{R}^3$ in frame i can be expressed in frame j as ${}^{j}r \in \mathbb{R}^3$ knowing the transformation matrix ${}^{j}R_i \in SO(3)$, with

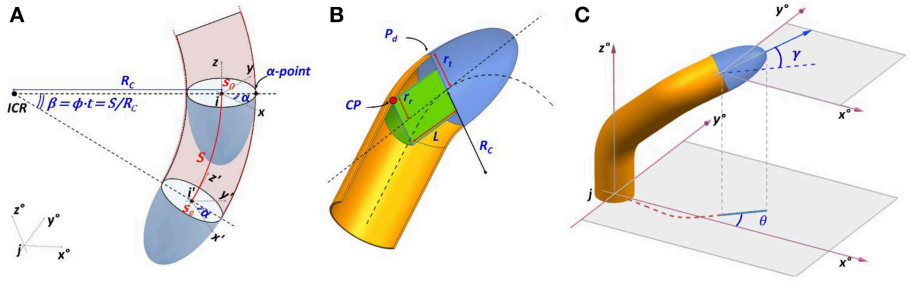

FIGURE 1 | (A) Schematic representation for the motion from the tip of growing robots. Frame ***i*** is integral with the tip, which moves within an inertial frame ***j***. A curvature with radius R_c is induced by a greater material deposition over the deposition plane (P_d) at a position identified with the angle α. After a period of time t have traveled a distance S of the arc around the center of rotation ***ICR***; **(B)** definition of pitch γ and heading θ angles; **(C)** visual overview of key parameters in the mechanics of growing robots with the contact point ***CP*** of internal components with the robot's body which define the minimum curvature radius.

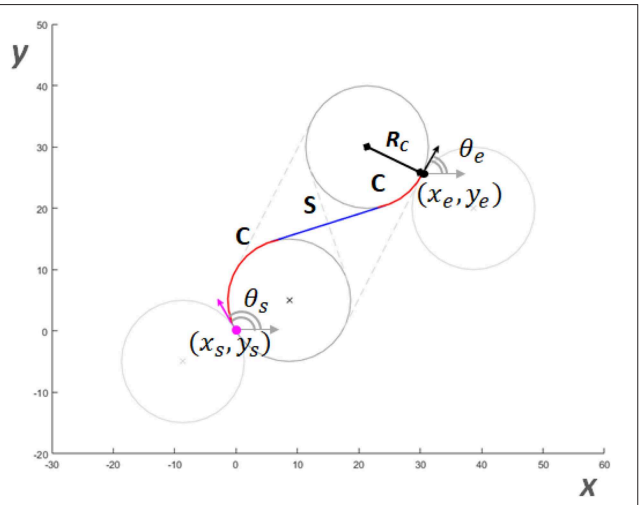

FIGURE 2 | An example of Dubin's path in 2D, from a starting configuration in position (x_s,y_s) and orientation θ_s respect to the x-axis, to a target configuration having position in (x_e,y_e) and orientation θ_e. The minimum path identified is composed by a first right curve, a straight line and a left curve. Each curvature has minimum curvature radius R_c.

the equation:

$$^{j}r = {}^{j}R_i \; i_r + {}^{j}p_i; \tag{2}$$

which can also be written as:

$$\begin{pmatrix} ^{j}r \\ 1 \end{pmatrix} = \begin{pmatrix} ^{j}R_i & ^{j}p_i \\ 0_{1\times3} & 1 \end{pmatrix} \begin{pmatrix} ^{i}r \\ 1 \end{pmatrix}, \tag{3}$$

where the first factor of the right hand is the homogenous transformation matrix $^{j}T_i \in SO(4)$. The forward kinematics of a growing robot can be described in the joint space, by identifying the joint-like position in the plane (P_d **Figure 1B**) between moving tip and body, where the process of growth is actuated. From a frame i, the next frame is obtained as a function of the growth velocity (g), position for the actuation of greatest material deposition [expressed as angle α w.r.t. the x axis in (frame) i] and intensity of bending in a unit of time (ϕ). With these actuation parameters we can formulate the sequence of post-multiplied transformations:

$$\begin{aligned} ^{i}T &= T_{z,\alpha} T_{tr,v} T_{y,\phi} T_{tr,-v} T_{z,-\alpha} \\ &= \begin{pmatrix} C_\alpha{}^2 C_\phi + S_\alpha{}^2 & C_\alpha S_\alpha C_\delta - C_\alpha S_\alpha & C_\alpha S_\phi & \frac{gC_\alpha(1-C_\phi)}{\phi} \\ C_\alpha C_\phi S_\alpha - C_\alpha S_\alpha & C_\alpha{}^2 + C_\phi S_\alpha{}^2 & S_\alpha S_\phi & \frac{gC_\alpha(1-S_\phi)}{\phi} \\ -C_\alpha S_\phi & -S_\alpha S_\phi & C_\phi & \frac{gS_\phi}{\phi} \\ 0 & 0 & 0 & 1 \end{pmatrix} \\ &= \begin{pmatrix} ^{i}R & ^{i}p \\ 0_{1\times3} & 1 \end{pmatrix}, \end{aligned} \tag{4}$$

where the first subscript of T indicates if T is a translation (tr) or a rotation matrix (by indicating around which axis), and the second subscript gives the angle of rotation or direction of translation (v); and by convention: $C_\alpha = \cos\alpha$ and $S_\alpha = \sin\alpha$. In (4), the greatest deposition is applied at the α-point along the circumference of the robot's tip, with respect to its x-y plane (**Figure 1A**) (the rotation $T_{z,\alpha}$ is used to localize this point and $T_{z,-\alpha}$ is used to rotate back the tip after the following transformations). Differently from Equation 6 in (Del Dottore et al., 2018a), the two discrete steps of motion (translation—for a vertical growth—and rotation—which describes a bending) are merged together in a single atomic action, obtained by $T_{tr,v}T_{y,\phi}T_{tr,-v}$, where v is the vector $[-R_c\ 0\ 0\ 1]^T$, which is used to localize the inertial center of rotation (ICR), and then the rotation of ϕ about the y axis (**Figure 1A**). Since R_c can be expressed as relation between the intensity of bending and growth velocity ($R_c = \frac{g}{\phi}$), the matrix in (4) can be obtained by substitution. When no bending is applied ($\phi = 0$), $\alpha = 0$ and the last column will define a straight growth. The kinematic chain that describes the moves done (or to be done) by the tip (with frame i) from an initial configuration s_0 to reach a final configuration s_e along its trajectory, in terms of frame j, is obtained by consecutive multiplication of the homogeneous transformation matrices obtained with Equation (4):

$$^{j}T_i(s_e) = \prod_{s_0}^{s_e} {}^{i}T(s_t). \tag{5}$$

As in mobile robotics, we can identify a path from s_0 to s_e composed by a sequence of turns and straight lines (Dubins, 1957; Siegwart et al., 2011), and obtain the transformation matrix ${}^{i}T\,(s_t)$ for each of the segments. The problem is to define a feasible path for the robot.

To approach this problem, we describe the kinematics in configuration space for the tip of a growing robot with:

$$\begin{cases} \dot{x} = g\cos\gamma\cos\theta \\ \dot{y} = g\cos\gamma\sin\theta \\ \dot{z} = g\sin\gamma \\ \dot{\theta} = u_1 \\ \dot{\gamma} = u_2, \end{cases} \tag{6}$$

where g, as previously defined, is the growth velocity, x, y, z are the components of ${}^{j}p_i$, θ is the orientation of the tip in the x-y plane of frame j, or heading, and γ is the orientation of the tip with respect to the plane x-y in frame j, or pitch (**Figure 1C**). u_1 and u_2 are the control inputs, that need to be determined and should satisfy geometric constraints imposed by the robot mechanics on a minimum curvature radius reachable by the system ($|R_c| \geq R_{\min}$).

From a geometric point of view, the $R_{\min}$ is the main parameter limiting the affordable workspace of a growing robot, given a maximum allowable body displacement or that should be reached within a certain time. The minimum curvature radius is defined by geometric parameters of the mechanism with the following relations:

$$R_{\min} = \frac{L^2 - {r_t}^2 + {r_r}^2}{2\cdot(r_t - r_r)}, \tag{7}$$

where r_t, r_r and L are parameters dependent on robot design (**Figure 1B**). As in vehicles, r_t is the distance between the central line and the external lateral line where the wheel is located or, as in the case of growing robots, where the material is incrementally added; L is the distance between the steerable component (represented by the material added in the plane of growth actuation P_d) and the backward extremity of non-steerable module, if any (ideally, the wheelbase in a vehicle); and r_r is the distance between the central line and the external side of the virtual cylinder encapsulating the internal components.

It should be noted that the parameters r_r and L in (7) strictly depend on the configuration of internal components, which can be arranged differently from a cylindrical shape; however, we can approximate the bulkiness with the virtual cylinder built around the most cumbersome component in the assembly, considering it symmetric respect to the central line.

$R_{\min}$ and the growth velocity g supply the maximum bending angle variation per unit of time [as in Equation (8)], which also represents the constraint for both control inputs (u_1 and u_2):

$$0 \leq u_i \leq \frac{g}{R_{\min}}. \tag{8}$$

The workspace of a growing robot can now be described by evolving Equation (6) and imposing the constraint (8). Formally, there is always a path from any two points in 3D space (free of obstacles) that the robot can perform, with a desired destination and orientation; the only limiting factor on the workspace, when only geometric parameters are considered, is basically imposed by the material available to grow.

Path Planning

Let's define an initial state $\mathcal{X}_s = \langle x_s, y_s, z_s, \theta_s, \gamma_s \rangle$ and a target final state $\mathcal{X}_e = \langle x_e, y_e, z_e, \theta_e, \gamma_e \rangle$ in the inertial frame. To find feasible paths for growing robots, solutions based on Dubin's path generation can be adopted bringing the tip from $\mathcal{X}_s$ to $\mathcal{X}_e$. Dubin's paths have been formalized for 2D motion planning of mobile robots and used to find optimal paths under curvature constraints (Dubins, 1957). In 2D, a minimum path is a path between a starting $\mathcal{Y}_s = \langle x_s, y_s, \theta_s \rangle$ and a final state $\mathcal{Y}_e = \langle x_e, y_e, \theta_e \rangle$ which can be composed by S straight segments or C curvatures, with several combinations: S, C, SC, CS, CSC, CC, CCC. If a solution with one or two segments is not available, the approach is to trace the tangent lines common to the four circles having $\mathcal{Y}_s$ and $\mathcal{Y}_e$ as tangent vectors, and selecting the path with minimum length (**Figure 2**). This approach guarantees the optimal solutions connecting $\mathcal{Y}_s$ to $\mathcal{Y}_e$. When moving the problem from 2D to 3D space, for instance to define the trajectory of unmanned aerial vehicles, the resolution of the minimum path becomes complex and computationally burdensome. For this reason, a suboptimal path by merging multiple approaches [e.g., Dubin's path, trajectory smoothing, interpolation between waypoints (Hwangbo et al., 2007; Ambrosino et al., 2009; Babaei and Mortazavi, 2010; Yu et al., 2015)] is typically proposed.

Similarly, we addressed the problem of finding a suboptimal solution in 3D by dividing the problem into two optimal problems with curvature constraints: find the optimal path in 2D over two selected planes, $\mathcal{T}_s$ and $\mathcal{T}_e$, that intersect each other (where $P_s = \begin{bmatrix} x_s\, y_s\, z_s \end{bmatrix}^T$ and $P_e = \begin{bmatrix} x_e\, y_e\, z_e \end{bmatrix}^T$ lie, respectively) (**Figure 3A**).

We adopted a similar approach to Babaei and Mortazavi (2010), in which a trajectory is traced from a starting position that lies on one plane to a target position lying on a second plane, and passing from a waypoint located at the intersection of the two planes. In fact, if the tip of the growing robot arrives to lie on the intersecting line, it can easily pass from one plane to another just changing the deposition point (its α angle).

To select $\mathcal{T}_s$ and $\mathcal{T}_e$ we traced the line $\mathcal{L}_t$ (**Figure 3A**) passing through P_s and P_e, and we defined $\mathcal{T}_s$ as the plane having the normal:

$$\hat{n}_s = \frac{\hat{v}_{se} \times \hat{v}_s}{\left\| \hat{v}_{se} \times \hat{v}_s \right\|_2}, \tag{9}$$

and analogously, $\mathcal{T}_e$ is selected as having the normal:

$$\hat{n}_e = \frac{\hat{v}_{se} \times \hat{v}_e}{\left\| \hat{v}_{se} \times \hat{v}_e \right\|_2}, \tag{10}$$

where $\hat{v}_s$ is the unit vector of the tip direction at starting position, $\hat{v}_e$ is the unit vector of the tip direction at final position, and $\hat{v}_{se}$ is obtained by:

$$\hat{v}_{se} = \frac{P_e - P_s}{\|P_e - P_s\|_2}. \tag{11}$$

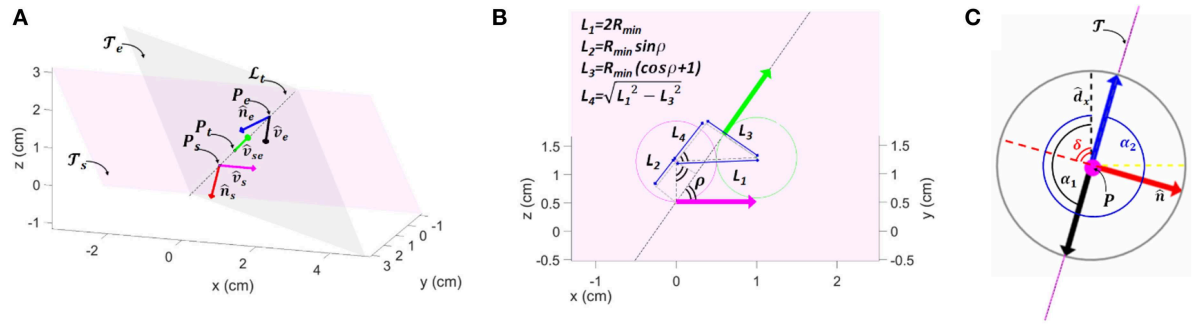

FIGURE 3 | Schematic representation for Dubin's path approach used for 3D resolution. **(A)** The two planes $\mathcal{T}_s$ and $\mathcal{T}_e$ where starting $\hat{v}_s$ and target $\hat{v}_e$ vectors lie on. **(B)** Key parameters to localize the target position along the line of intersection between $\mathcal{T}_s$ and $\mathcal{T}_e$. **(C)** Top view of growing robot rip, with the two angles α_1 and α_2 of the possible deposition allowing the robot to move over the plane $\mathcal{T}$. In **(C)** Dashed yellow line is the ***y***-axis of the tip coordinate system, black dashed line is the ***x***-axis and magenta is the ***z***-axis, where also the tip direction lies; blue and black arrows are the vectors toward the two possible angles of deposition.

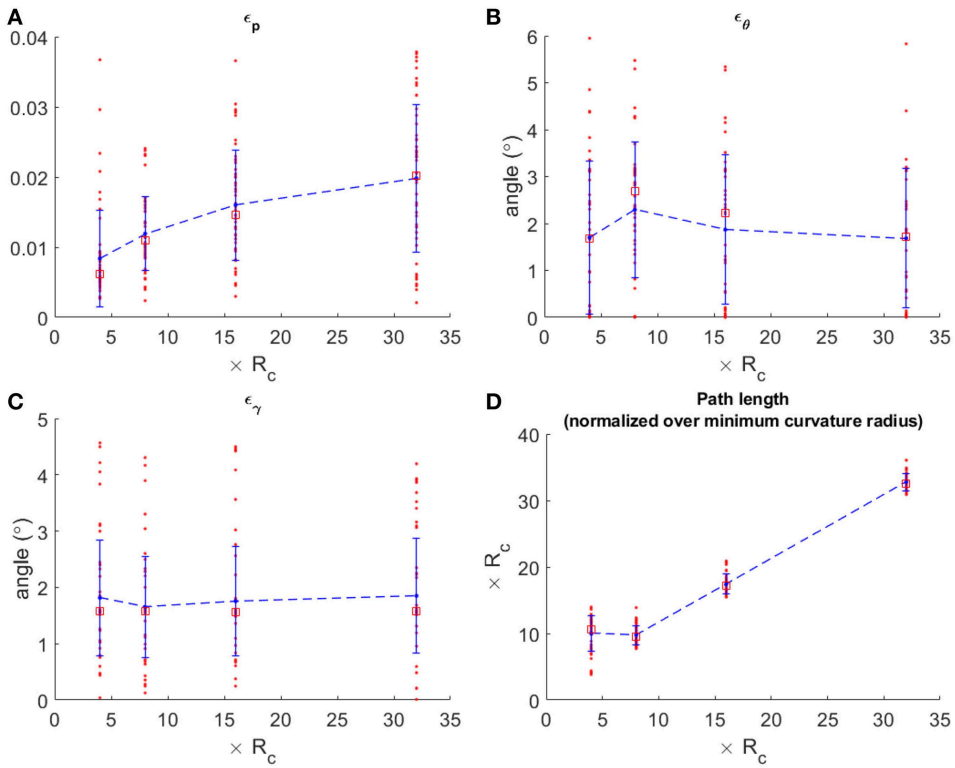

FIGURE 4 | Performance achieved with the plant-inspired growing robot (Sadeghi et al., 2017) in simulation. **(A)** positional error over four groups of simulation 50 repetitions each, having random starting and target position with Euclidean distance $4R_c$, $8R_c$, $16R_c$, and $32R_c$; **(B,C)** orientation errors, heading and pitch, respectively; **(D)** final path length of the random paths that have been performed, normalized over the minimum curvature radius. In each graph, the red dots are the single simulation and red squares are median values. Mean values are connected by the dashed blue lines.

This way, $\mathcal{L}_t$ is also the intersecting line between $\mathcal{T}_s$ and $\mathcal{T}_e$. Over this line we should now identify a waypoint P_t which will be target position over plane $\mathcal{T}_s$, as well as starting position over plane $\mathcal{T}_e$; whereas the orientation of the tip is defined by $\hat{v}_{se}$. A valid point P_t should not be too much close to P_s; this closeness can be defined by geometric constraints imposed by $R_{\min}$. To respect this constrain, we can define P_t as (**Figure 3B**):

$$P_t = P_s + \hat{v}_{se} y^*, \tag{12}$$

$$y^* = R_{\min}\sin\rho + \sqrt{(2R_{\min})^2 - (R_{\min}\cos\rho + R_{\min})^2} + \epsilon. \tag{13}$$

$$\rho = \cos^{-1}\frac{\hat{v}_s \cdot \hat{v}_{se}}{\|\hat{v}_s\|_2 \|\hat{v}_{se}\|_2}. \tag{14}$$

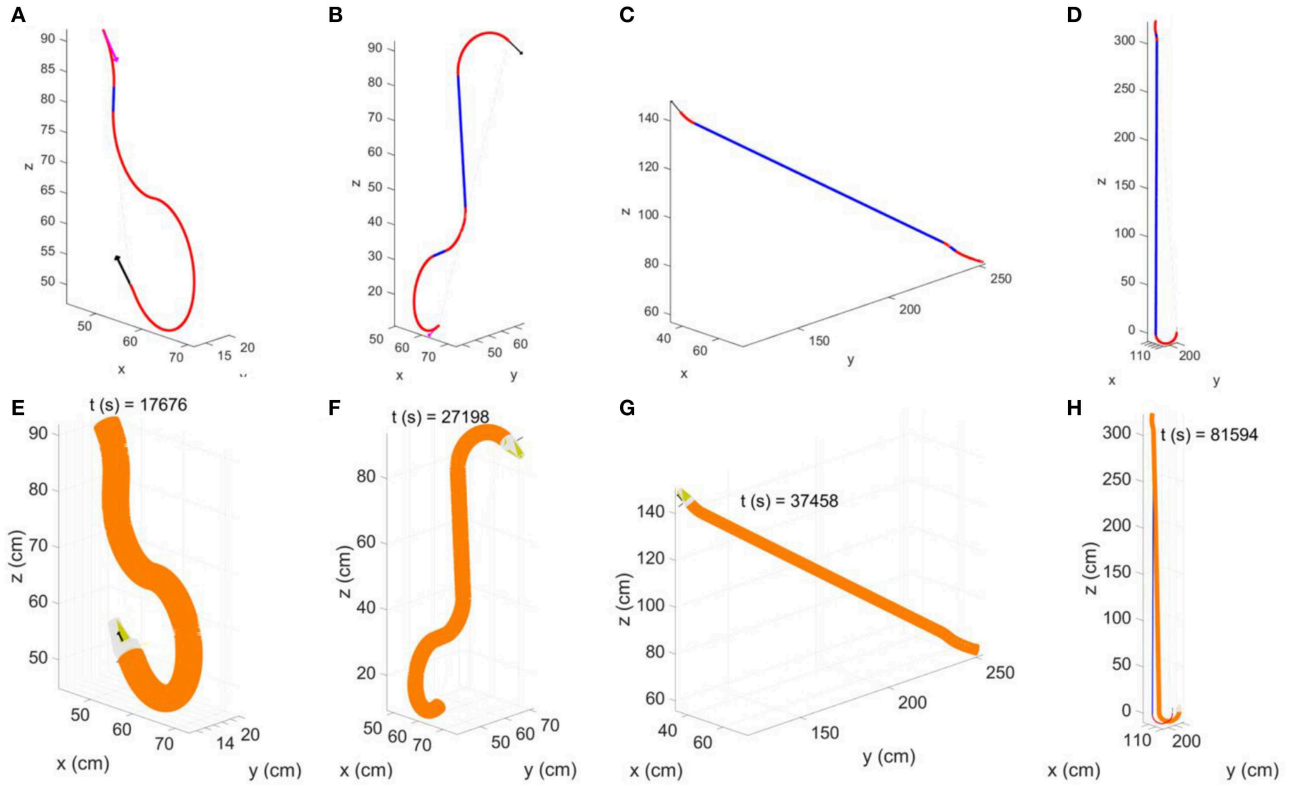

FIGURE 5 | Representative paths extracted from each of the four groups (paths having the positional error close to the median error value). First row shows the Dubins' path obtained by the proposed path planner, while the second row shows the final configuration reached by the simulated robot with the corresponding time required to grow. **(A,E)** configuration having starting and target position with Euclidean distance of $4R_c$; **(B,F)** of $8R_c$; **(C,G)** of $16R_c$, and **(D,H)** of $32R_c$. In the Dubin's paths, blue segments are straight lines and red segments are curvilinear paths; the starting tip position and orientation is described by magenta arrow, and target position and orientation is described by the black arrow. The output of the simulation is described in the figure by the final robot body (orange) and tip (white and yellow) configuration.

In (13), the ϵ is a small quantity (which can $\epsilon \to 0$) introduced just to overcome possible numerical approximation errors.

From now, the problem is divided in two 2D problems. We take the projection of P_s and P_t on the new reference system defined on plane $\mathcal{T}_s$ (17) by extracting the first two components from, respectively vector A and B ($\left[a_x\ a_y\right]^{-1}$ and $\left[b_x\ b_y\right]^{-1}$), which are obtained from the transformation:

$$M_s{}^{-1}P_s = A, \tag{15}$$

$$M_s{}^{-1}P_t = B, \tag{16}$$

$$M_s = \begin{bmatrix} \hat{v}_s & \hat{y}_s & \hat{n}_s & P_s \\ 0 & 0 & 0 & 1 \end{bmatrix}. \tag{17}$$

Vector $\hat{y}_s$ is obtained as the orthonormal vector between $\hat{n}_s$ and $\hat{v}_s$:

$$\hat{y}_s = \frac{\hat{n}_s \times \hat{v}_s}{\left\|\hat{n}_s \times \hat{v}_s\right\|_2}, \tag{18}$$

Analogously, to obtain the 2D coordinates of P_t and P_e on the reference system defined on plane $\mathcal{T}_e$ (21), we extract the first two components of vector C and D ($\left[c_x\ c_y\right]^{-1}$ and $\left[d_x\ d_y\right]^{-1}$):

$$M_e{}^{-1}P_t = C, \tag{19}$$

$$M_e{}^{-1}P_e = D, \tag{20}$$

$$M_e = \begin{bmatrix} \hat{v}_{se} & \hat{y}_e & \hat{n}_e & P_t \\ 0 & 0 & 0 & 1 \end{bmatrix}, \tag{21}$$

$$\hat{y}_e = \frac{\hat{n}_e \times \hat{v}_{se}}{\left\|\hat{n}_e \times \hat{v}_{se}\right\|_2}. \tag{22}$$

By definition Equations (17) and (21), we have the heading angles of starting poses equal to 0, while we can obtain the heading angles for the target poses as:

$$\theta_s = \cos^{-1} \frac{\hat{v}_s \cdot \hat{v}_{se}}{\left\|\hat{v}_s\right\|_2 \left\|\hat{v}_{se}\right\|_2}, \tag{23}$$

$$\theta_e = \cos^{-1} \frac{\hat{v}_e \cdot \hat{v}_{se}}{\left\|\hat{v}_e\right\|_2 \left\|\hat{v}_{se}\right\|_2}. \tag{24}$$

Therefore, the parameters of the minimum path problem on $\mathcal{T}_s$ are provided by the initial state ${\mathcal{Y}_s}^{\mathcal{T}_s} = \langle a_x, a_y, 0 \rangle$ and the final

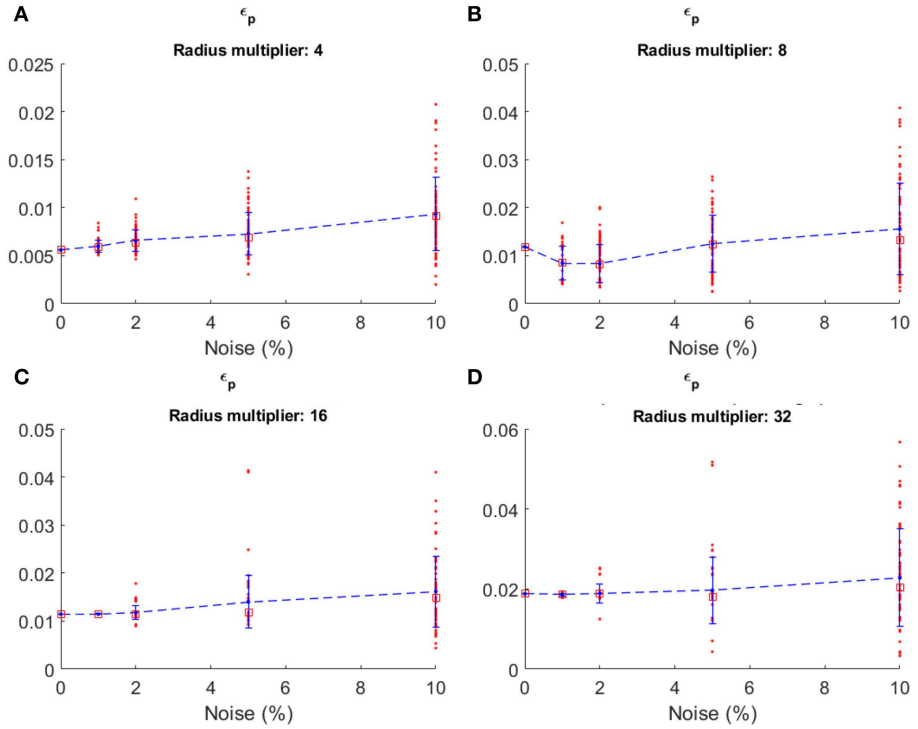

FIGURE 6 | Positional error obtained with four different level of noise by the plant-inspired growing robot (Sadeghi et al., 2017) in simulation, over the four different groups of path: **(A) 4R_c**, **(B) 8R_c**, **(C) 16R_c** and **(D) 32R_c**. In each graph, the red dots are the single simulation and red squares are median values. Mean values are connected by the dashed blue lines. The errors at 0 noise are the one obtained by the path closest to the median error from the previous set of simulations with no noise.

state ${\mathcal{Y}_e}^{\mathcal{T}_s} = \langle b_x, b_y, \theta_s \rangle$, while for $\mathcal{T}_e$ the parameters are ${\mathcal{Y}_s}^{\mathcal{T}_e} = \langle c_x, c_y, 0 \rangle$, and ${\mathcal{Y}_e}^{\mathcal{T}_e} = \langle d_x, d_y, \theta_e \rangle$.

Once we get the sequence of path segments, we can identify for each segment the action represented by the triple $\langle \alpha, \beta, S \rangle$, where $\beta = \int_{\phi dt}$ is the angle representing the arc of the circle to be performed, $S = \int_{gdt}$ is the segment length, and α is the angle opposite to the curvature, on the x-y plane of the robot, which will indicate the point of deposition. α is found by first evaluating the angle δ between the plane where the robot is supposed to move (with normal $\hat{n}$), with the robot's x axis unit vector ($\hat{d}_x$):

$$\delta = \cos^{-1} \frac{\hat{n} \cdot \hat{d}_x}{\left\| \hat{n} \right\|_2 \left\| \hat{d}_x \right\|_2}, \tag{25}$$

then defining the two possible deposition angles, which should lie on the perpendicular line respect to $\hat{n}$, as $\alpha_1 = \frac{\pi}{2} + \delta$ and $\alpha_2 = \frac{3}{2}\pi + \delta$; and finally picking as α for each segment of the path, the one among α_1 and α_2 that is on the opposite direction of the projection of the v_p vector (the next waypoint in the sequence to be reached) on the x-y plane of the tip ($v_\alpha \cdot v_{p_{xy}} = 1$) (**Figure 3C**).

The triple $\langle \alpha, \beta, S \rangle$ can thus be used as input parameter for Equation (4) to obtain ${}^{i}T$ for each of the segment, and by (5) we get the kinematic chain of the robot from $\mathcal{X}_s$ to $\mathcal{X}_e$.

TABLE 1 | Different parameterization of robot speed, curvature radius, and maximal intensity of bending ($\phi = \frac{g}{R_c}$).

	Δt (s)	g (cm/s)	R_c (cm)	ϕ (rad/s)	k
Robot A	18	0.0043	10	0.0004	0.0077
Robot A1	1.8	0.0430	10	0.0043	0.0077
Robot A2	0.18	0.4300	10	0.0430	0.0077
Robot A3	18	0.0043	30	0.0001	0.0026
Robot A4	1.8	0.0430	30	0.0014	0.0026
Robot A5	0.18	0.4300	30	0.0143	0.0026
Robot A6	18	0.0043	3.33	0.0013	0.0232
Robot A7	1.8	0.0430	3.33	0.0129	0.0232
Robot A8	0.18	0.4300	3.33	0.1290	0.0232

Δt represents the minimum time required by the robot for the minimum atomic step of growth. k is then defined as $\frac{g \cdot \Delta t}{R_c}$. All parameters for robot A have been extracted from the robot presented in Sadeghi et al. (2017); Del Dottore et al. (2018c).

RESULTS

Model Evaluation Over Different Distances of the Target Configuration

To evaluate the proposed kinematics we simulated the growth of a robot, implementing the equations of section Methods in MATLAB. We parametrized the simulations to fit the physical

TABLE 2 | Mean positional error (±SD) achieved by each robot parameterization, over the four groups of path, with 50 repetition each.

	$4R_c$	$8R_c$	$16R_c$	$32R_c$
Robot A	0.0084 ± 0.0069	0.0119 ± 0.0052	0.0160 ± 0.0079	0.0198 ± 0.0105
Robot A1	0.0086 ± 0.0045	0.0135 ± 0.0065	0.0150 ± 0.0087	0.0179 ± 0.0106
Robot A2	0.0089 ± 0.0063	0.0126 ± 0.0064	0.0129 ± 0.0058	0.0164 ± 0.0110
Robot A3	0.0031 ± 0.0019	0.0025 ± 0.0010	0.0038 ± 0.0022	0.0059 ± 0.0028
Robot A4	0.0026 ± 0.0013	0.0031 ± 0.0028	0.0042 ± 0.0026	0.0059 ± 0.0039
Robot A5	0.0031 ± 0.0016	0.0031 ± 0.0021	0.0045 ± 0.0026	0.0059 ± 0.0040
Robot A6	0.0223 ± 0.0152	0.0411 ± 0.0181	0.0459 ± 0.0243	0.0445 ± 0.0223
Robot A7	0.0250 ± 0.0156	0.0557 ± 0.0427	0.0472 ± 0.0397	0.0440 ± 0.0332
Robot A8	0.0291 ± 0.0224	0.0370 ± 0.0183	0.0447 ± 0.0290	0.0399 ± 0.0277

TABLE 3 | Parameters adopted for simulating the growth of robots having different size and growth velocity.

	Robot A	**Robot B**	**Robot C**
Δt	18 s	522 s	0.0020 s
g	0.0043 cm/s	0.012 cm/s	1000 cm/s
r_t	2.2 cm	5.75 cm	1.9 cm
R_c	10 cm	68 cm	3.8 cm
ϕ	0.0004 rad/s	0.01 rad/s	4.47 rad/s
k	0.0077	0.0921	0.5263

All parameters for robot A have been extracted from the robot presented in Sadeghi et al. (2017), Del Dottore et al. (2018c). Time of deposition Δt, the growth velocity g, the robot head radius r_t and the curvature radius R_c of robot B have been extracted from (Kayser et al., 2019), in which the robot was able to build 6.25 cm of structure in 8.7 min. From Hawkes et al. (2017) we extracted robot head dimension r_t and the growth velocity g for robot C. Δt has been obtained assuming to have 1 latch every 1 cm and alternated on opposite sides of the robot (on the same side, 2 consecutive latches have a distance of 2 cm). When pressurized, a latch releases 2 cm of material. Thus, for a single step of bending, robot C will have $h_1 = 1$ cm of material on one side and $h_2 = 3$ cm on the opposite side. In this case we evaluated $R_c = r_t \frac{h_1+h_2}{h_2-h_1}$, $\Delta t = \frac{h_1+h_2}{2} \frac{1}{g}$ and $\phi = \frac{h_2-h_1}{2r_t}$.

parameters of the growing robot implemented and deeply presented in Sadeghi et al. (2017) and Del Dottore et al. (2018c). The robot has an internal radius r_t of 2.2 cm, and an internal module with L equal to 4.8 cm and r_r of 1.2 cm, resulting in an $R_{\min}$ of 9.82 cm. This geometric evaluation agrees with the experiments performed on the robot and presented in Del Dottore et al. (2018c), in which we found a maximal deposition angle of 0.45° for a single layer having a maximal height of 0.095 ± 0.002 cm, thus resulting in an $R_{\min} = 9.79$ cm. In the current work, we imposed $R_c = 10\,cm \geq R_{\min}$ in all our simulations to find the path from starting $\mathcal{X}_s$ to the target configuration $\mathcal{X}_e$. Moreover, our robot is able to deposit a single layer of material in 18 s and consequently for the simulated robot ϕ is equal to $0.025/s$ and the growing velocity is $g = 0.0043$ cm/s.

Four different groups of simulations were performed, with 50 repetitions each. The groups were composed setting the Euclidean distance between starting and target position ($\|P_s - P_e\|_2$) of, respectively 4, 8, 16, and 32 times R_c, and choosing for each repetition a completely random starting $\mathcal{X}_s$ and target $\mathcal{X}_e$ pose. At the end of each simulation we evaluated the error in position (ε_p) as the distance between target position (P_e) and the simulated robotic tip position (T_e), normalized over the distance of the Dubin's path (l):

$$\varepsilon_p = \frac{\|T_e - P_e\|_2}{l}, \tag{26}$$

and the errors in the heading (ε_θ) and pitch angles (ε_γ) as the distance between the target and achieved angles:

$$\varepsilon_\theta = |\theta_t - \theta_e|, \tag{27}$$

$$\varepsilon_\gamma = |\gamma_t - \gamma_e|, \tag{28}$$

where θ_t and γ_t are, respectively the heading and pitch angle achieved by the simulated robotic tip. The normalized error in position seems to slightly grow with the distance (**Figure 4A**) with a mean ranging from a lower value of 0.0084 ± 0.0069 to a maximum of 0.0198 ± 0.0105. The errors on heading and pitch are instead not affected by the distance, mean rank of each group is not significantly different from the others (p-value for heading error is 0.4327, and for pitch error is 0.6420), thus we can estimate a mean heading error of 1.89° ± 0.28° (**Figure 4B**) and a mean pitch error of 1.77° ± 0.09° (**Figure 4C**). Also, in a short path ($\leq 4R_c$), the system due to its mechanical constraints is forced to travel a distance typically greater than the distance between starting and target pose, while in longer paths ($> 4R_c$) the distance traveled almost resemble the distance between P_s and P_e (**Figure 4D**). Videos showing a schematic representation of the kinematic and examples of robot growth evolution in simulation from $\mathcal{X}_s$ to $\mathcal{X}_e$ are available as **Supplementary Videos 1, 2**. The error is mainly due to the discrete process of deposition, which induces an error between the desired waypoint (in the sequence of Dubin's path) and the actual position reached. Due to the small amount of material added at each step (in our case less than 1 mm) and the small angle (0.45°), the positional error remains relatively low.

Contribution of Noise to the Model Error

To verify the accuracy of the model, we introduced a random noise component to perturb the system. From each of the previously obtained group of simulations ($4R_c$, $8R_c$, $16R_c$, $32R_c$) we extracted the path having ε_p closer to the median value of its group (**Figure 5**). For each of the selected path, we simulated

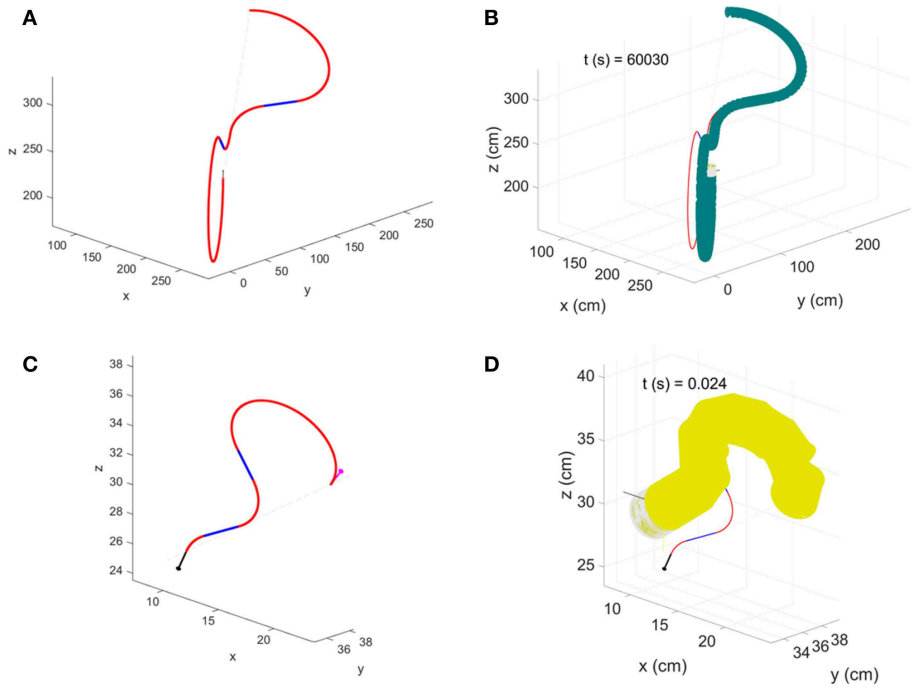

FIGURE 7 | Paths having the positional error closer to the median value for the group of simulations having $\mathbf{4R_c}$ as Euclidean distance between starting and target position. **(A)** Robot B Dubin's path and **(B)** configuration achieved at the end of simulation; **(C)** robot C Dubin's path and **(D)** configuration achieved at the end of simulation.

the growth of the robot testing ±1, ±2, ±5, and ±10% of noise, calculated as a percentage of the averaged growth rate g, and used as additive noise to g at each time step. We limited the analysis to ±10% since, in the real system, we do not expect an excessively high noise in the growth rate. In fact, from previous experiments on the robot growing straight (Del Dottore et al., 2018c) we could find on average an error of ±2% in filament deposition height. We performed 70 repetitions for each level of noise in each group. Results (**Figure 6**) show stronger effects of the noise over short distances [increasing values - in $4R_c$ (**Figure 6A**) - or irregular trends - in $8R_c$ (**Figure 6B**)] rather than over long distance traveled (**Figures 6C,D**) (the one-way ANOVA test is reported in section Statistical analysis of the noise effects on the positional error of **Supplementary Material**).

Effects of Robot Parameters Variation: Dimensions and Velocity

Additionally, we varied robot parameters to verify how robot dimensions and speed could affect model accuracy. Robot dimensions come into play in the kinematic model in the form of curvature radius ($R_c = \frac{g}{\phi}$ see Equations 4 and 7); thus, to analyze the behavior of the error, we created 8 different combination of g and R_c, preserving a constant number of deposition over the same displacement, by setting constant $g \cdot t = 0.3096$, where t is the time of material deposition for a single atomic step of growth (**Table 1**). To compare the performance among different robots, we calculated the index $k = \frac{g \cdot t}{R_c}$, which defines a ratio between robot minimum growth and its curvature radius. As before, we performed 4 different groups of path with 50 repetitions each having random $\mathcal{X}_s$ and $\mathcal{X}_e$. Positional errors with relative standard deviation are reported in **Table 2**. Ultimately, we looked at the error behavior emerging from robots having different time of deposition t. We set the parameters taking inspiration from the robots presented in Kayser et al. (2019) (named as robot B in the following) and Hawkes et al. (2017) (named as robot C), missing data have been estimated from the available information (**Table 3**). Also in this case, we performed four groups of simulations with 50 repetitions each, having random $\mathcal{X}_s$ and $\mathcal{X}_e$. Two examples of the paths performed by the simulated robot B and C are in **Figure 7**.

Results demonstrate that heading and pitch errors are unaffected by variation of parameters, showing a not significantly different behavior among all the simulations obtained with parameters as in **Tables 1**, **3** (p-value for heading error is 0.5578, and for pitch error is 0.1490) with an average error of $\sim 2^\circ$ ε_θ (**Figure 8A**) and $\sim 1.8^\circ$ ε_γ (**Figure 8B**). Whereas, ε_p tends to stabilize in long distances (path length $\geq 8R_c$) in robot B and C (p-value in long paths with robot B is 0.7719, and with robot C is 0.9160), reaching a mean error of 0.0043 ± 0.0023 with robot B and of 0.1655 ± 0.1089 with robot C (**Figure 8C**). Moreover, for constant k the error ε_p is not affected (the one-way ANOVA test is reported in section Statistical analysis to evaluate the significance of different parameterization of **Supplementary Material**), while it increases with k (**Figure 8D**). Conditions for high k values are small curvature radius or large discretization step ($g \cdot t =$ robot

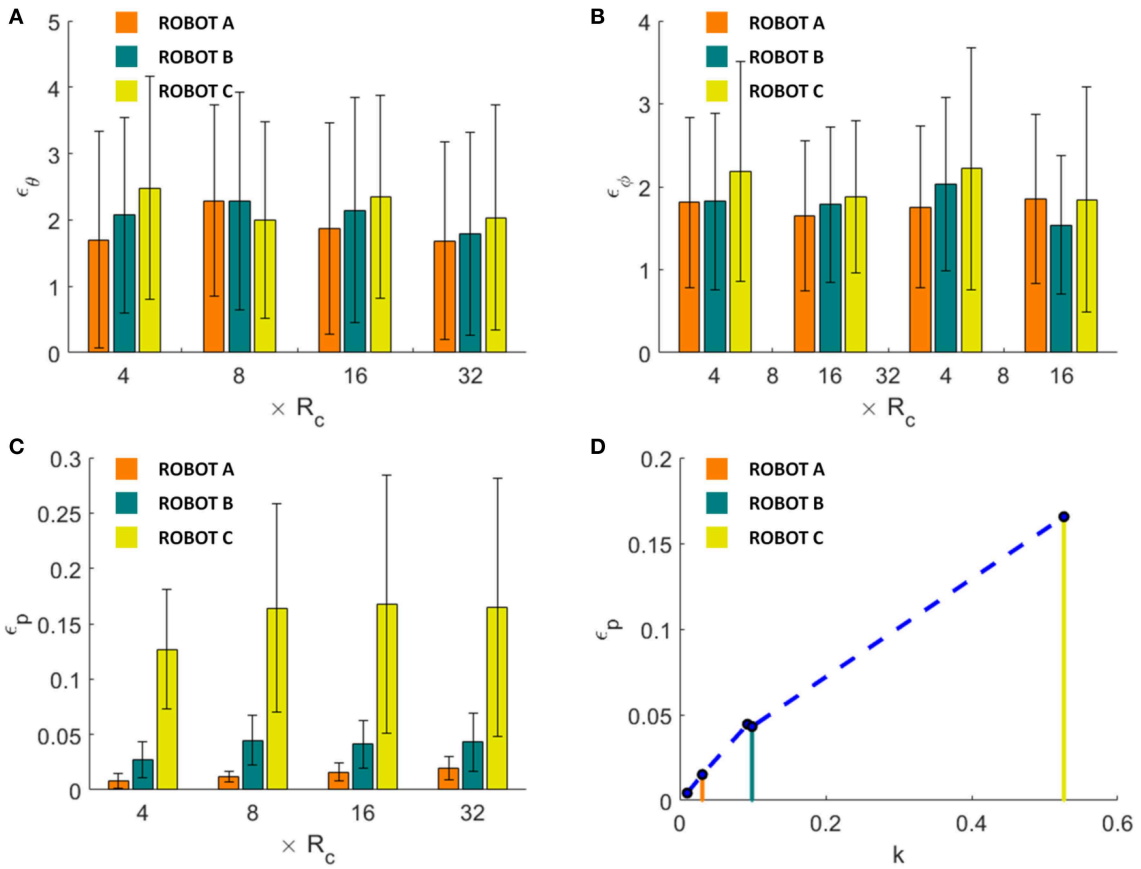

FIGURE 8 | Comparison of mean heading **(A)**, pitch **(B)** and positional **(C)** errors achieved by robot A, B and C for each of the simulation groups. In **(D)**, the positional error is shown as a function of the ratio ***k*** between discretization step (***g*** · ***t***) and curvature radius $\boldsymbol{R_c}$. The dots in graph B represent the mean positional errors achieved by the simulations with the parameters as presented in **Tables 1**, **3**, averaged among groups $\boldsymbol{8R_c}$, $\boldsymbol{16R_c}$, and $\boldsymbol{32R_c}$. Results obtained by robot are highlighted by the corresponding colored lines. Performances of robot A in all the graphs refer to the results as shown in **Figure 4**, but are here reported for easiness of comparison.

B 6.26 cm ≫ robot C 2 cm ≫ robot A 0.077 cm) (**Table 3**) which induces to accumulate errors in reaching each sequence target position and amplifies this effect in tight curvilinear paths (case of robot C with $R_c = 3.8$ cm).

DISCUSSIONS

The motion obtained by growing from the tip is becoming an attractive ability in robotics since it can enable robots to navigate their environments by adapting their bodies and morphologies to the constraints of the surrounding. The body is built in real-time by the robot, according to environmental and task demand, through the addition of new material at the tip, driving in this way the tip navigation. This means that the robot's path is not predictable *a priori*.

Navigation of unstructured environments cannot rely on classic map-based path planning strategies; the robot in those cases should move with a higher level behavior control, i.e., a stimuli-oriented control (Sadeghi et al., 2016). In this context, a perfect knowledge of the robot kinematic is fundamental for understanding the feasibility of the path chosen by the behavioral control. The proposed kinematic model can be adopted, coupled with the higher control, to help in localizing the robot or to predict its next position. Moreover, the proposed kinematic control can be used in short-distance navigation: when for instance the robot has the possibility to reconstruct the close surrounding by means of its own perception (e.g., vision, tactile, depth sensors). In this view, the robot can set a proximal waypoint, define its path, and reach the target.

The key parameter defining the path and the ability of a growing robot to adapt through different unknown patterns is the minimum curvature radius. This parameter is affected, and consequently, the space of maneuverability may be limited, by the design of the robot and particularly by the size of mechanical components (e.g. motors, other actuators, and components). Here, a parameterization of the growing system mechanical design is presented and formulation of the curvature radius in terms of that parameters proposed, giving a good agreement with experimental results, i.e., we geometrically evaluated the minimum curvature radius of our growing robot as $R_{\min} = 9.82$ cm, whereas by previous experiments we found $R_{\min} = 9.79$ (Del Dottore et al., 2018c).

Yet, our analysis has been limited to a geometric evaluation aimed at characterizing the motion of growing from the tip

robots. By looking at the kinematics, we evaluated the theoretical workspace of growing robots, however, when deepening in the analysis of the motion, dynamics of each specific system should be also considered. For instance, when a growing robot moves in the air, the weight of the tip and the suspended part of the built body should be carefully taken into account in the control dynamics, in order to prevent the structural collapse. In fact, speed and forces acting on a robotic system play a relevant role which could address the features of the robot from one application to another. Also, when designing the robot, the selection of the growth mechanism is particularly important when talking about applications. For instance, for biomedical applications, in the design of a growing robot, the reversibility of the system and the biocompatibility of the growth strategy and building material are fundamental, whereas, in a rescue scenario, the speed and robustness become much more relevant.

CONCLUSIONS

This paper formalizes the kinematics model for growing robots, setting the analogy with mobile non-holonomic systems, and shows the ability of the model to describe the motion of a plant-inspired growing robot. Given a starting and a final pose in the 3D space, here we defined a kinematic control to connect them. We propose to split the global movement into two optimal planar paths based on Dubin's solution and we formalize our approach finding the two planes and the trajectories above them. We verified our strategy with different poses in simulation demonstrating the ability of a plant-inspired growing robot to reach the expected final position with the desired orientation (maximal positional error of $\sim$6 cm in 320 cm of path length and $\sim 1.8^\circ$ in orientation errors). We also evaluated the effects of different level of noise, and the effects of different model parametrization. We noted that not only the curvature radius but also the specific discretization of the robot affect its ability in reaching, with high or low accuracy, the desired point and thus must be taken into account when defining a feasible path. However, our analysis generally shows the accuracy of the proposed strategy, when considering an almost continuous growth of the robot, the efficacy of the model and its applicability over different sizes, curvature radius, and growth speeds.

However, when moving from simulation to physical implementation, the kinematic analysis is not enough to correctly analyze robot motion. Future steps will focus on formalizing the optimal path considering specific characteristics of the robot into the model, particularly, evaluating how the dynamics (considering self-weight and other forces exercised in interaction with the environment during growth) would affect the path, and implementing the strategy on the robo-physical model (Sadeghi et al., 2017). Additionally, positional and orientation errors between simulation and a real robot would be considered and corrected, at least partially, by adopting internal odometry sensors and inertial measurement units, which would allow inserting feedback about the actual material deposition into a closed-loop control.

AUTHOR CONTRIBUTIONS

ED conceived and formalized the model. ED and AM discussed model and experiments. ED, AM, AS, and BM discussed results and wrote the paper.

FUNDING

This study was partially funded by the RoboCom++ project (FLAG-ERA Joint Transnational Call 2016), by SMASH—Smart Machines for Agricultural Solutions Hightech (Tuscany-Italy POR FESR 2014-2020) and by the European Union's Horizon 2020 Research and Innovation Programme under Grant Agreement No 824074 (GrowBot project).

SUPPLEMENTARY MATERIAL

The Supplementary Material for this article can be found online at: https://www.frontiersin.org/articles/10.3389/frobt.2019.00045/full#supplementary-material

REFERENCES

Aguilar, J., Zhang, T., Qian, F., Kingsbury, M., McInroe, B., Mazouchova, N., et al. (2016). A review on locomotion robophysics: the study of movement at the intersection of robotics, soft matter and dynamical systems. *Rep. Prog. Phys.* 79:110001. doi: 10.1088/0034-4885/79/11/110001

Ambrosino, G., Ariola, M., Ciniglio, U., Corraro, F., De Lellis, E., and Pironti, A. (2009). Path generation and tracking in 3-D for UAVs. *IEEE Trans. Control. Syst. Technol.* 17, 980–988. doi: 10.1109/TCST.2009.2014359

Armour, R., Paskins, K., Bowyer, A., Vincent, J., and Megill, W. (2007). Jumping robots: a biomimetic solution to locomotion across rough terrain. *Bioinspir. Biomim.* 2, S65–S82. doi: 10.1088/1748-3182/2/3/S01

Babaei, A. R., and Mortazavi, M. (2010). Three-dimensional curvature-constrained trajectory planning based on in-flight waypoints. *J. Aircr.* 47, 1391–1398. doi: 10.2514/1.47711

Bachmann, R. J., Boria, F. J., Vaidyanathan, R., Ifju, P. G., and Quinn, R. D. (2009). A biologically inspired micro-vehicle capable of aerial and terrestrial locomotion. *Mech. Mach. Theory* 44, 513–526. doi: 10.1016/j.mechmachtheory.2008.08.008

Choset, H., and Henning, W. (1999). A follow-the-leader approach to serpentine robot motion planning. *J. Aerosp. Eng.* 12, 65–73. doi: 10.1061/(ASCE)0893-1321(1999)12:2(65)

Cianchetti, M., Calisti, M., Margheri, L., Kuba, M., and Laschi, C. (2015). Bioinspired locomotion and grasping in water: the soft eight-arm OCTOPUS robot. *Bioinspir. Biomim.* 10:035003. doi: 10.1088/1748-3190/10/3/035003

Colomina, I., and Molina, P. (2014). Unmanned aerial systems for photogrammetry and remote sensing: a review. *ISPRS J. Photogramm. Remote Sens.* 92, 79–97. doi: 10.1016/j.isprsjprs.2014.02.013

Dario, P., and Mosse, C. A. (2003). "Review of locomotion techniques for robotic colonoscopy," in *2003 IEEE International Conference on Robotics and Automation (Cat. No.03CH37422)* (Taipei, Taiwan: IEEE), 1086–1091. doi: 10.1109/ROBOT.2003.1241737

Del Dottore, E., Mondini, A., Sadeghi, A., and Mazzolai, B. (2018a). "A plant-inspired kinematic model for growing robots," in *2018 IEEE International Conference on Soft Robotics (RoboSoft)* (Livorno: IEEE), 20–24. doi: 10.1109/ROBOSOFT.2018.8404891

Del Dottore, E., Sadeghi, A., Mondini, A., Mattoli, V., and Mazzolai, B. (2018b). Toward growing robots: a historical evolution from cellular to

plant-inspired robotics. *Front. Robot. AI* 5:16. doi: 10.3389/frobt.2018.00016

Del Dottore, E., Sadeghi, A., Mondini, A., and Mazzolai, B. (2018c). "Continuous growth in plant-inspired robots through 3D additive manufacturing," in *2018 IEEE International Conference on Robotics and Automation (ICRA)* (Brisbane, Australia: IEEE), 1–7. doi: 10.1109/ICRA.2018.8460616

Dubins, L. E. (1957). On curves of minimal length with a constraint on average curvature, and with prescribed initial and terminal positions and tangents. *Am. J. Math.* 79, 497–516. doi: 10.2307/2372560

Gilbert, H. B., Neimat, J., and Webster, R. J. (2015). Concentric tube robots as steerable needles: achieving follow-the-leader deployment. *IEEE Trans. Robot.* 31, 246–258. doi: 10.1109/TRO.2015.2394331

Hawkes, E. W., Blumenschein, L. H., Greer, J. D., and Okamura, A. M. (2017). A soft robot that navigates its environment through growth. *Sci. Robot.* 2:eaan3028. doi: 10.1126/scirobotics.aan3028

Hooper, S. L., and Büschges, A. (eds.) (2017). *Neurobiology of Motor Control: Fundamental Concepts and New Directions*. Hoboken, NJ: Wiley Blackwell.

Hwangbo, M., Kuffner, J., and Kanade, T. (2007). "Efficient two-phase 3D Motion Planning for Small Fixed-wing UAVs," in *Proceedings 2007 IEEE International Conference on Robotics and Automation* (Rome, Italy: IEEE), 1035–1041. doi: 10.1109/ROBOT.2007.363121

Kang, B., Kojcev, R., and Sinibaldi, E. (2016). The first interlaced continuum robot, devised to intrinsically follow the leader. *PLoS ONE* 11:e0150278. doi: 10.1371/journal.pone.0150278

Kayser, M., Cai, L., Bader, C., Falcone, S., Inglessis, N., Darweesh, B., et al. (2019). "FIBERBOTS: design and Digital Fabrication of Tubular Structures Using Robot Swarms," in *Robotic Fabrication in Architecture, Art and Design 2018*, eds J. Willmann, P. Block, M. Hutter, K. Byrne, and T. Schork (Cham: Springer International Publishing), 285–296.

Laschi, C., Mazzolai, B., and Cianchetti, M. (2016). Soft robotics: technologies and systems pushing the boundaries of robot abilities. *Sci. Robot.* 1:eaah3690. doi: 10.1126/scirobotics.aah3690

Makdah, A. A. A., Shammas, E., Daher, N., and ElHajj, I. (2016). "Modeling and optimal three-dimensional trajectory tracking for an autonomous underwater vehicle," in *2016 IEEE International Conference on Advanced Intelligent Mechatronics (AIM)* (Banff, AB: IEEE), 172–177. doi: 10.1109/AIM.2016.7576762

Mirats Tur, J. M., and Garthwaite, W. (2010). Robotic devices for water main in-pipe inspection: a survey. *J. Field Robot.* 27, 491–508. doi: 10.1002/rob.20347

Neumann, M., and Burgner-Kahrs, J. (2016). "Considerations for follow-the-leader motion of extensible tendon-driven continuum robots," in *2016 IEEE International Conference on Robotics and Automation (ICRA)* (Stockholm: IEEE), 917–923. doi: 10.1109/ICRA.2016.7487223

Phee, S. J., Ng, W. S., Chen, I. M., Seow-Choen, F., and Davies, B. L. (1997). Locomotion and steering aspects in automation of colonoscopy. I. A literature review. *IEEE Eng. Med. Biol. Mag.* 16, 85–96. doi: 10.1109/51.637122

Sadeghi, A., Mondini, A., Del Dottore, E., Mattoli, V., Beccai, L., Taccola, S., et al. (2016). A plant-inspired robot with soft differential bending capabilities. *Bioinspir. Biomim.* 12:015001. doi: 10.1088/1748-3190/12/1/015001

Sadeghi, A., Mondini, A., and Mazzolai, B. (2017). Towards self-growing soft robots inspired by plant roots and based on additive manufacturing technologies. *Soft Robot.* 4, 211–223. doi: 10.1089/soro.2016.0080

Sadeghi, A., Tonazzini, A., Popova, L., and Mazzolai, B. (2013). "Robotic mechanism for soil penetration inspired by plant root," in *Robotics and Automation (ICRA), 2013 IEEE International Conference on* (IEEE), 3457–3462. doi: 10.1109/ICRA.2013.6631060

Sadeghi, A., Tonazzini, A., Popova, L., and Mazzolai, B. (2014). A novel growing device inspired by plant root soil penetration behaviors. *PLoS ONE* 9:e90139. doi: 10.1371/journal.pone.0090139

Seto, M. L. (2013). *Marine Robot Autonomy*. New York, NY: Springer. Available online at: http://public.eblib.com/choice/publicfullrecord.aspx?p=1081972 (accessed 24 November, 2018).

Sfakiotakis, M., Lane, D. M., and Davies, J. B. C. (1999). Review of fish swimming modes for aquatic locomotion. *IEEE J. Ocean. Eng.* 24, 237–252. doi: 10.1109/48.757275

Siciliano, B., and Khatib, O. (eds.) (2008). *Springer Handbook Of Robotics: With 84 Tables*. Berlin: Springer.

Siegwart, R., Nourbakhsh, I. R., and Scaramuzza, D. (2011). *Introduction to Autonomous Mobile Robots*, *2nd ed.* Cambridge, MA: MIT Press.

Tsukagoshi, H., Arai, N., Kiryu, I., and Kitagawa, A., (2011). Tip growing actuator with the hose-like structure aiming for inspection on narrow terrain. *Int. J. Autom. Technol.* 5, 516–522. doi: 10.20965/ijat.2011.p0516

Verbelen, J.-P., Cnodder, T. D., Le, J., Vissenberg, K., and Baluška, F. (2006). The root apex of *Arabidopsis thaliana* consists of four distinct zones of growth activities: meristematic zone, transition zone, fast elongation zone and growth terminating zone. *Plant Signal. Behav.* 1, 296–304. doi: 10.4161/psb.1.6.3511

Yu, W., Shuo, W., Min, T., Chao, Z., and Qingping, W. (2015). Real-time dynamic dubins-helix method for 3-D trajectory smoothing. *IEEE Trans. Control Syst. Technol.* 23, 730–736. doi: 10.1109/TCST.2014.2325904

Conflict of Interest Statement: The authors declare that the research was conducted in the absence of any commercial or financial relationships that could be construed as a potential conflict of interest

frontiers in Robotics and AI

ORIGINAL RESEARCH
published: 12 July 2019
doi: 10.3389/frobt.2019.00052

RUBIC: An Untethered Soft Robot With Discrete Path Following

Hsing-Yu Chen[1,2†], *Richard Suphapol Diteesawat*[1,3†], *Alice Haynes*[1,4†], *Alixander James Partridge*[1,2*†], *Melanie Florine Simons*[1,4†], *Enrico Werner*[1,3†], *Martin Garrad*[1,3], *Jonathan Rossiter*[1,4] *and Andrew T. Conn*[1,2]

[1] *Bristol Robotics Laboratory, University of Bristol, Bristol, United Kingdom,* [2] *Department of Mechanical Engineering, University of Bristol, Bristol, United Kingdom,* [3] *EPSRC Centre for Doctoral Training in Robotics and Autonomous Systems (FARSCOPE), University of Bristol and University of the West of England, Bristol, United Kingdom,* [4] *Department of Engineering Mathematics, University of Bristol, Bristol, United Kingdom*

Soft robots have the potential to diminish the need for humans to venture into unsuitable environments or work in extreme conditions. While their soft nature gives them the advantage of being adaptable to changing environments, their control can be challenging because of the compliance that makes them effective. In this paper we present RUBIC: the Rolling, Untethered, Ballooning, Intelligent Cube, that overcomes some of the difficulties of 2D control by constraining motion to a discretised Cartesian space. RUBIC's method of locomotion is by rolling from one face of the cube to another, in any one of four directions. This motion causes it to move within a 2D grid structure, the dimensions of which are defined by the cube's characteristic length. When in its resting position RUBIC is inherently stable and forms a safe platform for tasks including taking measurements and soil samples, for localization and *ad hoc* network infrastructure, and as the foundation for larger robots and structures. We present the design of RUBIC's body, the four pneumatic ballooning actuators per face that generate its unique gait, and the control systems for locomotion and obstacle climbing. We consider constraints imposed by the design and fabrication methods including physical dimension and weight, material properties and control fidelity. An alternative locomotion scheme is proposed to improve the speed and linearity which also increases the distance traveled per roll. RUBIC travels with a mean locomotion accuracy of 4.58° deviation and successfully traverses steps up to 35% of its own height. The discretisation of a soft robotics workspace, as demonstrated by RUBIC, has advantages for safe and predictable locomotion and has applications in both structured and hazardous environments.

Keywords: soft robotics, locomotion, untethered, fluidic elastomer actuators, RoboSoft

OPEN ACCESS

Edited by:
Perla Maiolino,
University of Oxford, United Kingdom

Reviewed by:
Chaoyang Song,
Southern University of Science and Technology, China
Josie Hughes,
University of Cambridge, United Kingdom

****Correspondence:***
Alixander James Partridge
alix.partridge@bristol.ac.uk

† These authors have contributed equally to this work

Specialty section:
This article was submitted to Soft Robotics, a section of the journal Frontiers in Robotics and AI

Received: *19 October 2019*
Accepted: *24 June 2019*
Published: *12 July 2019*

Citation:
Chen H-Y, Diteesawat RS, Haynes A, Partridge AJ, Simons MF, Werner E, Garrad M, Rossiter J and Conn AT (2019) RUBIC: An Untethered Soft Robot With Discrete Path Following. Front. Robot. AI 6:52. doi: 10.3389/frobt.2019.00052

1. INTRODUCTION

Soft robotic locomotion is of interest due to the ability of compliant systems to deal with uncertain terrain. These techniques are typically inspired by biological organisms, such as caterpillars, snakes and insects (Kim et al., 2013). There are a range of different materials and soft actuators that can be used for the fabrication of such devices, such as elastomers (Marchese et al., 2015), shape memory alloys (SMAs) (Umedachi et al., 2016), dielectric elastomers (Li et al., 2018), and kirigami skins (Rafsanjani et al., 2018).

Of these materials, elastomers are a popular choice as they are highly versatile and compliant whilst being light-weight (Ilievski et al., 2011). For these reasons, they have been used in a variety of locomoting soft robots. One such soft robot designed by Shepherd et al. (2011) and Tolley et al. (2014a) demonstrates a crawling motion. The soft robot is completely manufactured with the elastomer silicone and uses this material to create a frictional difference with the ground between the leading and tail end of the robot that alternates as it moves to favor forward motion. However, the frictional contact between the elastomer and the ground leads to a high rate of wear, in turn causing a risk of puncture. This limitation can also be seen in the robot that uses vibrations to bounce across a surface on its elastomer bellows (Kühnel et al., 2016). The walking legged robots by Nemiroski et al. (2017) utilize elastomers to create joints to move more rigid components or legs. These are potentially better suited to traversing uneven terrains than crawling robots, not only as the soft elastomer is less likely to get damaged as it is not in contact with the surface, but also because they have a smaller surface area in contact with the ground, resulting in less energy being used to overcome friction and allowing them to navigate over obstacles (Siegwart and Nourbakhsh, 2004).

Rolling has the potential to be a faster method of locomotion for soft robots, however it comes at a cost of increased unpredictable path following and complex simulation and control (Li et al., 2018). Different technologies have been used to achieve the rolling motion. Li et al. (2018) created a soft robot with patterns of dielectric elastomers (DEAs) in the shape of a ring. Activating these DEAs results in extension of those regions and therefore deformation of the ring. Other methods of rolling have been achieved with pressurizing fabric tubes which have been constrained in certain directions to generate bending (Wang et al., 2019). Successful application of elastomers for the use of rolling locomotion has been demonstrated by Steltz et al. (2009) and Steltz et al. (2010) which uses a technique known as particle jamming. Silicone elastomer filled with particles and arranged in a sphere can be vacuumed to change its stiffness. Rolling is achieved when specific elastomer cells are unjammed causing them to reduce in stiffness. A central actuator then causes expansion of these cells and a change of shape of the sphere. Although a completely soft locomoting robot is achieved, the thickness of the elastomer and number of elastomer cells will limit the complete morphing ability of the robot.

Applications of soft robotics for locomotion are expansive and have overcome some of the challenges faced by rigid robots. However, their pliable nature comes with the challenge of control due to their high number of degrees of freedom. The non-linearities within the actuation of soft robots can result in systems that are difficult to predict and the repeatability of motion can be challenging. As such, control schemes for soft robotic systems often require intrinsic and extrinsic sensing and/or localization, alongside complex control systems for locomotion. Additionally, current systems generally lack the stability of conventional robotic systems and resting positions can vary from step to step (Tolley et al., 2014b). Soft robotic systems often also require tethering to off-board pneumatic and electronic components, resulting in long tethers that limit the robot's range of motion and reach (Shepherd et al., 2011).

We present RUBIC, the Rolling, Untethered, Ballooning, Intelligent Cube. The external structure, actuation mechanisms and internal structure are shown in **Figure 1**. RUBIC utilizes fluidic elastomer actuators to locomote from face to face, as shown in **Figure 1B**. In contrast to past soft robotic systems, RUBIC can approximately follow a discrete, predictable path along a grid. In addition, RUBIC is operable untethered as all electronics are on-board and commands are received via remote control. In this paper we describe the design of RUBIC, with focus on the characterization of the actuators and quantification of locomoting patterns.

2. ROBOT DESIGN

The fundamental concept of RUBIC is a cube that locomotes by rolling. Actuation is provided by 24 fluidic elastomer actuators, attached to the faces of the cube, that inflate to create a rolling motion, as shown in **Figure 1B**. To achieve locomotion in two dimensions, each face comprises four actuators in a 2 by 2 matrix. When two adjacent actuators on the bottom face of the cube inflate, they lift that side of the cube causing it to roll onto the adjacent face. Repeating this process allows RUBIC to navigate through its environment along a discretised path. The cubic structure ensures that the robot can be directed left, right, forwards or backwards with a simple control system. Power is provided via an on-board lithium polymer battery, allowing for approximately an hour of locomotion per charge. Control signals are sent via Bluetooth, allowing the robot to operate untethered.

A cube was selected as the base structure for the robot based on the outcome of analysis into the dynamics of platonic solids with equal volume. The five platonic solids were considered: tetrahedron, cube, octahedron, dodecahedron and icosahedron. These solids were then analyzed based on three factors: rotation angle; actuator volume and energy. For rotation angle α, we calculated the angle each solid must be rotated from its stationary position in order to roll to the next face, e.g., 45° for a cube.

$$\alpha = 90 - \arcsin(\frac{r_{in}}{r_{mid}}) \tag{1}$$

where r_{in} and r_{mid} are the inradius and midradius of the platonic solid, respectively. For actuator volume $V_{actuator}$, we modeled the fluidic elastomer actuators as spherical caps, such that we could calculate the volume they need to inflate to in order for the solid to rotate to the rotation angle.

$$V_{actuator} = V_{sphere} - V_{cap} = \frac{4}{3}\pi R^3 - \frac{1}{6}\pi h(3(\frac{c}{2})^2 + h^2) \tag{2}$$

with sphere volume V_{sphere}, spherical cap volume V_{cap}, sphere radius R, spherical cap height h, and actuator diameter c. For energy, we calculated the kinetic energy by comparing the potential energy in the resting position to the potential energy when rotated to the rotation angle.

$$KE = mg(H^{'} - H) = mg(r_{mid} - r_{in}) \tag{3}$$

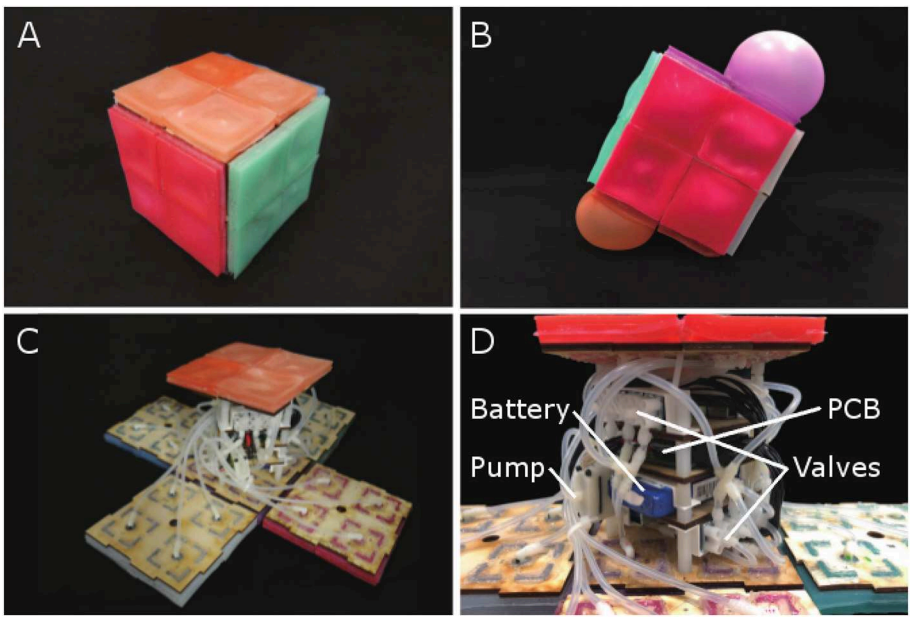

FIGURE 1 | (A) RUBIC, stationary. **(B)** Demonstration of untethered rolling via pneumatic actuators. **(C)** RUBIC with open casing. **(D)** The internal structure of RUBIC.

where H and H' are the height of the robot at resting and the turning position, respectively. For further details please see the **Supplementary Materials**.

The outcome of this analysis is that rotation angle, actuator volume and energy decrease with increasing number of faces, as shown in **Figure 2**. However, there is an exponential decrease in actuator volume. This indicates that tetrahedrons would require actuators to inflate to over four times larger than those actuating a cube.

Though icosahedron have the lowest values in all three metrics, there are other factors to consider. Fabrication complexity increases with the number of faces, as each face requires between 3 and 5 actuators, depending on the solid. Thus, cubes and octahedrons would require 24 actuators to enable multi-directional locomotion and dodecahedrons and icosahedrons would require 60. Another consideration is in the solid's stability when at rest, as it is anticipated that the resultant robot would be used in unstable environments. In this instance, a higher rotation angle is beneficial, as it means that the solid is less likely to roll due to environmental perturbations. As such, cubes were selected based on the low actuator volume required to reach the rotation angle compared with tetrahedrons and their stability compared with solids with more faces. Additionally, cubes are the only platonic solid capable of straight line locomotion, as all other solids follow angular paths when rolled from face to face.

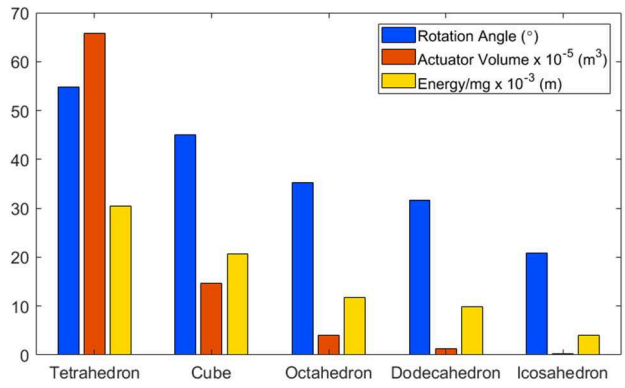

FIGURE 2 | A comparison of platonic solids, based on: (i) Rotation Angle: The angle each solid must be rotated in order to flip to the next face. (ii) Actuator Volume: The volume an actuator would have to inflate to in order to reach the rotation angle. (iii) Energy: The potential energy required to reach the rotation angle.

2.1. Robot Fabrication

2.1.1. Internal Structure

The internal structure of RUBIC can be seen in **Figures 1D, 3**. We designed the layout to allow for an even distribution of weight, thereby minimizing the interference with the kinematics of the cube. The components are fixed to 4 layers of laser cut plywood as shown in **Figure 3A**. The outer two layers house 12 3-way solenoid valves (5-6 V; Zonhen Electric Appliances), 6 on the top layer and 6 on the base layer. The middle two layers contain the PCB, the Lithium-ion Polymer battery (7.4 V; 1000 mAh, Turnigy) and 2 pumps (3 V, KPM14A; Koge Electronics CO., LTD.). Both pumps are connected to all 12 valves to ensure maximum pneumatic power, and each valve is connected to two actuators on opposite sides of the cube, as shown in **Figures 1D**, **3B**.

A key challenge in our design of RUBIC was to minimize size and weight in order to reduce the load on the pumps and increase locomotion speed. Size was a particular issue as actuating a larger

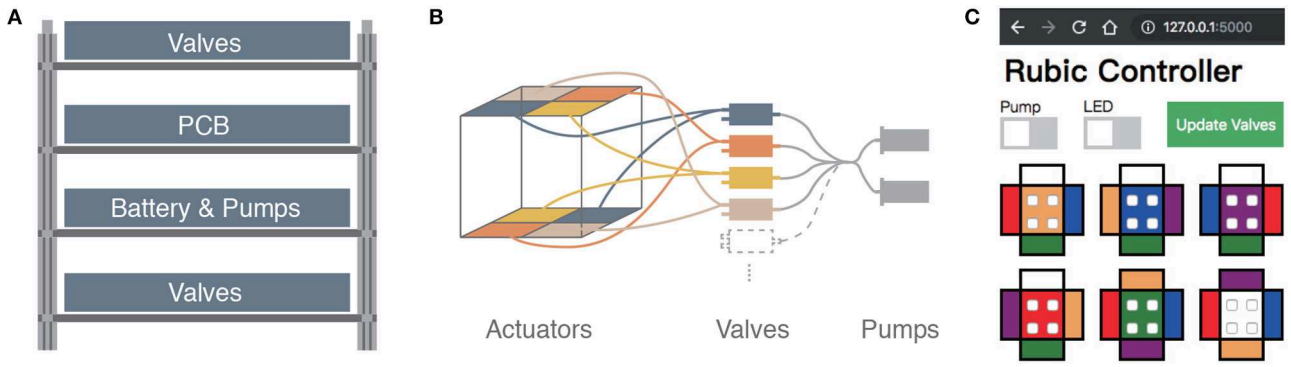

FIGURE 3 | (A) Schematic of layered structure inside RUBIC to house the battery, PCB and pneumatic system. **(B)** Schematic of pneumatic system for two of the six sides of RUBIC, from pumps (far right) to pairs of actuators via the valves. **(C)** Screenshot of the GUI used to control RUBIC.

cube would require a greater torque and create a greater distance for the actuators to lift in order to locomote. As a compromise, we chose to use 12 valves connected to opposing pairs of actuators, rather than having 24 valves with one valve per actuator. This saved on space and weight, allowing RUBIC to be a 10 cm cube and 0.83 kg, while containing all of the required electronics. However, this resulted in a decrease in speed since the pumps were then required to pump twice as many actuators at a time. It is also the cause of RUBIC's unique appearance when locomoting, observable in **Figure 1B**.

2.1.2. Actuators

We manufactured the pneumatic actuators from silicone elastomer (Ecoflex 00-30^{TM}; Smooth-On), as it is light-weight, versatile and highly compliant, reaching up to 900% expansion before tearing (Smooth-On, 2018). Further characterization of the elastomer has been performed by Sparks et al. (2015). Actuators were manufactured in a 2-step molding process. Bases and covers were fabricated separately, before being cured together along their edges to create a sealed air chamber, as shown in **Figure 4**. Each actuator measures 50 × 50 × 8 mm. The wall and ceiling thicknesses of each actuator are approximately 2 mm and 1.5 mm respectively. The base of the actuators are 3 mm thick and contain a constraining paper layer to limit expansion at the base (**Figure 4D**).

We designed the actuators with four right angled silicone extrusions to ease connection with the internal Medium-Density Fiberboard (MDF) body. A ring of silicone was also extruded from the center of the actuator to interface with the pneumatic input (external and internal diameters of 8 mm and 4 mm, respectively). Extruded structures are 4 mm in length, long enough to extend through holes in the 3 mm MDF body. Actuators were fixed to the internal structure of the cube with the use of silicone adhesive (Sil-Poxy^{TM}; Smooth-On). We dyed the actuators a different color for each side of the cube to make them distinguishable and to simplify setting up the control mechanism.

2.2. Principle of Operation

At start up, the Bluetooth communication channel is enabled (visual feedback is provided by an LED to confirm connection) and all valves and pumps are off. We control the robot from a PC or tablet via a graphical user interface (GUI) that was developed for ease of operation, as shown in **Figure 3C**. The GUI includes switches to initialize pumps and manipulate which valves are open or closed at any time. We update valves by selecting the actuator on each image that needs to be opened and then click "Update Valves," thus updating all valves at once. Opening a single valve translates to activating two actuators on the robot, as described in section 2.1.1 and illustrated in **Figure 3B**. We operate the robot by observing which side faces the ground, finding the corresponding colored face within the GUI and opening the two valves opposite to the direction of travel. The GUI updates all valves simultaneously, overcoming potential problems with off-setting actuation, which would result in an unwanted tilt.

We designed RUBIC to discretise the operable space surrounding it. This is a novelty that can be difficult to accomplish with soft robotic components, due to non-linearity of actuation and the high number of degrees of freedom that soft materials exhibit. In principle, this means that RUBIC translates its environment into a grid structure along which it locomotes. Inflating two actuators opposite to the direction of travel results in locomotion to the next grid point, either to the left, right, front or back. This discretisation allows for predictions to be made about how RUBIC can move in space. It also allows environments to be mapped such that routes can be planned prior to actuation of the robot.

3. ACTUATOR CHARACTERIZATION

The fluidic elastomer actuators are the fundamental components that allow locomotion of this robot. In this section we detail the steps taken to characterize these actuators.

3.1. Method

We designed RUBIC to operate untethered, thus increasing its operation space and eradicating restrictions resultant from a tethered connection. In order to operate untethered, all of the components had to be integrated inside the body of the

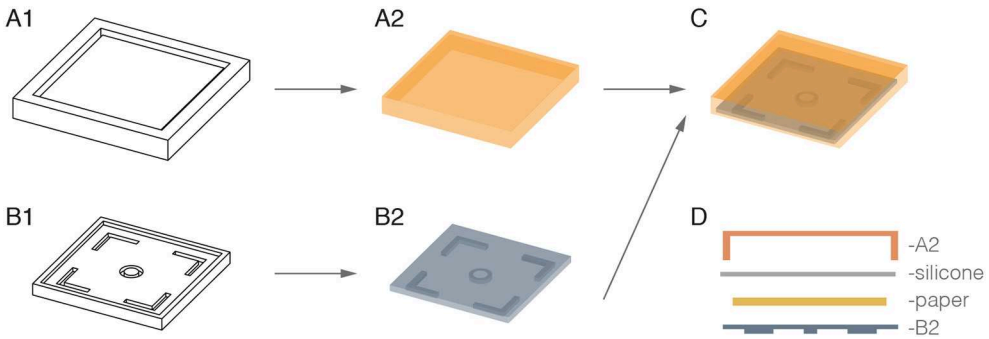

FIGURE 4 | Illustration of actuator fabrication in a 2-step molding process. The molds **(A1,B1)** were used to separately fabricate the silicone covers **(A2)** and bases **(B2)**. These were then cured together with another layer of silicone, into which a piece of paper was placed to create a complete air chamber with a radially constrained base **(C,D)**.

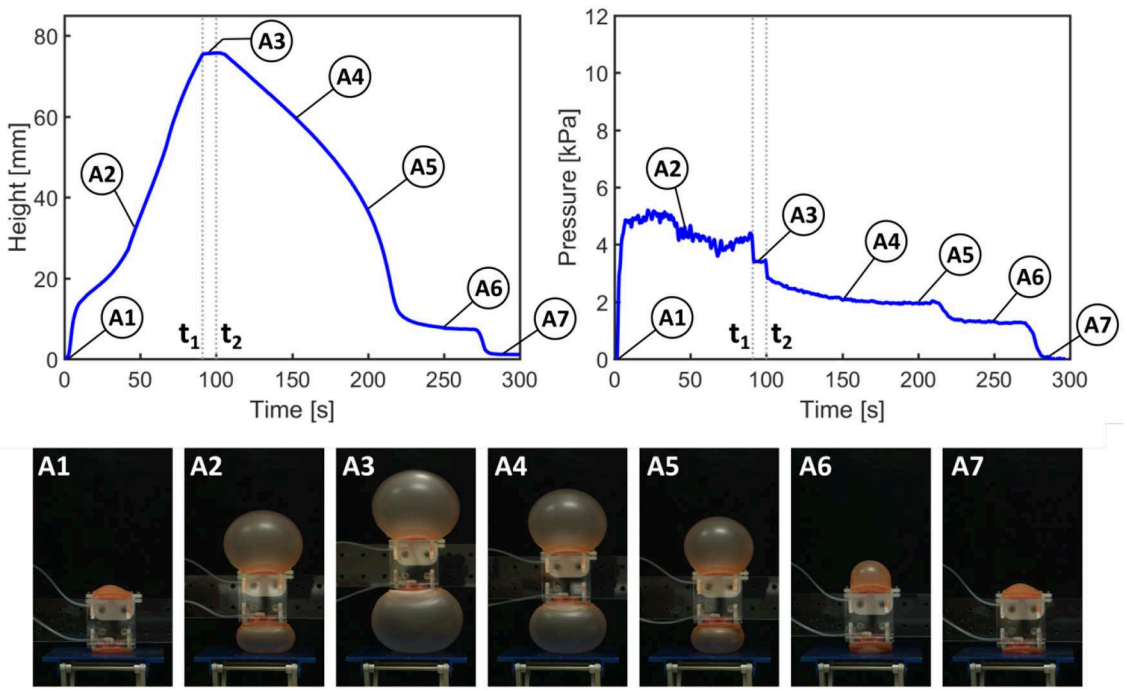

FIGURE 5 | Results of height and pressure measurements for actuation of paired actuators (as in RUBIC). t_1 signifies the time at which the pump is switched off; t_2 signifies the opening of the valve to release the air.

robot. To save space, smaller pumps had to be used and the number of valves reduced, as shown in **Figure 3** and discussed in section 2.1.1. Consequently, the pumps inflate two actuators simultaneously. To investigate the performance impact of this set-up we tested the actuators in terms of their vertical displacement and pressure reached with time for actuation of single and double (paired) actuators. We conducted tests with pumps equivalent to the on board pumps installed in RUBIC. Testing in this way allowed for a comparison in terms of both speed and pressure dynamics.

We attached the actuators to the bottom and, in the double actuator test, to the top of a linear guide. To test the performance of a single base actuator in lifting the robot, we set the weight of the supporting structure to match half of the robot's weight, as we assumed that one actuator provides half of the lift required for locomotion. We inflated the actuators until a height of 75 mm was reached, as this was the approximate height required to roll onto the next face, described in section 4.1 (**Figure 7**). We maintained this level until a valve (S070C-SBG-32; BEST Pneumatics Inc.) was opened to deflate the actuators. We measured the height with a laser displacement meter (LK-G152; Keyence) and the pressure inside the actuators with a pressure gauge (HSCDANN030PGAA5; Honeywell). The results we obtained

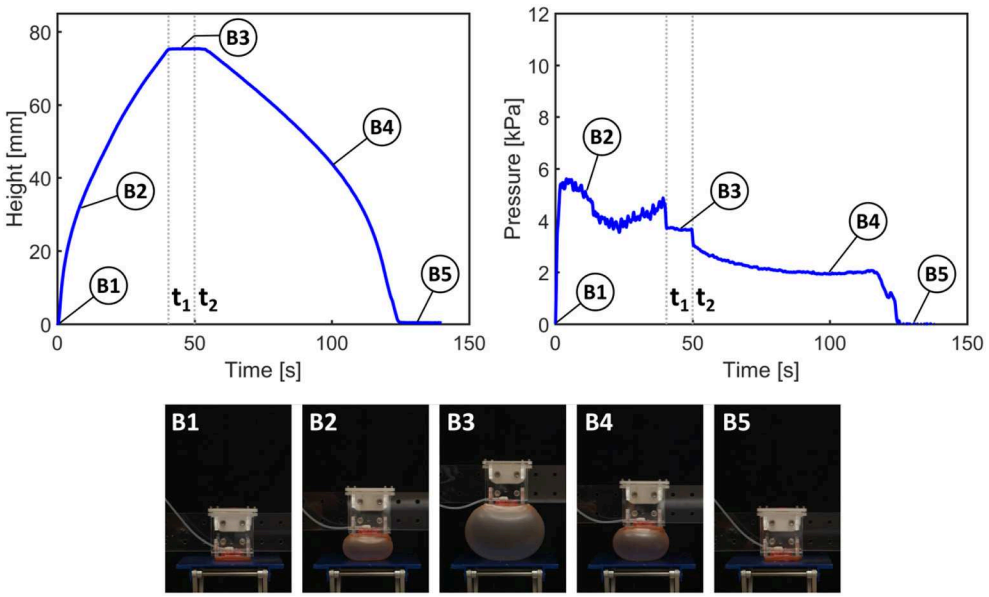

FIGURE 6 | Results of height and pressure measurement for actuation of a single actuator. t_1 signifies the time at which the pump is switched off; t_2 signifies the opening of the valve to release the air.

allow for comparison between the single (unpaired) and double (paired) actuators.

3.2. Results

In **Figures 5**, **6**, from time 0 to t_1, the pump is switched on to activate inflation of the actuators. From t_1 to t_2, the pump is switched off but the air is maintained in the system (i.e., the actuators are kept inflated); after time t_2 the valve is opened to release the air and allow the actuators to deflate.

Figure 5 shows the height and pressure measurements for actuation of the paired actuators, closely representing the actuation scheme used in RUBIC. For each pair of actuators, only the actuator on the bottom face of RUBIC is load-bearing and responsible for lifting the robot. To replicate this in the paired actuator experiment, we applied a load to one actuator and allowed the other to actuate freely. During the initial inflation period, the rate of vertical displacement drops temporarily (between A1 and A2) because the inflation of the top actuator is greater than that of the bottom actuator. As the pressure remains constant, this behavior can be explained by the slight difference in material thickness of the actuators and the additional external load acting on the bottom actuator (i.e., the weight of the test rig). While maintaining constant height, the actuator rapidly snapped through to a stable, high-strain ballooned state. This dynamic snap-through is a well studied phenomena with inflated hyperelastic membranes (Akkas, 1978). Toward the end of the deflation period (A6), the rate of pressure and height change levels due to a fold that developed in the bottom actuator. In that period, the top actuator deflated at a higher rate before both actuators returned to their initial configuration (A7).

The same general behavior can be observed using only one actuator. However, the actuator inflates at a steadier rate (B1 and B2 in **Figure 6**) as no mutual interference between the two actuators occurs. It also takes approximately half the time to reach the desired height. Considering the same general behavior for the two tested actuator configurations, the use of double actuator inflation is a valid trade-off to enable an untethered robot, although at the cost of locomotion speed.

4. LOCOMOTION CHARACTERIZATION

Locomotion of RUBIC is achieved by rolling from one face onto the next in a quantized Cartesian space. In this section, we describe the steps taken to characterize the locomotion abilities of RUBIC.

4.1. Analysis of Locomotion Schemes

4.1.1. Method

Locomotion of RUBIC consists of opening pairs of valves, allowing time for the actuators to fill with air and waiting for a tipping point to be passed (the moment at which the center of mass of the robot passes over the point of contact with the ground). A single step of the robot can be modeled simply by considering the leading edge of RUBIC as a hinge and then calculating the diameter the actuator has to inflate to (inflated diameter) in order to reach the tipping point, as depicted in **Figure 7A**. Assuming uniform weight distribution within the robot, we deduce that the angle required for the robot to reach its tipping point is 45° when the robot locomotes with rear actuators alone. We propose that a second locomotion pattern could reduce the time required to complete a single step. This second pattern consists of activating the rear actuators as before, but then activating the front actuators during the roll to assist the motion.

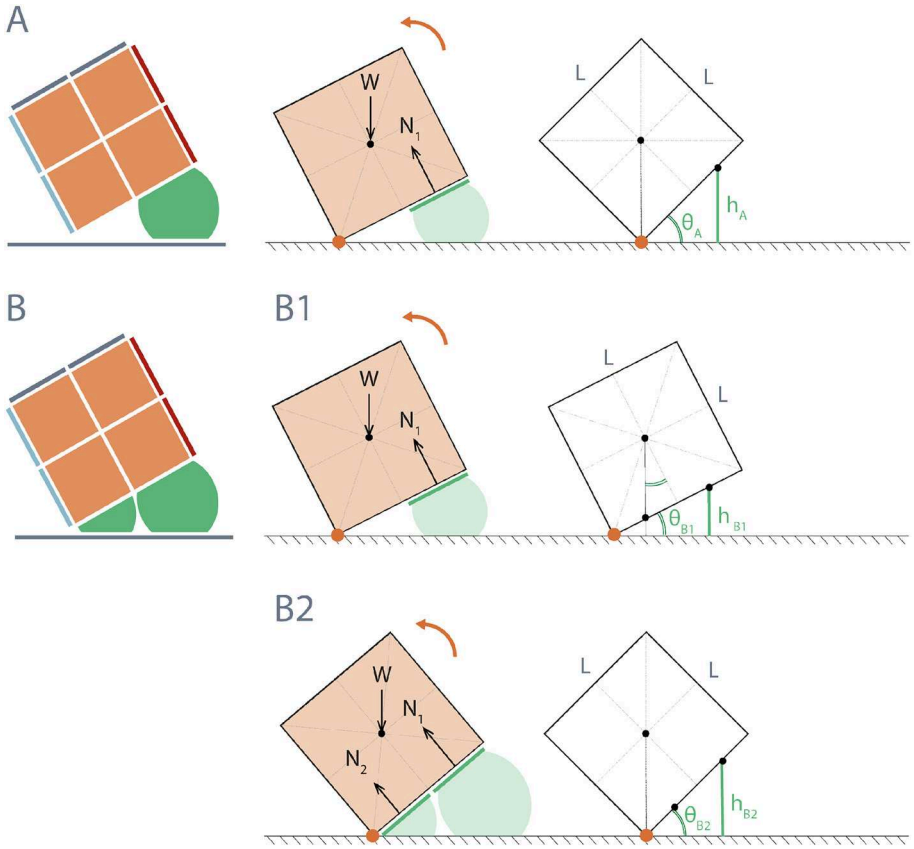

FIGURE 7 | Diagram of height required from actuators to reach tipping angle of RUBIC for two actuation schemes: **(A)** Rear actuators only; $\theta_A = 45°$, resulting in actuator height $h_A = 3L\sin\theta_A/4 = 53.03$ mm for $L = 100$ mm. **(B)** Front and rear actuators; **(B1)** rear actuators initially activated until RUBIC reaches minimum angle $\theta_{B1} = tan^{-1}(1/2) = 26.6°$, where the center of mass shifts beyond the center of the front actuators ($L/4$ from hinge point), $h_{B1} = 33.58$ mm for $L = 100$ mm, **(B2)** front actuators are then additionally activated until tipping angle $\theta_{B2} = 45°$ is reached, (where $h_{B2} = h_A$).

Figure 7B illustrates a theoretical model for this actuation pattern, again assuming uniform weight distribution. For the front actuators to assist, not impede, the roll, they must be activated once the center of mass has passed over the center of the front actuator. In doing so they provide additional torque about the hinge point. Activation prior to this point does not assist with locomotion, where the angle θ at which the front actuators should be activated was calculated from the geometry of a cube to be at least 26.6° as shown in **Figure 7B1**.

To test this alternative actuation pattern, we placed RUBIC in front of a blackout curtain with space to locomote forwards. We cut several freestanding plywood triangles to act as physical representations for each value of angle θ being tested and placed these in front of RUBIC. We then inflated the rear actuators until the base of RUBIC matched the freestanding representation of θ, at which point we inflated the front actuators as shown in **Figure 8A**. We performed three tests for θ = 10°, 15°, 20°, and 25°. We then extracted time-stamped data, including the point at which valves are opened, the point at which the front actuators are actuated and the end of the roll, from recorded video and used this data to evaluate the effect of changing angle θ.

To determine the linearity of RUBIC's locomotion, we measured the angle of deviation from a straight line path. A primary novelty for RUBIC is the quantization of its environment and its movement within a 2D grid. In order for this pattern of locomotion to be achievable and predictable, the path that RUBIC follows when rolling in any one direction must be as straight as possible.

We aligned the robot to a straight line on a large, flat surface and recorded its starting position. RUBIC then locomoted step by step along this line until two full rotations were complete (resulting in a total of 8 steps being taken). We then recorded the final position and calculated the angle of deviation. We ran 5 trials for both the original locomotion pattern (using rear actuators only) and the alternative pattern (using both rear and front actuators, with front actuators activated once RUBIC reached an angle of 15°, based on the results of the previous test). We also recorded position data for each step within two trials of the alternative actuation pattern to illustrate an example linear path. **Figure 9** shows the experimental set-up and an example path for the line-following experiment where lengths A and B equate to the measured distance and deviation of the final

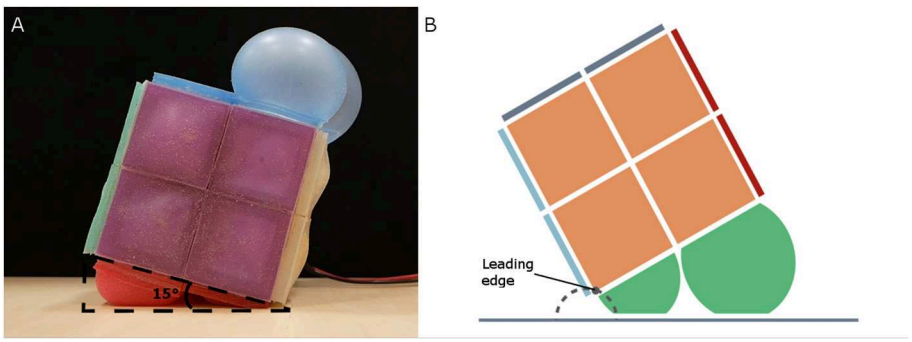

FIGURE 8 | (A) Test set-up for alternative actuation pattern, showing threshold angle (θ = 15° in this case). **(B)** Approximate leading edge trajectory (dashed gray) of RUBIC when alternative actuation pattern is used.

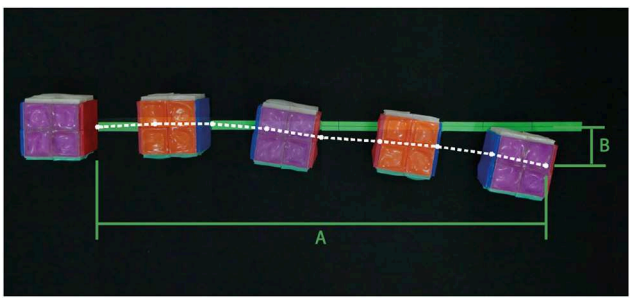

FIGURE 9 | Example deviation of RUBIC from the central line during the course of 2 full rotations using the alternative actuation scheme (front and rear actuators used). Measured trajectory of leading edge shown in white. Final displacement **(A)** = 909.75 mm and deviation from center **(B)** = 78.51 mm.

position relative to the central line. We calculated the overall deviation angle α as $\alpha = arctan(B/A)$.

To evaluate RUBIC's capabilities over uneven terrain, we devised a test to measure its performance traversing a surface that included steps that ranged from 20 to 40 mm in 5 mm increments. For each step, we aligned RUBIC such that the robot landed with the center of the robot just off the edge of the step, as shown in **Figure 10B**. In this way, the rear actuators were not on the step and were able to continue pushing the ground. The front actuators were then actuated once the base of the robot had reached a 15° angle with the step, making contact with the step and assisting the roll. It was expected that RUBIC would not be able to traverse a step greater than 50 mm since the pivot point between RUBIC and the step would be too high to lift the center of mass over. Video was taken of the experiment and the set up can be seen in **Figure 10**. We extracted time data from video recordings as a metric to compare different climbing methodologies.

4.1.2. Results

For the original locomotion scheme, **Figure 7A**, with only rear actuators activated, the angle required to make a step was calculated to be 45°. In practice, this was successful and one roll was found to take 55.03 s with standard deviation of 1.04 s across 3 trials.

The most time efficient control plan for activating the front actuators was at θ = 15°, decreasing the total time taken to roll to 51.70 s. Activating the front actuators at an angle of 10° failed, resulting in lifting the front side of RUBIC upward instead of assisting the roll. Additionally, it was found that actuation of the front actuators at θ = 15° increased the total step length by 1.10% as listed in **Table 1**. This occurred due to the inflation of the front actuators generating both a turning force in the direction of travel and an upwards force that lifted the leading edge of the cube from the ground. This has the effect of shifting the point of turn beyond the edge of the cube, resulting in an extended step length. The trajectory of the leading edge in this scenario is shown in **Figure 8B**.

Figure 9 gives an example trajectory of RUBIC as it traversed along the central line. As can be seen, the deviation of RUBIC from the central line increases with each roll. The total deviation and distance traveled by RUBIC were measured and the mean results can be seen in **Table 1**. The results show that the alternative locomotion scheme, while being faster than the original scheme as previously discussed, also results in a smaller deviation of RUBIC from the central line as it travels. Not only this, but the overall distance traveled by RUBIC for the two rotations was 10 mm further than in the rear actuator case.

The deviation of RUBIC from the central line was 12.18% of the distance traveled for the original locomotion scheme and 7.92% for the alternative scheme. While the alternative locomotion scheme (front and rear actuators) is faster and more precise than the original locomotion scheme (rear actuators only), the results of this test show that there is uncertainty in the discretised space RUBIC can navigate. The further RUBIC travels, the greater the uncertainty of its final position. Observation of video recordings shows that much of this uncertainty is due to irregularities in the fabrication of the actuators, as actuators will inflate to different sizes at different rates depending on the thickness of the actuator walls. This will be elaborated on in the discussion.

RUBIC was successfully able to climb step sizes of up to 35 mm, but was not capable of climbing a 40 mm step. The failure of RUBIC to navigate the 40 mm step was due to the

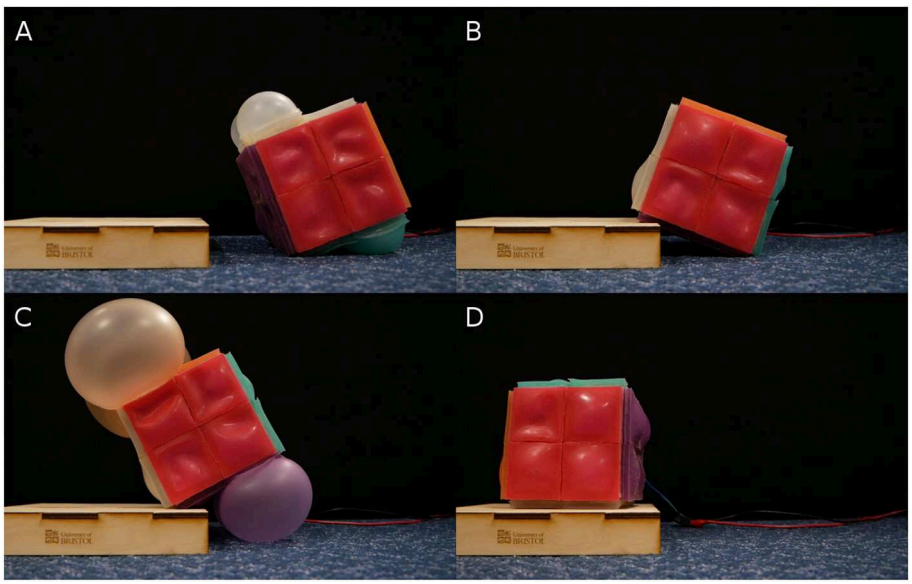

FIGURE 10 | Snapshots of RUBIC traversing up a 35 mm step in chronological order from **(A–D)**.

TABLE 1 | Mean deviation of RUBIC from the central line after two full rotations (eight individual rolls) across five trials for the original locomotion scheme and for the alternative scheme.

Locomotion scheme	Mean deviation (mm)	Mean distance (mm)	Mean angle (°)	SD of angle (°)
Original: rear actuator only	110.8	909.7	7.09	3.24
Alternative: front actuators activated at 15°	72.8	919.7	4.58	2.78

Angle calculated from deviation and total distance travelled.

maximum expansion of the actuators. However, completion of a 35 mm step is over a third of RUBIC's height and future iterations of RUBIC can be scaled according to the demands of the environment. In addition, less dramatic terrains with slopes and bumps, rather than sharp corners and steps, may be less of a challenge for RUBIC.

5. DISCUSSION

In this paper, we have demonstrated RUBIC's ability to locomote on a flat surface and across uneven terrain. We have also characterized the fluidic elastomer actuators and provided two differing locomoting patterns for RUBIC.

For the alternative locomotion scheme, an angle of 26.6° was calculated to be the optimal angle for actuation of the front actuators as illustrated in **Figure 7B**. However, in practice, the optimal angle was 15° which reduced the time per roll by 3.33 s. Two reasons are presented for this discrepancy between the theoretical and practical optimal angle. Firstly, when the front actuators are activated there is a short delay while they inflate before they touch the ground and provide active assistance. During this time, RUBIC continues to rotate and, therefore, the angle at which the front actuators are providing assistance is greater than the angle at which they are initially activated. Secondly, the theory does not take into consideration the added torque of the actuators inflating and pushing against each other. When the front actuators inflate they are enclosed by RUBIC and the inflated rear actuators, and so inflation generates a force against both. This force against the rear actuators would add to the torque acting to roll RUBIC.

Deviation from a straight line path while locomoting was also reduced with the alternative locomotion scheme, as shown in **Table 1**. The angle of deviation was reduced by 2.51° for two complete rotations (i.e., 8 individual rolls), resulting in a linear deviation of 7.92% of the distance traveled. In addition, the distance traveled was increased with the alternative scheme by 1.10% for two complete rotations. The reason for this being that the turning point is shifted forwards (in the direction of travel) during actuation, as actuating the front actuators raises the leading edge (previously the pivot point) of the robot from the ground as illustrated in **Figure 8B**.

We initially proposed the alternative locomotion scheme to improve RUBIC's locomotion speed. Though testing shows that only 3.33 s are saved per roll, a 6% improvement, the alternative locomotion scheme offers other benefits, such as stair climbing, as well. While discrete movement in space is beneficial for route planning and allowing for prediction of motion, there may be instances when RUBIC becomes stuck, or unable to take a full step in a specific direction and needs to locomote away from its grid path. An instance of this could be if RUBIC is moving within a narrow corridor and its movement grid is misaligned, such that operating in a straight line would result in hitting either

wall. In this instance, it would be beneficial to be able to realign RUBIC's locomotion grid, such that RUBIC can then navigate the corridor. Alternating between the alternative locomotion scheme and the original locomotion scheme provides one such method for realigning RUBIC's grid space, as each locomotion scheme has a different step length. This means that small adjustments can be made to RUBIC's locomotion to allow for such difficulties.

One of the major drawbacks in this iteration of RUBIC is the pairing of actuators. Due to the coupling of actuators to a single valve, if the power of the pumps is insufficient, the top, unloaded actuators inflate first until they reach the back pressure of the pumps (i.e., when the pressure in the actuator is equal to the pressure from the pumps) only after which the bottom loaded actuators will start to be inflated. The redundant actuation of the top actuators slows the speed down. Actuating a single actuator at a time, rather than two simultaneously as seen in RUBIC, significantly reduced inflation times and would, therefore, increase locomotion speed. However, due to limited internal space, a larger pump or more valves (to allow one valve per actuator) was not practical in this iteration of RUBIC. Future work will address this issue.

The biggest factor that limits the accuracy of the robot is irregularities in the fabrication of the actuators. Slight deviations in actuator wall thickness result in differences in inflation rate and maximum inflation diameter. As a consequence, the actuators rolling RUBIC are slightly imbalanced causing a tilt that sends RUBIC slightly off course as it rolls. This will be improved in future by refining the actuator fabrication method, ensuring precision and consistency. As a result, this deviation will be minimized and uncertainty in path following reduced.

Scalability of RUBIC is of interest for its suitability in applications that may require a smaller robot to navigate intricate environments, or a larger robot to overcome obstacles in a specific terrain. From the calculations approximating the actuator volume required for locomotion (see section 2 or **Supplementary Material**), we can calculate the actuator volume required for different length scales of RUBIC. This approximation gives a cubic increase in volume for a linear increase in side length. Therefore, doubling the side length of RUBIC to 0.2 m results in an 8-fold increase in actuator volume required to locomote and tripling side length to 0.3 m corresponds to a 27-fold increase in actuator volume required. If we assume a constant flow rate to the actuators this results in a cubic increase in time taken to actuate, significantly reducing locomotion speed. To increase the size of RUBIC, higher capacity pumps would be necessary to maintain performance. Reducing the size of RUBIC does not have this problem, but requires smaller valves, pumps and electronics to physically fit into the structure. These factors are limitations to the scalability of RUBIC.

In this paper, we demonstrate RUBIC, a robot with soft actuators that locomotes by rolling. The novelty of RUBIC compared with other rolling robots, such as Li et al. (2018), is that its path can be predicted, as it moves along a quantized Cartesian grid. To simplify the control mechanism, future iterations of the robot will include an Inertial Measurement Unit (IMU) so that the robot can self-sense which face is to the ground. The GUI would then indicate which face should be actuated, allowing for operation of the robot without line of sight and, ultimately, fully autonomous operation. Although many improvements can still be made, the current design of RUBIC is able to locomote untethered and across terrain that undulates by up to 35% of RUBIC's height. These are ideal properties for robots working in unstable structures, environmental monitoring and other challenging environments. Unlike other soft, rolling robots mentioned within the introduction, RUBIC is inherently stable on all of its faces and able to translate its environment to a grid space. As such, we propose future applications in environmental sampling, localization and *ad hoc* network infrastructure, or as a foundation for larger robots and structures. Future work will also explore miniaturizing the internal components and utilizing recent soft pumps and valves (Rothemund et al., 2018; Cao et al., 2019; Mahon et al., 2019) to allow for fully collapsible, untethered robots that can be readily deployed.

DATA AVAILABILITY

Data are available at the University of Bristol data repository, data.bris, at https://doi.org/10.5523/bris.3dxxbzlym53ne2ou9vcjn6if3i.

AUTHOR CONTRIBUTIONS

H-YC, RD, AH, AP, MS, and EW: contributed equally in the design of the robot and writing of the manuscript. MG, JR, and AC: provided guidance throughout the robot design and reviewed the written content. All authors read and approved the submitted version.

FUNDING

AC was funded by EPSRC grant EP/P025846/1; JR was funded by Royal Academy of Engineering as a Chair in Emerging Technologies and EPSRC grants EP/M020460/1 and EP/M026388/1; H-YC was funded by the University of Bristol; RD, EW, and MG are funded by EPSRC Centre for Doctoral Training in Future Autonomous and Robotic Systems (FARSCOPE, grant EP/L015293/1); AH, AP, and MS are funded by EPSRC DTP grants.

ACKNOWLEDGMENTS

We would like to thank Aaron Fishman and Gábor Sotér for helping us create the GUI and for moral support leading up to the RoboSoft Grand Challenge. We would also like to thank the organizers of the event for holding this exciting competition that brought us together as a team to build this innovative soft robot.

SUPPLEMENTARY MATERIAL

The Supplementary Material for this article can be found online at: https://www.frontiersin.org/articles/10.3389/frobt.2019.00052/full#supplementary-material

REFERENCES

Akkas, N. (1978). On the dynamic snap-out instability of inflated non-linear spherical membranes. *Int. J. Non-Lin. Mech.* 13, 177–183. doi: 10.1016/0020-7462(78)90006-9

Cao, C., Gao, X., and Conn, A. (2019). A magnetically-coupled dielectric elastomer pump for soft robotics. *Adv. Mater. Technol.* 1900128, doi: 10.1002/admt.201900128

Ilievski, F., Mazzeo, A. D., Shepherd, R. F., Chen, X., and Whitesides, G. M. (2011). Soft robotics for chemists. *Angew. Chem. Int. Ed.* 50, 1890–1895. doi: 10.1002/anie.201006464

Kim, S., Laschi, C., and Trimmer, B. (2013). Soft robotics: a bioinspired evolution in robotics. *Trends Biotechnol.* 31, 287–294. doi: 10.1016/j.tibtech.2013.03.002

Kühnel, D. T., Helps, T., and Rossiter, J. (2016). Kinematic analysis of vibrobot: a soft, hopping robot with stiffness- and shape-changing abilities. *Front. Robot. AI* 3:60. doi: 10.3389/frobt.2016.00060

Li, W., Zhang, W., Zou, H., Peng, Z., and Meng, G. (2018). A fast rolling soft robot driven by dielectric elastomer. *IEEE/ASME Trans. Mechatr.* 23, 1630–1640. doi: 10.1109/TMECH.2018.2840688

Mahon, S. T., Buchoux, A., Sayed, M. E., Teng, L., and Stokes, A. A. (2019). Soft robots for extreme environments: removing electronic control. *IEEE Int. Conf. Soft Robot.* 782–787. doi: 10.1109/ROBOSOFT.2019.8722755

Marchese, A. D., Katzschmann, R. K., and Rus, D. (2015). A recipe for soft fluidic elastomer robots. *Soft Robot.* 2, 7–25. doi: 10.1089/soro.2014.0022

Nemiroski, A., Shevchenko, Y. Y., Stokes, A. A., Unal, B., Ainla, A., Albert, S., et al. (2017). Arthrobots. *Soft Robot.* 4, 183–190. doi: 10.1089/soro.2016.0043

Rafsanjani, A., Zhang, Y., Liu, B., Rubinstein, S. M., and Bertoldi, K. (2018). Kirigami skins make a simple soft actuator crawl. *Sci. Robot.* 3:eaar7555. doi: 10.1126/scirobotics.aar7555

Rothemund, P., Ainla, A., Belding, L., Preston, D., Kurihara, S., Suo, Z., et al. (2018). A soft, bistable valve for autonomous control of soft actuators. *Sci. Robot.* 3, 1–10. doi: 10.1126/scirobotics.aar7986

Shepherd, R. F., Ilievski, F., Choi, W., Morin, S. A., Stokes, A. A., Mazzeo, A. D., et al. (2011). Multigait soft robot. *Proc. Natl. Acad. Sci. U.S.A.* 108, 20400–20403. doi: 10.1073/pnas.1116564108

Siegwart, R., and Nourbakhsh, I. R. (2004). *Introduction to Autonomous Mobile Robots*. Cambridge, MA: A Bradford Book.

Smooth-On (2018). *Ecoflex™ Series*. Technical bulletin, Smooth-On.

Sparks, J. L., Vavalle, N. A., Kasting, K. E., Long, B., Tanaka, M. L., Sanger, P. A. et al. (2015). Use of silicone materials to simulate tissue biomechanics as related to deep tissue injury. *Adv. Skin Wound Care* 28, 59–68. doi: 10.1097/01.ASW.0000460127.47415.6e

Steltz, E., Mozeika, A., Rembisz, J., Corson, N., and M Jaeger, H. (2010)."Jamming as an enabling technology for soft robotics," in *Proc. SPIE 7642, Electroactive Polymer Actuators and Devices (EAPAD)*, 764225. doi: 10.1117/12.853182

Steltz, E., Mozeika, A., Rodenberg, N., Brown, E., and Jaeger, H. (2009). "JSEL: jamming skin enabled locomotion," in *2009 IEEE/RSJ International Conference on Intelligent Robots and Systems, IROS,* 5672–5677. doi: 10.1109/IROS.2009.5354790

Tolley, M., Shepherd, R., Mosadegh, B., Galloway, K., Wehner, M., Karpelson, M., et al. (2014a). A resilient, untethered soft robot. *Soft Robot.* 1, 213–223. doi: 10.1089/soro.2014.0008

Tolley, M. T., Shepherd, R. F., Karpelson, M., Bartlett, N. W., Galloway, K. C., Wehner, M., et al. (2014b). "An untethered jumping soft robot," in *2014 IEEE/RSJ International Conference on Intelligent Robots and Systems* (Chicago, IL), 561–566.

Umedachi, T., Vikas, V., and Trimmer, B. A. (2016). Softworms: the design and control of non-pneumatic, 3d-printed, deformable robots. *Bioinspir. Biomimet.* 11, 025001–1–025001–16. doi: 10.1088/1748-3190/11/2/025001

Wang, J., Fei, Y., and Liu, Z. (2019). Locomotion modeling of a triangular closed-chain soft rolling robot. *Mechatronics* 57, 150–163. doi: 10.1016/j.mechatronics.2018.12.003

Conflict of Interest Statement: The authors declare that the research was conducted in the absence of any commercial or financial relationships that could be construed as a potential conflict of interest.

Advantages of publishing in Frontiers

OPEN ACCESS
Articles are free to read for greatest visibility and readership

FAST PUBLICATION
Around 90 days from submission to decision

HIGH QUALITY PEER-REVIEW
Rigorous, collaborative, and constructive peer-review

TRANSPARENT PEER-REVIEW
Editors and reviewers acknowledged by name on published articles

Frontiers
Avenue du Tribunal-Fédéral 34
1005 Lausanne | Switzerland

Visit us: www.frontiersin.org
Contact us: info@frontiersin.org | +41 21 510 17 00

REPRODUCIBILITY OF RESEARCH
Support open data and methods to enhance research reproducibility

DIGITAL PUBLISHING
Articles designed for optimal readership across devices

FOLLOW US
@frontiersin

IMPACT METRICS
Advanced article metrics track visibility across digital media

EXTENSIVE PROMOTION
Marketing and promotion of impactful research

LOOP RESEARCH NETWORK
Our network increases your article's readership